UNIVERSITAT POLITÈCNICA DE VALÈNCIA

DEPARTAMENTO DE COMUNICACIONES

NANOPHOTONICS TECHNOLOGY CENTER

Doctoral Thesis

Novel applications of Optical Diffraction Tomography: On-chip Microscopy and Detection of Invisibility Cloaks

Francisco Javier Díaz Fernández

Supervisors: Javier Martí Sendra

Carlos García Meca

December 2021, Valencia (Spain)

UNIVERSITAT POLITÈCNICA DE VALÈNCIA

DEPARTAMENTO DE COMUNICACIONES

Novel applications of Optical Diffraction Tomography: On-chip Microscopy and Detection of Invisibility Cloaks

Francisco Javier Díaz Fernández

Supervisors: Javier Martí Sendra
Carlos García Meca

Doctoral Thesis

submitted for the degree of
Doctor of Philosophy in Telecommunication Engineering

December 2021, Valencia

Francisco Javier Díaz Fernández
fradafer@ntc.upv.es; franj.vdo@gmail.com

Novel applications of Optical Diffraction Tomography: On-chip Microscopy and Invisibility Cloaks Detection
PhD Thesis, Nanophotonics Technology Center
Supervisors: Javier Martí Sendra and Carlos García Meca
UNIVERSITAT POLITÈCNICA DE VALÈNCIA

Cover: Natalia Mayordomo Giner

This thesis has been developed under grant FPI BES-2016-076818 funded by MCIN/AEI/ 10.13039/501100011033 and by the European Union

Version 3, December 2021

A mis padres,
a Mila y a Nata

"When bad things happen, I know you want to believe they are a joke.
But sometimes life is scary and dark.
That is why we must find the light."

BMO - Adventure time

Si alguna cosa volem la meva gent i jo
no és servir d'exemple, no és tenir raó.
Si alguna cosa anhelem és la vibració,
l'esclat de bogeria en els ulls de l'inventor.

Manel - Els entusiasmats

Dadnos, santos del cielo, rigor científico.
Dadnos, santos del cielo, una visión global bastante aproximada.

Amanece, que no es poco

Acknowledgements

No puedo empezar de otra forma que no sea recordando el carácter cooperativo de la investigación científica. El trabajo contenido en esta tesis doctoral no habría sido posible sin la ayuda y el apoyo de muchísimas personas.

Arquitectónicamente, son tres puntos de apoyo los necesarios para asegurar la estabilidad. En mi caso, he tenido la suerte de haber podido contar con el apoyo de tres personas imprescindibles. En primer lugar, quiero agradecer a Javier Martí la posibilidad de trabajar en el NTC de la UPV. La capacidad de Javier para ir varios pasos por delante del contexto científico no ha dejado de sorprenderme, y ha sido totalmente un privilegio trabajar a su lado. Otro punto de apoyo imprescindible ha sido el responsable de que no haya tirado la toalla en los momentos más difíciles: Carlos García Meca, quién me ha enseñado que la ciencia se cocina a fuego lento, a partir de tener bien claros los pilares más fundamentales y a través de mucho esfuerzo. Gracias por todas las tardes trabajando codo con codo, y lamento no haber sido capaz aún de asimilar ni un cuarto del rigor científico que bien te has esforzado en transmitirme, eres un ejemplo para la profesión de investigador. Mi tercer pilar es en realidad el primero que estuvo a mi lado y no dudó ni un segundo en ayudarme a colocarme en este gran mundo. Sergio Lechago, muchas gracias por dejarme ser tu padawan, por todas las enseñanzas, risas, por disparar el amistómetro, y por ser ejemplo tanto dentro como fuera del centro.

También quiero aprovechar estas líneas para agradecer a Elena Pinilla el transformar mis inquietudes en presentaciones a congresos. Me has ayudado a crecer tanto a nivel técnico (a través del SNOM) como a nivel personal. Muchas gracias Jaime García y Alejandro Martínez por la posibilidad de colaborar con vosotros. Gracias a Amadeu por la fabricación y a Maribel y David Zurita por ayudarme a encontrar soluciones.

Afterwards, I wish to thank Jochen Gück and Paul Müller, from the Max Planck Institute for the Science of Light. Your work is totally an inspiration to me as can be seen through this dissertation. It has been a pleasure to work with both of you and I hope to continue the collaboration in the near future.

This thesis has been reviewed by a panel of experts including YongKeun Park, Giovanna Calò and Romain Fleury. In addition, the three members of the evaluation panel for the thesis defense were Borja Vidal, Daniel Torrent and Giovanna Calò. I would like to thank them for the deference of dedicating their time to examine this thesis, which has been considerably improved thanks to their comments. It has been a real honor to have the opinion of these five distinguished scientists on this work.

El primer empujón hacia las puertas del centro me lo dio Jorge Ibáñez, ¡mil gracias!

Quienes hemos pasado por el NTC sabemos que hay un gran equipo detrás que permite que todo funcione. Muchas gracias a Jose, Cristina, Isabel, Carlos, Dora, Ortiz, Luis, Laurent, Juan, Alfredo, Guillermo, Satur, Tere... Fue una suerte aterrizar en la sala diáfana en un momento con tanta gente brillante e inspiradora, como son Carles, Angie, Marghe, Diego, Alex, Julio, Sara, Pau, Luis S., Álvaro, Antoine, Andrés, Alba y Rafaelle. De igual manera, quiero agradecer a los que han llegado después, por todo lo que me han enseñado, los momentos que hemos compartido, y los que nos quedan. Gracias Paula, Gus, Elena, Manel, Jose, Javi R., Yoannet, Antonio, Laura, Evelyn, Cristina, Roberto, Javi A. y Jorge. Muchas gracias Leo, por ser ejemplo vital y por *la cuadradita, la de abajo*.

Un grupo de personas a las que admiro ha alimentado mi motor vital durante todos estos años. Además de su diferente (pero acertada en cualquier caso) visión de la vida, y de la amistad que nos une y unirá; me han ayudado a crecer en diferentes aspectos. Gracias, Javi, por recordarme quién soy y quién quiero ser, y engancharme desde el primer día que pisaste este centro. Gracias, Luis, por la diversión, rigurosidad y pasión. Gracias, Kike, por tu amor y dedicación a la ciencia (¡y el blender!). Gracias, Seppo, por las recetas y la alegría que impregnas a los espacios. Gracias, Jad, por ser mi auténtico chamán y ejemplo de tenacidad. Gracias, Miguel, por expandir mi universo musical. Os quiero.

Indudablemente, mis inquietudes artísticas me han llevado a conocer a muchísimas personas, las cuáles me han enriquecido personalmente. Muchas gracias a Elena, Miriam, Cinta, Sergio, Jesther, Sergi, Javi, Sari, Vicky, Russell, Eze y David. Vuestras enseñanzas y apoyo me han permitido mantener la estabilidad mental necesaria para realizar la tesis.

En este sentido, quiero agradecer al GOPU de la UPV, y en concreto, a Cristina. And thank you very much Ari for your help with the defense!

Rememorando estos últimos años, muchos son los amigos que han estado apoyándome y acogiéndome cuándo los he necesitado. Tengo la suerte de que la lista sea prácticamente infinita, pero es de recibo nombrar por aquí a Torjo, Cris, Sergio, Juan, Jose, Sam, Angelillo, Sofía, Adri, Jorge, Saúl, Fabio, Juli, Carmen, Conce, Raquel, Pun, Bort, Nur, Cari, Manolillo, Angelda, Castillo, Vicen, Cris, Fini, Edu, Tom, Darío, López, Silvia, Ana, Vio, María, Ramón, Andrea, Marta, el equipo Napia y los Chavales.

Obviamente, me he dejado para el final a las personas que más quiero. El apoyo más importante, no sólo durante estos años, si no durante toda mi vida, ha venido por parte de mi familia. Bienvenido Lucca, que tienes la suerte de tener los mejores padres. Gracias a mis abuelos, a mis tíos, a mis primos, a Montse, Manu y Eduardo. Y muy especialmente, a mis padres, pues la libertad que me han proporcionado siempre es la principal responsable de cada uno de los pasos que he dado, incluido este, dejándome descubrir mi camino asegurándose de que no me falte nada. Gracias por supuesto a Mila, mi faro vital y a la que me gustaría servir de ejemplo. Y como no hay Flan sin Nata, gracias, constante mía. Tú, que podrías estar en la mesa de ricos y poderosos, has elegido formar hogar con este humilde manchego. Si alguna vez he conseguido ser constante en el trabajo, ha sido imitándote. Gracias por toda la felicidad y estabilidad que me aportas, y por compartir conmigo tu fascinante visión de lo que nos rodea.

Abstract

DIFFRACTION TOMOGRAPHY arises to improve previous imaging techniques by considering the wave nature of light. Whereas the first medical imaging systems relied only on non-diffracting sources, this approach results in an enhanced reconstruction of the object's refractive index distribution, allowing, for example, the study of subcellular structures. Likewise, the demand for increasingly faster and secure telecommunication networks led to the advent of photonics. Two decades ago, the combination of these two fields gave rise to the first optical diffraction tomography (ODT) systems, which have rapidly evolved during this century. In this thesis, we present two novel applications of ODT. The first one is related to the concept of tomographic phase microscopy (TPM), a version of ODT that enables the study of isolated cells, with many applications in biomedicine, such as the diagnosis and prognosis of cancer. Nevertheless, current TPM systems are expensive, heavy, and cumbersome. To solve these issues we propose the concept of on-chip TPM. For this purpose, we design a roadmap towards the first integrated tomographic device in the frame of lab-on-a-chip (LoC) technology and develop the first steps to this end: 1) Until now, only flat detectors have been used to obtain the refractive index maps of the objects studied in TPM, based on the detection of the forward scattering. However, fundamental physical principles indicate that measuring also the backscattered field should improve the resolution of the images. Moreover, a flat detector is not the optimal configuration for on-chip TPM. In this vein, we have explored the possibility of using circular detectors in this scenario as a more suitable technique for on-chip configurations, demonstrating at the same time that this approach provides a better resolution than the linear one. 2) We propose a TPM on-chip scheme based on the use of dielectric nanoantennas as the ODT light source and detector pixels, and experimentally characterize their near-field behavior via scanning near-field optical microscopy. As for the second application, we study the potential of ODT as a new paradigm in the detection of realistic invisibility cloaks, one of the most important applications of metamaterials. Up to now, the scattering cross section (SCS) has been used as the gold standard to design and observe the effectiveness of these devices in hiding objects. In our study, we show that ODT can detect practical invisibility cloaks with a higher sensitivity than that offered by the SCS, even at the optimal working frequencies.

Moreover, it is possible to obtain an image depicting the size and shape of the cloak, clearly revealing their existence. Finally, the conclusions drawn from the obtained results are discussed. In addition, future lines of action to address the challenges that have not been completed in this doctoral thesis are detailed.

Resumen

LA TOMOGRAFÍA POR DIFRACCIÓN surge para mejorar las técnicas de imagen al considerar la naturaleza ondulatoria de la luz. Mientras que los primeros sistemas de imagen médica se basaban únicamente en fuentes sin difracción, este enfoque consigue mejorar la reconstrucción del índice de refracción de los objetos, lo que permite, por ejemplo, el estudio de estructuras subcelulares. Del mismo modo, la demanda de redes de telecomunicaciones cada vez más rápidas y seguras ha propiciado la aparición de la fotónica. Hace dos décadas, la combinación de estos dos campos dio lugar a los primeros sistemas de tomografía por difracción óptica (ODT), los cuáles han evolucionado rápidamente durante este siglo. En esta tesis, presentamos dos nuevas aplicaciones de la ODT. La primera está relacionada con el concepto del microscopio tomográfico de fase (TPM), una versión de la ODT que permite el estudio de células aisladas, con muchas aplicaciones biomédicas, como el diagnóstico y la prognosis del cáncer. Sin embargo, los sistemas TPM actuales son caros, pesados y complejos. Para resolver estos problemas, proponemos el concepto de TPM en chip. Con este fin, diseñamos una hoja de ruta hacia el primer dispositivo tomográfico integrado en el marco de la tecnología *lab-on-a-chip* (LoC), y desarrollamos los primeros pasos para ello: 1) Hasta ahora, sólo se han utilizado detectores planos para obtener los mapas de índice de refracción de los objetos estudiados en TPM, basados en la detección del campo difractado hacia delante. Sin embargo, los principios físicos fundamentales indican que medir también el campo difractado hacia detrás debería mejorar la resolución de las imágenes. Además, un detector plano no es la configuración óptima para el TPM en chip. En esta línea, hemos explorado la posibilidad de usar detectores circulares en este escenario, como una técnica más adecuada para las configuraciones en chip, demostrando al mismo tiempo que este enfoque proporciona una mejor resolución que el lineal. 2) Proponemos un esquema de TPM en chip basado en el uso de nanoantenas dieléctricas como fuente de luz y píxeles detectores ODT, y caracterizamos experimentalmente su comportamiento mediante microscopía óptica de campo cercano. En cuanto a la segunda aplicación, estudiamos el potencial de la ODT como nuevo paradigma en la detección de capas de invisibilidad realistas, una de las aplicaciones más importantes de los metamateriales. Hasta ahora, el *scattering cross section* (SCS) se ha utilizado como modelo de referencia

para diseñar y observar la eficacia de estos dispositivos para ocultar objetos. En nuestro estudio, demostramos que la ODT puede detectar las capas de invisibilidad prácticas con una sensibilidad superior a la que ofrece el SCS, incluso a las frecuencias de trabajo óptimas. Además, es posible obtener una imagen representativa del tamaño y la forma de la capa, revelando claramente su existencia. Finalmente, se discuten las conclusiones extraídas de los resultados obtenidos. Además, se detallan las futuras líneas de trabajo para abordar los retos que no se han completado en esta tesis doctoral.

Resum

LA TOMOGRAFIA PER DIFRACCIÓ sorgeix per millorar les tècniques d'imatge anteriors en considerar la naturalesa ondulatòria de la llum. Mentre que els primers sistemes d'imatge mèdica es basaven únicament en fonts sense difracció, aquest enfocament aconsegueix millorar la reconstrucció de l'índex de refracció dels objectes, la qual cosa permet, per exemple, l'estudi d'estructures subcelulars. De la mateixa manera, la demanda de xarxes de telecomunicacions cada vegada més ràpides i segures ha propiciat l'aparició de la fotònica. Fa dues dècades, la combinació d'aquests dos camps va portar als primers sistemes de tomografia per difracció òptica (ODT), els quals han evolucionat ràpidament durant aquest segle. En aquesta tesi, presentem dues noves aplicacions de la ODT. La primera està relacionada amb el concepte del microscopi tomogràfic de fase (TPM), una versió de la ODT que permet l'estudi de cèl·lules aïllades, amb moltes aplicacions en biomedicina, com el diagnòstic i prognosi del càncer. No obstant això, els sistemes TPM actuals són cars, pesats i complexos. Per resoldre aquests problemes, proposem el concepte de TPM en xip. Per fer-ho, dissenyem un full de ruta cap al primer dispositiu tomogràfic integrat en el marc de la tecnologia *lab-on-a-chip* (LoC), i desenvolupem els primers passos a aquest efecte: 1) Fins ara, només s'han utilitzat detectors plans per a obtindre els mapes d'índex de refracció dels objectes estudiats en TPM, basats en la detecció del camp difractat cap avant. No obstant això, els principis físics fonamentals indiquen que mesurar també el camp difractat cap endarrere hauria de millorar la resolució de les imatges. A més, un detector pla no és la configuració òptima per al TPM en xip. En aquesta línia, hem explorat la possibilitat d'usar detectors circulars en aquest escenari, com una tècnica més adequada per a les configuracions en xip, demostrant al mateix temps que aquest enfocament proporciona una millor resolució que el lineal. 2) Proposem un esquema de TPM en xip basat en l'ús de nanoantenes dielèctriques com a font de llum i píxels detectors ODT, i caracteritzem experimentalment el seu comportament en camp pròxim mitjançant microscòpia òptica de camp pròxim. Pel que fa a la segona aplicació, estudiem el potencial de la ODT com a nou paradigma en la detecció de capes d'invisibilitat realistes, una de les aplicacions més importants dels metamaterials. Fins ara, el *scattering cross section* (SCS) s'ha utilitzat com a model de referència per a dissenyar i observar l'eficàcia d'aquests dispositius per a ocultar objectes.

En el nostre estudi, vam demostrar que la ODT pot detectar les capes d'invisibilitat pràctiques amb una sensibilitat superior a la que ofereix el SCS, fins i tot a les freqüències de treball òptimes. A més, és possible obtindre una imatge representativa de la grandària i la forma de la capa, revelant clarament la seua existència. Finalment, es discuteixen les conclusions extretes dels resultats obtinguts i es detallen les futures línies de treball per a abordar els reptes que no s'han completat en aquesta tesi doctoral.

Table of contents

Chapter 1

Introduction and objectives

Seeing through objects has stimulated human curiosity since the beginning of our existence as a species. The necessity to know what is occurring inside our bodies gave rise to the field of anatomy, probably the first known discipline of medicine as the early written evidence of medical studies suggests, which dates back to the third millennium BC [1]. The study of the human body has evolved throughout mankind's history, with different points of view depending on the hegemonic culture in each region of the world. Although the limits of human vision had already been exceeded centuries earlier, both on an astronomical and atomic scale (thanks to the invention of the telescope and the microscope), the advent of X-rays in 1895 [2, 3] opened a path in science, where all disciplines, from mathematics to biology, have been working together ever since.

Tomography, whose name comes from the Greek $\tau o \mu o \sigma$ (sectional) and $\gamma \rho \alpha \varphi \omega$ (representation), takes in the first place the mathematical approximations developed by Radon [4], to form images through projections, thus making it possible to see inside opaque objects with no need to open them. The appearance of Computed Tomography (CT) [5] allows us to generate these cross-sectional images through the attenuation of X-rays due to their interaction with the studied biological sample. The ability to use tomographic imaging certainly revolutionized the field of medicine, allowing a clear image of a patient's internal morphology without the need for surgery. The CT technique has wide but limited use, since ionizing radiation from X-rays can eventually produce cancer with long-term use [6], and it cannot be employed to differentiate some tumor types. This last limitation lies, among other concerns, in taking X-rays as waves traveling in a straight line only. This paradigm changes with different subsequently developed techniques, as those in which the source used to image objects consists of ultrasound [7] or microwaves [8]. In these cases, the propagation of energy is described by refraction and multi-path effects [9]. Other techniques are based on the introduction of radioactive tracers to mark high metabolic activity, as Positron Emission Tomography (PET) [10]. From here, different techniques have taken advantage of the interaction of

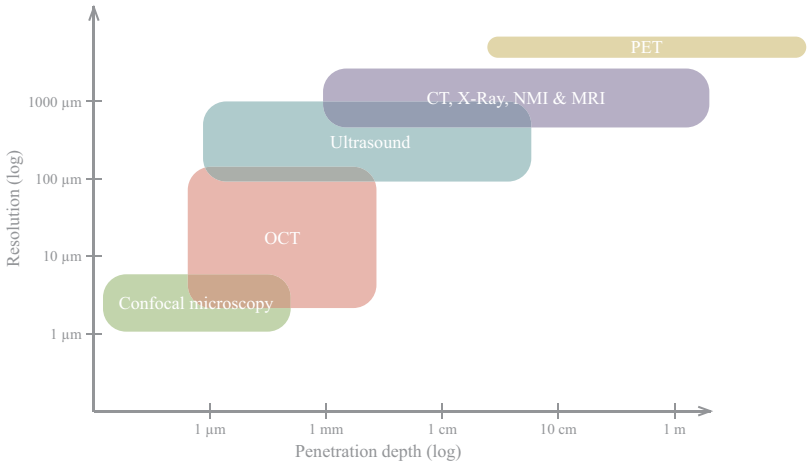

Fig. 1.1 Medical imaging technologies and their corresponding depth of penetration and resolution. OCT: Optical Coherence Tomography; CT: Computed Tomography; MRI: Magnetic Resonance Imaging; NMI: Nuclear Medical Imaging; PET: Positron emission tomography.

electromagnetic waves with matter to form a sectional image of objects and parts of the human body, with increasingly better resolution and greater depth in the tissues, as is detailed in Fig. 1.1 [11]. Each improvement in resolution and penetration depth achieved by these tomographic techniques is accompanied by a new field of research, resulting in the discovery of new diseases and novel diagnostics, leading to an improvement in the quality of life of mankind.

In the evolution of tomographic techniques, one of the most important steps forward has been taken by considering not only the propagation of waves, but also the diffraction produced by the studied objects. **Diffraction** describes the scattering of acoustic and electromagnetic waves as they propagate through objects and the space around them. The idea of using holography for the reconstruction of objects was proposed by Wolf decades ago [12], setting the groundwork for diffraction-based tomography [13]. Later, different algorithms for diffraction tomography were presented [14–16]. The leap of studying objects not only via attenuation, but also considering the variation of the phase of the field, results in an enhanced reconstruction of the object's refractive index (RI) distribution. The first proposed measurement systems used holographic techniques based on phase-shifting illumination for observing 3D phase structures [17]. As we will see below, novel technologies emerged within the framework of photonics. Two decades ago, this field gave rise to the first optical diffraction tomography (ODT) systems [18], initially without the possibility to measure the phase due to the complexity of the required characterization set-up. Later, these systems evolved so as to be able to measure the scattered and illuminating waves, and were additionally based on a Fourier space analysis,

which is a key aspect in DT algorithms [19]. The emergence of optical set-ups brought new advances in resolution and depth in biomedical imaging. For example, the technique of Optical Coherence Tomography [20] uses low-coherence interferometry to image internal tissue microstructures. The technique of **Tomographic Phase Microscopy** (TPM) also arises within the framework of tomographic methods, initially based on the projection theorem or inverse Radon Transform [21, 22], which does not consider light diffraction, and later extended to consider diffraction via ODT [23] (in this thesis, we will consider this enhanced scenario). TPM is an emerging bio-imaging optical method that uses digital holographic measurements of scattered fields to reconstruct 3D RI maps of cells [23] and other biological specimens, with sundry applications in biomedicine, such as the diagnosis and prognosis of cancer [24]. TPM is the tomographic evolution of Quantum Phase Imaging (QPI), and allows the reconstruction of the RI of unlabeled specimens via 2D phase maps recorded at multiple illumination angles. The state of the art regarding TPM will be discussed broadly in *Chapter 3*, where we see that current TPM systems are expensive, heavy, and cumbersome.

To solve these issues we propose the concept of on-chip TPM. Therefore, the search for such an integrated device has been one of the main lines of work followed in this thesis. To bring ODT into a chip, we have to take into account that only flat detectors have been used to obtain the RI maps of the objects studied in TPM, exclusively detecting the forward scattering. However, fundamental physical principles indicate that measuring also the backscattered field should improve the resolution of ODT images. Therefore, the circular detector scenario should be considered for integrated ODT. Finally, due to the difficulty in handling the exact electromagnetic field when solving the inverse scattering problem, we will use the so-called Born and Rytov approximations throughout the thesis, as is commonplace in ODT. The theory of diffraction tomography will be addressed in the following Chapter.

From the engineering perspective, each advance in imaging technology has been possible thanks to the evolution of electric and electronic devices. The advent of the transistor in 1947 was the milestone that paved the way for the miniaturization and increased processing power in electronics. The evolution of electronics has been following the well-known Moore's Law since Gordon Moore predicted in 1965 that the number of transistors on a chip would double every two years [25]. Although this law is probably coming to an end due to both economic and performance issues, [26], different technologies have been trying to overcome the electronic bottleneck, motivated by the demand for increasingly faster and secure telecommunication networks. One of the most important examples is **photonics**, the physical science dealing with the manipulation of light. Different photonic technologies have overcome the electronic boundaries in terms of bandwidth and energy efficiency [27]. In the context of this field, nanophotonics [28]

has been the core of an enormous range of applications, such as quantum photonics [29–31], data center interconnects [32, 33], high-performance computing devices [34, 35], or the development of the all-optical chip [36]. These photonic applications are possible via light control inside high index contrast waveguides, usually fabricated over silicon-on-insulator (SOI) wafers [37]. The key to this technology lies in the use of silicon, which, in addition to being the second most abundant material on the planet and having good mechanical properties, is the basis of complementary metal-oxide-semiconductor (CMOS) technology, which has an established industry worldwide, allowing the low-cost fabrication of photonic integrated circuits (PICs). In addition, CMOS technology is the bridge between traditional electronics and new optical devices and applications. Two of these remarkable applications, which are fundamental in the present thesis are:

- **Lab-on-a-chip (LoC)** devices [38–41], which consist of integrated circuits that can miniaturize different sensing processes in a wide range of applications over biological samples, with diverse uses in different fields such as medicine, biology, or security. LoC devices can operate on real samples (e.g., wastewater, urine, or blood) allowing fast in vitro diagnostics of illness conditions. With this aim, disposable LoCs can be used as portable point-of-care (POC) devices [42] to provide immediate results anywhere without the need for an expensive laboratory.

- On the other hand, in analogy with radio communications, we are attending the birth of the concept of **nanoantenna** [43–45]. The purpose of this element is to convert guided or localized optical energy into free propagating radiation and vice-versa. Although plasmonic nanoantennas, based on metals such as gold or silver, have proven to be an efficient solution for sensing or spectroscopic applications [46–50], their high absorption at optical frequencies and their low directivity do not allow them to efficiently reach far-field distances. However, the use of silicon nanoantennas [51], besides the CMOS compatibility of this material, does allow the construction on-chip wireless interconnects. The conception of a broadband, high directivity, low loss, and reconfigurable silicon photonics nanoantenna has opened the door to a full on-chip radiation control, enabling new functionalities in integrated photonics, such as wireless high-speed data transmission, compact low-crosstalk multi-port crossings, or reconfigurable pathways. Remarkably, an ultra-compact LoC microflow cytometer enabled by this kind of antenna has recently been proposed and demonstrated [52, 53]. This approach to the study of biological samples via PICs, using microfluidic channels to insert and extract the specimens under study, is a promising LoC technology.

In the framework of these LoC devices, and recalling the concept of phase tomography mentioned above, some approaches to the idea of on-chip TPM have been proposed,

although some elements of the tomographic processes remain always outside of the chip [54, 55], resulting in a "not all on-chip diffraction tomography". Along this line, the first objective of this thesis has been to develop a roadmap to achieve an all on-chip version of TPM, based on a set of optical nanoantennas in an SOI sample, as a **novel application** of ODT. This low-cost technology could be used in PoC devices for many applications, such as performing a quick diagnosis of different diseases like many cancers [24], as well as to quantify the efficacy of cell immunotherapy [56].

Back to tomography, it is worth mentioning that the search for objects that could not be detected by electric impedance tomography led to one of the first reported versions of transformation optics and of modern **invisibility cloaks** [57]. Advances in the field of metamaterials [58] have brought with them the possibility of building this kind of object, being one of the most high-impact developments in this field. These groundbreaking devices achieve a scattering reduction of the concealed objects, which has even been experimentally demonstrated [59–62]. So far, the so-called scattering cross section (SCS) has been the gold standard to assess the performance of these cloaks, providing a measure of their bandwidth [63]. However, the perspective that tomography could offer in the study of invisibility cloaks has been overlooked until now. In particular, since, as opposed to the SCS, diffraction tomography also takes into account the phase information of the field scattered by an object, its application to passive invisibility devices can be expected to provide us with more information on a given cloak. Hence, as the **second novel application** of ODT, we study in this thesis its potential as a new paradigm in the detection of realistic invisibility devices.

1.1 Objectives

The wide range of existing diffraction tomography algorithms and techniques is one of the cornerstones of many advances in fields such as medicine, biology, and even art. In this thesis, we first provide a brief introduction to non-diffraction tomography via the Inverse Radon Transform. Then, using Plain Wave Illumination (PWI) as the source, the **Fourier Diffraction Theorem** is studied for linearly- and circularly-shaped detectors. Both techniques are compared to analyze their differences in resolution. These ODT approaches form the base of the two aforementioned novel applications:

- On the one hand, fully integrated on-chip tomography is close to being a reality. However, cellular tomography has been achieved only using complex and expensive optical set-ups, required to perform the phase-contrast demanded by image formation. Besides, lensless handy systems have been developed, but the

illumination energy comes from elements external to the PIC, while the information is recorded by complex cameras. Here, we propose a new LoC technology to achieve the concept of **integrated tomographic microscopy**. In this system, a silicon nanoantenna radiates the illuminating wave, which interacts with the studied cell or object (placed at different points in the system through a microfluidic channel). The field scattered by the biological sample will be read with a set of receiving Si nanoantennas. Moreover, since, as we will see, a flat detector is not the optimal configuration for on-chip TPM, we explore the possibility of using a circular array of detectors. In this vein, one of the main goals of this thesis has been to elaborate a roadmap towards the concept of all-on-chip optical diffraction tomography and to take the first steps along this path.

- On the other hand, invisibility passive devices have been so far assessed using the SCS, a scalar quantity that only gives us global information on the hiding ability of the cloak. Here, we propose to use ODT as a new tool to improve the **detection of invisibility cloaks**.

To conclude, a set of partial objectives must be achieved to carry out the proposed work:

- The documentation, study, and implementation of the different algorithms for optical diffraction tomography for both configurations (linear and circular detector).
- The comparison between both kinds of detector.
- The study and characterization of the silicon nanoantenna (NA) that will be a key part of the on-chip TPM device. Its radiation performance will be validated in both the far and near field.
- The conception of the TPM device. A first cross-port circular design will be considered to validate the NAs array technology. Then, a baseline design will be fabricated and characterized to validate the algorithms.
- Designing a final device, which includes an optofluidic (OF) channel for the insertion and extraction of biological samples. This configuration must be able to read phase information, relevant for the correct use of ODT.
- The design and optimization of invisibility passive devices and the study of ODT as a potential detection tool with a higher sensitivity.

The complete picture of the roadmap to address these objectives can be seen in Fig. 1.2.

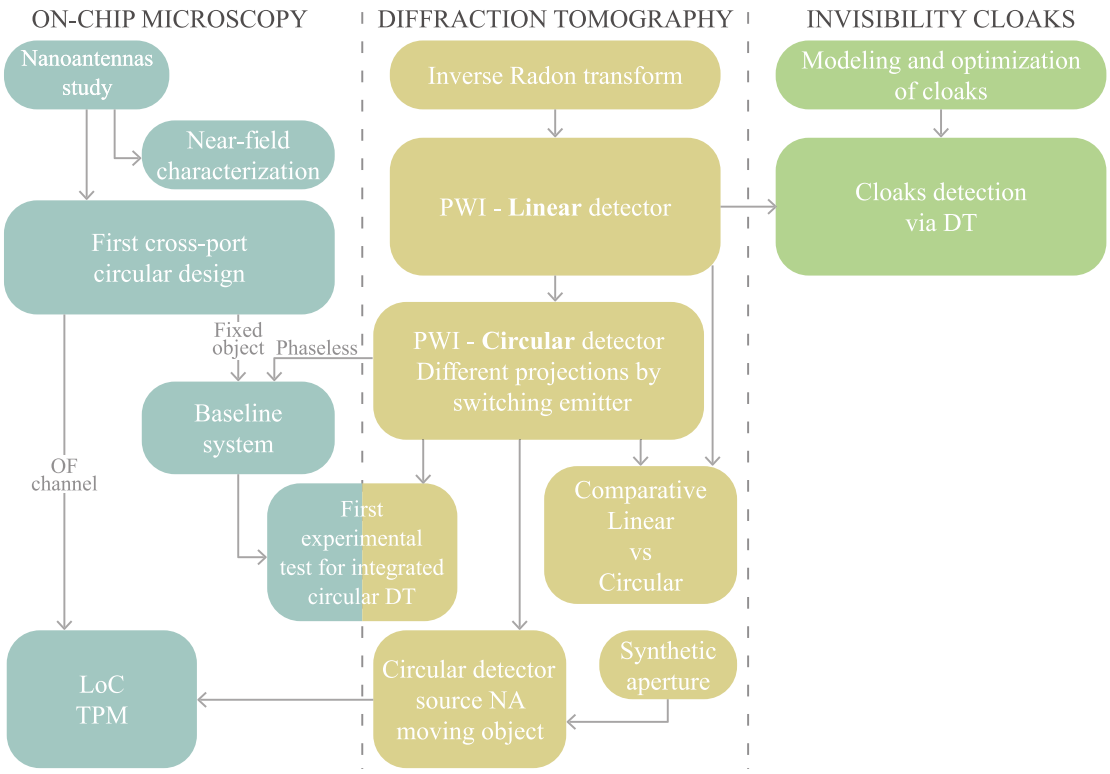

Fig. 1.2 Thesis objectives. NAs, Nanoantennas; PWI, Plane-wave illumination; DT, Diffraction Tomography; OF, Opto-fluidic; TPM, Tomographic Phase Microscopy.

The requirements to accomplish these aims encompass the study of the associated theoretical background and a proper use of simulation tools. We will also make adequate use of the facilities of the *Nanophotonics Technology Center* (NTC) of the *Universitàt Politècnica de València* (UPV, Polytechnic University of Valencia) at which this thesis has been carried out, including the clean room and the huge experience in PIC fabrication of its technicians, as well as the characterization laboratories, to carry out the experimental work.

1.2 Structure of the thesis

This dissertation describes the work presented to obtain the degree of *Doctor of Philosophy* (PhD) in *Telecommunication Engineering* under the doctorate program of the UPV. The research has been carried out at the NTC under the supervision of Dr. Carlos García-Meca and Prof. Javier Martí Sendra and, during a three-month research stay at the

Max Planck Institute for the Science of Light in Erlangen (Germany), under the guidance of Prof. Jochen Gück[1].

The contents of the dissertation are distributed along the following chapters:

- Chapter 1: *Introduction and objectives* provides an insight into the potential contribution of photonic science within the context of cellular tomography. Furthermore, the main goals of this thesis and the methodology to achieve them are detailed.
- Chapter 2: *Diffraction Tomography* addresses the origin and applications of ODT, as well as some implementations of this theory in systems with linear and circular detectors. Subsequently, both implementations are compared in the context of TPM, verifying that circular detectors, which have not been used so far in TPM, provide a better resolution.
- Chapter 3: *On-chip Optical Tomographic Microscopy* outlines the state of the art of TPM, as well as the first attempts to miniaturized cellular tomography. Our proposed device will be put in the context of LoC devices. The nanoantenna used in the proposed system and the experimental study of its near-field behavior are presented. The design, fabrication, and characterization of baseline configurations are detailed.
- Chapter 4: *Invisibility Passive Devices* provides the first known approach to the detection of cloaking systems via ODT. Three kinds of invisibility cloaks have been studied, based on the techniques of scattering cancellation and transformation optics.
- Chapter 5: *Conclusions and discussion* assesses the main findings of this dissertation. Especially, the further steps to be taken in future work are detailed as the roadmap to be followed to complete the tasks that could not be carried out in this thesis.

The thesis dissertation is concluded with numbered appendices. These begin with the phantoms used to test the implemented algorithms. Since this thesis is intended to serve as a tomography manual to consult for step-by-step algorithm implementations, the necessary appendices for further mathematical detail are added. Then, a section with the complete list of the Author's merits is appended, including the dissemination of the results in conferences and scientific journals. After that, the cited references are listed in order of appearance. Lists of figures, tables, and acronyms close the document.

[1] This internship was conducted remotely, due to travel restrictions caused by the Covid-19 pandemic, from April to July 2021.

Chapter 2

Diffraction Tomography

2.1 Introduction

Early medical imaging technologies that allowed to see through the body were based on non-diffracting techniques as the CT. This is the simplest and oldest projection reconstruction method, which could be described as drawing the plan of a house by looking through the windows [64]. Due to the limitations of this backprojection method, a new paradigm in imaging appeared, considering the wave nature of the light. Diffraction tomography algorithms [14, 15] overcome the limitations of the first medical imaging technologies, allowing the imaging of biological cells and tissues, which is central to biological research and medical diagnosis. For a biological specimen, the thickness and RI inhomogeneity determine how much light scattering it produces. Scattering defines the image contrast since, in the visible spectrum, most cells and tissues do not absorb light significantly. Moreover, the scattering generated by biological specimens is much weaker than the incident light, making it challenging to reveal the structure from an overwhelming incident light background. These specimens are phase objects since they only affect the phase of the incident field. To render them visible, one can convert them into amplitude objects using stains or fluorescent tags. The gold standard of histopathology is manual diagnosis on stained, several-micrometer-thick tissue slices, while fluorescence microscopy is the main imaging tool in cell biology. Stains and tags offer high-contrast imaging with molecular specificity, but they are qualitative and sample-preparation-dependent, while photo-bleaching and photo-toxicity limit fluorescent imaging of live cells. Furthermore, the use of exogenous labels (e.g., fluorescent proteins or dyes), may alter cell physiology, while labeled cells cannot be trivially re-injected into the human body. These limitations hinder advances in neuroscience, stem cell research, immunotherapy, etc. [56]. TPM is an emerging bio-imaging optical technique that uses digital holographic measurements of scattered fields to reconstruct 3D RI maps of biological specimens. This technique operates

on unlabeled specimens, being complementary to fluorescence microscopy, with the advantage of exhibiting lower photo-toxicity and no photo-bleaching, as well as being free of variability due to contrast agents [56]. There exists a wide range of TPM approaches (the state of art regarding TPM will be discussed broadly in *next chapter*), with the first demonstrations reported in 2006 and 2007 [22, 21]. In these works, the 3D reconstruction tomographic algorithm was based on a back filtered projection method (similar to that used in the aforementioned X-ray CT). This method can image the RI spatial distribution using the **inverse Radon transform**, a technique that will be briefly introduced in the following section. Although some advances have improved this method [65], the principal drawback of this technique resides in that it ignores diffraction, limiting these TPM systems to small sample RI variations in the wavelength scale. This problem is solved with the diffraction tomography technique [14–16, 66, 67]. In the standard version of this method (in which the detector is a line in 2D or a plane in 3D), to obtain the RI distribution $n(\mathbf{r})$ of a sample, it is illuminated with a plane wave. To solve the complex diffraction nature of the scattered wave, **the approximations of Born and Rytov** could be addressed, starting from the **Helmholtz equation**. Other studies use the diffusion equation as starting point to solve the inverse scattering problem [68, 69], resolving the optical absorption coefficient of tissues [70, 71], with the detriment that the diffusion equation requires a diffuse surrounding medium. Our interest of using approximations based on the Helmholtz equation lies in the search for a global algorithm that can reconstruct the RI map of samples embedded in any type of medium. Thus, after the so-called Born and Rytov approximations, the algorithm to solve the **ODT for a linear detector** is presented and implemented. The results using different phantoms as inputs are presented.

Moreover, the implementation of this linear detector algorithm allows us to use it in a novel application of ODT: we applied this algorithm over invisibility passive devices to detect them (see *Chapter 4*). This sets a new standard for characterizing these metamaterial-based devices.

In addition, TPM systems can benefit from a paradigm switch, from a flat detector scenario to a circular one, which would result in improved resolution. Hence, we study and implement an ODT algorithm considering a **circular detector**. Consequently, we compare the results of both diffraction tomography scenarios at the end of this chapter.

The author would like to end this introduction by pointing out that, nowadays, diffraction tomography algorithms are not only useful in studies of biological samples such as cells. For instance, they are used in geophysical explorations [72] or for art restoration purposes [73]. The large amount of literature produced in the field of diffraction tomography attests to the interest that it continues to arouse in the scientific community in a wide range of disciplines.

2.2 Diffraction Tomography Approximations

2.2.1 Inverse Radon Transform

To begin with the tomography approximations, it is useful to start by developing the inverse Radon transform. This approach does not consider the diffractive nature of the waves, but is serves to introduce tomography, as well as the terms *projection* and *sinogram*. In the Radon transform, a forward tomographic process uses projections recorded at $(N\text{-}1)$-dimensional planes to generate the N-dimensional function under study.

Considering a 2D sample, each point of the detector line will correspond to the integral of the line through the object, from the source of illumination in straight line to the detector, as seen in figure 2.1 a). The **projection**, for a certain angle ϕ_0 of rotation, is composed for the set of points along the detector [4].

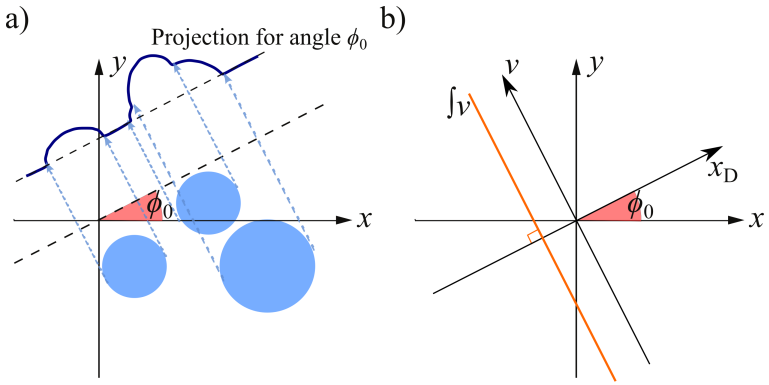

Fig. 2.1 a) Projection of the sample for a certain angle ϕ_0. b) Change of the coordinate system when the object is rotated.

Therefore, the projection p_{ϕ_0} could be expressed using the Radon transform operator R_{ϕ_0} as follows:

$$\begin{aligned} p_{\phi_0} &= R_{\phi_0}\{f(\mathbf{r})\} \\ &= \int f(x(v),y(v))dv \\ &= \int f(x_D\cos\phi_0 - v\sin\phi_0, v\cos\phi_0 + x_D\sin\phi_0)\,, \end{aligned} \tag{2.1}$$

$$r_{xy}^2 = x^2+y^2 = x_D^2+v^2\,, \tag{2.2}$$

being $f(\mathbf{r})$ the image function and r_{xy} the distance from the center of the system to the integration line (orange line in figure 2.1 b) for each point. From this point to the end of this dissertation, the angle $\phi_0 = 0$ will correspond to $x_D = x$. The set of projections for different angles form the **sinogram**. This name comes from the fact that the Radon

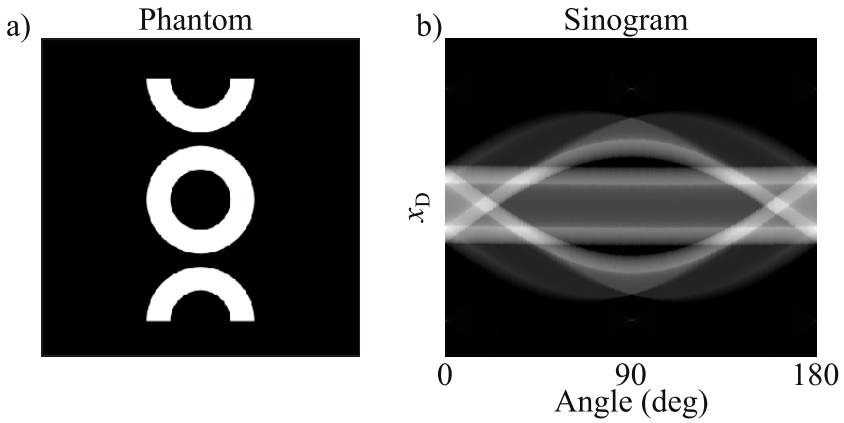

Fig. 2.2 Sinogram example. a) Logo of the Nanophotonics Technology Center. b) Sinogram from 0 to 180 degrees.

transform of an off-center point takes sinusoidal form. An example of a sinogram could be found in figure 2.2, where the logo of our Institute is used as the input phantom.

The central straight lines in figure 2.2 b) represent the sinogram of the central circle, since the sinogram of an axial symmetrical sample remains equal for each angle. Upper and lower semicircles complete the sinogram with the sinusoidal lines. Starting from the projections that form the sinogram, the original image function can be reconstructed using the Fourier Slice Theorem. First, the unitary angular frequency Fourier transform of a projection (along the one-dimensional data recorded at the detector line) will be addressed as follows:

$$\hat{P}_{\phi_0}(k_{\mathrm{Dx}}) = \frac{1}{\sqrt{2\pi}} \int p_{\phi_0}(x_{\mathrm{D}}) e^{-ik_{\mathrm{Dx}}x_{\mathrm{D}}} dx_{\mathrm{D}} \,. \tag{2.3}$$

Taking a step back, the 2-dimensional (2D) image function $f(x,y)$ can define its 2D Fourier Transform as:

$$\hat{F}(k_x,k_y) = \frac{1}{2\pi} \iint f(x,y) e^{-i(k_x x + k_y y)} dx dz \,, \tag{2.4}$$

which, performing the rotation by the angle ϕ_0 as Fig. 2.1 b) indicates, could be addressed as follows:

$$\hat{F}(k_{\mathrm{Dx}},k_v) = \frac{1}{2\pi} \iint f_{\phi_0}(x_{\mathrm{D}},v) e^{-i(k_{\mathrm{Dx}}x_{\mathrm{D}} + k_v v)} dk_{\mathrm{Dx}} dv \,. \tag{2.5}$$

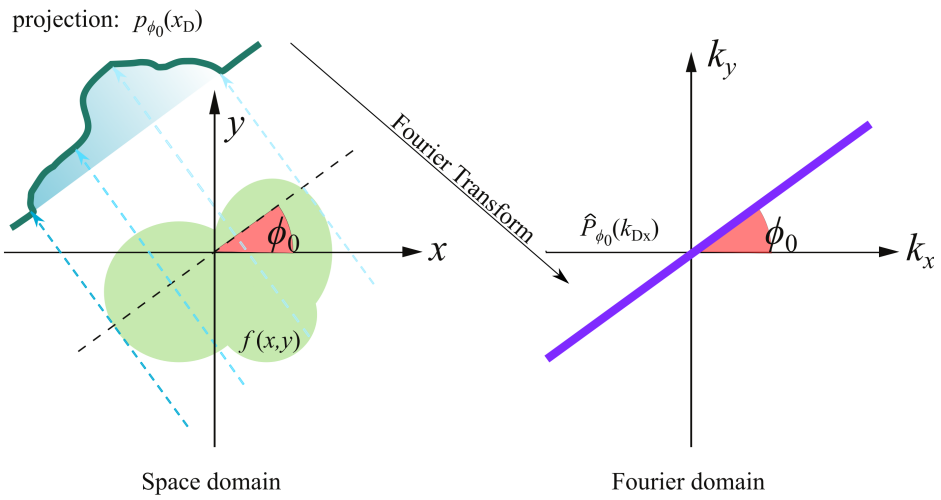

Fig. 2.3 **Fourier Slice Theorem:** The Fourier Transform of a projection recorded at an angle ϕ_0 is distributed along a line, at the same ϕ_0 angle, in the frequency Fourier space of the original image $f(x,y)$

Slicing $\hat{F}(k)$ at each angle, the 2DFT can be reduced considering $k_v = 0$:

$$\hat{F}(k_{Dx},0) = \frac{1}{2\pi}\int f_{\phi_0}(x_D,0)e^{-i(k_{Dx}x_D)}dk_{Dx}\,. \tag{2.6}$$

Finally:

$$\hat{F}(k_{Dx},0) = \frac{1}{\sqrt{2\pi}}\hat{P}_{\phi_0}(k_{Dx})\,. \tag{2.7}$$

Equation 2.7 explains the **Fourier Slice Theorem**: The Fourier Transform of a projection recorded at an angle ϕ_0 is distributed along a line, at the same ϕ_0 angle, in the frequency Fourier space of the original image $f(x,y)$ (see figure 2.3). Therefore, we can reconstruct the image and complete the inverse of the Radon Transform by interpolating $\hat{F}(k_x,k_y)$ from $\hat{P}_{\phi_0}(k_{Dx})$.

Implementation

The objective is to obtain the image $f(x,y)$ from the Fourier transform of each projection $\hat{P}_{\phi_0}(k_{Dx})$. On the one hand, combining equations 2.7 and 2.3, ones arrive to:

$$\hat{F}(k_{Dx},0) = \frac{1}{\sqrt{2\pi}}\frac{1}{\sqrt{2\pi}}\int p_{\phi_0}(x_D)e^{-ik_{Dx}x_D}dx_D\,. \tag{2.8}$$

On the other hand, performing the variable change $(k_x,k_y) \rightarrow (k_{Dx},\phi_0)$ over the inverse 2D Fourier Transform equation 2.5 (all the detailed steps are available at the

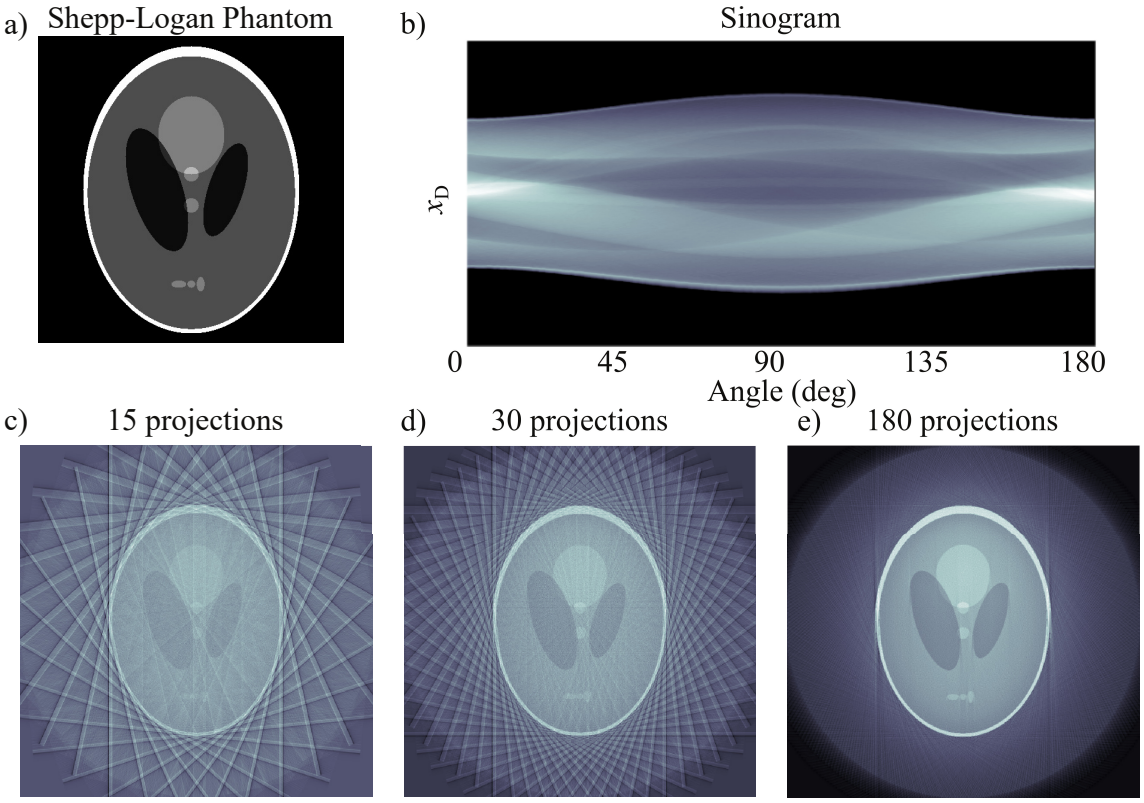

Fig. 2.4 Inverse Radon Solution. a) Shepp-Logan Phantom from [74]. b) Sinogram from 0 to 180 degrees. c-e) Solutions for 15, 30, and 180 projections.

Appendix B.1):

$$f(x,y) = \frac{1}{2\pi}\int\int_0^{\pi} |k_{\mathrm{Dx}}|\,\hat{F}(k_{\mathrm{Dx}})e^{ik_{\mathrm{Dx}}(x\cos\phi_0+y\sin\phi_0)}d\phi_0 dk_{\mathrm{Dx}}\,. \tag{2.9}$$

Finally, the implementation of the Fourier Slice Theorem, in other words, the reconstruction of the original image function $f(x,y)$ through the sinogram (set of projections $\hat{P}_{\phi_0}$ for each angle), is addressed as follows [66]:

$$f(x,y) = \frac{1}{2\pi}\int\int_0^{\pi} |k_{\mathrm{Dx}}|\,\frac{\hat{P}_{\phi_0}(k_{\mathrm{Dx}})}{\sqrt{2\pi}}e^{ik_{\mathrm{Dx}}(x\cos\phi_0+y\sin\phi_0)}d\phi_0 dk_{\mathrm{Dx}}\,. \tag{2.10}$$

The $|k_{\mathrm{Dx}}|$ ramp filter gives the *filtered backprojection* name to this algorithm. Without this filter, the solution will have an over-representation at the center of the solution. To test this algorithm, a Shepp-Logan phantom [1] has been used to obtain this sinogram (see Fig. 2.4). This image is a broadly used test envisioned to simulate a cross-sectional

[1] In this section, this phantom keeps its original values of RI and size, while in the rest of the dissertation, these values have been adapted (see the Appendix A.2).

image of a head [74]. The result of the filtered backprojection algorithm for 15, 30 and 180 projections could be seen in figure 2.4 c), d) and e) respectively. Besides the good approximations of these results, we must keep in mind that this backprojection algorithm assumes that light travels in a straight line, thus ignoring diffraction. The next sections address this concern and introduce the development and implementation of optical diffraction tomography (ODT).

2.2.2 Helmholtz Equation

The relationship of the light to the medium within space and time is addressed by the seminal Maxwell equations [75]. One of the most used approximations to these equations simplifies the vector model of the electromagnetic fields to a scalar description of waves. This approach, called wave equation, considers the possible inhomogeneous nature of the space cross by the light [76]. This equation remains time-dependent, which does not interest us due to the stationary character of the waves used in tomography. The time-independent form of the wave equation is known as the Helmholtz equation, and takes the following structure for a homogeneous medium:

$$\left(\nabla^2 + k_{\mathrm{M}}^2\right) u(\mathbf{r}) = 0 \,, \tag{2.11}$$

with $u(\mathbf{r})$ being the total field, k_{M} the wavenumber of the background medium. It is defined by its RI n_{M} as $k_{\mathrm{M}} = \dfrac{2\pi n_{\mathrm{M}}}{\lambda}$, and defining λ as the vacuum wavelength of the light. When the RI of the medium is not constant, or an object is placed in the propagation path of the light, the RI in this region could be expressed as $n(\mathbf{r}) = n_{\mathrm{M}} + \varepsilon_n(\mathbf{r})$. In this case, the propagation of the light could be expressed using the inhomogeneous Helmholtz equation, which is addressed as follows:

$$\left(\nabla^2 + k_{\mathrm{M}}^2\right) u(\mathbf{r}) = -f(\mathbf{r}) u(\mathbf{r}), \tag{2.12}$$

with

$$f(\mathbf{r}) = k_{\mathrm{M}}^2 \left[\left(\frac{n(\mathbf{r})}{n_{\mathrm{M}}} \right)^2 - 1 \right] \,, \tag{2.13}$$

as the scattering potential. We use a scattered field formulation, in which the total field is expressed as the sum of the incident u_0 and scattered u_{S} fields:

$$u(\mathbf{r}) = u_0(\mathbf{r}) + u_{\mathrm{S}}(\mathbf{r}) \,. \tag{2.14}$$

The field u_0 is the solution to Eq. (2.12) for the case in which there is no medium perturbation, i.e., for $n = n_{\mathrm{M}}$, which results in a homogeneous equation seen in Eq. (2.11).

This allows us to write:

$$\left(\nabla^2 + k_{\mathrm{M}}^2\right) u_{\mathrm{S}}(\mathbf{r}) = -f(\mathbf{r})u(\mathbf{r}). \tag{2.15}$$

2.2.3 Green's function solution

We can use Green's function $g(\mathbf{r})$, i.e., the impulse response of the inhomogeneous linear differential operator associated with the previous Helmholtz equation, to obtain a solution [77]. That is:

$$\left(\nabla^2 + k_{\mathrm{M}}^2\right) g(\mathbf{r}-\mathbf{r}') = -\delta(\mathbf{r}-\mathbf{r}')\,. \tag{2.16}$$

From now, all the equations will consider the space in 2D. Using the shifting property of the δ function:

$$\begin{aligned} f(\mathbf{r})u(\mathbf{r}) &= \int_{-\infty}^{\infty}\int_{-\infty}^{\infty} f(\mathbf{r}')u(\mathbf{r}')\delta(\mathbf{r}-\mathbf{r}')d^2r' \\ &= -\int_{-\infty}^{\infty}\int_{-\infty}^{\infty} f(\mathbf{r}')u(\mathbf{r}')\left(\nabla^2 + k_{\mathrm{M}}^2\right) g(\mathbf{r}-\mathbf{r}')d^2r' \\ &= -\left(\nabla^2 + k_{\mathrm{M}}^2\right)\int_{-\infty}^{\infty}\int_{-\infty}^{\infty} f(\mathbf{r}')u(\mathbf{r}')g(\mathbf{r}-\mathbf{r}')d^2r'. \end{aligned} \tag{2.17}$$

Comparing Eqs. (2.15) and (2.17), we find that the scattered field can be expressed as a convolution of the source with Green's function:

$$u_{\mathrm{S}}(\mathbf{r}) = \int_{-\infty}^{\infty}\int_{-\infty}^{\infty} f(\mathbf{r}')u(\mathbf{r}')g(\mathbf{r}-\mathbf{r}')d^2r'\,. \tag{2.18}$$

Since this equation has no analytical solution, it is necessary to find approximations to solve it. The Born and Rytov approaches take advantage of some conditions to find solutions to this problem, as we see in the following two subsections.

2.2.4 Born approximation

If $u_{\mathrm{S}} \ll u_0$, the scattered field can be approximated by the following expression:

$$u_{\mathrm{S}}(\mathbf{r}) = u_{\mathrm{B}}(\mathbf{r}) = \iint_S g(\mathbf{r}-\mathbf{r}')f(\mathbf{r}')u_0(\mathbf{r}')d^2r'\,. \tag{2.19}$$

This is known as the first Born approximation. The condition $u_{\mathrm{S}} \ll u_0$ leads to the necessity of a discussion about the validation of this approximation. Some observations have been performed in this direction. For instance, some studies focus on the phase change that light experiences through the sample to be studied, like [66]. In this work, Müller pointed that the phase change should be much smaller than 2π, which concerning the thickness of the sample (s), and the RI of the medium (n_{M}) and the sample (n_{S}), can be expressed as

$$s(n_{\mathrm{S}} - n_{\mathrm{M}}) \ll \lambda\,. \tag{2.20}$$

This condition arises the main drawback of the Born approximation when tomography faces with biological specimens: the studied samples should be thin if their variation of RI is large. Moreover, in this condition, once again we have to face the term "much smaller". To shed light in this direction, a numerical validation is studied in [78], yielding that the approximation will be valid when $s(n_S - n_M) < 0.08\lambda$ for the use of the filtered backpropagation algorithm.

2.2.5 Rytov approximation

When the wavelength of the illumination plane wave is smaller than the structure details of the biological specimens under study, the Rytov approximation arises as a better approach than the Born approximation [79]. This method has been used for decades in reconstruction algorithms [80]. In this case, the total field is expressed as follow:

$$u(\mathbf{r}) = u_0(\mathbf{r}) + u_S(\mathbf{r}) = e^{\varphi(\mathbf{r})} , \tag{2.21}$$

being $\varphi(\mathbf{r})$ the complex phase of the total field $\varphi(\mathbf{r}) = \varphi_0(\mathbf{r}) + \varphi_S(\mathbf{r})$. As [66, Eq. 3.34] indicates:

$$\left(\nabla^2 + k_M^2\right) \varphi_S(\mathbf{r}) = -u_0(\mathbf{r}) \left[(\nabla\varphi_S(\mathbf{r}))^2 + f(\mathbf{r})\right] . \tag{2.22}$$

The Rytov approximation estimates that the phase gradient $\nabla\varphi_S(\mathbf{r})$ is much smaller than the object function, therefore, $\varphi_S(\mathbf{r})$ can be approximated to the Rytov phase $\varphi_R(\mathbf{r})$. Applying the *Green function*:

$$\varphi_R(\mathbf{r}) = \frac{\int G(\mathbf{r}-\mathbf{r}')f(\mathbf{r}')u_0(\mathbf{r})d^3r'}{u_0(\mathbf{r})} , \tag{2.23}$$

being $\varphi_R(\mathbf{r})$ the complex phase of the Rytov scattered field $u_R(\mathbf{r}) = e^{\varphi_R(\mathbf{r})}$. The relation between both approximations could be obtained easily:

$$\varphi_R(\mathbf{r}) = \frac{u_B(\mathbf{r})}{u_0(\mathbf{r})} . \tag{2.24}$$

Once again, we must face a "much smaller" expression, since the Rytov approximation assumes that $[\nabla\varphi_S(\mathbf{r})]^2 \ll f(\mathbf{r})$. Analytically, like in the Born case, the validation of the Rytov approximation will depend on the width of the object crossed by the light (s) and the variation of the sample RI [66, Eq. 3.52]:

$$|\nabla n(\mathbf{r})| \ll \frac{\sqrt{2n_M|n(\mathbf{r}) - n_M|}}{s} , \; s > \lambda , \tag{2.25}$$

which indicates that the Rytov approximation is dependent on the gradient of the RI within the sample, which makes this approximation applicable to biological cells. Regarding the study performed in [78], the approximation has been numerically validated when $s(n_S - n_M) < 0.24\lambda$ for the use of the filtered backpropagation algorithm, which is 3 times less constrained than the Born approximation.

Finally, we are able to obtain the **Rytov to Born** relation for the scattered field:

$$u_0(\mathbf{r})\varphi_R(\mathbf{r}) = u_B(\mathbf{r}) \,, \tag{2.26}$$

$$e^{u_0(\mathbf{r})}e^{\varphi_R(\mathbf{r})} = e^{u_B(\mathbf{r})} \,, \tag{2.27}$$

$$e^{\varphi_R(\mathbf{r})} = e^{\frac{u_B(\mathbf{r})}{u_0(\mathbf{r})}} \,, \tag{2.28}$$

$$u_R(\mathbf{r}) = u_0(\mathbf{r})e^{\frac{u_B(\mathbf{r})}{u_0(\mathbf{r})}} - u_0(\mathbf{r}) = u_0(\mathbf{r})\left[\exp\left(\frac{u_B(\mathbf{r})}{u_0(\mathbf{r})}\right) - 1\right] \,. \tag{2.29}$$

On the other hand, the **Born to Rytov** relation follows:

$$u_R(\mathbf{r}) + u_0(\mathbf{r}) = u_0(\mathbf{r})e^{\frac{u_B(\mathbf{r})}{u_0(\mathbf{r})}} \,, \tag{2.30}$$

$$\ln(u_R(\mathbf{r}) + u_0(\mathbf{r})) = \ln(u_0(\mathbf{r})) + \ln\left[\exp\left(\tfrac{u_B(\mathbf{r})}{u_0(\mathbf{r})}\right)\right] \,, \tag{2.31}$$

$$\ln\left(\frac{u_R(\mathbf{r}) + u_0(\mathbf{r})}{u_0(\mathbf{r})}\right) = \tfrac{u_B(\mathbf{r})}{u_0(\mathbf{r})} \,, \tag{2.32}$$

$$u_0(\mathbf{r})\ln\left(\frac{u_R(\mathbf{r})}{u_0(\mathbf{r})} + 1\right) = u_B(\mathbf{r}) \,. \tag{2.33}$$

To sum up, the relation between both approximations can be addressed as follows:

$$u_R(\mathbf{r}) = u_0(\mathbf{r})\left[\exp\left(\frac{u_B(\mathbf{r})}{u_0(\mathbf{r})}\right) - 1\right] \quad , \quad u_B(\mathbf{r}) = u_0(\mathbf{r})\ln\left(\frac{u_R(\mathbf{r})}{u_0(\mathbf{r})} + 1\right). \tag{2.34}$$

2.3 Fourier diffraction theorem - Linear detector and plane-wave incidence

In 2D, the Green's function associated with Helmholtz's equation is given by:

$$g(\mathbf{r}) = \frac{i}{4} H_0^{(1)}\left(k_{\mathrm{M}}|\mathbf{r}|\right) \ , \tag{2.35}$$

where $H_0^{(1)}$ is the zeroth-order Hankel function of the first kind, which can be expressed as the following superposition of plane waves:

$$H_0^{(1)}\left(k_{\mathrm{M}}|\mathbf{r}|\right) = \frac{1}{\pi}\int_{-\infty}^{\infty} \frac{1}{k_z} e^{i(k_x x + k_z|z|)} dk_x, \tag{2.36}$$

with

$$k_z = \sqrt{k_{\mathrm{M}}^2 - k_x^2} \ . \tag{2.37}$$

Therefore:

$$u_{\mathrm{B}} = \iint_S \frac{i}{4\pi} \int_{-\infty}^{\infty} \frac{1}{k_z} e^{i(k_x(x-x') + k_z|z-z'|)} dk_x f(\mathbf{r}') u_0(\mathbf{r}') d^2 r' \ . \tag{2.38}$$

We assume that the detector is placed at $z = z_{\mathrm{D}} > 0$ and that the incident field is a plane wave:

$$u_0(\mathbf{r}) = a_0 e^{ik_{\mathrm{M}}\mathbf{s}_0\cdot\mathbf{r}} = a_0 e^{i\mathbf{k}_{\mathrm{I}}\cdot\mathbf{r}}, \tag{2.39}$$

where $\mathbf{s}_0$ is a unit vector. Since the function $f(\mathbf{r}') \neq 0$ only for $z' < z_{\mathrm{D}}$, the factor $|z-z'| = z-z'$ at $z = z_{\mathrm{D}}$ for all relevant values of $\mathbf{r}'$, and we can write:

$$\begin{aligned}
u_{\mathrm{B}}(\mathbf{r}) &= \iint_S \frac{i}{4\pi} \int_{-\infty}^{\infty} \frac{1}{k_z} e^{i[k_x(x-x') + k_z(z-z')]} dk_x f(\mathbf{r}') a_0 e^{i\mathbf{k}_{\mathrm{I}}\cdot\mathbf{r}'} d^2 r' \\
&= \frac{ia_0}{4\pi} \iint_S \int_{-\infty}^{\infty} \frac{1}{k_z} e^{i[k_x(x-x') + k_z(z-z')]} f(\mathbf{r}') e^{i\mathbf{k}_{\mathrm{I}}\cdot\mathbf{r}'} dk_x d^2 r' \\
&= \frac{ia_0}{4\pi} \int_{-\infty}^{\infty} \iint_S \frac{1}{k_z} e^{i[k_x(x-x') + k_z(z-z')]} f(\mathbf{r}') e^{i\mathbf{k}_{\mathrm{I}}\cdot\mathbf{r}'} d^2 r' dk_x \\
&= \frac{ia_0}{4\pi} \int_{-\infty}^{\infty} \iint_S f(\mathbf{r}') e^{-i[(k_x - k_{\mathrm{I}x})x' + (k_z - k_{\mathrm{I}z})z']} d^2 r' \frac{1}{k_z} e^{i\mathbf{k}\cdot\mathbf{r}} dk_x \\
&= \frac{ia_0}{4\pi} \int_{-\infty}^{\infty} \iint_S f(\mathbf{r}') e^{-i[(\mathbf{k} - \mathbf{k}_{\mathrm{I}})\cdot\mathbf{r}']} d^2 r' \frac{1}{k_z} e^{i\mathbf{k}\cdot\mathbf{r}} dk_x.
\end{aligned} \tag{2.40}$$

Although some algorithms use different distances to the detection plane to obtain the different projections to form the sinogram [81], the most common approach to achieve these different projections is to rotate the sample under study or the measurement system around it. Assume that the sample is rotated by an angle ϕ, as shown in Fig. 2.5.

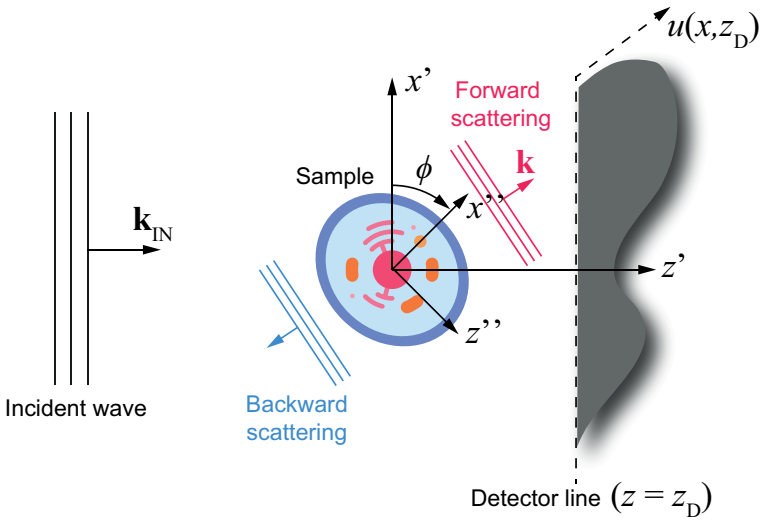

Fig. 2.5 Diffraction tomography concept

The refractive index is now described by the function:

$$f_2(\mathbf{r}') = f(\mathbf{r}'') = f(R_\phi \mathbf{r}') \,, \tag{2.41}$$

where R_ϕ is the rotation-by-ϕ operator that connects the coordinate systems (x',z') and (x'',z''), which in matrix notation satisfies the following relation:

$$\begin{pmatrix} x'' \\ z'' \end{pmatrix} = R_\phi \begin{pmatrix} x' \\ z' \end{pmatrix} = \begin{pmatrix} \cos\phi & \sin\phi \\ -\sin\phi & \cos\phi \end{pmatrix} \begin{pmatrix} x' \\ z' \end{pmatrix} \,. \tag{2.42}$$

That is, for a rotation angle ϕ, we have:

$$u_{B\phi}(\mathbf{r}) = \frac{ia_0}{4\pi} \int_{-\infty}^{\infty} \iint_S f(\mathbf{r}') e^{-i[(\mathbf{k}-\mathbf{k}_I)\cdot\mathbf{r}']} d^2r' \frac{1}{k_z} e^{i\mathbf{k}\cdot\mathbf{r}} dk_x \,. \tag{2.43}$$

We now perform a variable change from (x',z') to (x'',z'') (we use the fact that R_ϕ is a unitary operator with Jacobian $J = 1$):

$$u_{B\phi}(\mathbf{r}) = \frac{ia_0}{4\pi} \int_{-\infty}^{\infty} \iint_S f(\mathbf{r}'') e^{-i\left[(\mathbf{k}-\mathbf{k}_I)\cdot R_\phi^{-1}\mathbf{r}''\right]} d^2r'' \frac{1}{k_z} e^{i\mathbf{k}\cdot\mathbf{r}} dk_x \,. \tag{2.44}$$

Given two 2D vectors $\mathbf{a}$ and $\mathbf{b}$, their scalar product can be expressed as the following matrix product:

$$\mathbf{a}\cdot\mathbf{b} = AB = \begin{pmatrix} a_1 & a_2 \end{pmatrix} \begin{pmatrix} b_1 \\ b_2 \end{pmatrix} \,, \tag{2.45}$$

additionally, the orthogonality of the operator R_ϕ ($R_\phi^{-1} = R_\phi^{\mathrm{T}}$) allows us to write (note that $(\mathbf{a}\cdot\mathbf{b})^{\mathrm{T}} = \mathbf{a}\cdot\mathbf{b}$ because $\mathbf{a}\cdot\mathbf{b}$ is a scalar):

$$\begin{aligned}\mathbf{a}\cdot R_\phi^{-1}\mathbf{b} &= AR_\phi^{-1}B = (AR_\phi^{-1}B)^{\mathrm{T}} = B^{\mathrm{T}}(AR_\phi^{-1})^{\mathrm{T}} = B^{\mathrm{T}}(R_\phi^{-1})^{\mathrm{T}}A^{\mathrm{T}} = B^{\mathrm{T}}(R_\phi^{-1})^{\mathrm{T}}A^{\mathrm{T}} \\ &= B^{\mathrm{T}}RA^{\mathrm{T}} = \mathbf{b}\cdot R\mathbf{A} = R\mathbf{A}\cdot\mathbf{b}\,. \end{aligned} \tag{2.46}$$

Hence:

$$\begin{aligned}u_{\mathrm{B}\phi}(\mathbf{r}) &= \frac{ia_0}{4\pi}\int_{-\infty}^{\infty}\iint_S f(\mathbf{r}'')e^{-i\left[R_\phi(\mathbf{k}-\mathbf{k}_{\mathrm{I}})\mathbf{r}''\right]}d^2r''\frac{1}{k_z}e^{i\mathbf{k}\cdot\mathbf{r}}dk_x \\ &= \frac{ia_0}{4\pi}\int_{-\infty}^{\infty}2\pi\hat{F}\left(R_\phi(\mathbf{k}-\mathbf{k}_{\mathrm{I}})\right)\frac{1}{k_z}e^{i\mathbf{k}\cdot\mathbf{r}}dk_x\,, \end{aligned} \tag{2.47}$$

where F is the 2D Fourier transform of f:

$$\hat{F}(\mathbf{k}) = \hat{F}(k_x,k_z) = \frac{1}{2\pi}\iint_S f(\mathbf{r})e^{-ik_xx}e^{-ik_zz}d^2r = \frac{1}{2\pi}\iint_S f(\mathbf{r})e^{-i\mathbf{k}\cdot\mathbf{r}}d^2r\,. \tag{2.48}$$

At the detector line, the field reads:

$$u_{\mathrm{B}\phi}(x,z_{\mathrm{D}}) = \frac{ia_0}{2}\int_{-\infty}^{\infty}\hat{F}\left(R_\phi(\mathbf{k}-\mathbf{k}_{\mathrm{I}})\right)\frac{1}{k_z}e^{ik_zz_{\mathrm{D}}}e^{ik_xx}dk_x\,. \tag{2.49}$$

Defining the inverse Fourier transform (iFFT) of a function H as:

$$h(x) = \mathrm{TF}^{-1}[\hat{H}(x)] = \frac{1}{\sqrt{2\pi}}\int_{-\infty}^{\infty}\hat{H}(k_x)e^{ik_xx}dk_x, \tag{2.50}$$

we obtain:

$$u_{\mathrm{B}\phi}(x,z_{\mathrm{D}}) = \frac{ia_0}{2}\sqrt{2\pi}\mathrm{TF}^{-1}\left[\hat{F}\left(R_\phi(\mathbf{k}-\mathbf{k}_{\mathrm{I}})\right)\frac{1}{k_z}e^{ik_zz_{\mathrm{D}}}\right](x). \tag{2.51}$$

Taking the Fourier transform with respect to x:

$$\begin{aligned}\hat{U}_{\mathrm{B}\phi}(k_x,z_{\mathrm{D}}) &= \mathrm{TF}[u_{\mathrm{B}\phi}(x,z_{\mathrm{D}})](k_x) = \int_{-\infty}^{\infty}u_{\mathrm{B}\phi}(x,z_{\mathrm{D}})e^{-ik_xx}dx \\ &= ia_0\sqrt{\frac{\pi}{2}}\hat{F}\left(R_\phi(\mathbf{k}-\mathbf{k}_{\mathrm{I}})\right)\frac{1}{k_z}e^{ik_zz_{\mathrm{D}}}\,. \end{aligned} \tag{2.52}$$

Solving for F:

$$\hat{F}\left(R_\phi(\mathbf{k}-\mathbf{k}_{\mathrm{I}})\right) = \sqrt{\frac{2}{\pi}}\frac{k_z}{ia_0}e^{-ik_zz_{\mathrm{D}}}\hat{U}_{\mathrm{B}\phi}(k_x,z_{\mathrm{D}})\,, \tag{2.53}$$

with k_z as defined in Eq. 2.37.

2.3.1 Implementation

The objective is to obtain the image function $f(x,y)$ from the Fourier transform of each projection $\hat{U}_{B\phi}(k_x, z_D)$, similar to the algorithm obtaining in section 2.2.1. Now, the difference is that the points defined in the Fourier space for each projection are places in a semi-circumference space instead of a straight line. The first step starts performing the iFFT to equation 2.53:

$$f(\mathbf{r}) = \sqrt{\frac{2}{\pi}} \frac{1}{ia_0 2\pi} \iint k_z e^{-ik_z z_D} \hat{U}_{B\phi}(k_x, z_D)\, e^{i\left(R_\phi(\mathbf{k}-\mathbf{k}_I)\right)} dk_x dk_z. \tag{2.54}$$

A variable change, from (k_x, k_z) space to (k_{Dx}, ϕ) can be done, being k_{Dx} the Fourier space along the detector line (perpendicular to the illumination source) and ϕ the angle of rotation of the sample. As seen in [66], the coordinate change can be addressed as follows:

$$k_x = k_{Dx}\cos\phi - \left[\sqrt{k_M^2 - k_{Dx}^2} - k_M\right]\sin\phi\ , \tag{2.55}$$

$$k_z = k_{Dx}\sin\phi + \left[\sqrt{k_M^2 - k_{Dx}^2} - k_M\right]\cos\phi\ , \tag{2.56}$$

while the Jacobian follows:

$$J = \frac{\partial k_x \partial k_z}{\partial k_{Dx} \partial \phi} = \begin{pmatrix} \cos\phi + \dfrac{k_{Dx}}{\sqrt{k_M^2 - k_{Dx}^2}}\sin\phi & -k_{Dx}\sin\phi - \left(\sqrt{k_M^2 - k_{Dx}^2} - k_M\right)\cos\phi \\ \sin\phi - \dfrac{k_{Dx}}{\sqrt{k_M^2 - k_{Dx}^2}}\cos\phi & k_{Dx}\cos\phi - \left(\sqrt{k_M^2 - k_{Dx}^2} - k_M\right)\sin\phi \end{pmatrix}, \tag{2.57}$$

whose determinant, while $\cos^2\phi + \sin^2\phi = 1$, could be expressed as:

$$\begin{aligned} det(J) &= k_{Dx} - \left(\frac{k_{Dx}\left(\sqrt{k_M^2 - k_{Dx}^2} - k_M\right)}{\sqrt{k_M^2 - k_{Dx}^2}}\right) \quad = k_{Dx} - \left(\frac{k_{Dx}\sqrt{k_M^2 - k_{Dx}^2}}{\sqrt{k_M^2 - k_{Dx}^2}} - \frac{k_{Dx}k_M}{\sqrt{k_M^2 - k_{Dx}^2}}\right) \\ &= \frac{k_{Dx}k_M}{\sqrt{k_M^2 - k_{Dx}^2}}\ . \end{aligned} \tag{2.58}$$

Performing the variable change over equation 2.54, considering that the FT of the projection will be taken along the detector line $\left[\hat{U}_{B\phi}(k_x, z_D) = \hat{U}_{B\phi}(k_{Dx})\right]$ and considering from equation 2.37 that $k_z' = \sqrt{k_M^2 - k_{Dx}^2}$, ones arrive to:

$$f(\mathbf{r}) = \sqrt{\frac{2}{\pi}} \frac{1}{ia_0 2\pi} \int \int_0^{2\pi} \left| \frac{k_M k_{Dx}}{k'_z} \right| k'_z e^{-ik'_z z_D} \hat{U}_{B\phi}(k_{Dx})\, e^{i\left(R_\phi(\mathbf{k}-\mathbf{k}_I)\right)} d\phi dk_{Dx}$$
$$= \frac{k_M}{ia_0(2\pi)^{3/2}} \int \int_0^{2\pi} |k_{Dx}|\, e^{-ik'_z z_D} \hat{U}_{B\phi}(k_{Dx})\, e^{i\left(R_\phi(\mathbf{k}-\mathbf{k}_I)\right)} d\phi dk_{Dx} \,. \tag{2.59}$$

The last step to achieve the continuous solution has been done considering the transversal and perpendicular coordinates of the space, regarding the angle ϕ of rotation, which could be addressed easily as $x' = x\cos\phi + z\sin\phi$ and $x' = -x\sin\phi + z\cos\phi$, following the rotation operator describes in Eq. 2.42. The introduction of the rotational operator R_ϕ transforms the object function as follows:

$$f(\mathbf{r}) = \frac{k_M}{ia_0(2\pi)^{3/2}} \int_0^{2\pi} R_\phi \left\{ \int |k_{Dx}|\, e^{-ik'_z z_D} \hat{U}_{B\phi}(k_{Dx})\, e^{i\left[k_{Dx}x' + (k'_z - k_M)z'\right)} dk_{Dx} \right\} d\phi \,. \tag{2.60}$$

Due to the relation between k_{Dx} and k'_z, the iFFT must be performed for each value of ϕ before the rotation. Besides, a 2π factor arises when the iFFT in one dimension is applied:

$$f(\mathbf{r}) = \frac{k_M}{ia_0 2\pi} \int_0^{2\pi} R_\phi \left\{ iFFT_{1D} \left\{ |k_{Dx}|\, e^{-ik'_z z_D} \hat{U}_{B\phi}(k_{Dx})\, e^{i(k'_z - k_M)z'} \right\} \right\} d\phi \,. \tag{2.61}$$

To implement the algorithm in the MATLAB environment, the solution must be discretized. Finally, the backpropagation algorithm for N projections for linear detector in two dimensions can be expressed:

$$f(\mathbf{r}) = \frac{k_M}{ia_0 2\pi} \sum_{n=1}^{N} \frac{2\pi}{N} R_{\phi_n} \left\{ iFFT_{1D} \left\{ |k_{Dx}|\, \hat{U}_{B,\phi_n}(k_{Dx})\, e^{-ik'_z z_D} e^{i(k'_z - k_M)z'} \right\} \right\} d\phi \,. \tag{2.62}$$

In contrast to the implementation carried out in [66], the sinogram could be used directly without the necessity of a previous normalization. There is a huge difference between this algorithm and the filtered backprojection (Eq. 2.10) since the iFFT should be performed for each angle since both exponential factors are k'_z dependent, and $k'_z = \sqrt{k_M^2 - k_{Dx}^2}$. Once each iFFT has been performed, the resulting 2D RI map is rotated and added to the reconstruction canvas.

2.3.2 Results

The implementation has been performed in MATLAB following equation 2.62 and the Python library described in [82]. The same sinogram used by Müller obtaining from a simulated 2D cell has been introduced in our algorithm, to test the code in the first place.

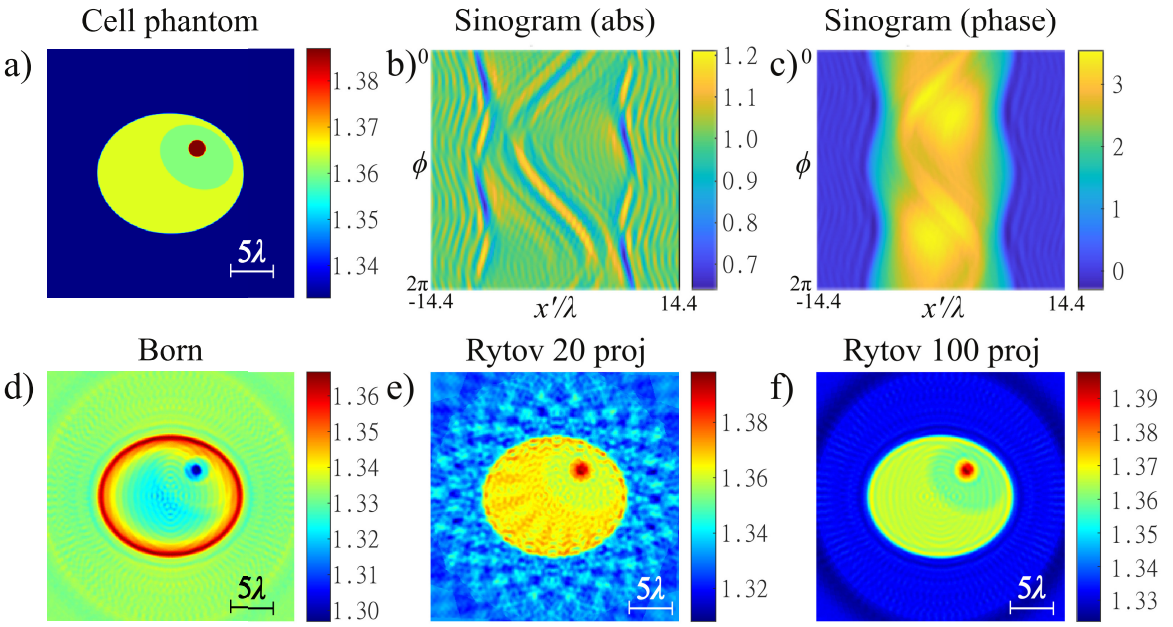

Fig. 2.6 Solution of linear detector tomography using Müller sinogram as input. a) Cell phantom. The sinogram generated by Müller has been shown in their absolute value b) and the phase c). d) Solution for the Born approximation with 100 projections. Solution for the Rytov approximation for e) 20 projections and f) 100 projections. The size of images a) d) e) and f) is $28.8\lambda \times 28.8\lambda$.

A detailed design of this cellular phantom could be found in Appendix A.1. The algorithm returns the expected result for this sinogram, as seen in Fig. 2.6, validating our algorithm.

Although the result with 100 projections differentiates the three zones of the cell (see Fig. 2.6 f), a ripple appears in the cytoplasm. As explained in [82], 100 projections are an insufficient amount of data in this complex scenario. To extend our study, and to learn how to devise sinograms using any phantom, we model the same cell in the software COMSOL MULTIPHYSICS. In this software, the 2D model is built, assigning the permittivity value for each segment as the square of its corresponding RI. After that, the mesh is generated, and the scattered field is calculated through the module of Electromagnetic Waves, Frequency Domain (emw) via MUMPS solver (Multifrontal Massively Parallel sparse direct Solver). Since different angles of rotation to the sample are applied, the scattered field recorded in a detector line for each value of ϕ corresponds to each projection, forming the sinogram with a set of projections. In [82, Fig 3. a)], it can be noticed how 150 projections are enough for this cell model since the reconstruction is not improved for a higher number of illumination angles. A 50λ-wide linear detector has been placed at a length detector of $l_D = 12\lambda$ from the center of the configuration to record our sinogram. To ensure at least 10 points per λ, each projection records data of the scattering field at 500 points. As 150 projections have been calculated, a 150×500 sinogram is used

as input to the algorithm. The results of the tomographic process (hereinafter referred to as *tomogram*) can be seen in figure 2.7, where a reconstruction space of $30\lambda \times 30\lambda$ is shown.

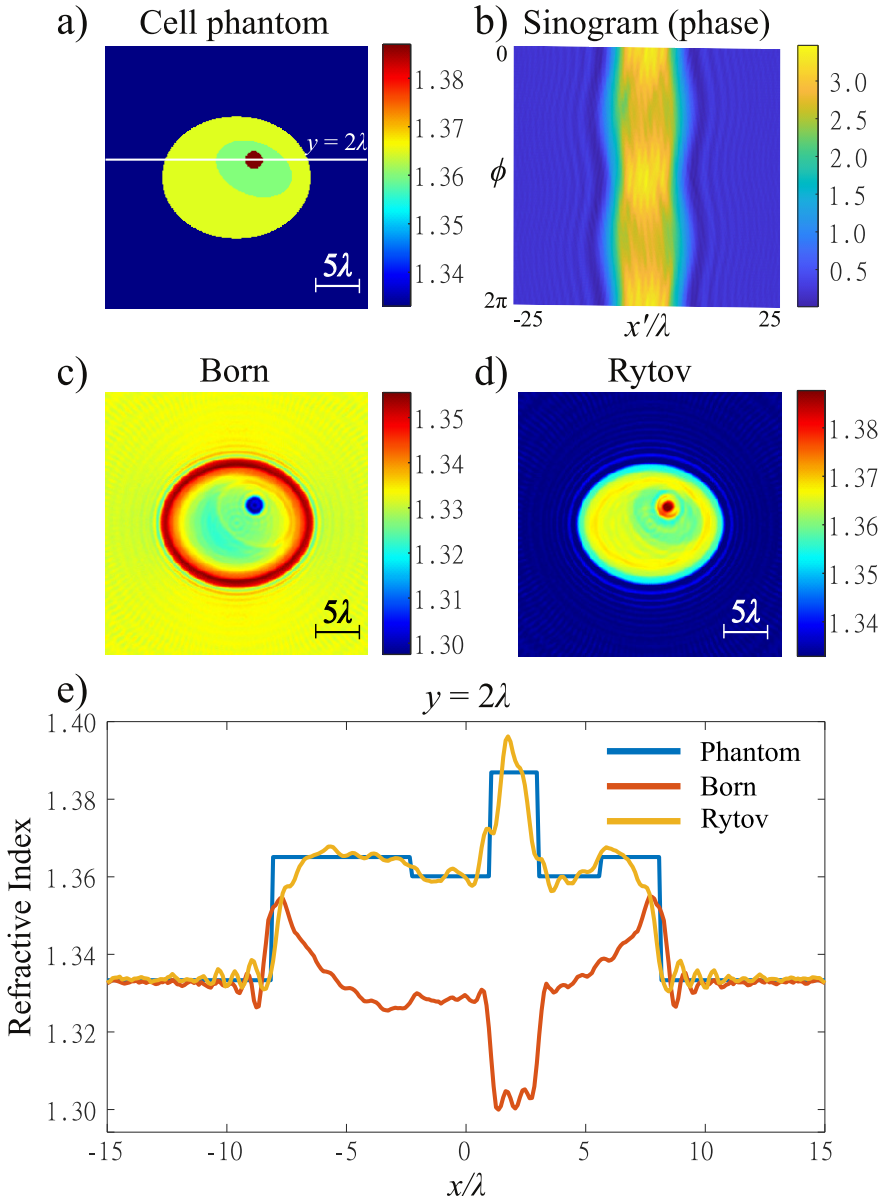

Fig. 2.7 Solution of the linear detector tomography using the sinogram generated in COMSOL as input. a) Cell phantom. b) Unwrapped phase of the sinogram. c) Tomogram for the Born approximation. d) Tomogram for the Rytov approximation. e) RI profile of the cell phantom, and both solutions, at the line $y = 2\lambda$, indicated in a) with a white line. The size of images a), c) and d) is $30\lambda \times 30\lambda$.

To measure the reconstruction quality, the normalized root-mean-square (RMS) error has been introduced for 2D as indicates in [82, Eq. 1]:

$$E_{RMS} = \sqrt{\frac{\sum_{VOL}(n_{PH} - n_{SOL})^2}{(n_{PH} - 1)^2}}, \tag{2.63}$$

being n_{PH} the RI of the phantom, n_{SOL} the RI of the reconstructed solution, and VOL the reconstruction volume, which makes E_{RMS} the RMS error of the solution compared with the phantom at the reconstructed space. For 2D cell phantoms with the RI appropriated for biological cells studied in [82], the E_{RMS} varies from 10^{-2} and 10^{-1} for the Born approximation, taking values less than 10^{-2} in the case of the Rytov approximation. In our case, the error values are in line with the expected, since $E_{RMS,Born} = 2.5 \times 10^{-2}$ and $E_{RMS,Rytov} = 7.9 \times 10^{-3}$. Moreover, in Fig. 2.7 c) and d) the results are like those seen in Fig. 2.6. Regarding the profile of the tomogram at the line for a fixed value of $y = 2\lambda$ (figure 2.7 e), the tomogram for the Born approximation is in line with the shown in [82, Fig 1. f)]. A good approximation is also seen in the case of the Rytov approximation, although the result is not perfect. There is an explanation for this behavior, since our results fit with the unfocused version of the Müller results, as seen in [83, section 3.2.2]. The lack of numerical focusing produces a corrugation in the solution. However, the E_{RMS} value, besides it is in line with the expected, is far from the 25% limit (a validation error threshold defined in [78]), and the cell areas are differentiated. Therefore, the numerical focusing improvement should be studied in future work and could not be addressed at this time.
At this point, it is worth mentioning that all the sinograms used as input for the tomography algorithms for the rest of this dissertation have been generated in COMSOL MULTIPHYSICS software, like in this example.
The following test is performed using an adapted version of the Shepp-Logan phantom. This interpretation of the Shepp-Logan mask is defined by two parameters , which brings its RI variation with the background closer to a cell sample scenario. On one hand, the size can be chosen by the size factor f_S. On the other hand, the RI is tuned by the index factor f_N. The detailed explanation of this phantom could be found in Appendix A.2. The first sinogram obtained through this phantom has 250 projections, recording the scattering data in 500 points for each detector line as in the previous test. The phantom is tuned using $f_S = 7.5$ and $f_N = 0.02$. The result for a $24\lambda \times 24\lambda$ reconstructed space can be seen in figure 2.8.

In this case, the RMS errors of the results are higher than for the cell model, since $E_{RMS,Born} = 0.256$ and $E_{RMS,Rytov} = 0.228$. The reconstruction by the Born approximation has an error over the threshold of 25%. As seen in figure 2.8 c), the solution is blurry, and only areas *c*, *d*, and *e* are differentiated in this case of the Born reconstruction. Three lines are chosen to observe the quality of the RI reconstruction. The central vertical slice for

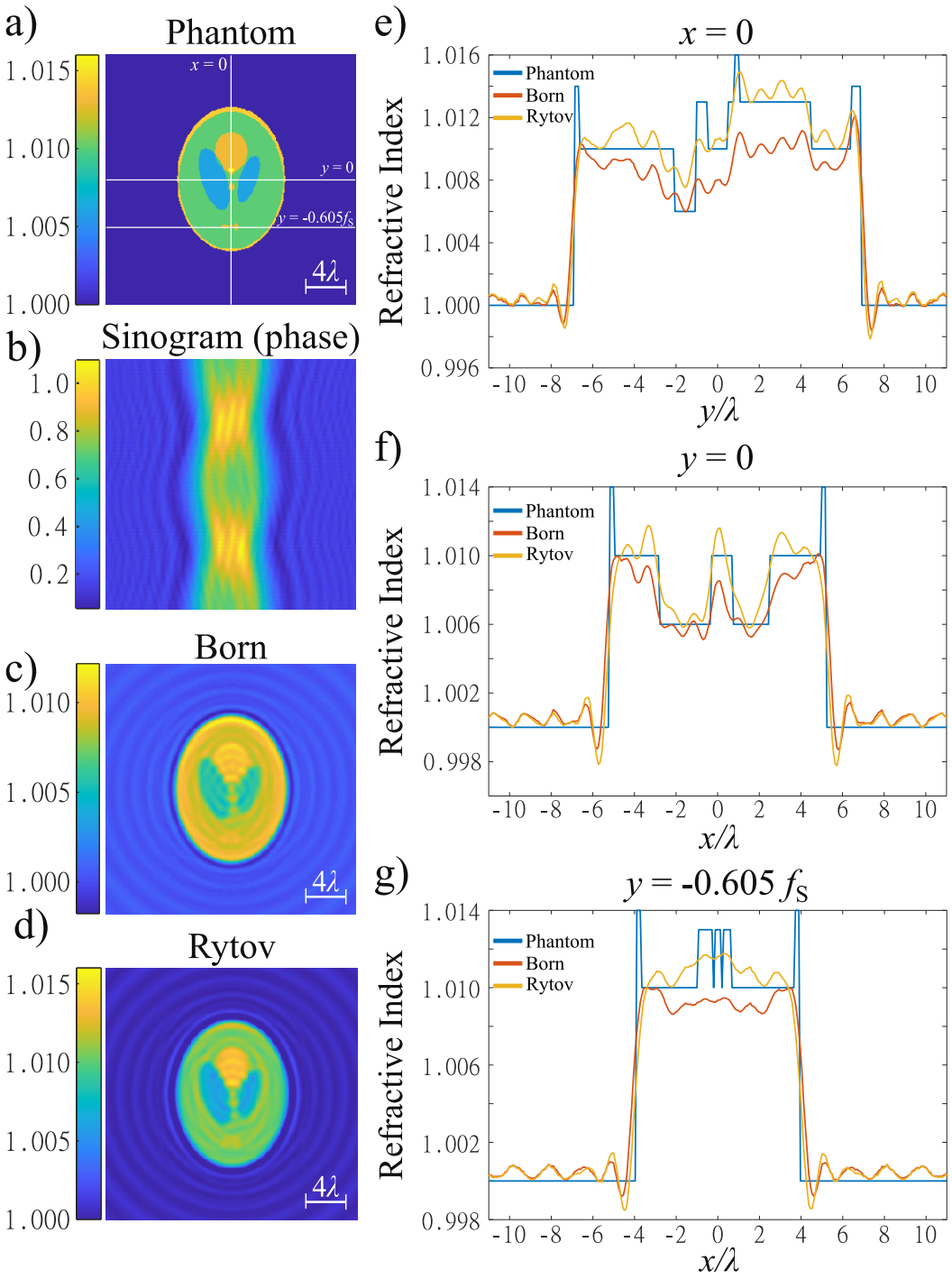

Fig. 2.8 Linear detector tomography solution for a Shepp Logan adapted phantom using $f_S = 7.5$ and $f_N = 0.02$. a) Phantom, white lines indicate the places where the profiles in e), f) and g) are taken. b) Unwrapped phase of the sinogram. c) Tomogram for the Born approximation. d) Tomogram for the Rytov approximation. RI profile for the fixed values of e) $x = 0$, f) $y = 0$ and g) $y = -0.065 f_S$. The size of images a), c) and d) is $24\lambda \times 24\lambda$.

a fixed value of $x = 0$ and the horizontal line for $y = 0$ (Fig. 2.8 e) and f) manifest that, albeit almost all areas can be differentiated, the lack of numerical focusing produces a ripple. Moreover, the contour of the phantom (segment *a*) is quite thin, consequently, the reconstruction failed in this area. The tomogram in the case of the Rytov approximation (Fig. 2.8 d) are in good shape with the original phantom, although the segments *h*, *i*, and *j* cannot be differentiated in the reconstruction of either approach. This is confirmed by the profile at the line $y = -0.605 f_S$ (Fig. 2.8 g). This resolution problem is an issue to deal with in section 2.5.

The following test is performed using the same Shepp-Logan adapted phantom but changing the model parameters to $f_S = 10$ and $f_N = 0.025$. To compare with the previous case, the same tomography scenario is proposed: the detector is placed at $l_D = 10\lambda$, and its size is 50λ-wide, while the sinogram has a size of 250×500. The result for a $28\lambda \times 28\lambda$ reconstructed space can be seen in figure 2.9.

An error of $E_{RMS,Born} = 0.38$ confirms that when the size of the sample under study is larger (from 15λ to 20λ), the Born approximation tends to be less accurate. This can be seen in Fig. 2.9 c) by comparing it with the previous case in figure 2.8. The error for the Rytov approximation is the same as for the previous solution, $E_{RMS,Rytov} = 0.228$, while the tomogram is similar too, as seen in Fig. 2.9 d). As in the previous reconstruction, the edge of the phantom is overly thin, and only the slightly wider upper boundary is barely visible.

To finish the linear detector test, the old logo of NTC is used as a phantom. As in the case of the adapted Shepp-Logan version, the phantom is modeled by parameters. The detailed explanation of this phantom could be found in Appendix A.3. Now, a size factor of $f_S = 1$ and a RI of $n_{OBJ} = 1.025$ are used. For this test, 360 angles of illumination are considered, and the detector is placed at $l_D = 8\lambda$ while its size is 70λ-wide, then, to take 10 data points per λ, the sinogram has a size of 360×700. The result for a $20\lambda \times 20\lambda$ reconstructed space can be seen in figure 2.10. Although the error of these results is elevated ($E_{RMS,Born} = 0.38$ and $E_{RMS,Rytov} = 0.31$), the profiles shown in figure 2.10 d) and e) clearly show the separation between sample figures. The ripple observed at the edge of the cylinders is quite similar to the observed in [78], where it is also shown how the Born reconstruction taken to its limit almost matches the Rytov reconstruction, which is closer to the phantom. This phantom, for a smaller size of the figures, is used in section 2.5.

In addition to the aforementioned section, the use of this linear detector algorithm is also used in Chapter 4: Invisibility Passive Device, where, besides being an indispensable tool in our study, it is completely validated through the reconstruction of cylindrical, square, and hexagonal uncloaked objects.

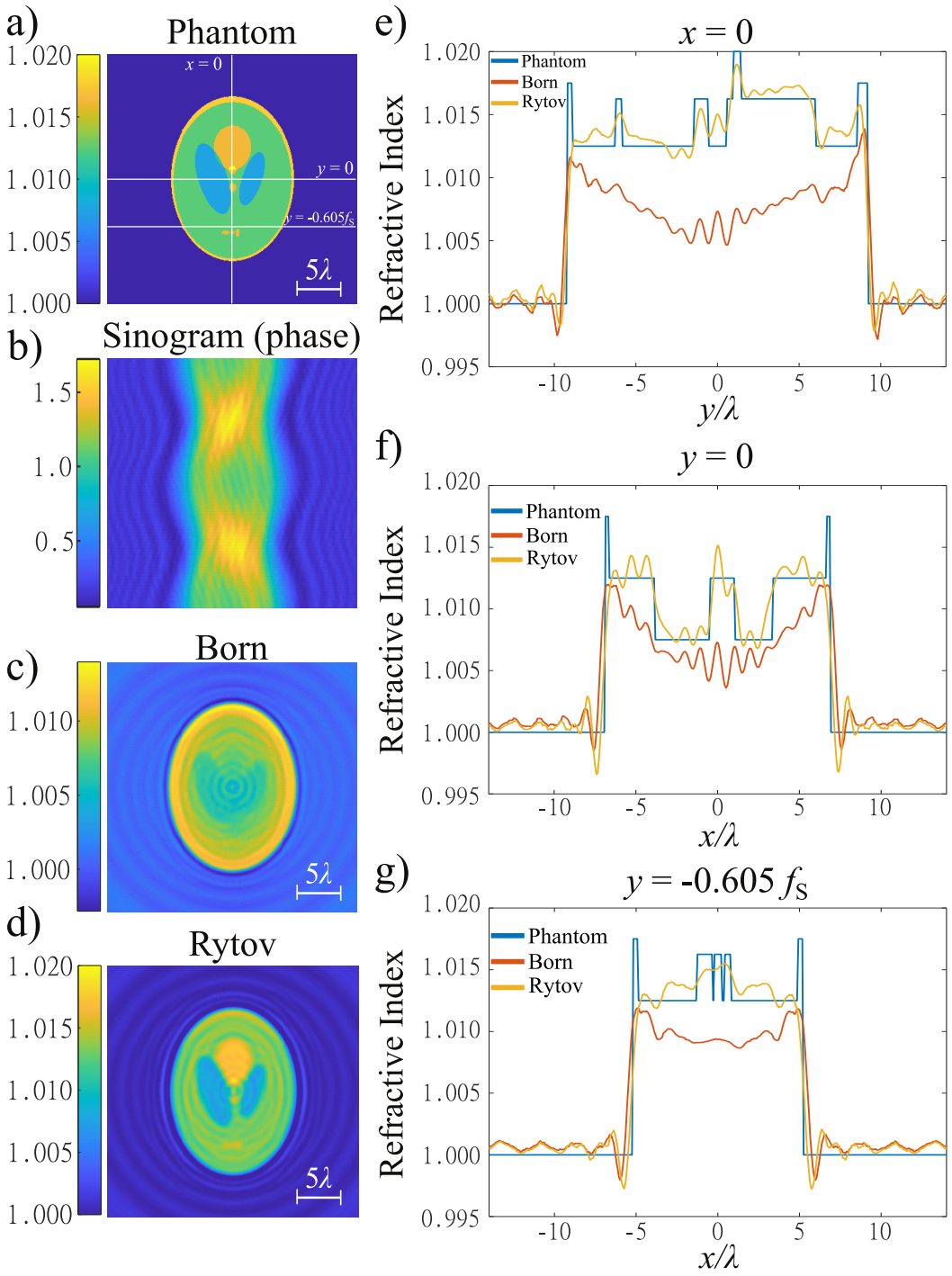

Fig. 2.9 Solution of linear detector tomography for a Shepp Logan Phantom using $f_S = 10$ and $f_N = 0.025$. a) Phantom, white lines indicate the places where the profiles in e), f) and g) are taken. b) Unwrapped phase of the sinogram. c) Tomogram for the Born approximation. d) Tomogram for the Rytov approximation. RI profile for the fixed values of e) $x = 0$, f) $y = 0$ and g) $y = -0.065 f_S$. The size of images a), c) and d) is $28\lambda \times 28\lambda$.

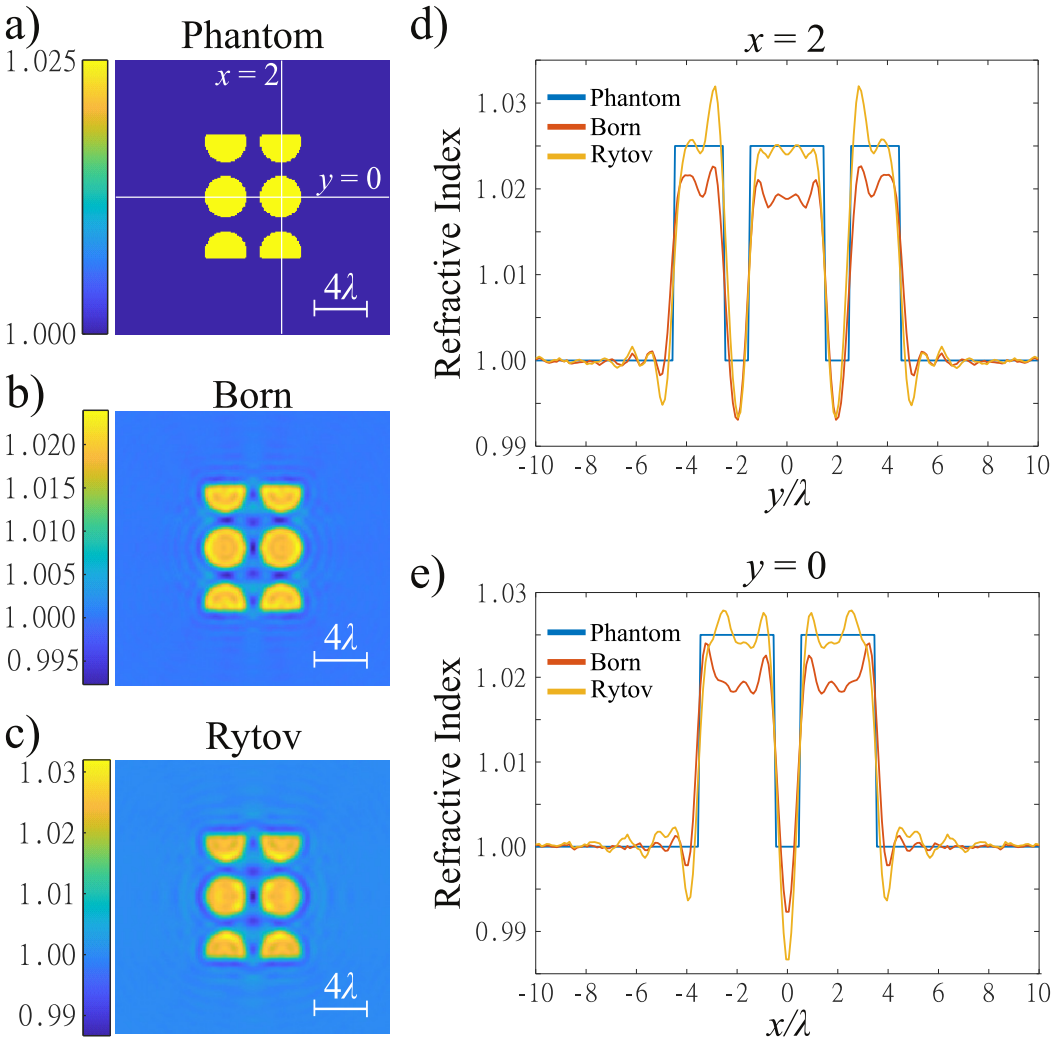

Fig. 2.10 Linear detector tomography solution for NTC Logo $f_S = 1$, $n_{OBJ} = 1.025$ phantom. a) Phantom, white lines indicate the places where the profiles in d) and e) are taken. b) Tomogram for the Born approximation. c) Tomogram for the Rytov approximation. RI profile for the fixed values of d) $x = 2$ and e) $y = 0$. The size of images a), b) and c) is $20\lambda \times 20\lambda$.

2.4 Circular Detector

Most ODT studies have been developed using linear detectors as a sensor to read the scattered signal, because of the simplification of the method. Some studies even directly apply the linear algorithm to circular detection systems [84], which does not solve the problem of inverse scattering for circular detectors. However, ODT with a circular array detector could be achieved without complex systems, as notable results have been obtained with simple phantoms [85, 86]. To develop an algorithm for circular detector tomography, we start following the steps described in [87], which also starts with the inhomogeneous Helmholtz equation, but introducing the object function $o(\mathbf{r})$ as follows:

$$(\nabla^2 + k_M^2)u(\mathbf{r}) = k_M^2 o(\mathbf{r})u(\mathbf{r}) \, . \tag{2.64}$$

The tomography problem lies in solving object function from the measured scattered field. For that, the plane wave scattering amplitude of the object is used, which is defined, for the case of 2D objects, by the equation [87, eq. 3]:

$$f(\mathbf{s},\mathbf{s}_0) \equiv k_M^2 \iint o(\mathbf{r})u(\mathbf{r};\mathbf{s}_0)e^{-ik\mathbf{s}\cdot\mathbf{r}}d^2r \, , \tag{2.65}$$

where $\mathbf{s}_0$ and $\mathbf{s}$ are the two-dimensional unit vectors that can range over the entire unit circle, $u(\mathbf{r};\mathbf{s}_0)$ is the total field $u = u_S + u_0$ generated by illumination plane wave with $\mathbf{s}_0$ as this unit propagation vector. Applying the *Born approximation* and reducing the total field by the illumination wave ($u(\mathbf{r};\mathbf{s}_0) = e^{ik_M\mathbf{s}_0}$), the scattering amplitude follows:

$$f(\mathbf{s},\mathbf{s}_0) \approx k_M^2 \iint o(\mathbf{r})e^{-ik(\mathbf{s}-\mathbf{s}_0)\cdot\mathbf{r}}d^2r \; = k_M^2 O[k_M(\mathbf{s}-\mathbf{s}_0)] \, , \tag{2.66}$$

where $\hat{O}(\mathbf{k})$ is the 2DFT of the object profile over the frequency space defined in $\mathbf{k} = k_M(\mathbf{s}-\mathbf{s}_0)$:

$$\hat{O}(\mathbf{k}) = \iint o(\mathbf{r})e^{-i\mathbf{k}\cdot\mathbf{r}}d^2r \, . \tag{2.67}$$

Since covering the entire frequency space is an impossible task, the solution of the object profile is a "Low-Pass approximation" when the 2D iFFT is resolved:

$$o_{LP}(\mathbf{r}) = \frac{1}{(2\pi)^2} \iint \hat{O}(\mathbf{k})e^{i\mathbf{k}\cdot\mathbf{r}}d^2k \, . \tag{2.68}$$

Equations 2.66 and 2.68 are related:

$$o_{\mathrm{LP}}(\mathbf{r}) = \frac{1}{(2\pi k_{\mathrm{M}})^2} \iint f(\mathbf{s},\mathbf{s}_0) e^{i\mathbf{k}\cdot\mathbf{r}} d^2k \,, \tag{2.69}$$

and a variable change could be performed, defining χ_0 and χ as the angles formed by $\mathbf{s}_0$ and $\mathbf{s}$ concerning a fixed reference direction. Then, χ_0 is the angle of illumination and χ is the angle of detection in our circular algorithm. The frequency space defined $\mathbf{k} = k_{\mathrm{M}}(\mathbf{s}-\mathbf{s}_0)$ is related to these angles as follows:

$$\begin{aligned} k_x &= k_{\mathrm{M}}(\cos\chi - \cos\chi_0) \,, \\ k_y &= k_{\mathrm{M}}(\sin\chi - \sin\chi_0) \,, \end{aligned} \tag{2.70}$$

therefore, the Jacobian for the variable change satisfies the following relation:

$$det(J) = det\left(\frac{\partial k_x \partial k_y}{\partial\chi\partial\chi_0}\right) = \begin{vmatrix} \frac{\partial k_x}{\partial\chi} & \frac{\partial k_x}{\partial\chi_0} \\ \frac{\partial k_z}{\partial\chi} & \frac{\partial k_z}{\partial\chi_0} \end{vmatrix} = \begin{vmatrix} -k_{\mathrm{M}}\sin\chi & k_{\mathrm{M}}\sin\chi_0 \\ k_{\mathrm{M}}\cos\chi & -k_{\mathrm{M}}\cos\chi_0 \end{vmatrix} = k_{\mathrm{M}}\sin(\chi-\chi_0). \tag{2.71}$$

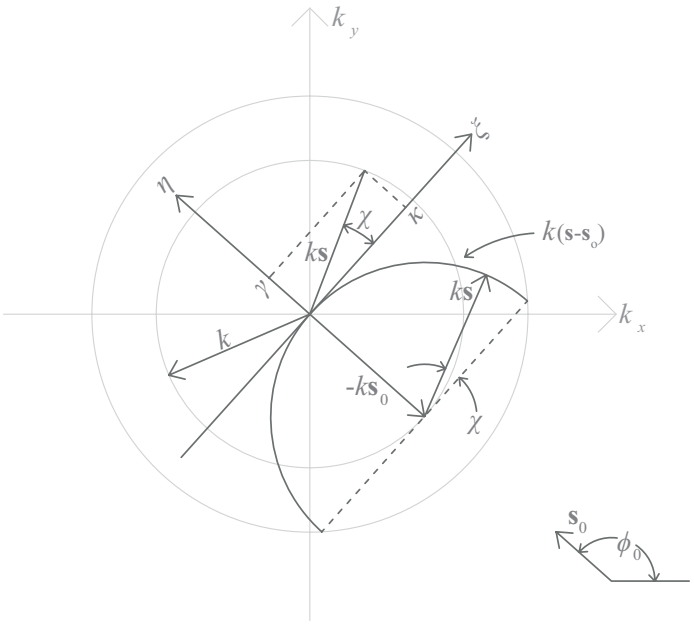

Fig. 2.11 The geometry used to evaluate the χ integral [14].

Being $\mathbf{s} = (\cos\chi, \sin\chi)$ and $\mathbf{s}_0 = (\cos\chi_0, \sin\chi_0)$, as Fig. 2.11 pointed, this relation could be addressed:

$$\begin{aligned}\mathbf{s}\cdot\mathbf{s}_0 &= \cos\chi\cos\chi_0+\sin\chi\sin\chi_0\\ &= \frac{1}{2}(\cos(\chi+\chi_0)+\cos(\chi-\chi_0))+\frac{1}{2}(\cos(\chi-\chi_0)-\cos(\chi+\chi_0))\\ &= \cos(\chi-\chi_0)\,,\end{aligned} \tag{2.72}$$

thus resulting in the Jacobian for the variable change as:

$$J = k_{\mathrm{M}}^2(1-\mathbf{s}\cdot\mathbf{s}_0). \tag{2.73}$$

From here, and adding a $1/2$ factor due to the double coverage of space, the inversion formula follows:

$$o_{\mathrm{LP}}(\mathbf{r}) = \frac{k_{\mathrm{M}}^2}{2(2\pi)^2}\int_{-\pi}^{\pi}\int_{-\pi}^{\pi}\sqrt{1-(\mathbf{s}\cdot\mathbf{s}_0)^2}f(\mathbf{s},\mathbf{s}_0)e^{ik(\mathbf{s}-\mathbf{s}_0)\cdot\mathbf{r}}d\chi d\chi_0\,. \tag{2.74}$$

Once the inversion formula is obtained, a scattering amplitude function $f(\mathbf{s},\mathbf{s}_0)$ should be defined to obtain a reconstruction of the object profile. This issue has been studied broadly, especially by Porter [88], who proposed a two-step procedure that requires in the first place a holographic image formed from the measured field, and the Fourier transform of this image field later. To avoid both steps, a more direct method is used [87]. For the case of plane wave illumination on a circle of radius R centered at the origin, one arrives at [87, Eq. 15], which is reproduced next (all the previous steps are detailed in Appendix B.2):

$$f(\mathbf{s},\mathbf{s}_0) = 4i\int_0^{2\pi} u_{\mathrm{s}}(\sigma;\mathbf{s}_0)F_{\mathrm{R}}(\chi-\sigma)d\sigma\,. \tag{2.75}$$

In this case, σ and χ are the angles made by $\mathbf{r}'$ and $\mathbf{s}$ with an arbitrary reference direction, $u_{\mathrm{s}}(\sigma;\mathbf{s}_0)$ denotes the scattered field at the angle σ and the function $F_{\mathrm{R}}(\mathrm{X})$ is given by

$$F_{\mathrm{R}}(\chi-\sigma) = \frac{1}{(2\pi)^2}\sum_{n=-\infty}^{\infty}\frac{i^n}{H_n(k_{\mathrm{M}}R)}e^{in(\chi-\sigma)}\,, \tag{2.76}$$

where H_n is the n-th order Hankel function of the first kind, and $(\chi-\sigma)$ is the difference between the angle associated with the detecting point and the integration angle.

2.4.1 Implementation with far-field approximation

A *Fourier Diffraction Theorem (FDT) for Circular Array* has been proposed as follows [86]: *The scattered field measured with a large circular array surrounding the object is*

proportional to the Fourier transform of the object profile taken on the circumference of a circle of radius equal to the wavenumber and centered at $(-k_{\mathrm{M}}\cos\chi_0, -k_{\mathrm{M}}\sin\chi_0)$, (see Fig. 2.12).

The far-field approximation follows in [86] has been performed replacing the Hankel function like in [89, p. 364, eq. 9.2.3]:

$$H_\nu^{(1)} \sim \sqrt{2/(\pi z)}e^{i\left(z-\frac{1}{2}\nu\pi-\frac{1}{4}\pi\right)} \qquad (-\pi < \arg(z) < 2\pi)\ . \tag{2.77}$$

Now, following Eq. 2.66, using the scattering amplitude defined in equations 2.75 and 2.76 and the far-field approximation (Eq. 2.77), the inverse problem is reduced to:

$$\begin{aligned} k_{\mathrm{M}}^2\hat{O}[k_{\mathrm{M}}(\mathbf{s}-\mathbf{s}_0)] &= f(\mathbf{s},\mathbf{s}_0) \\ &= 4i\int_0^{2\pi} u_{\mathrm{s}}(\sigma;\mathbf{s}_0)\,\frac{1}{(2\pi)^2}\sum_{n=-\infty}^{\infty}\frac{i^n}{\sqrt{2/\pi k_{\mathrm{M}}R}e^{i\left(kR-\frac{n\pi}{2}-\frac{\pi}{4}\right)}}e^{in(\chi-\sigma)}\,d\sigma \\ &= \frac{4i}{(2\pi)^2}\int_0^{2\pi}\sqrt{\frac{\pi k_{\mathrm{M}}R}{2}}u_{\mathrm{s}}(\sigma;\mathbf{s}_0)\,e^{-i\left(k_{\mathrm{M}}R-\frac{\pi}{4}\right)}\sum_{n=-\infty}^{\infty} i^n\,e^{+i\frac{n\pi}{2}}e^{in(\chi-\sigma)}\,d\sigma. \end{aligned} \tag{2.78}$$

The previous step is solved with this affirmation:

$$\sum_{n=-\infty}^{\infty} i^n\,e^{+i\frac{n\pi}{2}} = 0. \tag{2.79}$$

Finally:

$$k_{\mathrm{M}}^2\hat{O}[k_{\mathrm{M}}(\mathbf{s}-\mathbf{s}_0)] = \frac{4i}{(2\pi)^2}\int_0^{2\pi}\sqrt{\frac{\pi k_{\mathrm{M}}R}{2}}u_{\mathrm{s}}(\sigma;\mathbf{s}_0)\,e^{-i\left(k_{\mathrm{M}}R-\frac{\pi}{4}\right)}\sum_{n=-\infty}^{\infty} e^{in(\chi-\sigma)}\,d\sigma, \tag{2.80}$$

with $k_{\mathrm{M}} = \dfrac{\omega}{c_o}$ as the wavenumber of the field surrounding the object. This equation is the starting point of [86, eq. 1]:

$$k_{\mathrm{M}}^2\hat{O}[k_{\mathrm{M}}(\mathbf{s}-\mathbf{s}_0)] = \frac{4i}{2\pi}\int_{-\pi}^{\pi} u_{\mathrm{s}}(R,\sigma,\chi_0)\sqrt{\frac{\pi k_{\mathrm{M}}R}{2}}\,e^{-i\left(k_{\mathrm{M}}R-\frac{\pi}{4}\right)}\sum_{n=-\infty}^{\infty} e^{in(\chi-\sigma)}\,d\sigma, \tag{2.81}$$

Where χ_0 is the angle of illumination and $\mathbf{s}_0$ is his vector, while σ is the angle of the received signal in respect to $\mathbf{s}_0$. χ is the angle of the scattered field, and $\mathbf{s}$ is his vector. The term $(\chi-\sigma)$ comes from $\mathbf{s}\cdot\mathbf{r} = R(\cos\chi\cos\sigma+\sin\chi\sin\sigma) = R\cos(\chi-\sigma)$ being R the radius,

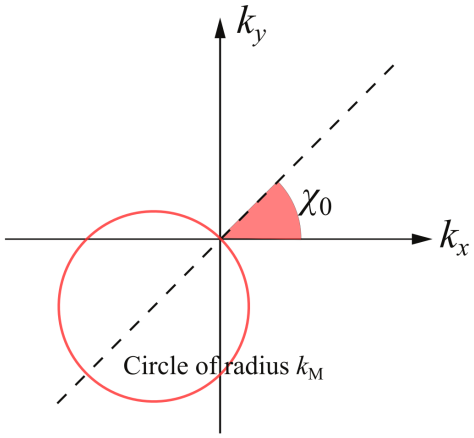

Fig. 2.12 As indicates in [86, Fig. 1], the u_S received by a circular array is proportional to the object Fourier transform on the showed circle for an angle of incidence $\pi/4$.

i.e., the distance to the detector from the center of the studied sample.

To continue with the reduction of the expression, the term $e^{in(\chi-\sigma)}$ is $n-$periodic:

$$e^{in(\chi-\sigma)} = \cos(n(\chi-\sigma)) + i\sin(n(\chi-\sigma)). \tag{2.82}$$

As we can express $\int e^{i\omega(\chi-\sigma)}d\omega = 2\pi\delta(\chi-\sigma)$, we are able to affirm that $\sum_{n=-\infty}^{\infty} e^{in(\chi-\sigma)} = 2\pi \sum_{m=-\infty}^{\infty} \delta(\chi-\sigma-2m\pi)$. Consequently, we can work with Eq. 2.81 dividing by k_M^2 into both sides of the equation, and replacing terms inside the integral:

$$\hat{O}[k_M(\mathbf{s}-\mathbf{s}_0)] = \frac{4i}{2\pi k_M^2}\sqrt{\frac{\pi k_M R}{2}}\, e^{-i\left(k_M R-\frac{\pi}{4}\right)} \int_{-\pi}^{\pi} u_s(R,\sigma,\chi_0)\; 2\pi \sum_{m=-\infty}^{\infty} \delta(\chi-\sigma-2m\pi)\, d\sigma\,. \tag{2.83}$$

Moreover, the term $2\pi \sum_{m=-\infty}^{\infty} \delta(\chi-\sigma-2m\pi)$ only takes a non-zero value in the integration interval $(-\pi,\pi)$, when $\sigma=\chi$. Besides, as we see, the points where the 2D Fourier transform takes values are: $(\mathbf{k}-\mathbf{k}_0) = (k_M(\cos\chi-\cos\chi_0), k_M(\sin\chi-\sin\chi_0))$.

The last change consists of $i = e^{i\frac{\pi}{2}}$, then $e^{-ik_M R}e^{+i\frac{\pi}{4}}e^{i\frac{\pi}{2}} = e^{-ik_M R}e^{i\frac{3\pi}{4}} = e^{-i\left(k_M R-\frac{3\pi}{4}\right)}$. Finally, we arrive at the equation of the Theory of Diffraction Tomographic Imaging with a Circular Array [86, Eq. 2]:

$$\hat{O}[k_M(\cos\chi-\cos\chi_0), k_M(\sin\chi-\sin\chi_0)] = \frac{4}{k_M^2}\sqrt{\frac{\pi k_M R}{2}}\, e^{-i\left(k_M R-\frac{3\pi}{4}\right)}\, u_s(R,\chi,\chi_0), \tag{2.84}$$

which could be summarized as the 2D Fourier transform of the object function, evaluated on a circle of radius k_{M} and centered at $(k_x = k_{\mathrm{M}}\cos\chi_0, k_y = k_{\mathrm{M}}\sin\chi_0)$, is equal to the observed scattered field on a large circle multiplied by a factor.

For the reconstruction algorithm, the angle of illumination χ_0 varies 360° by switching on one sensor to transmitter mode and keeping the remaining sensors in receiver mode. Keeping R value constant, the received field can be expressed as a function of two parameters:

- χ_0 : Angle of illumination.
- χ : Angular coordinate of each sensor.

Then every point could be **mapped** from (χ_0, χ) space onto (k_x, k_y) space:

$$\cos\chi - \cos\chi_0 = \frac{k_x}{k_{\mathrm{M}}}, \qquad \sin\chi - \sin\chi_0 = \frac{k_y}{k_{\mathrm{M}}}\,. \tag{2.85}$$

A **reverse map** is also possible, with two solutions for each pair of (k_x, k_y) space index (see Appendix B.3 for a complete development):

$$\chi_0 = \tan^{-1}\left\{\frac{-k_y - k_x\sqrt{\frac{2}{p}-1}}{-k_x + k_y\sqrt{\frac{2}{p}-1}}\right\}, \qquad \chi = \tan^{-1}\left\{\frac{+k_y - k_x\sqrt{\frac{2}{p}-1}}{+k_x + k_y\sqrt{\frac{2}{p}-1}}\right\}, \tag{2.86}$$

$$\chi_0 = \tan^{-1}\left\{\frac{-k_y + k_x\sqrt{\frac{2}{p}-1}}{-k_x - k_y\sqrt{\frac{2}{p}-1}}\right\}, \qquad \chi = \tan^{-1}\left\{\frac{+k_y + k_x\sqrt{\frac{2}{p}-1}}{+k_x - k_y\sqrt{\frac{2}{p}-1}}\right\}, \tag{2.87}$$

where:

$$p = \frac{k_x^2 + k_y^2}{2k_{\mathrm{M}}^2}\,. \tag{2.88}$$

An implementation problem arises, since the values of (χ_0, χ) that we will obtain may not correspond to the points where the scattered field is observed, therefore some form of interpolation must be used. This interpolation also works to adapt the input data to a rectangular grid, a necessary step to perform the iFFTs that will return the solution. Finally, the algorithm is implemented in MATLAB. Moreover, the algorithm is implemented as a Python library too, thanks to the virtual internship performed at the Guck Division of the Max Planck Institute for the Science of Light in Erlangen (Germany), supervised by Prof. Jochen Gück and Dr. Paul Müller. The results shown in this chapter correspond to the MATLAB obtained ones. In the first place, the library created for the implementation includes a function that forms the sinogram via the recorded data in COMSOL MULTIPHISICS. In this case, the far-field scattered field, available in the module

of Electromagnetic Waves, Frequency Domain *(emw)* of the software, is calculated for different angles of illumination and is recorded in a circular detector place at a distance of R from the center of the simulated sample. The next step of the algorithm is to interpolate the sinogram, from the observed (k_x, k_y) space obtained with the illumination χ_0 and received χ angles (via Eq. 2.86), to the rectangular empty matrix of (k'_x, k'_y) corresponds to the Fourier space. Then, applying the factor defined in equation 2.84, the discrete 2D iFFT is applied. The final step is to transform the object function $o(\mathbf{r})$ in $f(\mathbf{r})$, comparing Eq. 2.64 with Eq. 2.12,

$$f(\mathbf{r}) = -o(\mathbf{r})k_{\mathrm{M}}^2, \tag{2.89}$$

and then, the RI of the reconstruction $n(\mathbf{r})$ can be obtained via Eq. 2.13.

Results

To verify the algorithm, the phantoms described in Appendix A are used as in the previous section, although the test using the NTC logo as the input phantom is explained in the following section. In the first place, the far-field generated by the cell phantom is recorded via COMSOL MULTIPHISICS under 720 angles, in a circular detector with a radius of 30λ. Since 720 detector points are used to read the scattered field (to achieve a square sinogram), almost 4 points per λ are utilized. The results can be seen in Figure 2.13, where a reconstruction space of $30\lambda \times 30\lambda$ is shown. To quantify the reconstruction quality, the RMS error is calculated following Eq. 2.63 as in the linear detector tomography. An error of $\mathrm{E_{RMS}} = 8 \times 10^{-3}$ is observed, which is close to the error obtained for the Rytov reconstruction in the linear detector tomography case. The tomogram shown in Fig. 2.13 b) confirms that the circular detector algorithm can differentiate the three areas of the cell. Although, as seen in the profile for a fixed value of $y = 2\lambda$ (Fig. 2.13 c), the nucleolus RI value is not achieved completely. Besides, the edge of the phantom is enhanced, which is a problem for the cell model, but an advantage for the Shepp-Logan adapted design, as seen as follows.

For the following test, the Shepp-Logan adapted phantom whose modeling parameters are $f_{\mathrm{S}} = 10$ and $f_{\mathrm{N}} = 0.025$ is used. In this case, the circular detector is placed at a distance of $R = 20\lambda$, using the same sinogram size as before, with 720×720 input data. Therefore, for this test, we ensure the presence of almost six detectors per λ. The result for a $14\lambda \times 14\lambda$ reconstructed space can be seen in figure 2.14.

In this case, the calculated error is $\mathrm{E_{RMS}} = 0.11$, half that observed for the Rytov approximation for this phantom in the linear detector case. As seen in Fig. 2.14, all areas can be differentiated in the reconstruction, including those in the slice with a fixed value of $y = -0.065 f_{\mathrm{S}}$. The explanation for this behavior is discussed in more depth below, in section 2.5, where this reconstruction is compared with the tomogram for linear detector

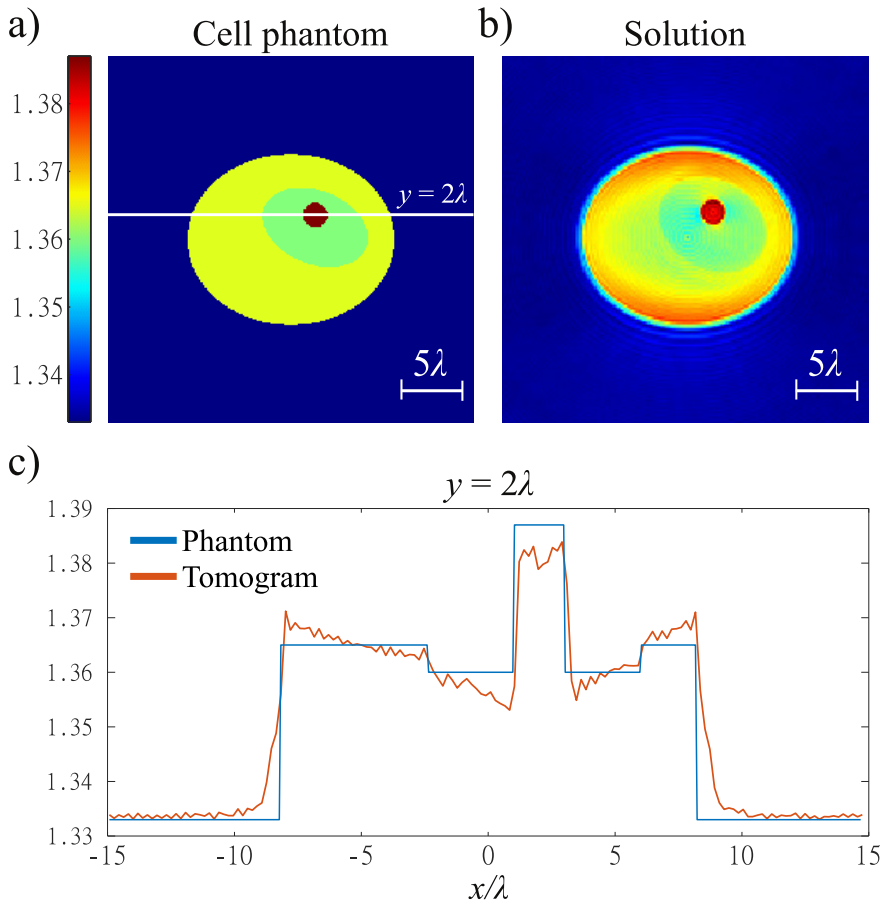

Fig. 2.13 Solution of circular detector tomography using the sinogram generated in COMSOL as input. a) Cell phantom. b) Solution for the far-field approximated algorithm. c) RI profile of the cell phantom and tomogram, at the line $y = 2\lambda$, indicated in a) with a white line. The size of images a) and b) is $30\lambda \times 30\lambda$.

with the same number of projections. Regarding the profiles seen in Fig. 2.14 c) and e), on the one hand, it is clear that for a fixed value of $y = 0$, the result shows a slight ripple, with a period similar to wavelength. On the other hand, at $x = 0$, the most conspicuous error is a slight decay of the reconstructed RI at the center of the profile, as also occurred for the result of the cellular reconstruction.

2.4.2 Implementation without far-field approximation

For this implementation, the approximation of the Hankel function performed in Eq. 2.77 is ignored, therefore, following Eq. 2.66, using the scattering amplitude defined in equations 2.75 and 2.76, the inverse problem is defined as follows:

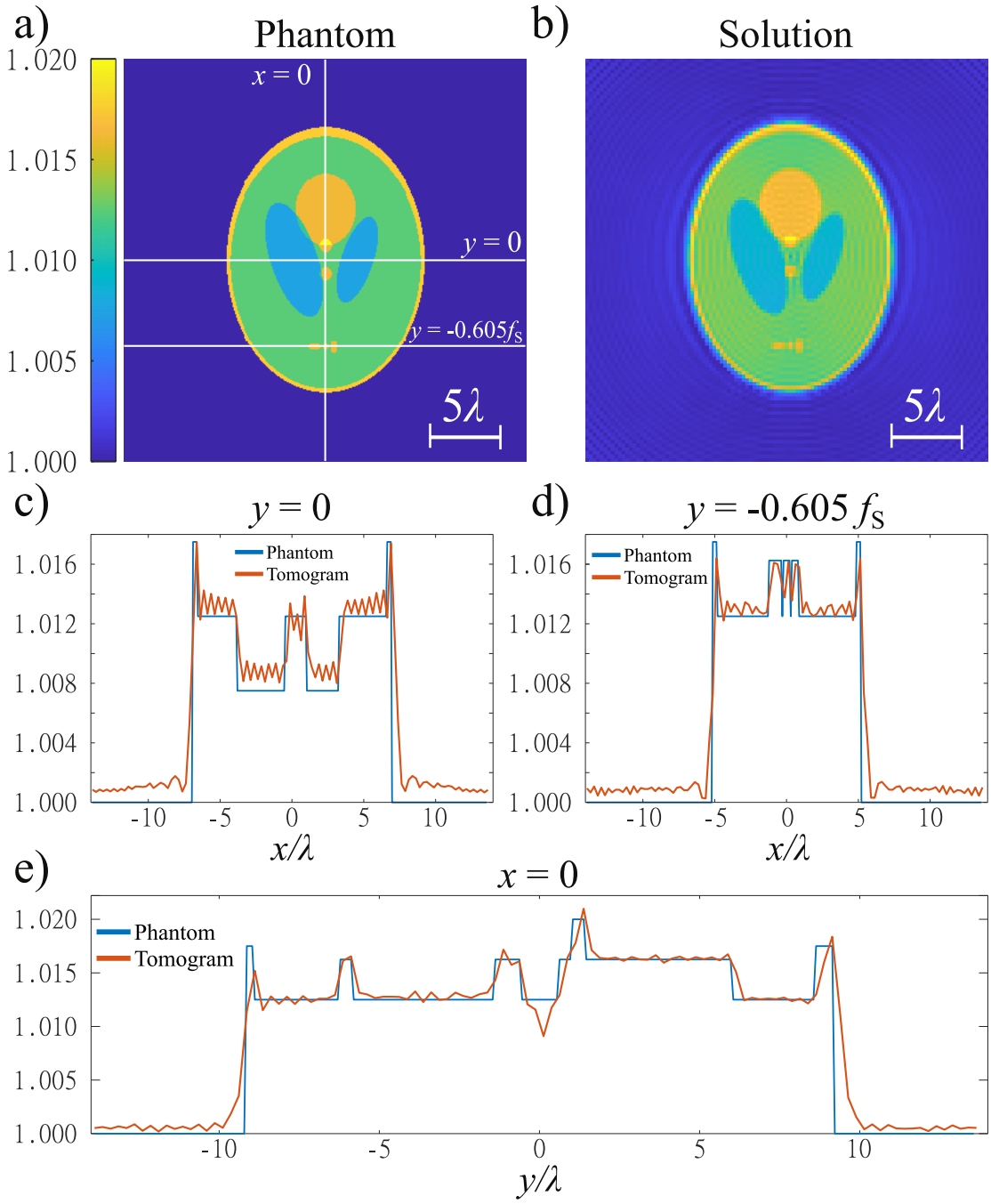

Fig. 2.14 Solution of circular detector tomography for a Shepp-Logan Phantom using $f_S = 10$ and $f_N = 0.025$. a) Phantom, white lines indicate the places where the profiles in c), d) and e) are taken. b) Tomogram solution. RI profile for the fixed values of c) $y = 0$, d) $y = -0.065 f_S$ and e) $x = 0$. The size of images a), c) and d) is $28\lambda \times 28\lambda$.

$$k_M \hat{O}[k_M(\mathbf{s}-\mathbf{s}_0)] = f(\mathbf{s},\mathbf{s}_0) = 4i \int_0^{2\pi} u_s(\sigma;\mathbf{s}_0) \frac{1}{(2\pi)^2} \sum_{n=-\infty}^{\infty} \frac{i^n}{H_n(k_M R)} e^{in(\chi-\sigma)} d\sigma \,. \tag{2.90}$$

As in the previous section, the (k_x, k_y) space will be covered in a $2k_M$ radius space, depending on the angle of incidence and the angle of detection data. Dividing the k_M^2 term in both sides, the previous equation could be expressed as:

$$\hat{O}[k_M(\cos\chi - \cos\chi_0), k_M(\sin\chi - \sin\chi_0)] = \frac{i}{(k_M\pi)^2}\int_0^{2\pi} u_s(\sigma;\mathbf{s}_0)\sum_{n=-\infty}^{\infty}\frac{i^n}{H_n(k_M R)}e^{in(\chi-\sigma)}d\sigma\,. \tag{2.91}$$

This implementation will be addressed in future work. For that, via MATLAB environment, and taking into account that the scattered field has been recorded only in a few σ angles, the problem should be discretized as follows:

$$\hat{O}[k_M(\cos\chi - \cos\chi_0), k_M(\sin\chi - \sin\chi_0)] = \frac{2\pi i}{(k_M\pi)^2}\sum_{J=0}^{N}\left[u_s(\sigma_J;\mathbf{s}_0)\sum_{n=-\infty}^{\infty}\frac{i^n}{H_n(k_M R)}e^{in(\chi-\sigma_J)}\right]\,. \tag{2.92}$$

2.5 Linear vs. Circular detector tomography

Intuitively, and before performing any tests, it is to be expected that the circular tomography gets a better result since, in linear tomography, only the forward scattering is measured. When the Fourier space is observed for both configurations, as seen in Fig. 2.15, the circular detector tomography manages to fill more regions of the frequency space. Figure 2.15 b) shows the region of the Fourier space covering for the circular

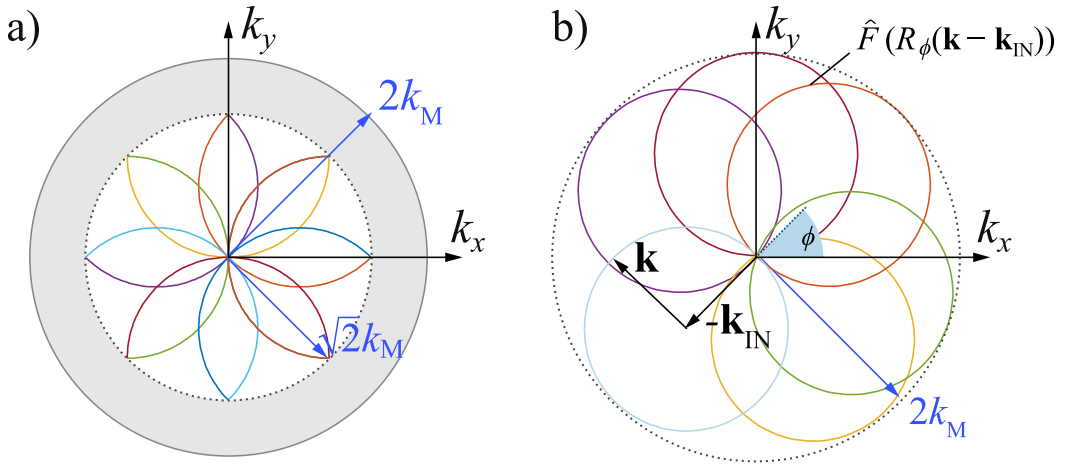

Fig. 2.15 Regions of Fourier space at which F is obtained (delimited by a dashed curve). a) Linear detector case: circle of radius $\sqrt{2}k_M$. b) Circular detector case: circle of radius $2k_M$.

detector case, where the best (i.e., minimum) image resolution (related to the highest distinguishable sample spatial frequency $k_{MAX} = 2k_M$) is $\lambda_{MIN} = \lambda_0/(2n_M) = \lambda/2$, which is

the well-known diffraction limit in a medium with RI n_M. However, if only the forward scattered field is measured (which, as we can see in Section 3.1.1, is the case in all reported TPM configurations to our knowledge), the region at which $\hat{F}$ is obtained is a semi-circumference, the rotation of which sweeps a circle of radius $\sqrt{2}k_M$, yielding a worse resolution (Fig. 2.15 a). The author of this thesis has not found any other comparison between the studied algorithms beyond the one described in [86], where only the reconstruction of two concentric cylinders was compared. To extend the cited study, and to give evidence of the resolution improvement through circular tomography, the following two tests are proposed.

First, the adapted Sheep Logan Phantom, defining the parameters $f_S = 10$ and $f_N = 0.025$, reconstructed for 720 projections in the previous section, is studied under 720 projections for the linear detector scenario. Next, both linear and detector tomography are solved, count with a 720×720 sinogram as input, to compare both configurations. The result for a $28\lambda \times 28\lambda$ reconstructed space is shown in Fig. 2.16.

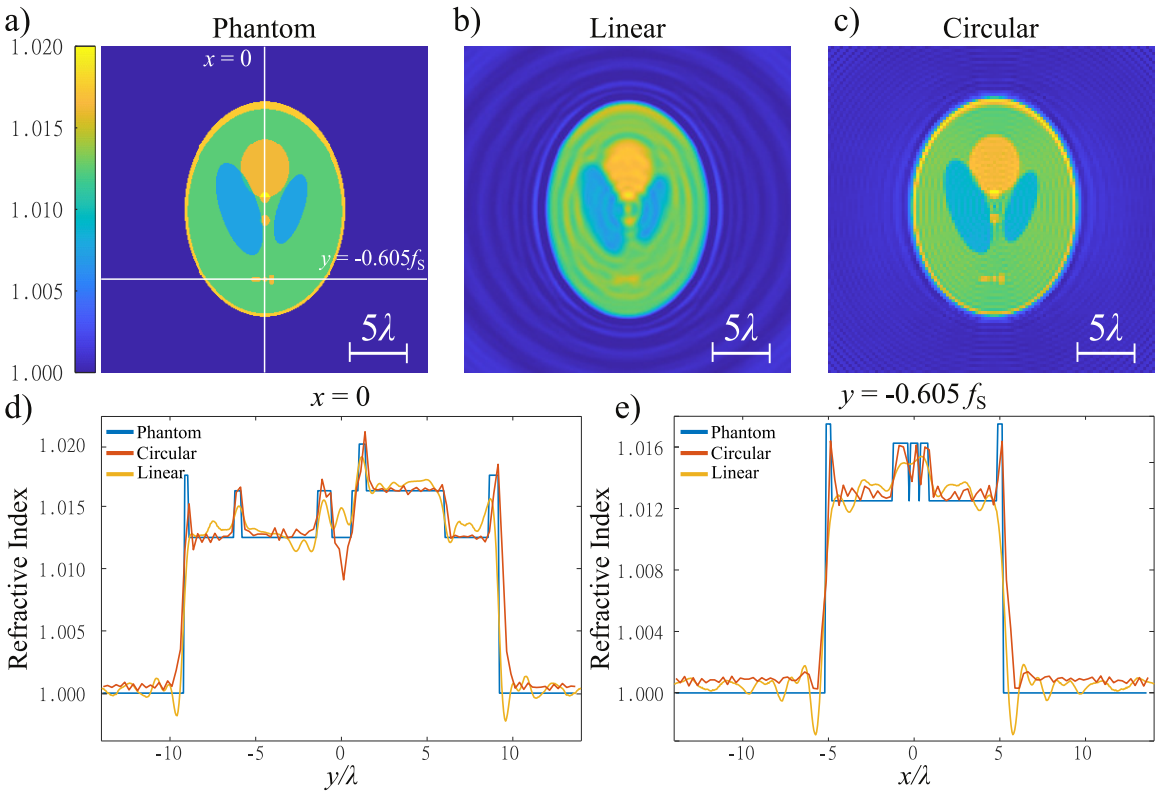

Fig. 2.16 Solution of linear and circular detector tomography for a Shepp Logan Phantom using $f_S = 10$ and $f_N = 0.025$. a) Phantom, white lines indicate the places where the profiles in d) and e) are taken. b) Solution for the Rytov approximation with the linear detector. c) Solution for the circular detector. RI profile for the fixed values of d) $x = 0$ and e) $y = -0.065 f_S$. The size of images a), b) and c) is $28\lambda \times 28\lambda$.

Since more projections are used in this test for the linear detector tomography than for the first section reconstruction, the calculated error has improved until $E_{RMS} = 0.184$. However, the circular case is better because the RMS error for this configuration is $E_{RMS} = 0.11$. The circular detector has a radius of $R = 20\lambda$, while the linear detector is placed at $l_D = 10\lambda$ and its length is 40λ-wide. Significantly, even the number of detector points per λ used to read the scattered field is three times higher for the linear configuration (18 vs 5.73), the result is more accurate when the reconstruction is performed with the circular detector. The results for the RI profile resulting at the line for a fixed value of $x = 0$ (Figure 2.16 d) are similar for both scenarios, with a slight error in the central position of $(x,y) = (0,0)$. However, the three small areas at the bottom of the phantom are clearly differentiated in the circular reconstruction, while they remain blurred for the linear configuration, as seen in Fig. 2.16 e). Furthermore, the edge of the phantom is noticeable only in the circular detector diffraction scenario.

To corroborate this resolution improvement via circular detector tomography, the following test is devised. The NTC Logo Phantom is modeled using a size factor of $f_S = 0.25$, while a RI of $n_{OBJ} = 1.03$ is used to ensure correct performance of both approximations in linear detector tomography. Tuning this model with these parameters, the central circle diameter is 0.75λ, which sets the separation between figures to a distance of only 0.25λ. The result for an $8\lambda \times 8\lambda$ reconstructed space can be seen in figure 2.17.

As can be seen from the color map values of Fig. 2.17 d), the circular detector tomogram is not able to fully achieve the correct value of $n_{OBJ} = 1.03$. This is reflected in the RMS error, since, for this circular tomography, it takes the value of $E_{RMS} = 0.423$. Nevertheless, this error is higher for the linear detector case, with a value of $E_{RMS} = 0.58$ for both Born and Rytov approximations (due to the similar result in this test, only the Rytov result is shown). The profile illustrated in Fig. 2.17 c) confirms that only linear detection tomography is capable to reach the value of $n_{SOL} = 1.03$, although this only happens in the central cylinders. Besides, this configuration is not able to separate the figures correctly. This separation between elements is unquestionably resolved in the reconstruction with the circular detector, as seen at the tomogram seen in Fig. 2.17 d). This result verifies the improvement of the resolution of diffraction tomography via a circular detector.

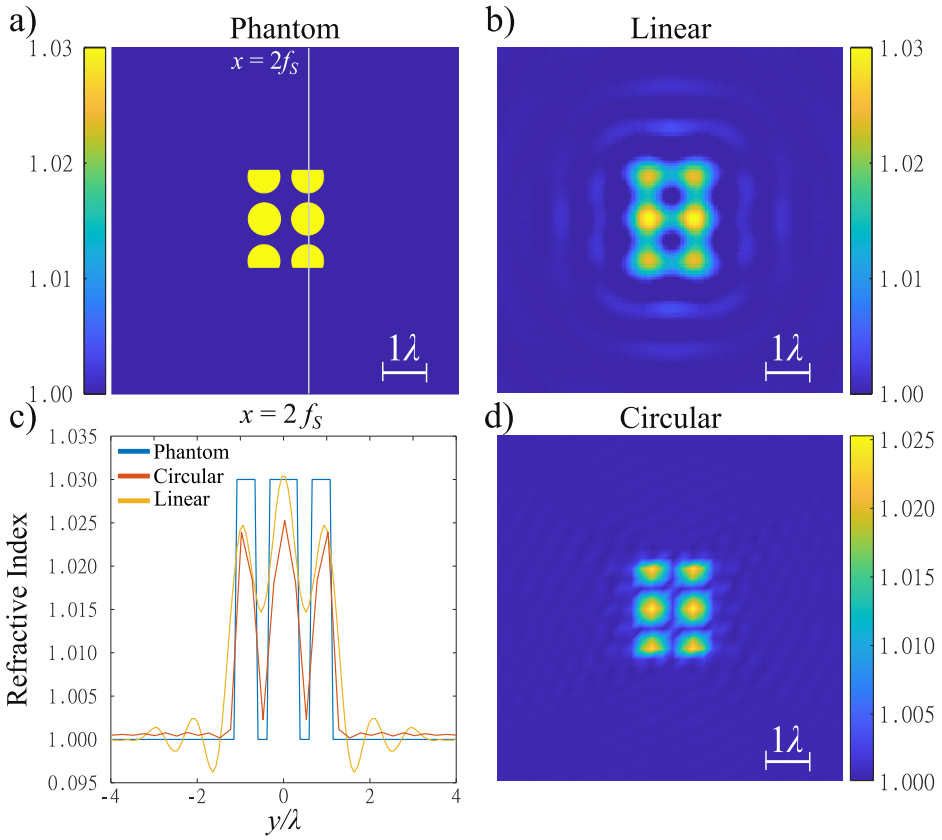

Fig. 2.17 Solution for linear and circular detector tomography for NTC Logo $f_S = 0.25$, $n_{OBJ} = 1.03$ phantom. a) Phantom, gray line indicates the place where the profile in c) is taken. b) Solution for the Rytov approximation with the linear detector. c) RI profile for the fixed values of $x = 2f_S$. d) Solution for the circular detector. The size of images a), b) and d) is $8\lambda \times 8\lambda$.

Chapter 3

On-chip Tomographic Phase Microscopy

3.1 Introduction

Tomographic Phase Microscopy (TPM) arises as the evolution of Quantum Phase Imaging (QPI) technique [21, 22]. TMP has been introduced and contextualized in the first two chapters of this thesis dissertation. To begin this chapter, we discuss the **applications** that justify and highlight the scientific advances that have been made on this imaging technique. TPM will probably be adopted as a routine method in cell biology, in vitro drug testing, and automated cell culture monitoring [56] and can potentially solve many long-standing problems in biomedicine [90]. Immunocyte phenotyping, stem cell multipotency identification, cancer cell screening, and tissue pathology are promising directions in which TPM may contribute [24]. Applications in which TPM has shown its potential include:

- **Label-free tomographic imaging of live cells.** TPM can retrieve cell volume and dry mass, enabling cell size quantification for the study of cell growth, proliferation, apoptosis, etc. [91–95]. Live cell morphology is significantly altered by disease states such as viral infection or cancer, and the TPM characterization of these alterations has several benefits. The morphology and internal structures of yeast and bacteria have also been measured using 3D QPI [56, 96].
- **Lipid droplets (LDs)** in live cells can be clearly identified from RI tomograms [56]. LDs have important roles in lipid storage and metabolism, being related to several pathologies such as cancer, obesity, and diabetes mellitus.

- Quantitative and label-free imaging capability makes TPM an effective method for **blood screening** [97, 98]. Morphologies of blood cells (BCs) can be retrieved and translated to hemoglobin concentration. Measuring these parameters for red BCs is useful in hematology, including thrombocyte activation, diabetes, and sickle cell disease [99].

- TPM allows us to determine the contribution of specific organelles to light scattering, which helps **diagnose the precursors of many cancers** [24, 100]. TPM can also quantify the efficacy of **cell immunotherapy** [56].

3.1.1 Tomographic Phase Microscopy: State of the art

Within the wide range of TPM approaches, those using ODT [14–16, 66] are best capable of resolving small variations of RI, as can be inferred from Chapter 2. In the standard version of ODT (in which the detector is a line in 2D or a plane in 3D), to obtain the RI distribution $n(\mathbf{r})$ of a sample, it is illuminated with a plane wave (Fig. 3.1 a).

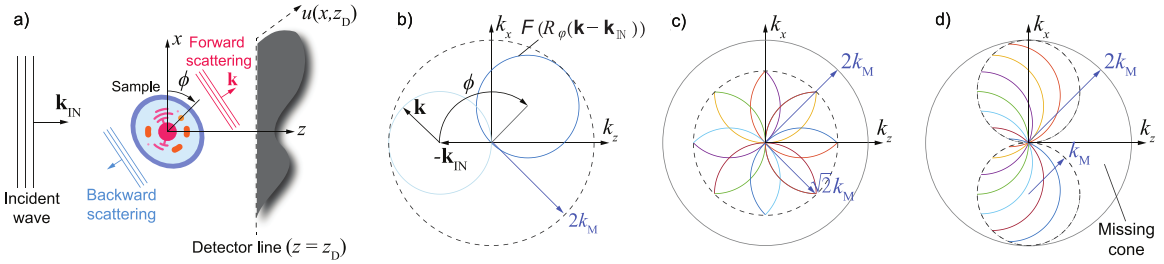

Fig. 3.1 a) Diffraction tomography concept. b-c) Regions of Fourier space at which F is obtained (delimited by a dashed curve). b) In the best case, it is a circle of radius $2k_M$. c) If only the forward scattering is measured, the circle radius reduces to $\sqrt{2}k_M$. d) If the illumination angle is changed without moving the detector, the region is a double circle.

As detailed in section 2.5, the best image resolution is $\lambda_{MIN} = \lambda/2$, the well-known diffraction limit in a medium with RI n_M (note that rotating the sample is equivalent to simultaneously rotating the source and the detector). This is achieved by the use of a circular detector. This implies that $\hat{U}_\phi(k_x, z_D)$ takes the values of $\hat{F}$ along a circumference of radius k_M, centered at $(x = 0, z = -k_M)$, and rotated by an angle ϕ about the center of the spatial frequency domain (SFD), as seen in Fig. 3.1 b). Therefore, if the sample is rotated by all possible angles and for each of them $u_\phi(x, z_D)$ is measured at all possible diffraction angles, we obtain the value of F at all points of a circle of radius $2k_M$ in the SFD.

However, if only the forward scattered field is measured (which is the case in all reported TPM configurations to our knowledge, and corresponds to measuring the scattered field only at half of all possible angles), the region at which F is obtained is a semi-circumference, the rotation of which sweeps a circle of radius $\sqrt{2}k_M$, resulting in a

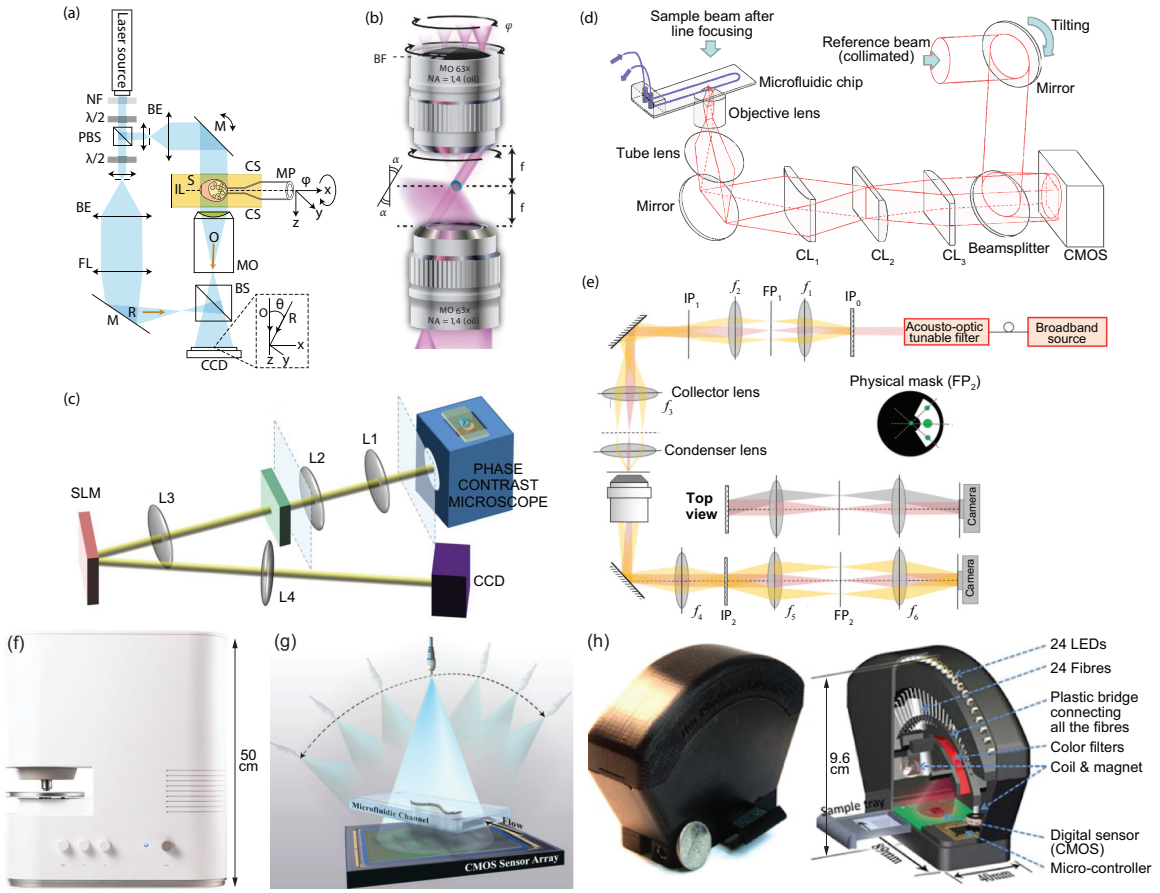

Fig. 3.2 Set-up of the main TPM microscopes. (a) Standard set-up. Different illumination angles are obtained by rotating either the sample S (angle ϕ) or the incident beam (by moving the mirror M) [56]. (b) TPM configuration containing two opposed objectives [101]. (c) White-light TPM [56]. (d) TPM of a sample continuously flowing in a microfluidic channel [102]. (e) Scanning color optical tomography [103]. (f) *Tomocube* HT microscope. [104]. (g) Holographic OF TPM [105]. (h) Portable lensless TPM [106].

worse resolution (Fig. 3.1 c). The other most typical situation is that in which the light source is rotated while keeping the detector fixed. In this case, the semi-circumference sweeps a region consisting of two circles of radius k_M. This gives rise to the **missing cone problem (MCP)**, the region inside the solid circle and outside the dashed circles in Fig. 3.1 d). The problem of missing SFD regions appears in all TPM configurations reported to our knowledge, which leads to a fundamental drawback of current TPM devices.

In 2009, a diffraction tomography version of TPM was demonstrated with improved results [23]. As mentioned above, the illumination angle can be varied either by rotating the sample (e.g. via mechanical rotation, holographic optical tweezers, microfluidic channels, or optical traps [107, 108]) or the illumination beam (using galvanometric mirrors, liquid-crystal-based spatial light modulators, or digital micromirrors) (Fig. 3.2 a).

Alternatively, optical diffraction tomography can be realized by using partially-coherent light, where the focal plane of the objective lens is axially scanned through the sample (Fig. 3.2 c) [56]. The speed of data acquisition in these techniques is limited by the mechanical scanning of a mirror or sample stage. Recently, 3D cell imaging using a focused line beam, which allows interrogation of the cells continuously flowing in a microfluidic channel, has been conducted (Fig. 3.2 d) [102]. Tomographic images can also be obtained by illumination wavelength scanning, although in this case a source with a tunable frequency is required (Fig. 3.2 e) [103]. Finally, 3D tomographic images can be obtained by training an artificial neural network (ANN) to reproduce the complex amplitude of the measured scattered light, obtaining better image quality than standard methods [109]. The optical elements required by the main TPM approaches are shown in Fig. 3.2. As seen, all of them are based on many standard discrete optical components such as lenses, objectives, beam splitters, masks, mirrors, and fibers. These elements are **heavy**, **bulky**, and **expensive**. Moreover, many of these devices have moving mechanical parts that are prone to **calibration errors**. White-light TPM additionally requires a phase contrast microscope with a motorized focus drive. This kind of instrument is considerably more expensive than a LoC device. For instance, the phase contrast microscope employed in [110] *(Axio Observer Z1)*, has a cost of the order of 20k€-30k€. Scanning color optical tomography would also have a high cost, as a frequency-tunable source is needed. This device can be used to introduce the TPM devices available on the market.

Commercial devices: Over the last few years, it has been exciting to witness the successful promotion of the TPM technique into the industry. Two representative cases are *NanoLive Inc.* (founded in 2013) and *TomoCube Inc.* (founded in 2016). Both companies use angle-scanning optical diffraction tomography to obtain label-free 3D images of entire cells and tissue slices [24]. Nevertheless, these devices suffer from the above-mentioned drawbacks. For instance, the HT microscope weighs 23 kg and has a size of $180 \times 445 \times 500$ mm (Fig. 3.2 f, [104]). The elimination of lenses is the first step to reduce the complexity of these measurement set-ups. The idea of lensless imaging has also been explored in on-chip microscopy [111]. To our knowledge, there exists no reported precedent of on-chip TPM. The closest approach is lensless TPM (Fig. 3.2 g-h), in which the sample is placed above an image sensor chip with a spacing of less than 1 mm, without any imaging lenses in between. The sensor records an in-line hologram of the sample under partially coherent illumination, from which the RI of the original object can be reconstructed digitally [55, 112, 113]. The resolution of this technique is limited by the pixel size of the CMOS detector and needs to record several projection holograms while the sample flows above the sensor array, which are then digitally synthesized into a single super-resolved hologram, achieving a lateral resolution of 1 μm [105]. The light source is rotated as usual to record holograms of the objects at different angles (Fig. 3.2 g). To avoid the mechanically-moving source required to illuminate

the sample from different angles, an improved version of this device includes an array of light-emitting diodes (each butt-coupled to an optical fiber) controlled through a microprocessor to sequentially illuminate the sample (Fig. 3.2 h). To generate pixel super-resolved holograms, multiple shifted holograms are recorded at each illumination angle by electromagnetically actuating the optical fibers using coils and magnets [106]. As seen, although the device is cheaper, lighter, and more compact than other TPM microscopes, it still has a high degree of complexity, with many off-chip components (including moving parts), which hampers mass manufacturability, and which introduces discrete-component potential failures and mechanical misalignment. Moreover, only the forward scattering can be captured, and the set of illuminating angles is considerably restricted. This gives rise to the MCP and other missing regions in the SFD, yielding a poor axial resolution of 7 μm, complicating the imaging of cells.

3.1.2 Lab-on-a-chip motivation

Once the state of the art has been presented, we can infer that the drawbacks present in TPM devices are the following:

- The **elements employed in TPM equipment are heavy, bulky, and expensive**. Moreover, external (off-chip) elements such as sources, lenses, detectors, and fibers are prone to calibration and misalignment errors (as well as the moving mechanical parts that many TPM devices have).
- Due to their off-sample illumination, all tomographic microscopes to our knowledge use flat detectors, which severely constrain the accessible regions in the domain of spatial frequencies and thus **limit the device resolution**. This includes effects such as the previously described missing cone problem.
- **Low throughput**: current TPM systems have a very limited field of view ($\sim$100 $\times$ 100 μm), with which only a few cells can be observed in one RI tomogram. This makes the process really slow, since the sample is static and has to be constantly replaced to measure large cell series (often using a non-automated process).

To overcome these limitations, this thesis proposes to revolutionize the field of biomedical imaging by developing a radically new lab-a-on-chip technology: The **integrated tomographic microscopy**. This unprecedented technique will be enabled by pushing forward the science of on-chip wireless photonics (OWP) and optical diffraction tomography. The integrated tomographic microscopy could introduce key advantages in terms of resolution, sensitivity, throughput, parallelization, and energy efficiency. To this end, we will look for radically different TPM scheme based on the concept of photonic integrated circuit (PIC), which integrates multiple photonic functions on a single chip.

PICs are gearing up for numerous applications such as high-performance computing, high-speed interconnects, and **lab-on-a-chip (LoC)** devices, and are expected to revolutionize conventional electronics by offering a disruptive performance in terms of speed, bandwidth, and energy consumption [28]. Current PICs are based on the use of photonic waveguides as interconnects since this is the most energy-efficient way of conveying light within the chip. Notwithstanding, wired photonics has fundamental drawbacks that are insurmountable without a radical standpoint change. In particular, we draw attention to the fact that the inherent strong light confinement to the guiding structures prevents their interaction with the background medium at far-field distances, a feature required in a variety of sensors and devices [114], as well as in applications related to microparticle control and acceleration [115]. OWP can overcome this limitation. The OWP concept emerged in 2010 [44], showing that the transmission between plasmonic nanoantennas (NAs) would possess a higher efficiency than plasmonic wires [43]. Nevertheless, plasmonic NAs possess unacceptable low directivity $D < 8$ dB and high dissipation [116]. In 2017, a new dielectric NA concept with considerably superior features ($D > 23$ dB, zero dissipation loss, ultra-broadband properties) was proposed by a team of the NTC, enabling the first on-chip wireless data transmission demonstration [52]. This NA will be detailed in the next section. However, being a very recent field, the true potential of OWP is yet to be discovered; just as radio and microwave antenna technology enabled countless applications, radiating electromagnetic fields within a chip in a controlled manner may open the door to ground-breaking functionalities.

One of the most interesting OWP application directions is related to the concept of LoC devices [53], which integrate several laboratory functions on a chip to achieve automation and high throughput. Particularly, **opto-fluidic (OF)** LoC nanotechnology is one of the main candidates for solving the drawbacks of traditional biomedical equipment (large, complex, expensive devices that often demand trained expert users, have a long response time, and a high preparatory and operational cost). It provides crucial pros such as being highly-sensitive, compact, fast, automated, label-free and requiring low sample volumes [40, 117].

Leveraging the latest advances on LoC OF PICs, we will unfold the full potential of dielectric on-chip NAs by paving the way to achieve the first on-chip TPM microscope. Therefore, the pursuit for this integrated tomographic microscopy leads us first to know how NAs work by performing for the first time an experimental observation of the near field they radiate. Next, we propose the first circular array of nanoantennas on PIC in order to observe their behavior in systems with and without an object. It consists of a wireless circular cross-port crossing. Finally, we model, fabricated, and characterized a baseline system, to experimentally test the circular tomography algorithm on a chip for the first time. These are the next sections of this chapter.

3.2 Nanoantennas

The nanoantenna (NA) is the device that leads the OWP technology, as described above. Although the context of these devices has already been explained, the author want to highlight the leap from the use of plasmonic to silicon NAs. Most studies on wireless on-chip devices are based on the use of plasmonic nanoantennas made up of metals such as gold or silver, which can constitute an efficient solution in some applications belonging to the fields of spectroscopy or optical sensing, as a consequence of their ability to concentrate electromagnetic fields [43, 49, 50, 118]. However, plasmonic nanoantennas do not normally yield an optimal staging when trying to establish non-guided communications or data transmission in the near-infrared wavelengths, as a result of their poor radiation properties and high metallic absorption at optical frequencies. The radiation ability of silicon particles has been demonstrated in different studies [51, 119], establishing the superior efficiency of silicon nanoantennas in comparison with plasmonic ones. Recently, a novel PIC paradigm based on the use of a new kind of ultra-directive (directivity higher than 23 dB), low-loss, highly-efficient (total efficiency close to 90%) and broadband silicon nanoantenna has been proposed by the team formed by Dr. Lechago and the supervisors of this thesis [52]. This alternative platform has enabled new on-chip applications, including reconfigurable networks and ultra-integrated biomedical devices, while the silicon as the constituent material assures their compatibility with the CMOS technology. This remarkable study has captured the attention of the scientific community. This NA is already able to radiate the field with a directivity higher than 17 dB. Nonetheless, to further improve the directivity of the inverted taper nanoantenna while maintaining a reduced footprint, the authors of the study added different planar structures working as directors (in the same way as in typical Yagi-Uda antennas [120]). The full antenna is shown in Fig. 3.4. Another version of this NA (confining the light between two guides and using a C-shape tip) has been presented in [121]. However, we will not delve into the design of the NAs in this section, and we refer directly to [52] for more detail.

The aforementioned silicon nanoantenna consisting of a 10-μm-long inverted taper presented in [52] is the one used for our study, for two specific reasons.
On the one hand, this NA has been validated to enable an ultra-compact **LoC micro-flow cytometer** (Fig. 3.3 a), achieving a high signal-to-noise ratio [53]. This study proves that the chosen NA is capable to illuminate objects inside a microfluidic channel within the SOI devices, as well as the same NAs can detect 0.5 μm-diameter particles, operating as signal receivers, using a wavelength of illumination of λ =1.55 μm. Moreover, the maximum acquisition rate of 3300 events/second confirms high throughput. The reduced footprint of this cytometer and the SOI platform used guarantee the mass production of these devices, solving two other issues to be addressed in our TPM device: cost and system

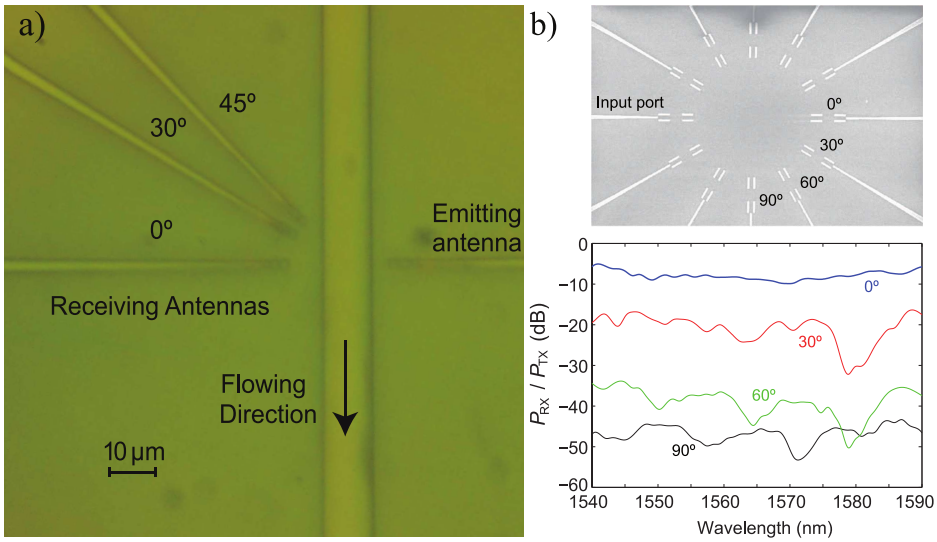

Fig. 3.3 a) Optical microscope image of the referenced microflow cytometer [53]. b) SEM image and measure efficiency for the receiving ports associated with the cited wireless 12-port crossing [52].

size.

On the other hand, a **12-port wireless crossing** has been presented in [52], using the 2-directors NA as the radiating element, as seen in Fig. 3.3 b). This multi-port scheme paves the way to our circular detector tomographic microscopy, although several considerations must be taken into account. For example, the distance between ports must be larger, in order to include the microfluidic channel inside, as well as the number of antennas must be increased.

Before the first baseline system, the author denotes that, while the far-field behavior of the aforementioned antennas (e.g., directivity and radiation efficiency) has been deeply studied, their near-field properties remain mostly unexplored. To this aim, a first experiment is designed, in which we fabricate (see Fabrication) and thoroughly study the near-field behavior of this kind of antenna both numerically and experimentally (see Near-field Measurements). This study has been published [122] [1] and is explained below since the fabrication processes and laboratory setups are repeated in the subsequent samples in this chapter. All designs and experiments correspond to a wavelength $\lambda = 1550$ nm. We chose the inverted-taper NA followed by two pairs of directors as the structure under study (Fig 3.4), since this configuration already satisfies the directivity requirements of our experiment and simplifies the design and fabrication of the sample.

To enable not only the near-field characterization of the proposed antennas but also far-field testing (see Far-field Characterization) we chose a basic 2-port nanolink consisting of two identical antennas with a gap distance d between them (see Fig. 3.5).

[1] This paper has obtained the *2020 Premium Award for Best Paper in IET Optoelectronics.*

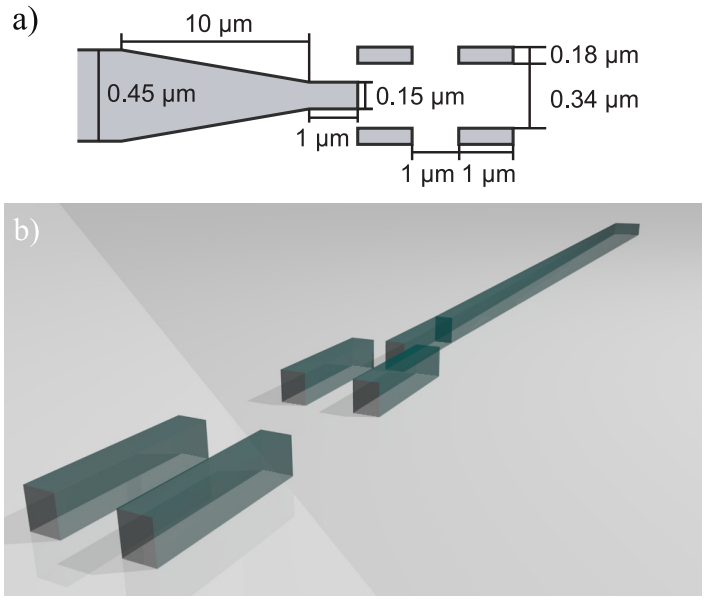

Fig. 3.4 a) Schematic (not to scale) top view of NA and directors. b) 3D representation of the antenna used to build the studied links.

Note that the performance of the nanolink in terms of power efficiency is maximized when the nanoantennas are covered with a thick SiO_2 layer. Therefore, this is a basic requirement for low-loss high-speed data transmission applications. However, this thick SiO_2 layer entails a strong limitation concerning near-field measurements, since the intensity of the evanescent field of the mode supported by this structure is too weak. To mitigate this problem, we performed different simulations of the optical response of the nanolink as a function of the thickness of the SiO_2 layer. We chose the minimum thickness of this layer (220 nm) that ensured a similar behavior of the near-field intensity through all the elements of the nanolink, while keeping a sufficient long-distance transmission capacity to allow the aforementioned far-field characterization. Throughout the whole study, we operate in TE mode. In this respect, the width of the silicon waveguides carrying light to/from the nanoantennas (450 nm) was designed to operate in a monomode regime.

With these considerations in mind, we designed and fabricated a sample containing three different nanolinks (labeled as Link a, Link b, and Link c) with a gap $d = 30$ µm, allowing us to verify the repeatability of the process. Input and output grating couplers [123, 124] enabled vertical light injection (extraction) to (from) the chip. The connection between the nanoantennas and the gratings was performed via tapered waveguides (see Fig. 3.5 a).

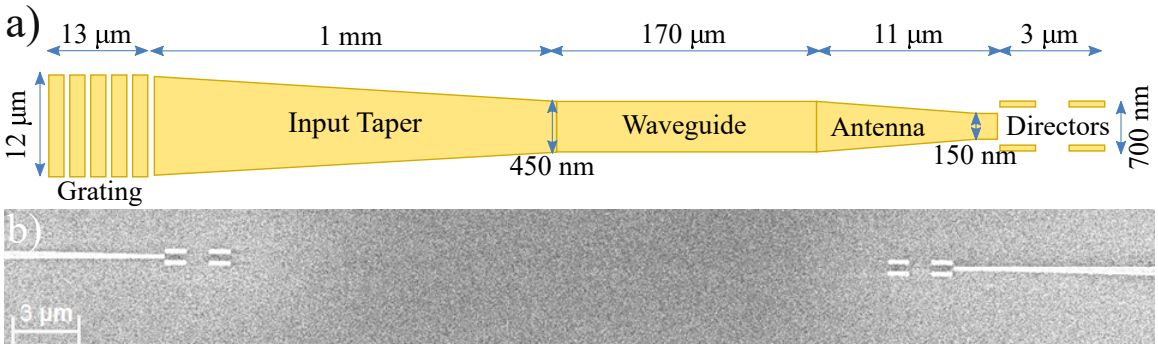

Fig. 3.5 a) Schematic top view (not to scale) of the vertical coupler grating, waveguides, and nanoantenna. b) Scanning Electron Microscope (SEM) image of the fabricated 2-port-link.

3.2.1 Fabrication

In the first place, the design of the sample containing the three different nanolinks is carried out using the KLAYOUT software. The silicon antennas, grating couplers, and waveguides were fabricated over standard silicon-on-insulator (SOI) samples from SOITEC (Bernin, France) wafers (see Fig. 3.6 a) with a top silicon layer thickness of 220 nm (resistivity $\rho \sim 1-10$ Ωcm^{-1}, with a lightly p-type background doping of $\sim$ 1015 cm^3) and a buried oxide layer thickness of 220 nm. The fabrication is based on an electron-beam direct-writing process, CMOS-compatible, performed on a coated 100-nm hydrogen silsesquioxane (HSQ) resist film. This electron-beam exposure was performed with a Raith150 tool and has been optimized to reach the required dimensions employing an aperture size of 30 µm with an acceleration voltage of 30 KeV. After developing the HSQ resist using tetramethylammonium hydroxide, the resist patterns were transferred into the SOI samples using fluoride gases via an optimized inductively coupled plasma-reactive ion etching process. Finally, a 220 nm-thick silicon dioxide upper cladding was deposited on the SOI sample by using a plasma-enhanced chemical vapor deposition system from Applied Materials. The fabrication process is summarized in the illustration shown in Figure 3.6 c). The entire fabrication process is carried out in the clean room facilities of the Nanophotonics Technology Center (class 10-100-1000-10000). Scanning Electron Microscope (SEM) images are taken focusing on the nanolinks to ensure the correct fabrication of the sample (see Fig. 3.5 b).

3.2.2 Far-field characterization

Prior to the study of its near-field behavior, the link was characterized in the far-field to verify its correct performance. In particular, the link power efficiency $\eta_P = P_{RX}/P_{TX}$ (P_{RX} and P_{TX} are the received and transmitted power, respectively) of the three fabricated 30-µm-long nanolinks was experimentally measured. For this purpose, an External Cavity

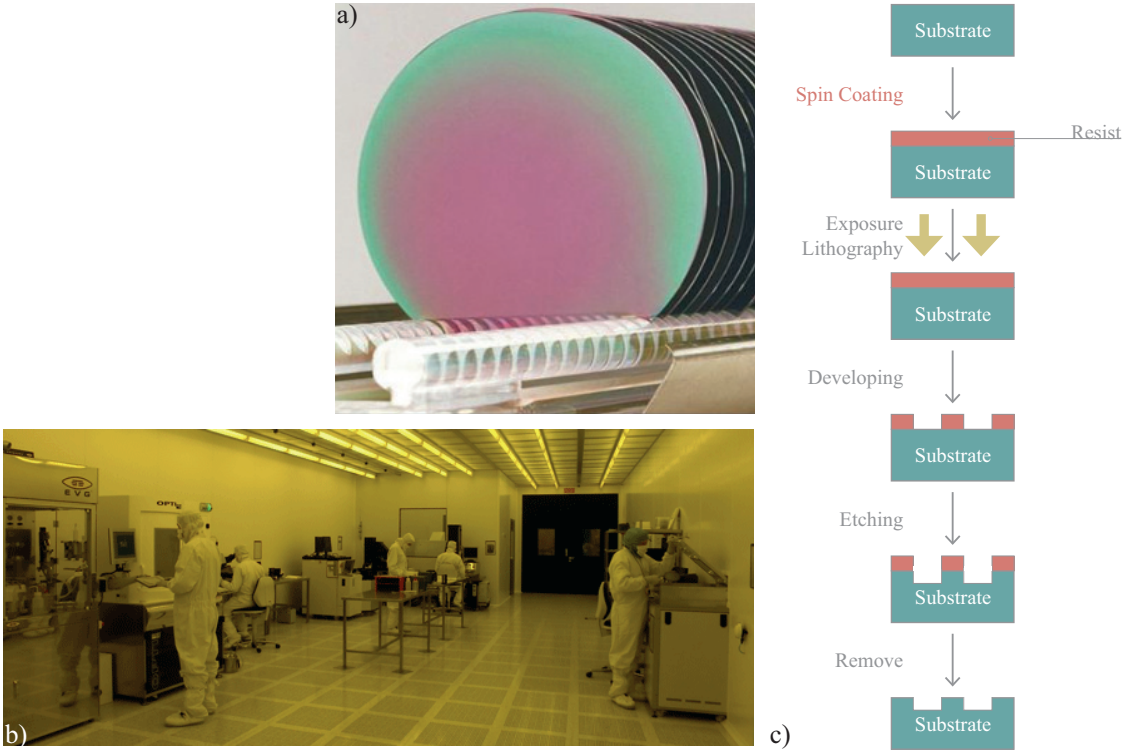

Fig. 3.6 a) Virgin silicon wafers. b) Clean room facilities in NTC. c) Fabrication process.

Laser (ECL) was employed to inject light to the input vertical gratings of the sample via an optical fiber at wavelengths of 1540-1590 nm. The signals exiting the output gratings were received with a photodetector. Maximum power efficiency was ensured by optimizing the polarization of the signal and through the previous alignment of the input and output fibers with the help of an optical microscope. Both laser and photodetector have been controlled by a PC via LABVIEW software, as well as the microscope image. Vacuum is generated under the sample to hold it in a fixed place. The complete setup can be seen in Fig. 3.7.

As a reference, η_P was also simulated using CST Microwave Studio. According to the simulations, the power efficiency should be around -34 dB for a wavelength of 1550 nm, showing a good agreement with the experimental results (see Fig. 3.8). It is worth mentioning that an additional structure consisting of two vertical grating couplers linked by an almost lossless 12-μm-wide waveguide was measured to quantify the experimental loss introduced by the grating couplers. This loss was subtracted from the measured values of η_P to allow a direct comparison with the simulation.

Note that the SiO_2 layer employed to cover the 30-μm-long links was significantly thinner than in previous designs [52] (220 nm vs 2 μm) to allow a near-field characterization of the device, which resulted in a lower link power efficiency. A frequency

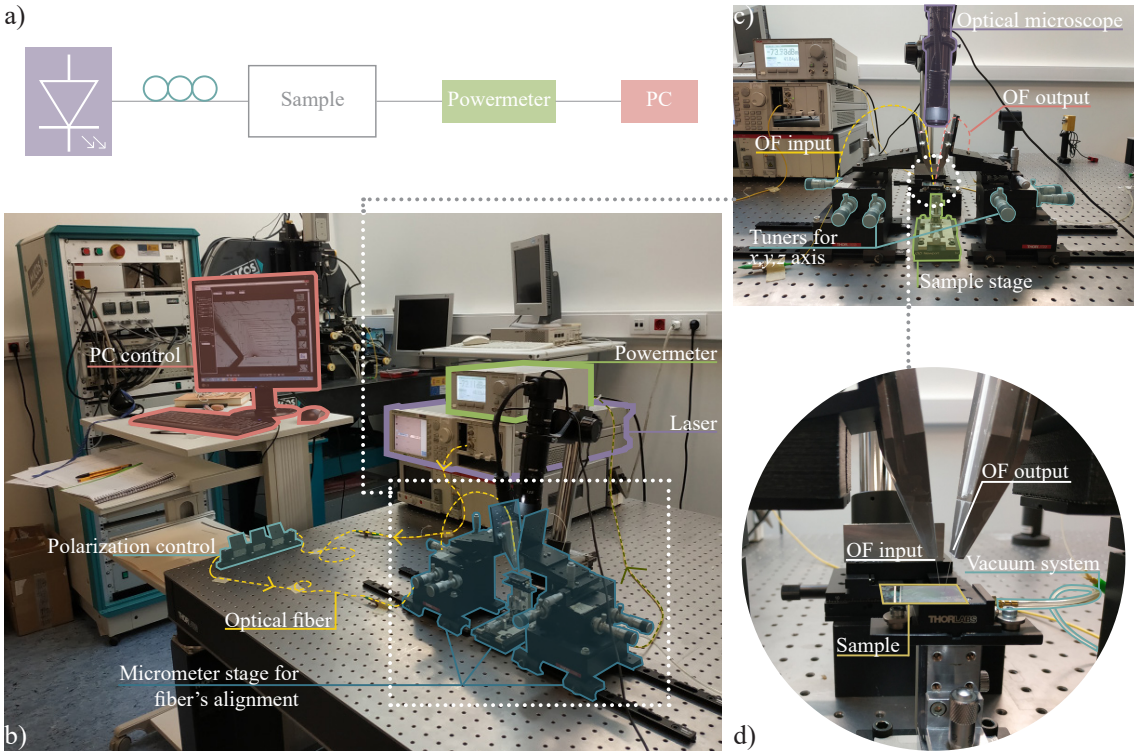

Fig. 3.7 a) Schematic view of the setup. b-d) Pictures of the setup.

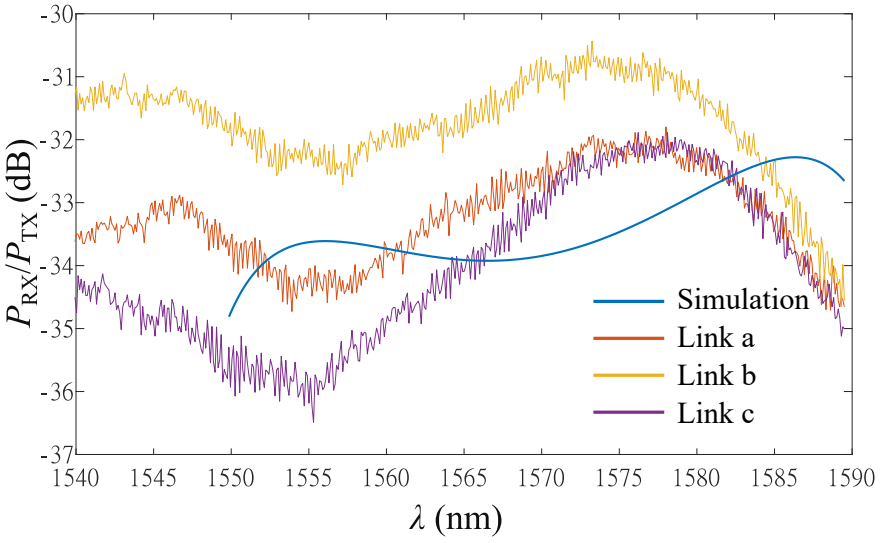

Fig. 3.8 Experimental (red (Link a), yellow (Link b) and purple (Link c)) and theoretical (blue) power efficiency η_P of the different fabricated links.

shift between the experimental and theoretical results is noticed, which might be a result of deviations introduced in the fabrication process. In particular, the plasma-enhanced chemical deposition technique used to build the 220-nm SiO_2 layer that covers the

sample, and the free-space link gap is prone to introduce small air bubbles within it, giving rise to inhomogeneities in the aforementioned free-space region, which can alter its optical response. Secondly, since the upper surface of this SiO_2 layer coincides with that of the antennas (where the field intensity is higher), the effect of its roughness can be significant as compared to a typical (thicker) cover layer. Finally, some imbalances caused by the exposure field of the e-beam when lithographing the nanolinks may happen, providing slightly altered gap distances or antenna misalignments. In any case, the good agreement observed in terms of power efficiency assures the expected radiation behavior of the nanoantennas, and hence the presence of the sought near field to be explored via SNOM technology, which is the purpose of this fabricated sample.

3.2.3 SNOM measurements

After we have made sure that the nanoantennas radiate as expected, it is time to verify their near-field behavior. We study this feature through Scanning Near-field Optical Microscopy (SNOM), a microscopic technique at the nanometer scale. This technique achieves sub-wavelength spatial resolution by the use of short-range interactions between the sample and a sharply pointed probe by the evanescent waves. [125].

SNOM setup

SNOM measurements were performed with a commercial MultiView 4000 system (Nanonics Imaging Ltd.) working in collection mode. A bent fiber tip (Nanonics Imaging Ltd) with a 400 nm aperture, Cr/Au coated, pre-mounted on a tuning-fork working in tapping mode at 36.94 kHz was used to scan the lithographed sample while it was kept fixed (see Fig. 3.9 a). The sample was vertically illuminated with an optical fiber mounted on a 3D stage. Since the vertical grating coupler has been designed to couple light at 11°, we achieved this angle using an adjustable angle mounting plate (see Fig. 3.9 b). The whole system (sample, input fiber, and SNOM tip) could be pre-visualized with a vertical optical microscope that enables a correct fiber-sample alignment and an accurate positioning of the SNOM probe on top of the lithographed structures (a sketch of the setup can be seen in Fig. 3.9 c). The optical fiber was connected to a tunable laser (EXFO FLS-2600) at a fixed light polarization and a power of 0 dBm was used (λ = 1550 nm). The SNOM was controlled through the Nanonics Imaging Ltd Software and the near-field signal was detected using a FWPR-S Femtowatt Photoreceiver. In addition to the near-field study of NAs, this setup has also been used by the author in two collaborations. These works can be consulted in the following publications [48, 126].

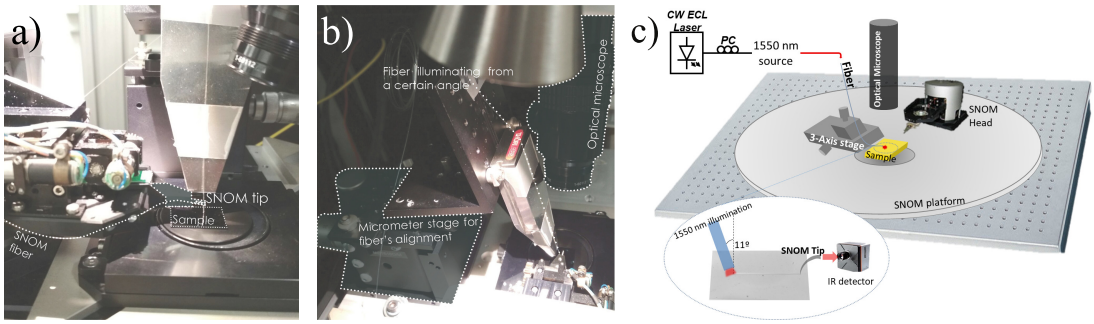

Fig. 3.9 a-b) Pictures of the setup. c) Schematic view of the setup.

Near-field Measurements

To guide and verify the SNOM characterization, we first studied numerically the near-field behavior of the fabricated nanoantennas via CST Microwave Studio for a wide range of vertical distances. The near-field intensity was collected by the SNOM working in collection mode, with the tip placed perpendicular to the sample, allowing a mode matching between the tip and the measured structures [127, 128]. Measurements at different vertical distances z_{LIFT} or z_{L} over the sample were performed. Particularly the SNOM tip was placed at $z_{\mathrm{L}} = 0.1$ μm and $z_{\mathrm{L}} = 0.4$ μm. The details for each case are discussed below. The measured images were edited using the WSxM Scanning Probe Microscopy Software [129].

Constant plane z_{L} = 0.1 μm In this case, the SNOM tip was retracted 100 nm over the sample, allowing us to operate in lift mode, scanning a constant plane without risk of crashing the probe due to irregularities at the sample topography (resulting from the lack of planarization after the fabrication process).

Emitting antenna: As expected, the simulation results show an electric field concentration at the inverted taper. Additionally, a slight field concentration can also be identified between the first pair of directors (see Fig. 3.10 a). However, the corresponding measurements of the fabricated emitting antenna showing the electric field radiation between the first pair of directors were not in good agreement with the simulations (see Fig. 3.10 b). These divergences could be attributed to fabrication failures, and the lack of planarization previously mentioned. It is worth mentioning that this discrepancy was solved by raising the tip height at $z_{\mathrm{L}} = 0.4$ μm, as detailed below.

Propagation: The SiO_2 region between the emitting and receiving antennas was studied at a retracted tip height of 0.1 μm, giving us a portrait of the electric field propagation. The simulated radiated field distribution (see Fig. 3.11 a) was recognizable in the performed SNOM measurement (see Fig. 3.11 b). This information could be

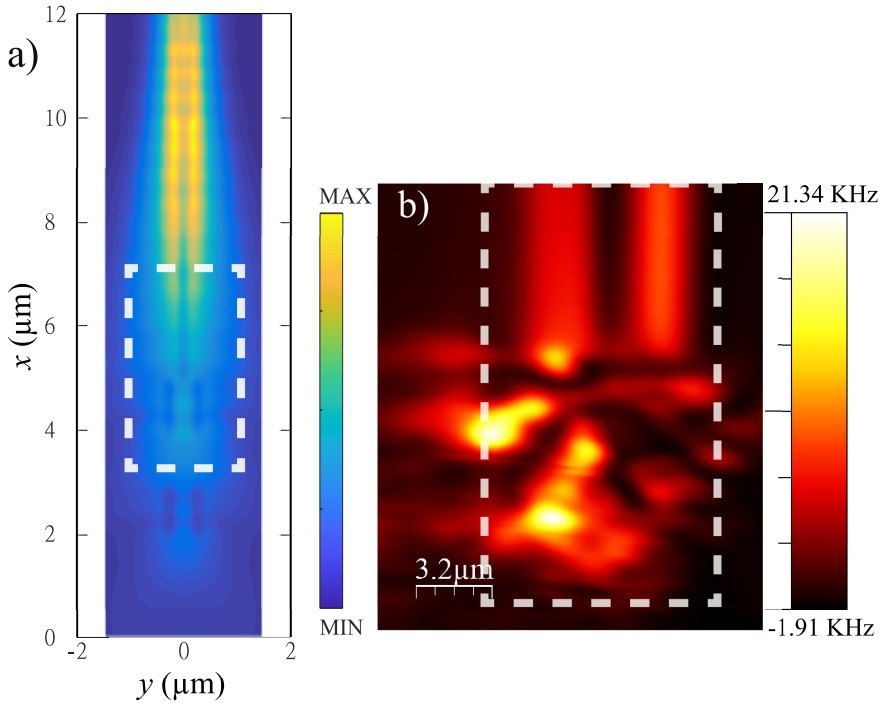

Fig. 3.10 Simulated (a) and measured (b) near-field intensity above the emitting antenna at $z_L = 0.1$ μm. Areas enclosed by dashed lines represent the same region in both images.

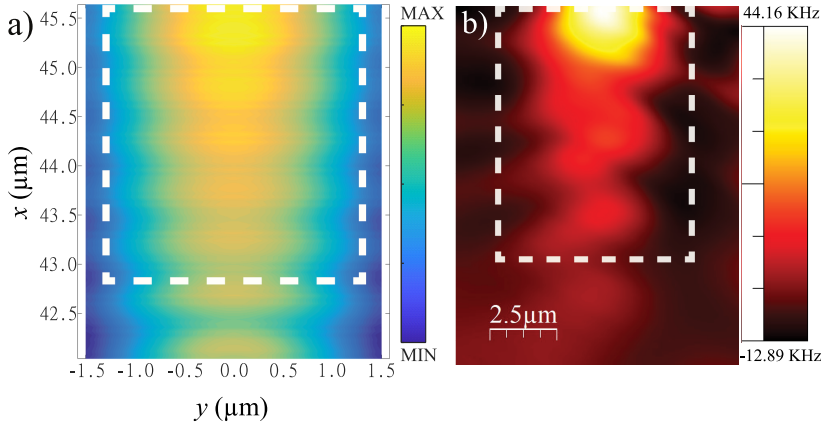

Fig. 3.11 Simulated (a) and measured (b) near-field intensity propagated between antennas at $z_L = 0.1$ μm. Areas enclosed by dashed lines represent the same region in both images.

exploited to obtain the radiation features of the antenna without demanding far-field characterization.

Grating: Furthermore, the near-field intensity was measured in the output grating (see Fig. 3.12). Even though the vertical grating was designed to work at 11°, and that the SNOM tip was perpendicular to the sample, we were able to verify the field concentration

at the center of the grid, confirming the correct behavior of this device.

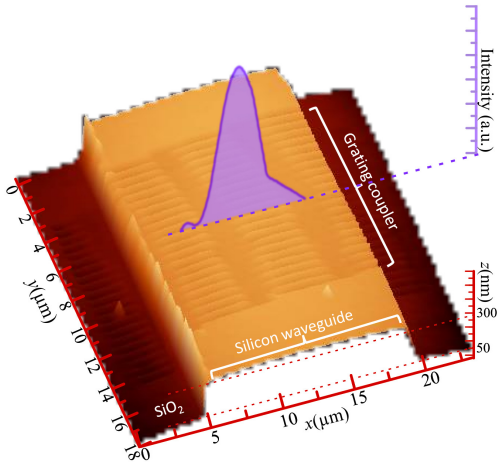

Fig. 3.12 3D representation of the AFM image of the grating coupler. In purple, near-field intensity measured at a distance of $z_L = 0.1$ μm above the grating coupler.

Constant plane z_L= 0.4 μm Emitting antenna: The differences seen between the simulation and the measurement close to the sample at a tip height of 0.1 μm disappeared when raising the SNOM tip to 0.4 μm. In this case, the measurement above the directors of the emitting antenna showed the typical field concentration of this kind of element, in good agreement with the numerical simulation (see Fig. 3.13).

These results show for the first time the near-field response of an on-chip wireless link, helping us to better understand its fundamental principles. This additional information will be useful to improve the design and optimization processes of these integrated photonic devices and could lead to the development of new applications in a variety of fields.

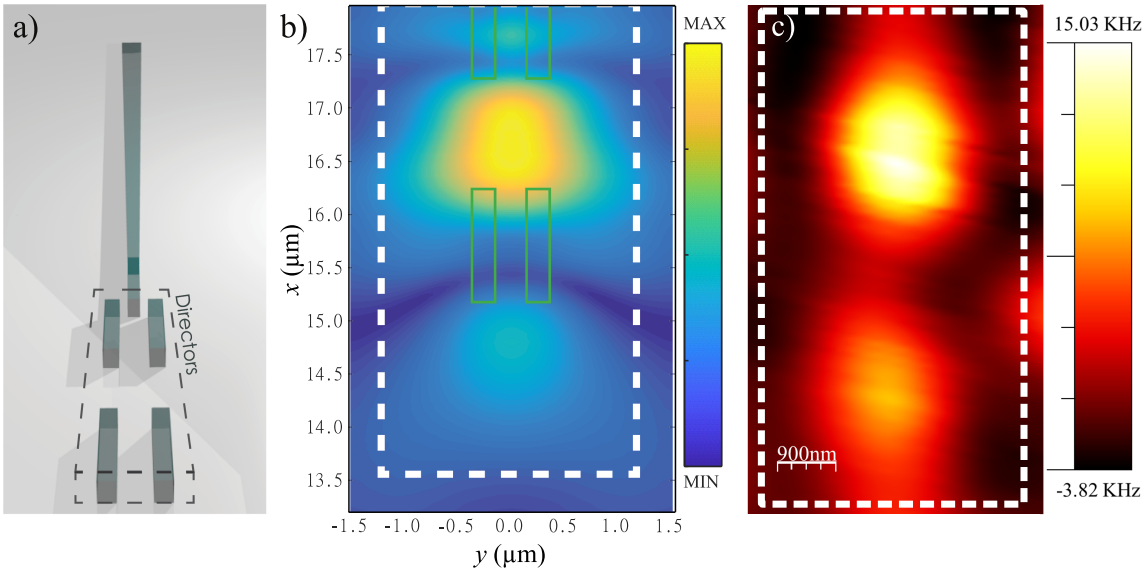

Fig. 3.13 (a) Top view representation of the emitting antenna. Simulated (b) and measured (c) near-field intensity above the fabricated emitting antenna between directors at a distance of $z_{\mathrm{L}} = 0.4\ \mu\mathrm{m}$. Areas enclosed by dashed lines represent the same region in all images.

3.3 First cross-port circular design

Conceiving an all-on-chip TPM based on SOI technology might seem an impossible task, due to the significant concerns that can arise in the development process of this device. However, scientific knowledge has been achieved step by step, sometimes inspired by unattainable goals. The first step in the path to a TPM device that can operate on a SOI platform was to choose the radiating elements. Silicon NAs have been studied as the best choice for radiating and receiving wireless information within a photonic chip. Then, the next task is positioning these NAs in the SOI sample. With this aim, a circular detector configuration seems the best option to model the tomographic device, as inferred from chapter 2. Therefore, the 12-port crossing defined in [52] (Fig. 3.3 b) could be the first approach to this circular detector tomography. Nevertheless, some concerns have to be considered, since this device has been developed for cross-port communications. On the one hand, the high directivity of the NAs used in this cross-port does not meet the requirements of a tomography system, since a wide wavefront will be better for illuminating the objects to be studied (the algorithms have been developed using a plane wave illumination). On the other hand, this 12-port crossing only has a 10 μm spacing between facing NAs, which is a small size if a biological sample has to be inserted within the system. Moreover, the wireless signal transmitted to the output ports above 90° was so low that it was outside the detector range, even using the two-directors configuration in the NAs. Then, extra requirements must be achieved, since to reduce the MCP, the back-scattering signal must be read when the object to be studied is placed in the center of the NAs array.

To solve these concerns, a **circular cross-port device** is proposed, in two configurations. In the first one, the space between the NAs is empty, which will be useful to measure the system in **background** conditions. The second one counts with an **object** place in the center of the system (see Fig. 3.14), to observe the differences with the background configuration, and to verify the ability of the NAs receiving back-scattering. Both configurations use tapered silicon NAs without directors, to ensure lower directivity than the previous 12-port crossing. Since the purpose of these systems is to verify the NAs behavior in a low directivity scenario while the back-scattering has been reading, a simple way to place an object in the center of the NA circular array is to make it out of silicon, fabricating the complete system and the object at the same time. Given that silicon has a RI of 3.45 at $\lambda = 1.55$ μm and the environment in which the complete system is embedded (SiO_2) counts with a RI of 1.45, the RI variation is enormous for a TPM system because it is not possible to validate the Born or Rytov approximations without compromising the diffraction limit in this case. Nevertheless, the experimental verification of the issues

explained above justifies the modeling, simulation, fabrication, and characterization of this first cross-port circular device in the two proposed configurations.

3.3.1 Modeling and numerical simulations

The complete system is modeled directly in the simulation environment: the CST MICROWAVE STUDIO commercial software. The circular array of NAs is designed with a gap of 25 μm between facing nanoantennas, allowing the use of 16 NAs spaced almost 5 μm apart. In addition to the NAs tips and inverted tapers, near-lossless curves [130] are added to the design since ports in CST Studio must be placed perpendicular to the *XY* plane, as seen in Fig 3.14 c). The second configuration is achieved only by placing a cylinder in the center. The antennas are labeled counterclockwise to facilitate the analysis of the system. A schematic of the model can be seen in figure 3.14 a). The final diameter of this cylinder ($\varnothing = 4$ μm) is chosen after different simulations, swiping the radius of this object from 2 μm to 6 μm, even other figures such as squares, or triangles, have been considering. The final choice of the smallest cylinder responds to two reasons: on the one hand, the axial symmetry of this object allows to check the effect of the external elements of the system (bends and waveguides to the ports). On the other hand, as can be seen in Fig. 3.16, the wavefront can reach the entire object. The material assigned for all these elements is silicon, with the cited RI value of $n_s = 3.45$.

Numerical simulations are performed using the full-wave solver within CST MICROWAVE STUDIO, which implements the Finite Integration Technique (FIT). This method is a generalization of the Finite-Difference Time-Domain (FDTD) technique. The mesh type used is hexahedral, with 10 cells per wavelength, resulting in a mesh with 51.5 million of meshcells. The input ports are configured to excite the fundamental TE mode. The entire system (waveguides, curves, and nanoantennas) is considered to be surrounded by silica ($n_M = 1.45$), as seen in Fig. 3.14 b). Open boundary conditions (perfectly matched layers) are chosen for all external faces to avoid undesirable reflections, considering a magnetic plane of symmetry ($H_t = 0$) in the *XZ* plane.
First, the configuration of the device without any object inside is simulated. Sixteen simulations are performed using all ports (1 to 16) as input ports and obtaining the S-Parameters in all these 16 ports. These S-Parameters are related to the power efficiency $\eta_P = P_{RX}/P_{TX}$ as in the previous experiment. The results of the frequency sweep for different input ports are compared with the measurements later. At the moment, the analysis of this empty configuration is performed at the working frequency of the NAs, $f = 193.5$ THz (which corresponds to a $\lambda = 1550$ nm). The results of the simulations at this frequency are shown in Fig. 3.15. Facing antennas (NA 9 when illumination comes from

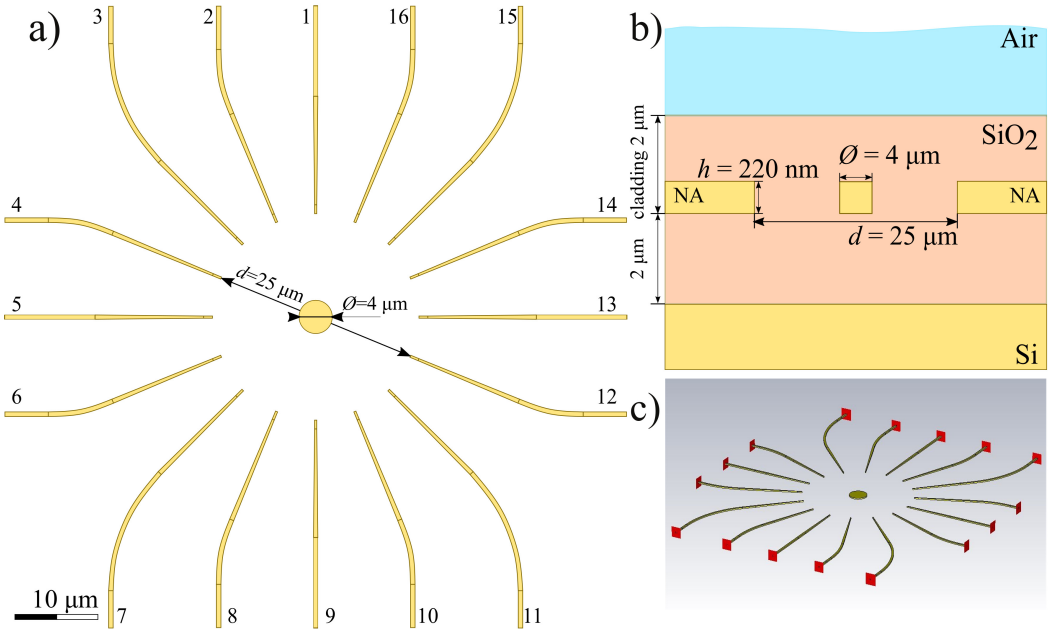

Fig. 3.14 Circular cross-port. a) Schematic of the simulated model, to scale. b) Vertical profile of the sample, not to scale: Upper air, SiO_2 covering layer and surrounding the silicon object and NAs. c) CST Microwave Studio image, where the complete system and ports (in red) are shown.

NA 1, 10 when 2, and following) receive around -15 dB in all the cases, as well as nearby antennas receive similar power. The differences appear when the distance with the facing antenna is greater than 66.7°, in other words, for perpendicular antennas and closer to the transmitter.

To look for similarities, the analysis of the results is divided into 4 scenarios. Nanoantennas 1, 5, 9, and 13 do not require bends to connect them to their input port. The transmission efficiency using these ports is compared in figure 3.15 a). First, it can see how NA 5 and NA 13 have almost the same behavior, as expected due to the symmetry of the model. However, NA 1 and NA 9 have similar behavior but are mirrored for higher degrees. This could be for the orientation of the bends, which change in a mirrored way. This chiral symmetry, widely exemplified in the literature by the human hands, is present in the results in other cases. For example, NAs 2 and 10 have similar transmission efficiency, as can be seen in Fig. 3.15 b); which is the same, but mirrored, when NAs 8 or 16 are illuminating. The same case occurs for NAs 4 and 12, they have the same behavior but mirroring that NAs 6 and 14 (Fig. 3.15 d). Only NAs 3, 7, 11, and 15 behave similarly, slightly changing the transmission efficiency for the antenna adjacent to the transmitter, as seen in Fig. 3.15 b). Efficiency variations are produced along the path to conduct the light from (to) the port to (from) the NAs. Moreover, the close position between antennas (about 5 µm) produces that part of the input signal ends up going directly to neighboring

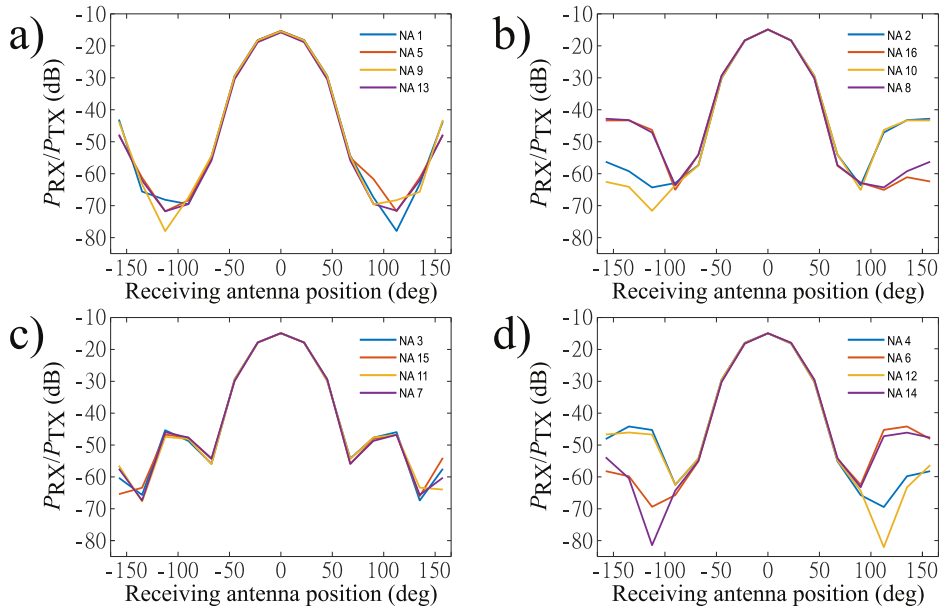

Fig. 3.15 Simulated transmission efficiency in cross-port circular device, background configuration at $f = 193.5$ THz. The different graphs correspond to the different input ports. The x-axis represents the difference between the facing and the receiving antenna.

antennas. However, this irregular behavior is not relevant for this experiment, as these changes will also occur for the next configuration, with a centered object. Then, since these simulations represent the study of the background configuration, the total behavior could be normalized when an object is positioned to be detected, and we can normalize the irregular effect of curves and guides external to the antennas.

Following the study of the background configuration, the cylinder with a diameter $\varnothing = 4$ µm is placed at the center of the model (Fig. 3.14). The simulation is configured in the same way as the previous one. Simulations are performed using the 1 to 5 as input ports and obtaining the S-Parameters on all 16 ports. The reason for simulating only the behavior of these ports responds to the analogies seen in the background configuration, since the performance on ports 9 and 1 is mirrored, as in pairs 2-10 with 16-9, and 4-12 with 6-14. Similarly, the behavior expected by illuminating the NA 13 is the same as using the NA 5 as input port; while the ports 7, 11, and 15 will be like the simulation by illuminating via port 3. The results of the electric field in the plane perpendicular to the ports (*XY* plane) can be seen in figure 3.16. On the one hand, the left column represents the electric field when the input port is the first (a), third (c), fourth (e), and fifth (f). The second port is not shown, since its result is similar to the fourth one. On the other hand, the right column shows the power relation, to see the field on a logarithmic scale.

The power efficiency response for different links at different frequencies will be discussed by comparing them with the experimental sample measurements. First, it is

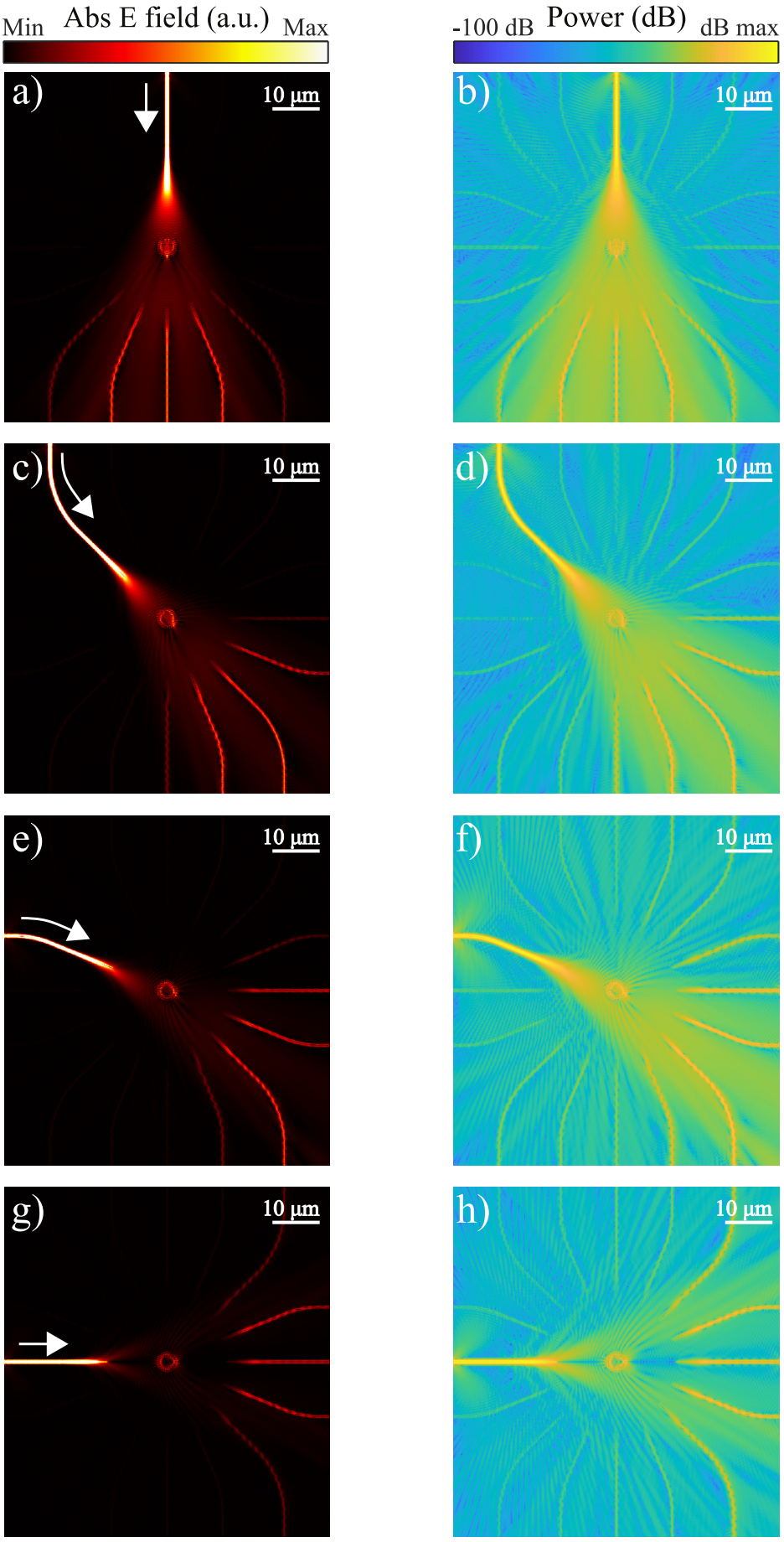

Fig. 3.16 Simulated electric field ($\lambda = 1550$ nm) and power for the input port 1(a, b), 3 (c, d), 4(e, f) and 5 (g, h).

worth comparing the differences observed at central frequency before the fabrication of the devices. For that purpose, and to verify the effect of the object in the system, the power efficiency simulated at a frequency of $f = 193.5$ THz (which corresponds to a $\lambda = 1550$ nm) is compared like in the previous configuration.

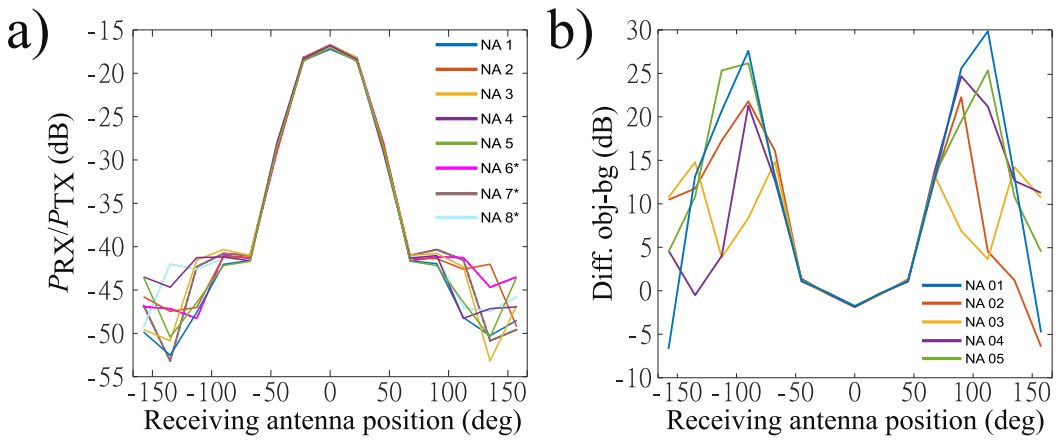

Fig. 3.17 a) Simulated transmission efficiency in circular cross-port object configuration at $f = 193.5$ THz. The x-axis represents the difference between the facing and the receiving antenna. *Data for some ports have been estimated from the mirroring of simulated ports. b) Difference between the efficiency with and without the object for the five first ports.

The efficiency between ports can be seen in figure 3.17 a). Antennas facing each other with less than 67.5° degrees than the emitter one has similar efficiency, which occurs in the background configuration. The differences appear from the perpendicular NAs. Moreover, an efficiency better than -55 dB in the worst case seems promising to measure the back-scattering signal. For this purpose, this SOI device is fabricated in both configurations (background and object). To conclude the simulation analysis, the efficiencies for both configurations are compared in figure 3.17 b), where, as expected, there are significant differences between positions greater than 67.5° degrees.

3.3.2 Fabrication and characterization

Gratings and waveguides are added manually in the KLAYOUT software. The details of the fabrication sketch can be seen in Fig. 3.18. 16 gratings are added, to illuminate or extract light from the NAs, 8 to the left and 8 to the right of the design. Therefore, as can be inferred from the model in Fig. 3.18, when NAs 1 to 8 are illuminated, only NAs 9 to 16 can be measured, and vice-versa. Moreover, a triangle silicon path is added for each grating in the opposite direction of the transmission to avoid reflections (see Fig. 3.18 c). The taper to reduce the 12 μm-wide from gratings to the 450 nm-wide waveguides is the same as those detailed in Fig. 3.5 a). Lossless curves with a radius of 20 μm are added

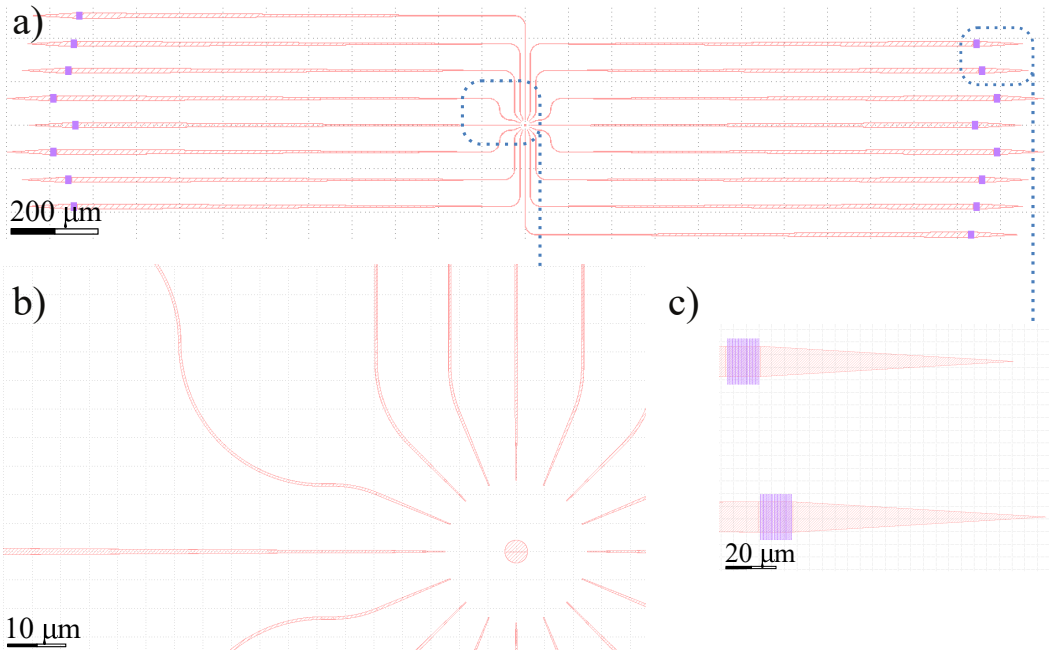

Fig. 3.18 Klayout file of the circular cross-port device. a) Complete model (purple lines correspond to gratings). Areas enclosed by dashed lines represent the areas where detail images b) and c) are taken.

to place the gratings and tapers in a longitudinal position, to avoid a bulky setup in the laboratory. To study the effects that the gratings might introduce into the measurement, a pair of grating links joined only by a lossless guide is added to the sample.

The fabrication is carried out in the clean room facilities of our Institute as detailed in section 3.2.1. A microscope image of the sample, with details at background and object configurations, can be seen in Fig. 3.19, where the input and output fibers are also seen.

3.3.3 Results: simulation and characterization

The SOI sample containing both configurations with 16 ports each, and two links to measure the effect of the gratings, are measured in the far-field characterization setup explained in the previous section. The results are discussed below, first, the configuration with no object inside (the so-called *background configuration*), followed by the analysis of the measurements of the *object configuration*.

Background configuration

For this system, the first eight gratings are used as input ports, using ports from 9 to 16 as output. This is the reason why most of the data obtained correspond to measurements with low degrees of separation of the NA facing the illumination, and

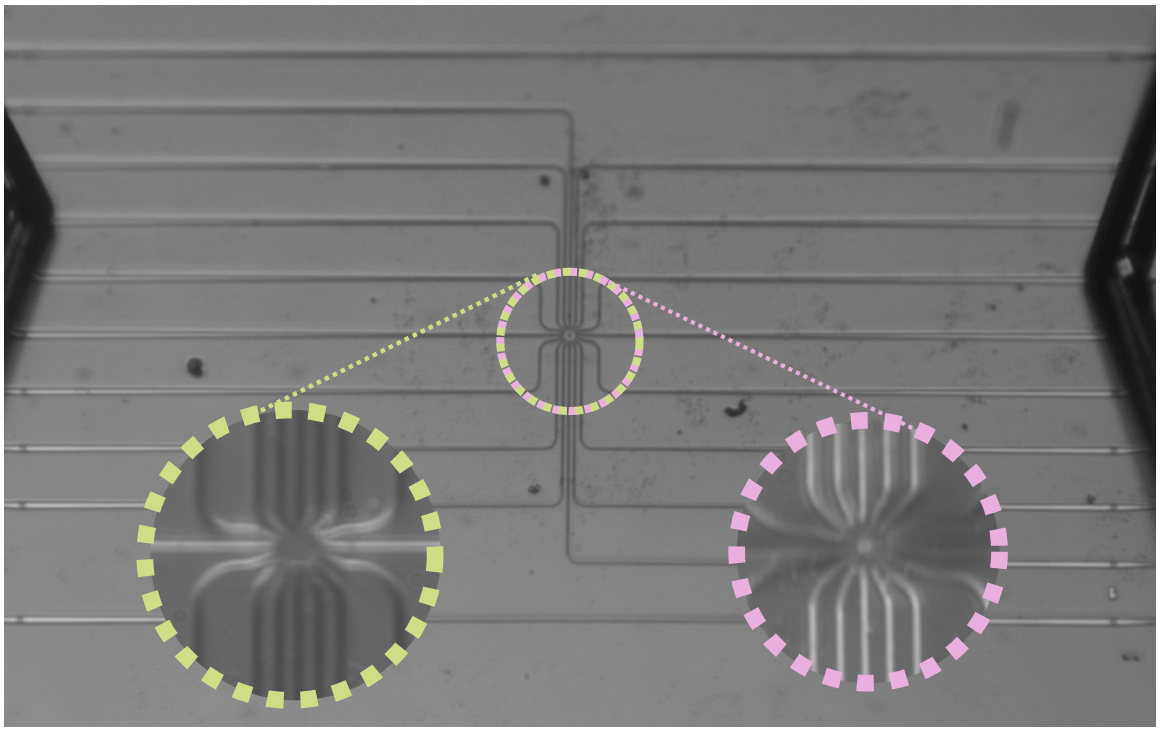

Fig. 3.19 Microscope image of cross-port circular device, object configuration. In the insets, details for background configurations (green) and object (pink).

few port combinations correspond from a neighboring nanoantenna. The results are presented in Fig. 3.20 in different plots, comparing the links with the same angle to the NA in front of the emitter. We show more than half of the measurements taken, ignoring some with similar behavior, since plotting 64 measurements to compare with the 64 corresponding simulations results in a cumbersome figure. Besides, only two simulations for each set of data are placed in the figure, using dashed blue lines, which is enough to put the measurements in context. At this point, the author wants to emphasize that the behavior of the gratings is compensated in the results, since an average of the measurements made on the test gratings has been added to the data taken (this technique has been used in previous studies [52, 122]).

To begin with the analysis of the results, the behavior of the main link (0°) is irregular and dependent on the pair of NAs used, as can be seen in Fig. 3.20 a). Nevertheless, the shape of the wavelength response is almost plane, and the value of the power efficiency is around -15 dB, which agrees with the simulation. The measurements of the following NAs are presented in Fig. 3.20 b), where a 5 dB efficiency reduction is expected based on the simulation. Once again, the power values of the different measurements are around the calculated, although a ripple starts to appear in some measurements. This behavior is also observed for antennas positioned at 45 degrees to the transmitters (Fig. 3.20 c), with good agreement in power efficiency. From 67.5 degrees onward, measurement problems

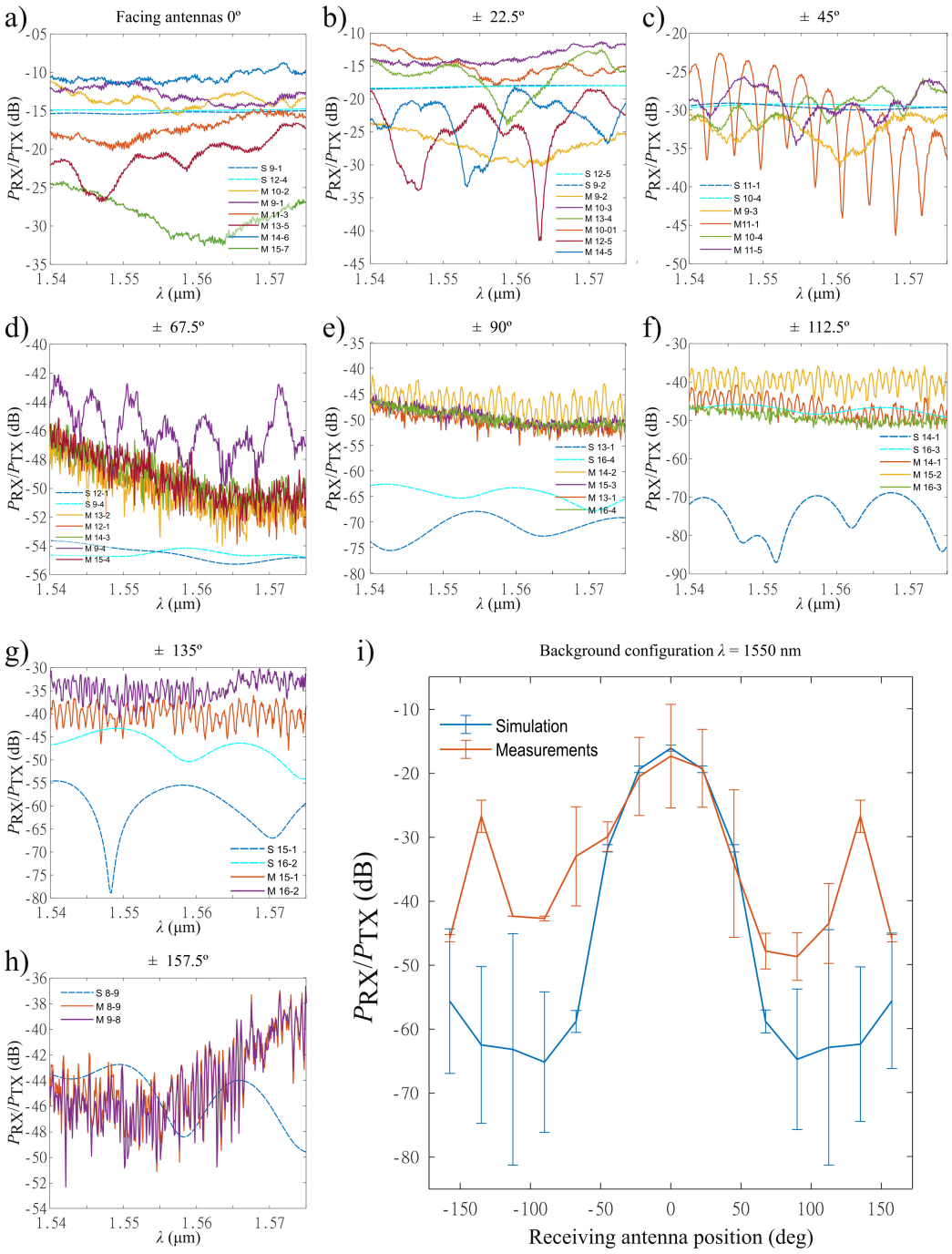

Fig. 3.20 Circular cross-port device, experimental validation of the background configuration. a-h) Comparison of Measurements (M) with their equivalent Simulations (S, dashed lines) of the link for different angles with the illumination antenna. The legend explains the output and input ports for each line. i) Average power efficiency for different ports for the simulations and measurements at $\lambda = 1550$ nm, where error bars indicate the maximum and minimum measure for each angle.

could be expected, as seen from the three noisy readings in Fig. 3.20 d). However, the data taken is similar in the three scenarios, and their power efficiency is still better than expected in the simulations, which also have a similar behavior among them. This behavior in which the measurements share similar result, with a better than expected power efficiency, is observed in the NAs perpendicular to the emission one (Fig. 3.20 e). For the following NAs, the measurements match with the better-expected efficiency (Fig. 3.20 f), while the simulations differ from each other. At this point, we can already state that measurements for degrees greater than 90° are possible, which was not the case with the 12-port crossing with more directive NAs. The few links that could be measured for 135° degrees show better power efficiency than expected from the simulations (Fig. 3.20 g), while NAs 8 and 9, which are close to each other, are measured in both directions (Fig. 3.20 h). The resulting measure is practically the same, and it also shares the efficiency value expected by the simulation.

To conclude the analysis of the background configuration, we focus on the measured and simulated efficiency for the NAs at working frequency ($f = 193.5$ THz). In Fig. 3.20 i), the simulations seen in Fig. 3.15 are compared with all the measurements performed. The blue curve shows the average of the 16 simulations (one per each input port), using error bars for the deviation, which result higher for higher angles, as can be inferred from the simulation curves shown above. Average power efficiency has been obtained also for the measurements (red curve), although it is not possible to make many measurements for antennas with high angles, due to the configuration of the sample, as explained above. Comparing both results, it can be seen who the measurements from -45° to 67.5° match with the expected from the simulation. From perpendicular NAs to beyond, the measurements result in a better behavior than expected. Nevertheless, this is not a drawback, since as explained above, this behavior is going to be normalized when an object is placed to be sensed.

Object configuration

Once the background configuration has been analyses, the scenario with a cylinder ($\varnothing = 4$ μm) placed in the center of the device, is studied. In this configuration, the 128 possible measurements are conducted (8 output ports for each of the 16 ports used as inputs). Due to the SOI sample model, it is not possible to measure all links with high degrees, as seen in Fig. 3.18. Nevertheless, it is possible to measure for all receiving angles, which verifies that the back-scattering of the sample can be measured via this device. Moreover, the lack of high degrees links comes with the advantage of many possibilities to measure NAs facing illumination, as well as NAs closer the these. For the sake of simplicity, only two

simulation curves are shown in the results of figure 3.21, comparing them with some of the most representative measurements.

As in the previous analysis, grating effects are considered in this data representation. Firstly, it is worth mentioning that the response of the confronted NAs is about 5 dB lower than expected, as can be seen in figure 3.21 a). For following NAs, the efficiency behavior associated for the different wavelengths matches the simulations (Fig. 3.21 b, c), although the link with input 5 and output 14 results in a large efficiency drop around $\lambda = 1.55$ nm, which is not a drawback since the average of the measures coincides with the simulations, as can be seen in Fig. 3.21 i) at the 22.5° position. The 67.5°, 90°, and 112.5° scenarios (Fig. 3.21 d-f) are in good agreement with the shape of the calculations, but with a shift in wavelength and power efficiency. While most of the measurements have a mimic behavior, the local minimum at 67.5° and local maxima at 90° and 112.5° are close to the expected by the simulations (only 5 nm of difference). The measurements also turned out better than expected in terms of power efficiency for the higher angle cases, as can be seen in Fig. 3.21 g, h).

We conclude the analysis by focusing again on the average power efficiency and its deviations at the working frequency of the NAs in Fig. 3.21 i). As could be inferred from the detail of the calculations throughout the figure, the variation in the simulations is smaller than for the background configuration. Comparing the shape between measured and simulated average efficiency, there is a good agreement, except for two considerations: On the one hand, NAs from perpendicular to higher angles give better than expected power efficiency, **validating** the possibility of **measuring the back-scattering** of a sample via this device. On the other hand, and contrary to what was predicted by the calculations, the average efficiency measured at facing antennas (0°) is lower than received in the closer to these antennas. Nevertheless, these measurements demonstrate that the issues that needed to be addressed in this device have been solved, since **NAs without directors** have been validated to build a **working link with greater distance** than in the previous 12-port crossing. In addition, the signal has been read for all orientations, even those greater than 90°, which is evidence that back-scattering has been detected. With these considerations, the modeled, fabricated, and characterized cross-port circular device paves the way toward the first lab-on-a-chip TPM.

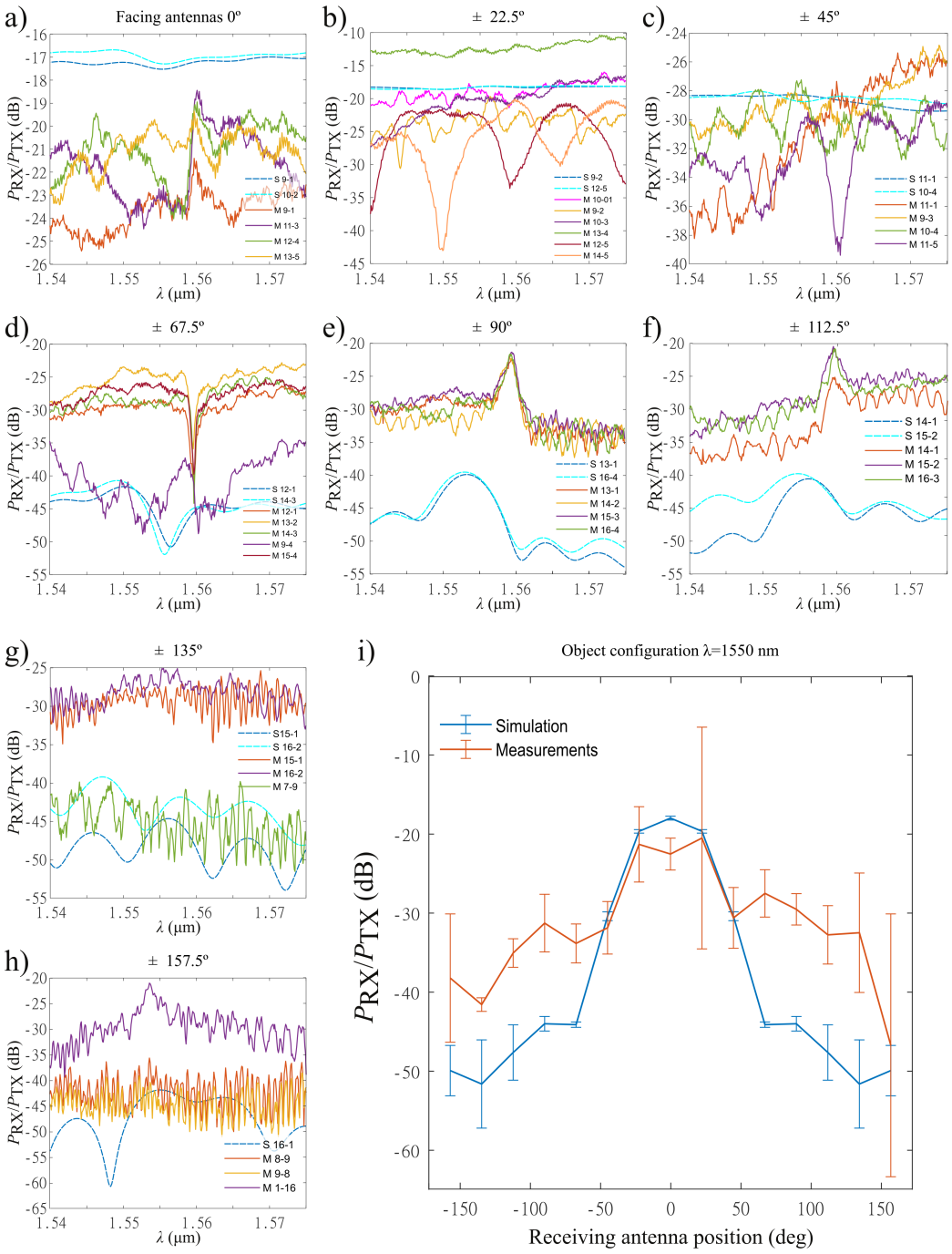

Fig. 3.21 Circular cross-port device, experimental validation of the object configuration. a-h) Comparison of Measurements (M) with their equivalent Simulations (S, dashed lines) of the link for different angles with the illumination antenna. The legend explains the output and input ports for each line. i) Average power efficiency for different ports for the simulations and measurements at $\lambda = 1550$ nm, where error bars indicate the maximum and minimum measure for each angle.

3.4 Circular tomography in baseline system

The implementation of the SOI-based all-on-chip TPM was an unattainable goal a priori. In the previous section, some concerns have been solved to achieve this target: the use of NAs has been validated, which have sufficient directivity to carry the signal from input to output ports, while the wavefront is wide enough to cover an object. Besides, it has been possible to read the back-scattering signal, hence circular detectors algorithms can be used to obtain tomographic results with the best possible resolution.

The previous design shed light on a new issue to be solved since as the number of NAs increases, the complexity of the SOI sample increases. Moreover, another complex concern to solve is the introduction of a holographic design to deal with the phase information of the signal. Due to the complexity of the SOI device required to solve this issue, this shortage will be studied in the future work. Besides, another main issue in biological systems is to consider the technique to place the sample in the exact position to be studied. This is not going to be a serious drawback, as microfluidic channels have been used to carry out samples in fabricated SOI devices, for example, in the aforementioned cytometer [53]. Nevertheless, before taking these steps, we consider to study a simple fixed sample framework, to verify the circular tomography algorithm in an experimental environment.

Then, the tomographic study of a simple object with a RI profile close to the surrounding medium seems the next step to consider. Besides corroborating the circular algorithm, the baseline design to be modeled must face a further increase in the number of nanoantennas and the distance between them. These concerns make the new device more complex, and therefore it should be tested experimentally. One idea to reduce the complexity of this device is the study of an object with axial symmetry, allowing the characterization using only one NA as emitter and the rest as receivers. In this way, we can obtain one projection for an object with axial symmetry, which could be replicated to obtain the complete sinogram. Moreover, only half of the NAs are needed, since we can read the scattered field from $-\pi$ to 0 rad, and replicate this behavior for the angles from 0 to π.

When we choose the cylindrical object to be placed in the center of the configuration, a possibility arises: instead of using a single material, we make a sample with a circular opening in the center, and we fill it with different materials in each characterization. With this aim, dilutions in de-ionized water (DIW) are considered. Firstly, ethanol-DIW dilution is proposed, since its RI at $\lambda = 1550$ nm and T=25°C is $n_{\text{eth}} = 1.376$ for a 90% ethanol volume [131], close to the RI of the SiO_2 medium ($n_{\text{m}} = 1.45$). However, this possibility must be discarded due to the volatile behavior of the ethanol, which can complicate laboratory measurements as it can evaporate.

We propose two materials as follows to have two different scenarios, with a RI higher and

lower than n_{m}. On the one hand, **glycerol** offers a RI of 1.4571 at $\lambda = 1550$ nm [132]. On the other hand, a 60% sucrose concentration in a **sucrose-DIW dilution** has a RI of 1.425 [132]. Both configurations are first tested by obtaining sinograms via the COMSOL MULTIPHYSICS software, using the circular detector tomography algorithm explained in the previous chapter. Firstly, a glycerol cylinder of radius $r = 1.5\ \lambda$ is studied under a detector with $R = 20\ \lambda$, using 512 points and 512 projections.

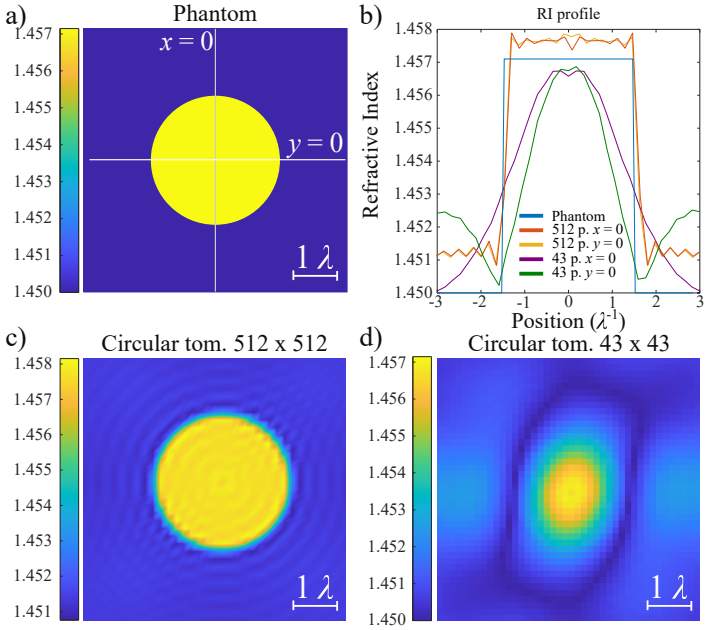

Fig. 3.22 Solution for circular detector tomography for glycerol cylinder phantom a) Phantom, whites lines indicate the place where the profiles in b) are taken. b) RI profiles for different solutions. c) Tomogram for a 512×512 sinogram. d) Tomogram for a 43×43 sinogram. The size of images c) and d) are $3\lambda \times 3\lambda$.

The result of this tomography can be seen in Fig. 3.22 c). Since the use of 256 NAs is a step too far at this point in the study, other formulas are considered. For instance, by reducing the number of points and projections 12 times, a 43×43 sinogram is obtained, which results in the tomography eye is not perfect, as seen in Fig. 3.22. Nevertheless, this could be the first approach to build a reference device, since for this sinogram it is only necessary to use 22 NAs as receivers because 21 of them will mimic its result. The sucrose-DIW dilution is also tested, using the same cylinder size and tomography settings. The results are shown in Fig. 3.23.

For the 512×512 sinogram scenario, the tomogram shows a good result, as can be seen in Fig. 3.23 c). However, when the input is reduced to the 43×43 sinogram, the RI is not well resolved, as is the case for the glycerol setting. However, the cylinder radius could be inferred in the RI profile at $y = 0$ (green line in Fig. 3.23 b), which is a result that this baseline device could give us. Keeping in mind that the tomographic result with only 43

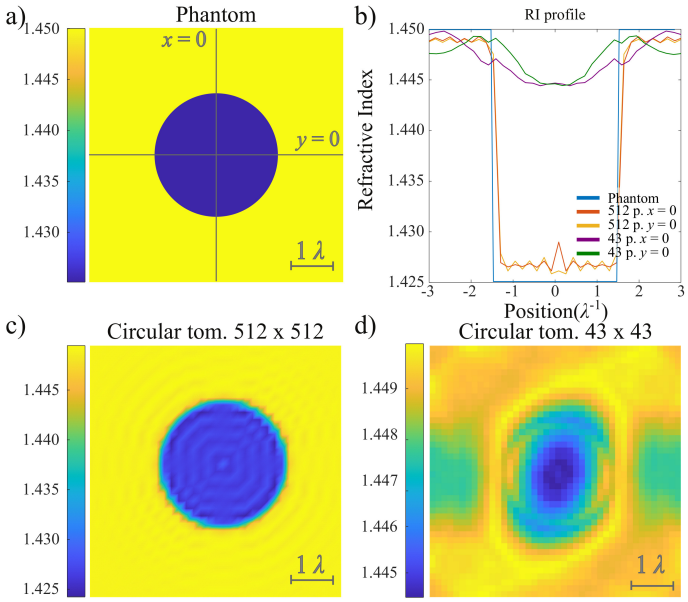

Fig. 3.23 Solution for circular detector tomography for 60% sucrose-DIW dilution phantom a) Phantom, whites lines indicate the place where the profiles in b) are taken. b) RI profiles for different solutions. c) Tomogram for a 512×512 sinogram. d) Tomogram for a 43×43 sinogram. The size of images c) and d) are $3\lambda \times 3\lambda$.

projection data (corresponding to one detector each 3 λ) will not be perfect, the baseline device is modeling and fabricated to its characterization. The purpose is to observe the behavior of the nanoantennas without directors at a larger size distance between them, and to see if it is possible to obtain a first tomographic result, although we do not yet have holographic phase measurements (this will be discussed at the end of the chapter).

3.4.1 Baseline device modeling and simulations

To achieve the tomography via circular detector with radius of $R = 20\ \lambda$, the facing antennas are placed at a distance of 62 μm. The rest of 21 NAs are placed oriented towards the center of the configuration, with a difference of 8.24° between them. The schematic of this model is showed in Fig. 3.24. Lossless curves are added to the design, since the ports in CST Studio must be placed in the corresponding plane, as seen in Fig. 3.24 c). For the first configuration, the central object is removed. To perform the simulation, 23 ports are placed: one to the first NA, which serves as an illumination antenna, keeping the rest of 22 ports to receive the signal. The input port is configured to excite the fundamental TE mode. The simulation is performed using ten cells per lambda, considering the air and silicon slab (as detailed in Fig. 3.25 a), which produces a mesh with 523 million

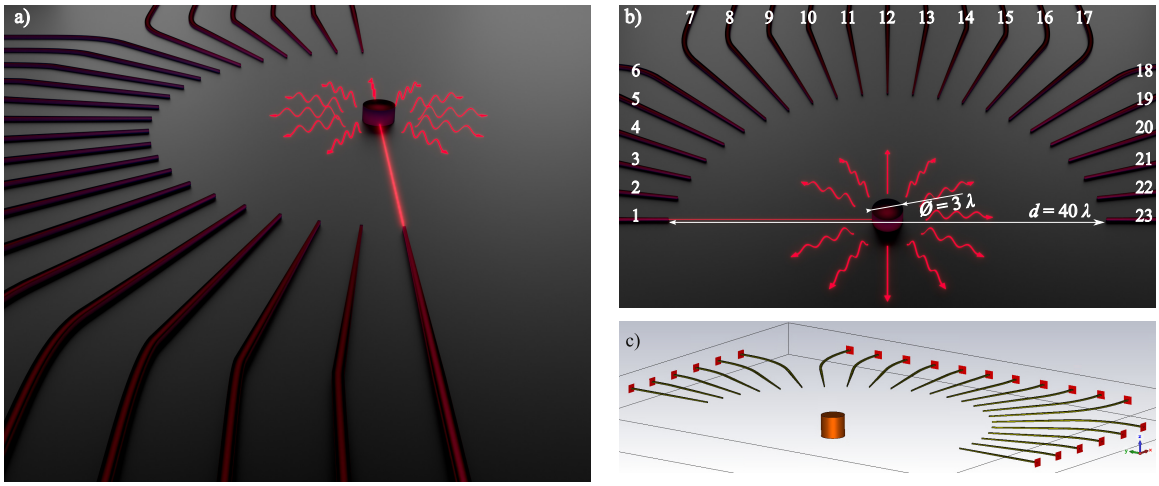

Fig. 3.24 Baseline device. a-b) Schematic of the simulated model. c) CST Microwave Studio image, where the complete system and ports (in red) are shown.

meshcells [2]. The whole system (waveguides, curves, and nanoantennas) is considered to be surrounded by silica ($n_{\mathrm{M}} = 1.45$). Open boundary conditions (perfectly matched layers) are chosen for all external faces to avoid undesirable reflections. At the end of this chapter, the simulation results are compared with the measurements. It is worth mentioning that the secondary rays reflected at the Air-SiO2 and SiO2-Si interfaces (see Fig. 3.25) might become important. We performed an analysis similar to that explained in the Supp. Material of [52], which shows that, in our case, the two secondary rays interfere destructively, giving a combined contribution whose power is approximately equal to a 0.3% of that of the direct ray. As a result, we can neglect the effect of reflections for this configuration.

We model the next configurations by adding the ($\varnothing = 3\lambda = 4.65$ μm) cylinder, with a height exceeding the silica coverage. The **first object configuration** is simulated with the same parameters as the previous one, but considering that the central cylinder, located between NAs 1 and 23, as can be seen in Fig. 3.24 a), is composed of **glycerol**, with the cited RI of 1.4571. With the same parameters, the next object configuration considers **DIW** as the cylinder material, with a RI of 1.333. The last configuration repeats all the steps as the previous one, but considering the inner cylinder is filled with the sucrose concentration of 60% within a **DIW-sucrose dilution**, considering its RI of 1.425. The results of these three simulations are also discussed below, comparing them with the characterization of the SOI sample.

3.4.2 Fabrication and characterization

Gratings and waveguides to them are added manually in the KLAYOUT software. To illuminate the emitter NA, a grating is added to the left side of the device and a tapered waveguide is placed to carry the signal. This taper to reduce the grating width from 12 µm to the 450 nm waveguide is the same as detailed in Fig. 3.5 a). It is worth mentioning that, for this experiment, the grating on the left side is used as an input port, while the rest are considered as output ports. Meanwhile, the remaining 22 NAs are connected to the 22 output gratings via tapers, waveguides, and lossless bends with a 20 µm radius. Moreover, a triangle silicon path is added for each grating at the opposite direction of the transmission, to avoid reflections (as seen in Fig. 3.18 c). To study the effects of these gratings, a pair of grating links joined only by a wide lossless guide are added to the sample. Fabrication is carried out in the clean room facilities of our institute as detailed in section 3.2.1, however, in this experiment, we complete the process in two steps. Initially, two identical 23-port devices are fabricated, with no object in the center, as detailed in Fig. 3.25 a). This background configuration is characterized in the first place. In Fig. 3.26, two microscope images of this background configuration are shown. In Fig. 3.26 a) it is possible to see the complete 23 port device, plus the grating test. In Fig. 3.26 b), the image illustrates the fiber alignment when the output fiber is placed on port 16.

After the characterization of the background configuration, the second step of the fabrication is achieved, via Raith 150, by drilling a hole inside the sample through SiO_2 cladding (Fig. 3.25 b). The result of this step can be seen in Fig. 3.26 c) and in the SEM images in Fig. 3.27, where an almost perfect circle appears (the rest of the sample is barely visible because it is covered by silica).

[2] Using a computer with 64 GB of RAM and 3.3 GHz of CPU, the simulation solves in ∼90 hours.

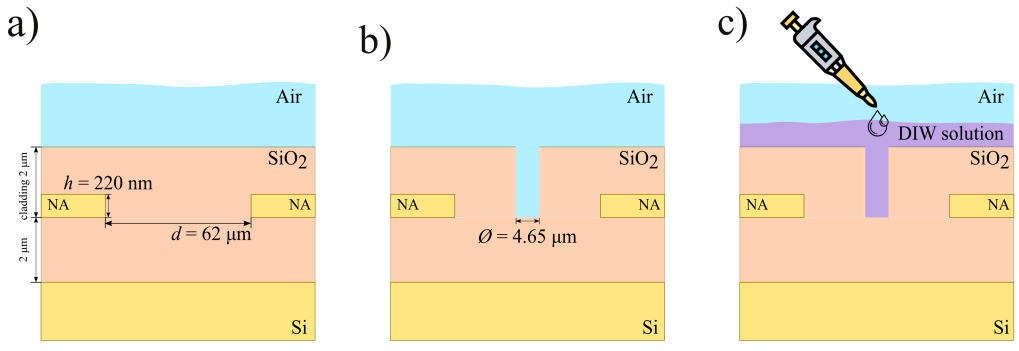

Fig. 3.25 Vertical profile of the baseline device, not to scale: Upper air, SiO_2 covering layer and surrounding the silicon object and NAs. a) First background step. b) Fabricated gap. c) Flooded gap filling with a micro-pipette.

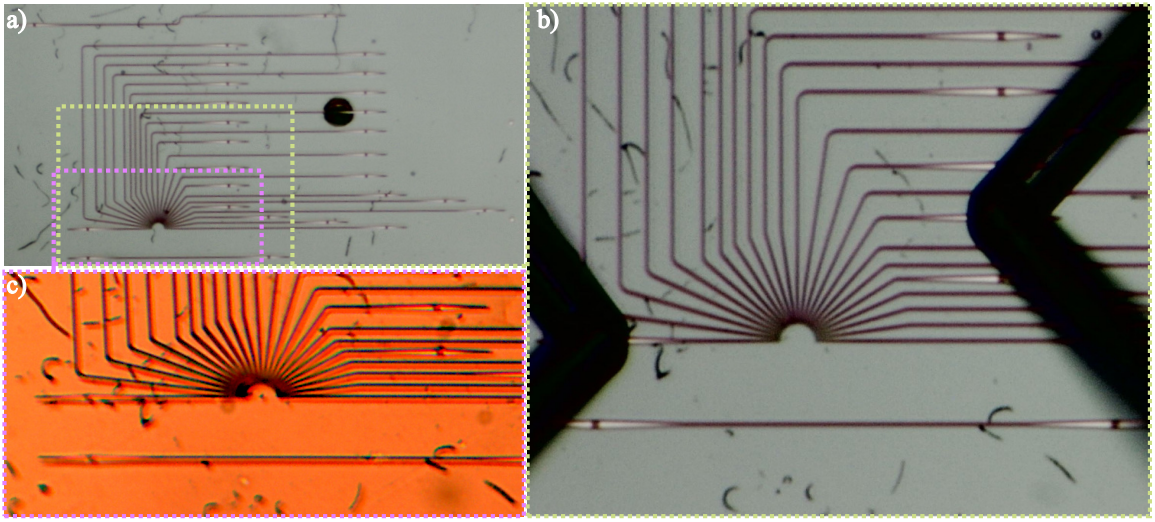

Fig. 3.26 Optical Microscope images of baseline system. a) General, in background configuration. b) Close view, with fibers placed at port 1 and 16. c) Close view, for object configuration.

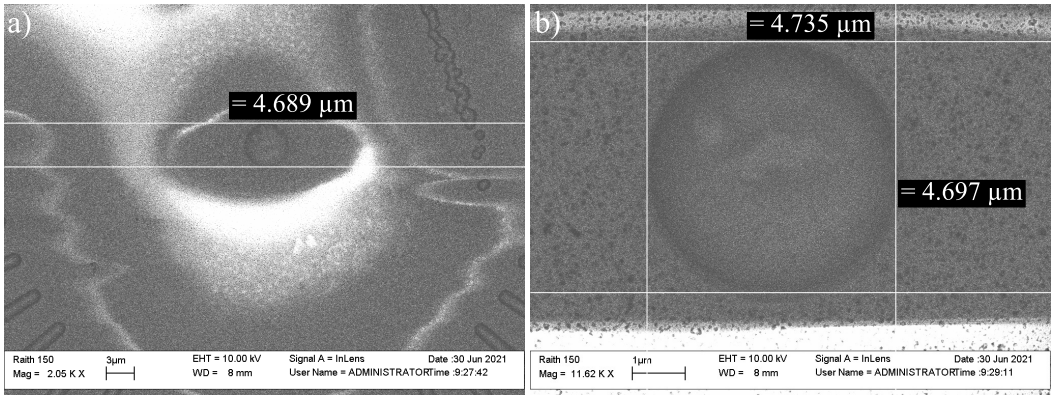

Fig. 3.27 Scanning Electron Microscope images of baseline system. a) General. b) Close view.

Finally, the sample is filled by flooding through a micro-pipette, as detailed in figure 3.25 c). First of all, the glycerol is used to flood the sample, with the difficulty that this material is viscous, and it is necessary to wait for it to settle. After the characterization of the glycerol configuration, the SOI sample is cleaned via the so-called piranha process, detailed as follows:

- Before cleaning, the sample was functionalized with AG protein for a VEGF bounding.
- **0:** Remove adhesive channel - Acetone.
- **1 - Ox:** Piranha (3:1) Sulfuric acid (H_2SO_4) and hydrogen peroxide (H_2O_2). The sample is immersed into the piranha for 30 min.

- **2 - Ox:** Acetone + IPA cleaning (standard procedure). Sample attached to the holder of the coater with carbon conductive tape, programmed to spin turn.
- **3 - Ox:** O_2 plasma cleaning at TePla system for 10 min.

After the sample is cleaned, the gap is filled, using 1000 µl of DIW. The third set of measurements is then performed. Once the characterization of the DIW configuration is finished, the sample is cleaned again via the piranha process. The last flooding of the sample is carried out with 1000 µl of the DIW-sucrose dilution. All the measurements are commented on below. All characterizations are carried out in a far-field set-up as described in section 3.2.2.

3.4.3 Results

The results of the simulations and measurements are compared. The sweep from $\lambda = 1535$ nm to $\lambda = 1565$ nm is shown among the calculated and measured wavelengths, which centered the results on the working wavelength of the NAs at $\lambda = 1550$ nm. Some measurements around the perpendicular antennas are quite noisy, as seen below. Plots are shown with reduced opacity to facilitate the readability of the simulations in these cases. Once again, all measured values are compensated with the gratings measured within the sample (therefore, some links between facing NAs can be seen almost lossless). Simulations and measurements (if possible) are compared at $\lambda = 1550$ nm at the end of each subsection.

Background configuration

Two identical devices are fabricated without objects in the center of the NAs array. We perform the measurements on both systems before manufacturing the gap to be filled with the dilutions of the following configurations. One of these systems can be seen in the eyes of the optical microscope in Fig. 3.26 b-c). Since both background systems are measured, the average of the results is shown in 3.28 in straight lines.
The results are shown from the smallest angle of confrontation with the emitter antenna (NA 23, with 0°) to the antenna closest to the transmitter (NA 2, with an angle of -171.8°). Firstly, the averages of the two measurements performed on both NA 23 and 22 show a better efficiency than the simulations (Fig. 3.28 a). For the following links, from NA 21 to NA 16 (Fig. 3.28 b-d), the measurements are in agreement with the simulations in terms of the efficiency value, while the shape due to the wavelength dependence is not as flat as expected. The noise starts to appear in the measurements from antenna 15, with an angle of 65.5° (Fig. 3.28 e).

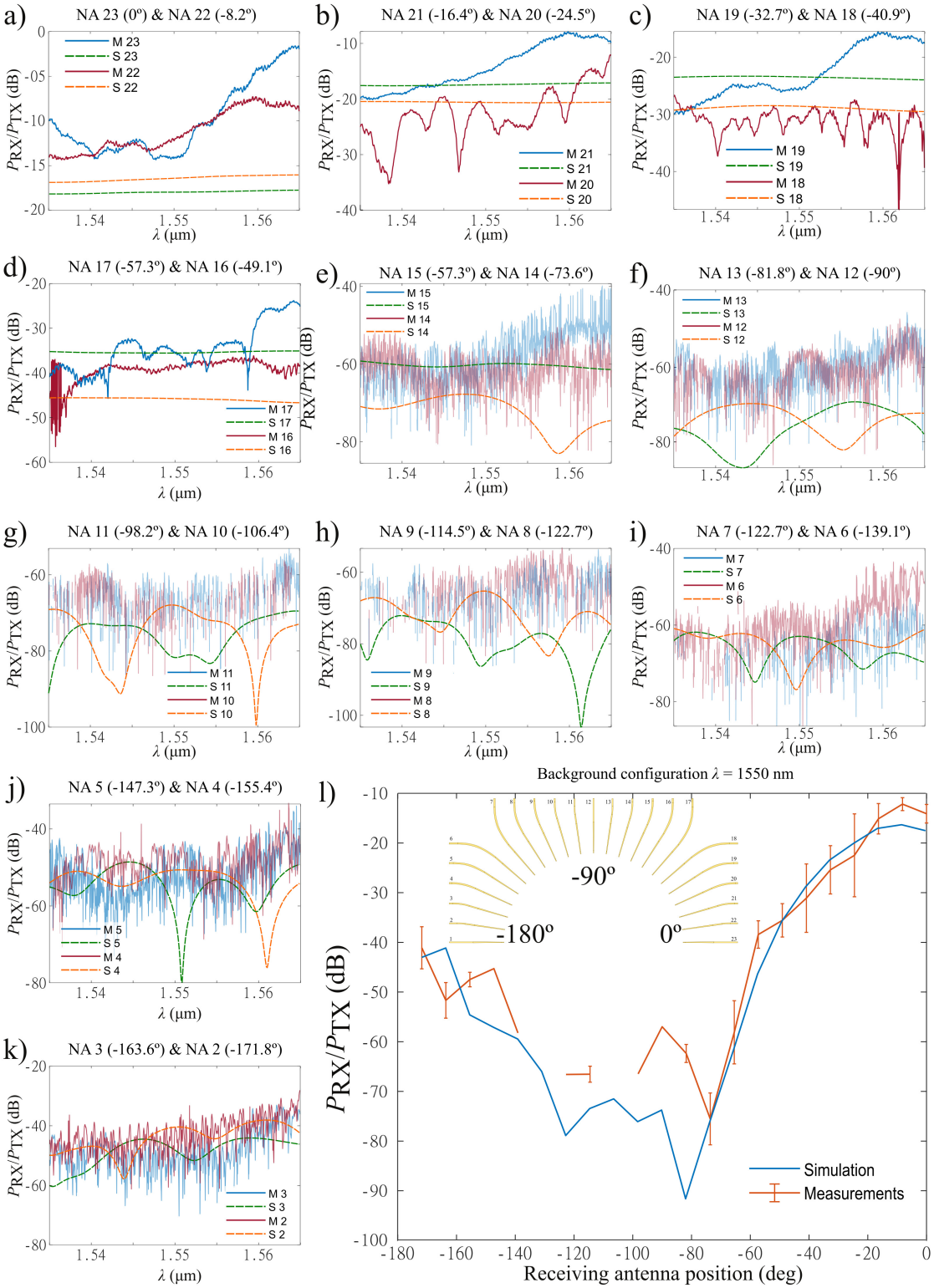

Fig. 3.28 Baseline semicircular device: Background configuration, measurements and simulations. a-k) Comparison of Measurements (M) (average, gratings compensated) with their equivalent Simulations (S, dashed lines) of the link for different angles, using the NA 1 as the illumination antenna. The legends explain the output port for each line. l) Average power efficiency for different ports for measurements, where error bars indicate the maximum and minimum measure for each angle, and simulation, at $\lambda = 1550$ nm.

However, the alignment is possible for all the links in this configuration, even for those links with weaker efficiency (Fig. 3.28 f-i), although the measurement is not possible in the complete set of wavelengths. Simulations of these weak links show a non-flat behavior, while this pattern is hardly seen in the measurements. In the cases of NAs 5 and 4 (Fig. 3.28 j), the wavelength dependence of the measurements is again seen, although it does not match that the simulated for both NAs. This is not the case for the closer NAs to the emitter one, since the measurements in NAs 3 and 2 are in good agreement with the simulations (Fig. 3.28 k).

To finalize the analysis of the results in the background configuration of the baseline system, we delve into the central wavelength (Fig. 3.28 l). The simulation shows a curve with a local minimum close to the expected -90° position, improving the power efficiency as we move away from the antenna perpendicular to the emitted antenna. The measurements verify this behavior, since it is difficult to measure in the perpendicular positions. Moreover, the behavior of the curve is coincident for the rest of the NAs, especially from 0° to -57.3°, as predicted by the measurements analyzed. The error bars on the measurement line show the maximum and minimum measured value since two different background configurations are characterized, being the central line the average of both recordings. The most significant behavior observed in the simulations can be seen for the 0°, -8°, and -16° positions, as NA 22 receives a more powerful signal than NAs 23 and 21, which is corroborated in the measurements.

Glycerol configuration

After the fabrication of the gap in the center of the device, as seen in Fig. 3.27, the first configuration is measured with the object. A large amount of glycerol is placed on the sample, enough to cover a large part of the device. We wait for the glycerol to settle and fill the gap, then, output NAs are measured while the first NA is illuminated. The characterization results are compared with the simulations for each port in Fig. 3.29. From here, only one device is measured in each configuration.

In this case, in contrast to the background configuration, simulations indicate that the power efficiency of the NA 23 link is slightly higher than for the NA 22, as seen in Fig. 3.29 a). Nevertheless, the measurement indicates the opposite, even though the almost flat behavior of the measurement is similar to that expected. Another anomalous measurement is observed in the case of NA 20, as the power efficiency measurement for this link is far below the expected (Fig. 3.29 b). Nevertheless, measurements are possible on links from -32.7° to -57.3°, resulting in higher power efficiency than expected from simulations (Fig. 3.29 c, d). As in the previous background configuration, the noisy measurements appear from angle -65.5° to -139°, as seen in fig. (Fig. 3.29 e-i).

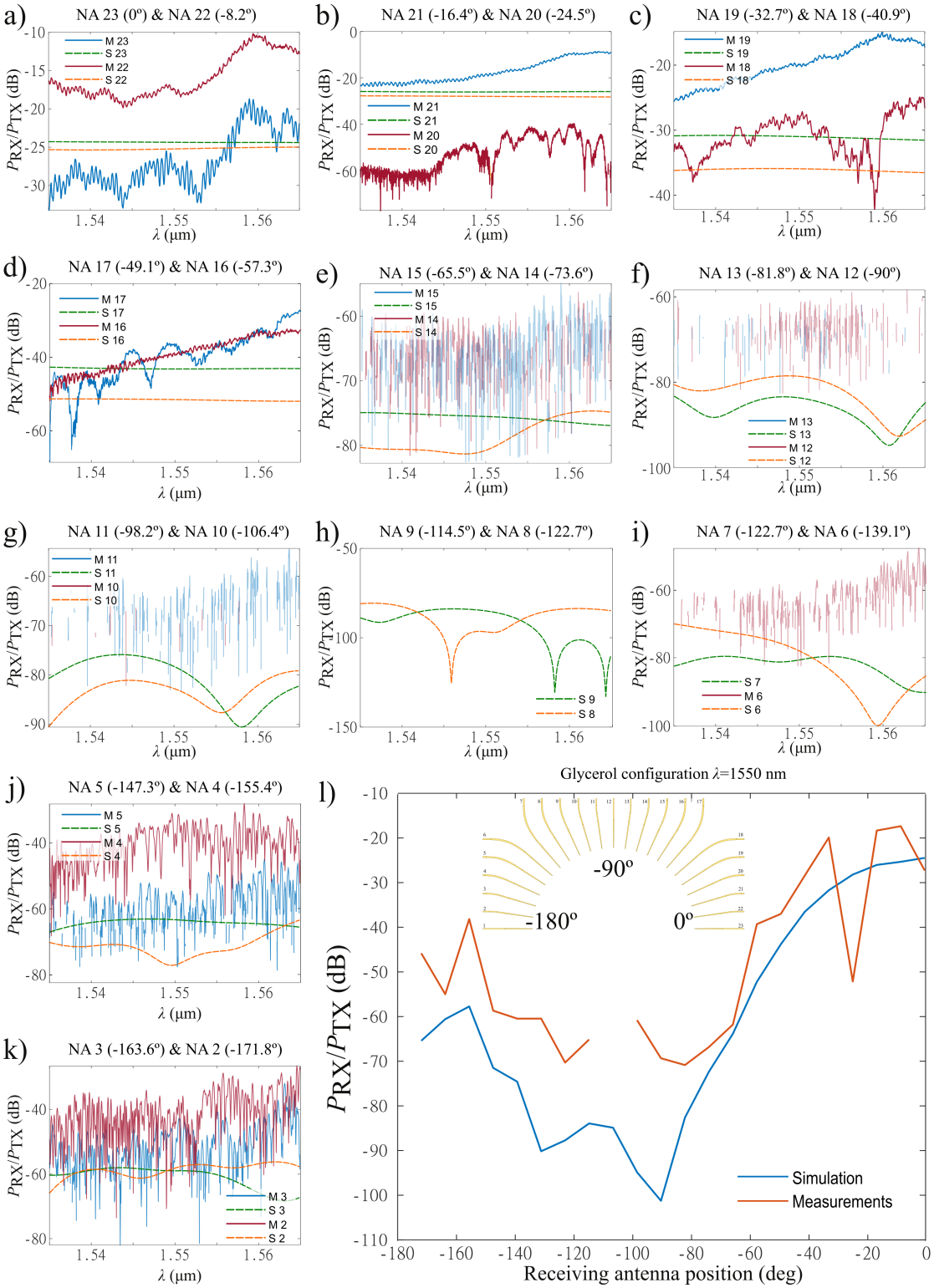

Fig. 3.29 Baseline semicircular device: Glycerol configuration, measurements and simulations. a-k) Comparison of Measurements (M) (gratings compensated) with their equivalent Simulations (S, dashed lines) of the link for different angles, using the NA 1 as the illumination antenna. The legend explains the output port for each line. l) Power efficiency for different ports for measurements and simulations at $\lambda = 1550$ nm.

In addition, most of the links receive data in few wavelengths, or the alignment is impossible, such as in the links containing NAs 7, 8, and 9. It is understandable that measurements are not possible in these links, due to the fact that the expected efficiency is below 80 dB. We can measure, albeit slightly noisy, from NAs 5 to 2 (Fig. 3.29 j-k), where the simulation again shows lower power efficiency than the measured.
This framework, in which the measurements have better power efficiency than the simulations, is seen in the study for the center frequency of $f = 193.5$ THz (Fig. 3.29 l). The shape of the simulation curve keeps similarities with the measurements, except for the aforementioned nanoantennas 20 and 23. In addition, the fact that the perpendicular and near perpendicular positions cannot be read is a drawback that we can turn into an advantage: these positions can be used to place the microfluidic channel to introduce the biological samples to be tested. We will be able to remove these NAs without loss of information since the back-scattering wave is recorded from the NAs placed from -171.8° to -122.7°.

DIW configuration

After we clean the sample, the gap is filled, using 1000 µl of de-ionized water (DIW) over the device. Then, the characterization is carried out using the far-field setup. The results are compared with the simulations for each port in figure 3.30.

Firstly, once again, the link containing NA 22 offers higher power efficiency than NA 23, which is consistent with the simulations, as seen in Fig. 3.30 a). The port that fails again is number 20, resulting in lower efficiency than expected according to the simulation (Fig. 3.30 b). The key to these consecutive failures could be in the distance from the NA 20 to his correspondence grating, since, as seen in figure 3.26 a), grating 20 is the farthest away from its nanoantenna in that part of the device. Then, the path from the NAs may have been damaged in some of the cleaning or transportation process.
Continuing with the rest of the links, measurements on NAs 19, 18, and 17 result in almost flat behavior as expected, introducing some noise from NA 16, but keeping good agreement between experimental demonstration and simulations (Fig. 3.30 c, d). From here on, once again the path from NAs to the gratings may affect the measurements, since the alignment on the even ports has been easier than on the odd ports. This is also reflected in the measurements (except in the NA 7, Fig. 3.30 e-k). The measured power efficiency, if possible, matches the simulated on, or even slightly exceeds it.
Delving deeper into the behavior of the device at the central wavelength, the characterization and simulation maintain a similar profile, as seen in Fig. 3.30 i), except for the mentioned NA 20. In addition, the perpendicular positions are kept without measurements for $\lambda = 1550$ nm, supporting the aforementioned idea of using this space to place the microfluidic channel.

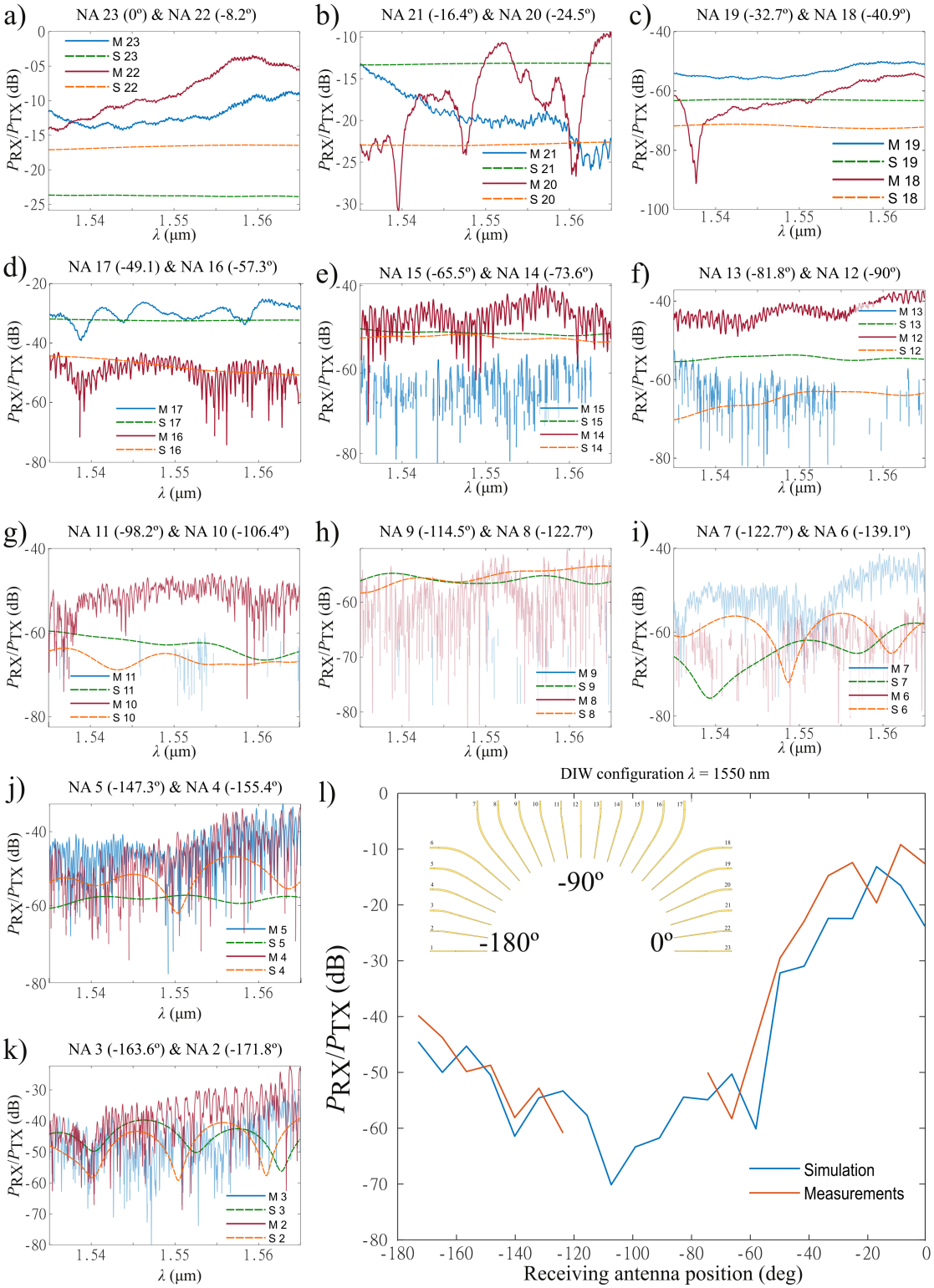

Fig. 3.30 Baseline semicircular device: DIW configuration, measurements and simulations. a-k) Comparison of Measurements (M) (gratings compensated) with their equivalent Simulations (S, dashed lines) of the link for different angles, using the NA 1 as the illumination antenna. The legend explains the output port for each line. l) Power efficiency for different ports for measurements and simulations at $\lambda = 1550$ nm.

60 % sucrose-DIW dilution configuration

After the sample cleanup for the last time, the gap is filled, now using a 1000 µl of 60% sucrose concentration in DIW over the device. Characterization is then carried out using the far-field setup. Measurements are compared with the simulations for each port in figure 3.31.

To begin the analysis, once again the simulation of the link with NA 22 returns better power efficiency than the NA 23, but this behavior is observed in the measurements only at wavelengths that differ from the central ones, as seen in Fig. 3.31 a). For nanoantennas ranging from 22 to 15, the power efficiency values are still always slightly higher than expected, as in the previous configurations (Fig. 3.31 b-e). The noticed drawback on the odd antennas is repeated from NA 13 to NA 7, which gives us more evidence that the difference in paths could affect the measurements (Fig. 3.31 e-j). For instance, while the alignment on ports 11 and 9 becomes an impossible task, ports 10 and 8 can receive the signal with better power efficiency than the simulated one. Finally, the noisy measured power efficiency of NAs 3 and 2 is in concordance with the simulated one, as NA 3 shows better efficiency even though it is an odd port, as seen in Fig. 3.31 k).
Differences between NAs 2 and 3 are more evident if only the working center frequency of the nanoantennas is considered (Fig. 3.31 l). This last analysis shows similar behavior between simulation and measurements, except for the NA 20 (as in previous cases). The gap left by the 90° to -122° positions supports, for the last time, the use of these positions to place the OF channel.

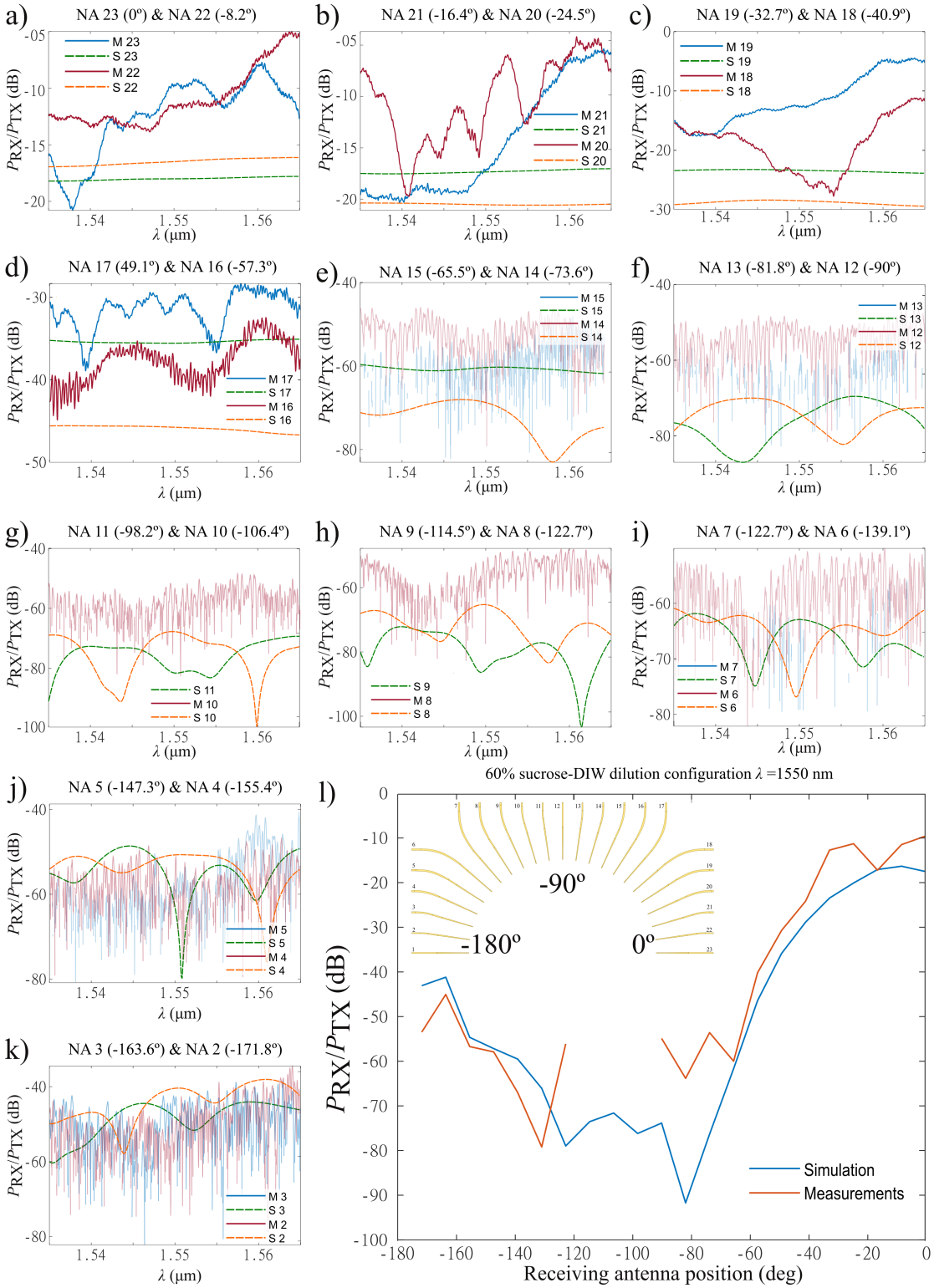

Fig. 3.31 Baseline semicircular device: sucrose-DIW dilution configuration, measurements and simulations. a-k) Comparison of Measurements (M) (gratings compensated) with their equivalent Simulations (S, dashed lines) of the link for different angles, using the NA 1 as the illumination antenna. The legend explains the output port for each line. l) Power efficiency for different ports for measurements and simulations at $\lambda = 1550$ nm.

3.4.4 Tomography results

To conclude this chapter, the attempt to verify the circular algorithm via the fabricated and characterized baseline system is discussed, for two different materials with the same cylinder size. It should be noted that, besides the reduction of the sinogram size to 43 projections with 43 data each, the phase information is not read from the baseline system, which is expected to reduce the quality of the reconstruction. Before checking the reconstruction using the baseline device, we study the reconstruction for a phaseless 43×43 sinogram, both for the 60% sucrose-DIW dilution (Fig. 3.32 b) and the glycerol case (Fig. 3.33 b).

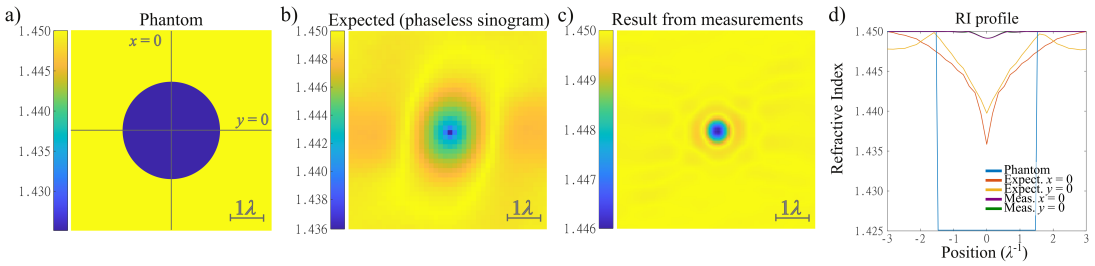

Fig. 3.32 Solution for circular detector tomography for 60% sucrose-DIW dilution with phaseless sinogram a) Phantom, gray lines indicate the place where the profiles in d) are taken. b) Tomogram for a 43×43 sinogram only with absolute information. c) Tomogram, using the measurement data as input. The size of images b) and c) are $6\lambda \times 6\lambda$. b) RI profiles for different solutions.

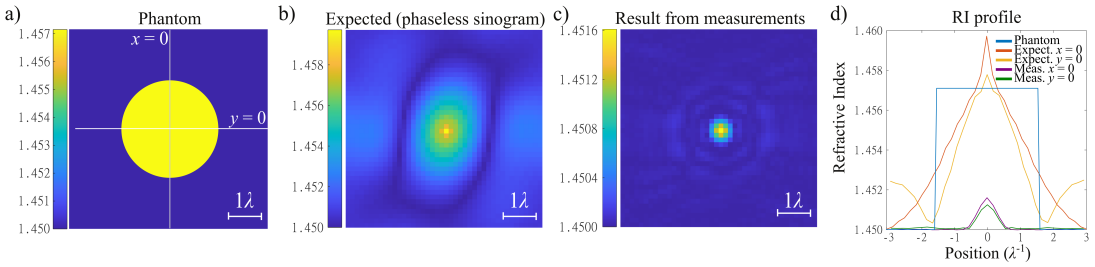

Fig. 3.33 Solution for circular detector tomography for glycerol with phaseless sinogram a) Phantom, gray lines indicate the place where the profiles in d) are taken. b) Tomogram for a 43×43 sinogram only with absolute information. c) Tomogram, using the measurement data as input. The size of images b) and c) are $6\lambda \times 6\lambda$. b) RI profiles for different solutions.

Using as input 43×43 phaseless sinograms in both configurations, we obtain as a result a low-quality reconstruction. Only the profile at $y = 0$ keeps the size of the phantom, and the RI value is only achieved for this profile in the center of the glycerol configuration, as can be seen in Fig. 3.33 d). Nevertheless, these reconstructions are shown for comparison with the result of the tomography process using the measurements discussed above. In the case of the sucrose-DIW dilution, a small cylinder can be appreciated (Fig.

3.32 c), but could be a coincidence, since circular tomography tends to produce circular patterns. Only in the glycerol configuration, the profiles can be slightly related to the phaseless reconstruction (Fig. 3.33 b), since they could represent a scaled version of the same.
In conclusion, this baseline device is not valid for the experimental verification of the optical diffraction tomography for a circular detector on a chip. Some drawbacks that have been appeared may be interfering with this objective.

- On the one hand, the finite character of the studied object could be determinant. The ODT circular algorithm has been implemented for a 2D configuration, while NAs and the object have a third dimension in the z-plane.
- On the other hand, the lack of phase scattering data turns out to be more determinant than expected at first, therefore, the holographic configuration should be studied in the next steps.

Nevertheless, it has been verified in the experimentation of this baseline system, up to four times, that the positions perpendicular to the transmitting antenna did not completely receive the scattered signal. This feature could be exploited by using these positions to place the microfluidic channel that will carry the biological samples. Finally, the number of NAs has to be increased to guarantee higher resolution, which, together with the circular algorithm, allows to obtain clear and useful results for the progress of tomography phase microscope technology. These concerns will be addressed as future work, which is outlined in the last chapter of this thesis.

Chapter 4

Invisibility Passive Devices

4.1 Introduction

Invisibility has been one of the most challenging effects pursued by humankind for centuries. The possibility of hiding objects to the naked eye has recently leaped from science fiction to a feasible reality thanks to the advent of metamaterials [58]. Among a wide range of applications that arises through the exploitation of this kind of materials not available in nature, invisibility cloaks are one of the most high-impact developments [59, 60]. The impressive ability of these devices to hide objects by reducing the scattering they produce has even been experimentally demonstrated [61, 62], boosting the impact of this field of study over the last two decades. Different approaches to the achievement of invisibility have followed in different fields besides optics. For instance, a variety of cloaking devices have been experimentally demonstrated also in acoustics, thermodynamics and mechanics [133].

However, cloaking devices are not perfect. It has been shown that outside the design frequency, realistic cloaks may become significantly visible [63]. Conversely, as technology improves, detecting a cloak at the design frequency might be a challenging task. In most previous studies, the scattering cross section (SCS) has been used as an indicator of the effectiveness of realistic invisibility cloaks [134, 135, 63, 136]. The SCS is a measurement that estimates the total energy scattered by an object (see Appendix C.1). Therefore, the use of this scalar value has the disadvantage that it does not take into account the phase changes produced by the cloak and, in the case of devices without rotational symmetry, it usually considers only one direction of illumination. It is thus reasonable to imagine that a suitable measurement and processing of these missing data would provide more information on the cloak, which, as predicted in [63], should be more sensible to interferometric techniques than to the SCS. Actually, looking back at the origins of invisibility cloaks, we find that one of the first known invisibility devices was conceived as a material undetectable by tomographic techniques [57], which aim at

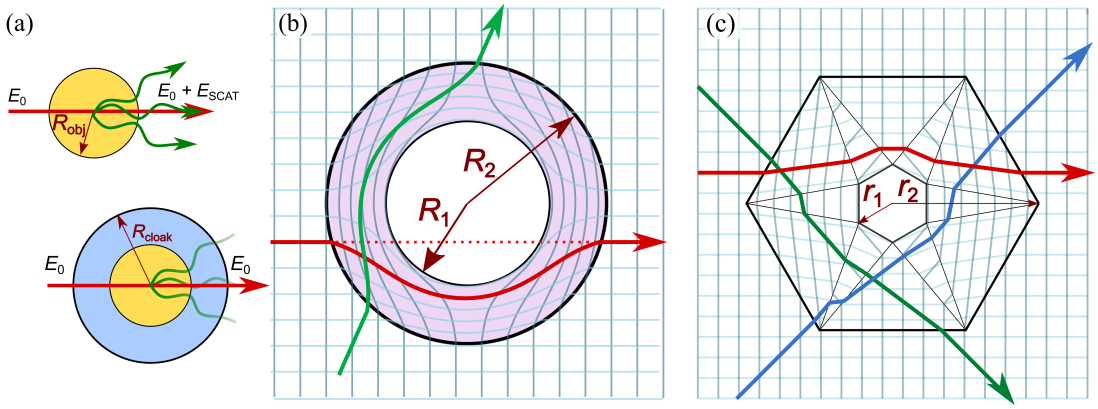

Fig. 4.1 Scheme of the invisibility cloaks concepts. a) Scattering cancellation cloak. b) Optical transformation [60]. c) Polygonal cloak [137].

reconstructing the refractive index (RI) profile of an object by illuminating it from each possible direction, and smartly combining the complex amplitude (magnitude and phase) of the resulting scattered waves [14]. Therefore, diffraction tomography (DT) is expected to detect invisibility devices more accurately, and even has the potential of revealing the shape of the cloak (see Fig. 4.2).

In this thesis, we explore this possibility, keeping the spotlight on studying the behavior of passive cloaks under DT around their design frequency, at which the SCS measurement is less effective and may fail to unveil their presence. Particularly, we analyze three of the most representative kinds of invisibility devices: plasmonic cloaks based on scattering cancellation (SC), blow-up-a-point inhomogeneous cloaks based on transformation optics (TO), and homogeneous polygonal cloaks, also based on TO (see Fig. 4.1). In all cases, we consider realistic material implementations. Additionally, it is worth mentioning that DT is constrained by the diffraction limit, i.e., it is suited for imaging objects with dimensions larger than $\lambda/2$, where λ is the wavelength of light, if both the forward and backward scattering are measured. If the latter is not considered, which is the common situation and the one we will consider in this work, the limit rises to $\lambda/\sqrt{2}$ [66], so we will restrict our study to this class of objects. Moreover, we will focus on two-dimensional (2D) problems for simplicity, although the extension to the three-dimensional case is straightforward. Likewise, we restrict ourselves to TE waves (electric field polarized along the z component and magnetic field contained in the XY plane), with analogous results for TM waves.

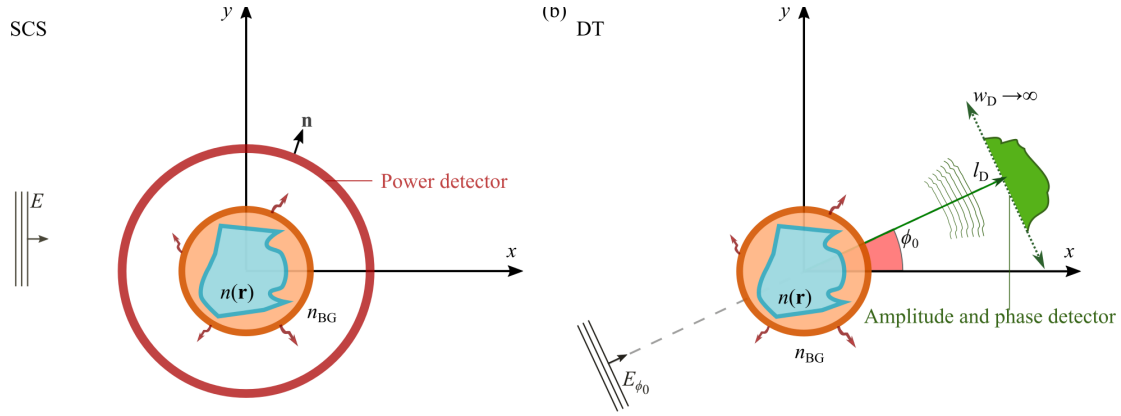

Fig. 4.2 Scheme of the difference between the SCS and DT detection techniques. (a) The SCS is a number related to the total scattered power for a given incident direction. The phase of the scattered field is not taken into account. (b) DT uses different angles of illumination to obtain a 2D refractive index map of the object from the phase and amplitude of the scattered field.

4.2 Scattering Cancellation

The first approach to invisibility cloaking that we will study is scattering cancellation. This technique reduces the scattering produced by a dielectric object with a positive permittivity by covering it with a negative-permittivity coating [134]. SC has also been applied to cloak objects immersed in a uniform static magnetic field [138] or in a diffusive light scattering medium [139]. An interesting application of this type of cloak is the possibility of cloaking a sensor without affecting its capability to measure an incoming signal [140]. Typically, the SC set-up consists of a core-shell spherical or cylindrical structure in which the oppositely signed permittivities of the inner and outer materials are designed to cancel the first-order scattered field at a given frequency (the design frequency) [134].

Note that the SC effect is maximized for objects with electrically small dimensions [134]. Therefore, taking into account the diffraction limit of DT, we will analyze objects with longitudinal dimensions in the interval $[\lambda/\sqrt{2}, 2\lambda]$. Moreover, to satisfy the Born and Rytov approximations usually employed in DT [66, 78], the maximum contrast between the object RI and that of the background is fixed to 5%. In particular, we apply the SC technique to cloak dielectric cylinders of radii $\lambda/2$ and λ, with a RI $n_{\mathrm{OBJ}} = 1.05$, and immersed in a vacuum background with RI $n_{\mathrm{BG}} = 1$. These cloaks have been optimized to minimize the SCS following the procedure described in [141] (see Appendix C.2) . This yields optimum metallic shells with a permittivity $\varepsilon_{\mathrm{S}} = -2.7$ and an outer radius $r_{\mathrm{S}} = 0.508\lambda$ for the $r = \lambda/2$ cylinder and $r_{\mathrm{S}} = 1.0205\lambda$ for the $r = \lambda$ cylinder. As mentioned above, the electric field is assumed to be polarized along the z component

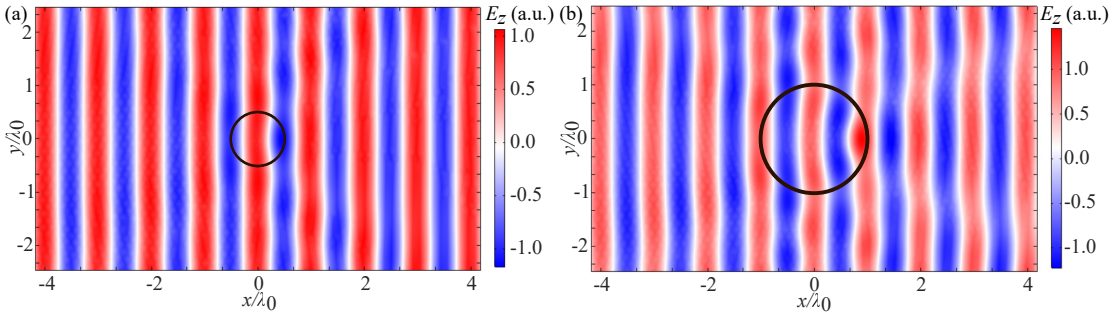

Fig. 4.3 Simulated z component of the electric field resulting from the illumination of an SC-cloaked dielectric cylinder of radius r with an x-directed plane wave. (a) $r = \lambda/2$. (b) $r = \lambda$.

(parallel to the cylinder axis). Figure 4.3 shows the distribution of this field for both studied SC cloaks under plane wave incidence.

To quantify the effectiveness of the cloak in terms of the SCS reduction it attains, we define the relative observability as:

$$O_{\mathrm{SCS}} = \frac{\mathrm{SCS_C}}{\mathrm{SCS_{NC}}}, \tag{4.1}$$

where $\mathrm{SCS_C}$ and $\mathrm{SCS_{NC}}$ are the SCS of the object with and without cloak, respectively. That is, the lower the value of O_{SCS}, the higher the efficiency of the cloak. In the case of the $r = \lambda/2$ cylinder, a value of $O_{\mathrm{SCS}} = 0.7$ is achieved, while for the $r = \lambda$ cylinder, $O_{\mathrm{SCS}} = 0.66$.

On the other hand, to obtain tomographic images (called *tomograms*) of all the cloaks studied in this work, the scattered field is recorded on a detector line (these data are called a *projection*) placed at a distance l_{D} from the set-up center, as shown in Fig. 4.2(b). In the case of the SC cylinders, we set $l_{\mathrm{D}} = 10\lambda$. Ideally, the detector line should be infinite to capture the complete forward scattered wave. In practice, in the simulations we use a finite line length w_{D} such that the missed scattered field is negligible. In the case of the SC cylinders, $w_{\mathrm{D}} = 220\lambda$. A tomogram is built upon the information provided by different projections corresponding to different values of the illumination angle ϕ_0 [see Fig. 4.2(b)]. To ensure a good tomographic quality, we take 250 projections and, at least, record the field of each projection at 8 points per λ (a total of 1760 points in this case).

The obtained tomograms for the non-cloaked cylinders are shown in Fig. 4.4, yielding a good approximation to the original RI profile of the cylinders. It is worth mentioning that the reconstructed RI has a smooth variation instead of the abrupt RI change of the original cylinders, as we can see in Fig. 4.4(a), and Fig. 4.4(c). These results are in line with those expected for the tomography of a centered cylinder [78]. Notably, the RI recovered by the tomogram for the cloaked $r = \lambda/2$ configuration [Fig. 4.4(a)] exhibits a higher variation amplitude than that of the non-cloaked configuration (0.1 with cloak, 0.06 without it). This increment of the RI range is more evident for the $r = \lambda$ cylinder, as

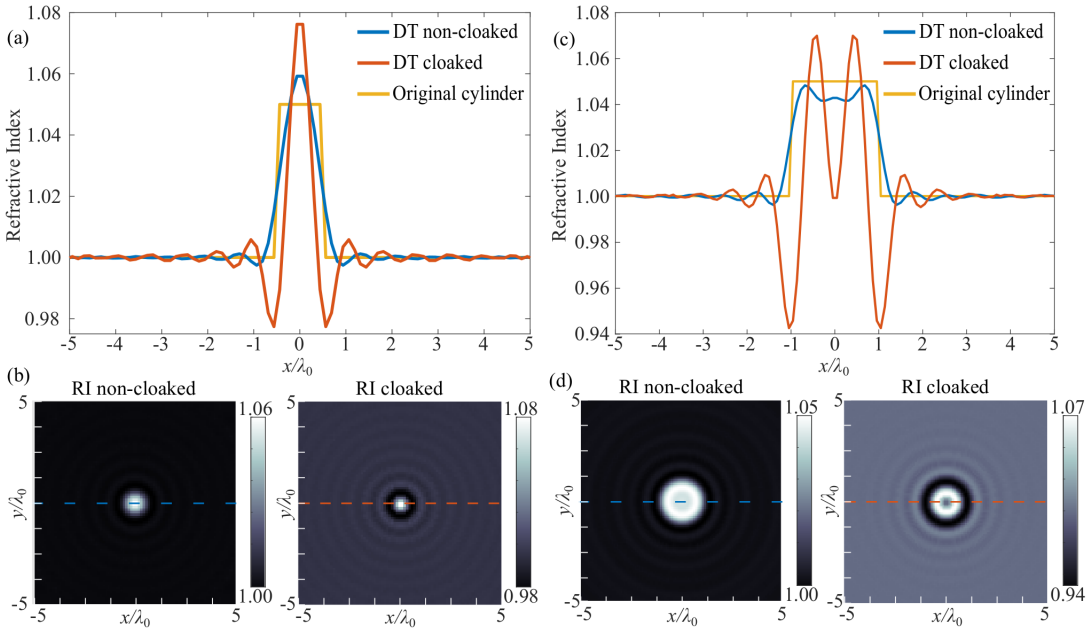

Fig. 4.4 Linear tomography (Rytov approximation) of non-cloaked and cloaked dielectric cylinders of radius $r = \lambda/2$ (a,b) and $r = \lambda$ (c,d). Full tomograms are shown in panels (b) and (d). Panels (a) and (c) show a detail of the RI along the dashed lines depicted in (b) and (d).

can be seen in Fig. 4.4(c). Additionally, in this case, the RI profile shows two lobes instead of one.

Following the work in Ref. [63], it is worth analyzing the behavior of the cloak under DT at different frequencies. For that, the cloak was considered to be made of lossless silver [63], and was modeled by a Drude permittivity $\varepsilon_s = \varepsilon_\infty - f_p^2/f^2$, with a plasma frequency $f_p = 2175$ THz and $\varepsilon_\infty = 5$ [142]. As a consequence, the ideal cloak permittivity is obtained at $f_0 = 783.8$ THz (i.e., $\lambda_0 = 382.7$ nm). To quantify the sensitivity of DT in the detection of a given cloak, we define the presence of an object according to its tomogram as:

$$p = \frac{\sum_{i=1}^{I}\sum_{j=1}^{J}|n_{\mathrm{DT}}(i,j) - n_{\mathrm{BG}}|}{IJ}, \tag{4.2}$$

where $n_{\mathrm{DT}}(i,j)$ is the RI at the pixel i,j of a tomogram of size $I \times J$. This is similar to the way in which the error of tomographic techniques is tested [78]. As in the case of the SCS, the effect of the cloak is quantified as the presence of the cloaked object divided by the presence of the bare object, i.e.:

$$O_{\mathrm{DT}} = \frac{p_{\mathrm{C}}}{p_{\mathrm{NC}}}. \tag{4.3}$$

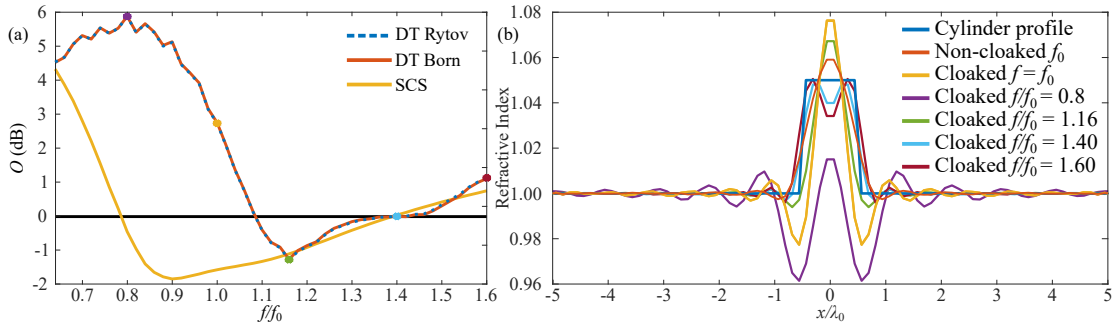

Fig. 4.5 (a) Comparison between the relative observability obtained via SCS and DT for an SC-cloaked cylinder with $r = \lambda_0/2$ and $n_{\mathrm{OBJ}} = 1.05$ as a function of frequency. (b) Corresponding RI along a line passing through the center of the cylinder as retrieved via DT for some selected frequencies [highlighted with colored points in (a)].

The detection ability of both measurement methods (SCS and DT) is shown in Fig. 4.5(a) for the $r = \lambda_0/2$ cylinder. The corresponding tomogram profiles along a line passing through the center of the cloak are shown in Fig. 4.5(b) for some selected frequencies.

As expected, O_{SCS} shows a local minimum close to $f = f_0$, since f_0 is the design frequency. As noted in Ref. [63], there is a frequency range around f_0 for which the cloak reduces the scattering produced by the concealed object (that is, $O_{\mathrm{SCS}} < 1$ or, equivalently, $O_{\mathrm{SCS}} < 0$ dB), while the SCS is higher for the cloaked object in the rest of the spectrum ($f < 0.8 f_0$ and $f > 1.4 f_0$ in our case), as can be seen in Fig. 4.5(a). This corresponds to the values greater than 0 dB in this figure, which represent the frequencies at which the cloak not only fails at hiding the object, but enhances its presence, making it more detectable. Remarkably, in the eyes of DT, the presence of the cloaked system is almost always greater than that of the non-cloaked one in the studied band, even at the frequencies for which the cloak reduces the object SCS. Additionally, we have $O_{\mathrm{DT}} \geq O_{\mathrm{SCS}}$, so we conclude that DT will be more effective in discovering objects hidden by SC cloaks.

Besides allowing a presence measurement, DT provides information on the apparent shape of the cloaked object. In the tomograms of the studied cylinders, they appear to have a smaller radius and a larger RI variation than their bare counterparts (Fig. 4.4). Consequently, we ask ourselves whether it would be possible to take advantage of this apparent shrinking, which suggests that covering small dielectric particles with SC coatings may facilitate their differentiation when being closely packed. To study this possibility, we analyze a new configuration consisting of two kissing cloaked cylinders ($r = \lambda$, $n_{\mathrm{OBJ}} = 1.01$), immersed in a vacuum background ($n_{\mathrm{BG}} = 1$) and covered by optimized shells with $\varepsilon_S = -2$ and $r_S = 1.0049\lambda$. The simulation of the corresponding electric field is shown in Fig. 4.6(a). Tomograms of this cylinder arrangement are obtained both with and without SC shells (we use 180 projections). Very similar results are obtained for the Born and Rytov approximations. The tomograms for the latter are shown in Fig. 4.6(b), from

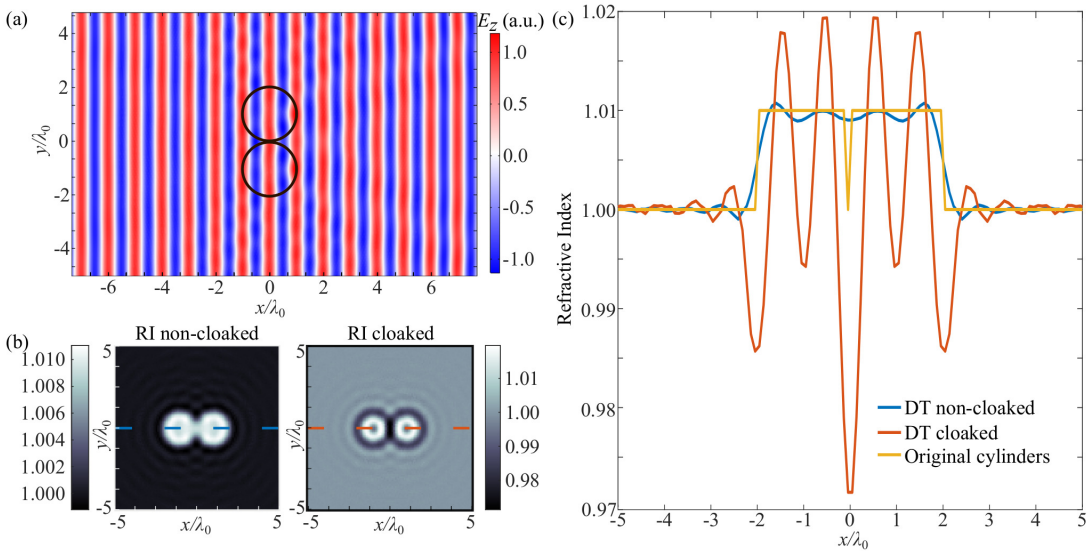

Fig. 4.6 (a) Simulated z component of the electric field resulting from the illumination of two SC-cloaked cylinders ($r = \lambda$) with an x-directed plane wave. (b) Tomograms of the non-cloaked and cloaked cylinders obtained via DT (Rytov approximation). (c) Detail of the RI along the dashed lines depicted in (b).

which we observe that the bare cylinders are hardly distinguishable, and can be mistaken for a single object [they appear as a cylinder of radius 2λ along the central line, as can be seen in Fig. 4.6(c)]. On the contrary, the tomogram of the cloaked cylinders shows two clearly separate profiles, as seen in Fig. 4.6(b), even though they are touching each other, which is a remarkable feature. This fact, combined with the enhanced range between the minimum and maximum RI values, provides a notable advantage in the recognition of closely packed objects, which may find application, for instance, in particle counting or bioimaging.

4.3 Transformation Optics

A more sophisticated passive cloaking technique that can remove scattering at all orders is based on transformation optics [143, 60]. With this method, a given region of space is hidden by redirecting the illuminating wave around it, avoiding any light absorption or scattering. The rays traversing the cloak bypass the concealed region and turn back to the original path. To study the behavior of this kind of device under DT, we analyze the original 2D cloak proposed in [144], where a cylindrical region of radius R_1 is hidden by a concentric cylindrical shell of radius R_2 (see Fig. 4.7). This cloak requires the following radius-dependent, anisotropic relative permittivity (ε) and permeability (μ)

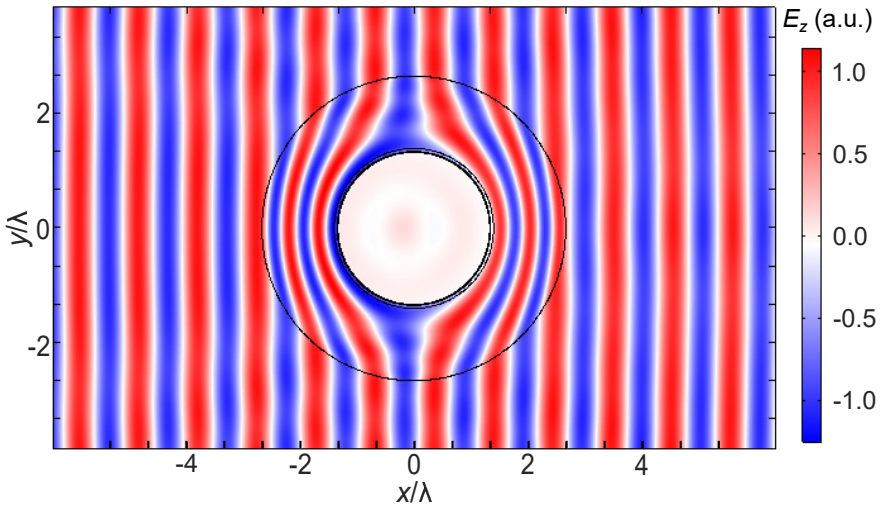

Fig. 4.7 Simulated z component of the electric field resulting from the illumination of a dielectric cylinder covered by a lossless dispersive TO cloak with an x-directed plane wave.

tensor components (in cylindrical coordinates):

$$\begin{aligned} \varepsilon_r = \mu_r &= \frac{r-R_1}{r}, \\ \varepsilon_\phi = \mu_\phi &= \frac{r}{r-R_1}, \\ \varepsilon_z = \mu_z &= \left(\frac{R_2}{R_2-R_1}\right)^2 \frac{r-R_1}{r}. \end{aligned} \tag{4.4}$$

To account for causality and losses, we analyze a realistic version of the cloak in which the permittivity and permeability tensor components with values less than unity (ε_r, μ_r, ε_z, μ_z) are modeled by Drude and Lorentz dispersive relations, respectively [63, 145]:

$$\varepsilon_{r\mathrm{D}}(\mathbf{r}) = \varepsilon_r(\mathbf{r})\left(2 - \frac{f_0^2}{f(f+i\gamma_1)}\right), \tag{4.5}$$

$$\varepsilon_{z\mathrm{D}}(\mathbf{r}) = \varepsilon_z(\mathbf{r})\left(2 - \frac{f_0^2}{f(f+i\gamma_1)}\right), \tag{4.6}$$

$$\mu_{r\mathrm{L}}(\mathbf{r}) = \mu_r(\mathbf{r})\left(1 - \frac{F}{1+(i\gamma_2/f)-(f_0^2/f^2)}\right), \tag{4.7}$$

$$\mu_{z\mathrm{L}}(\mathbf{r}) = \mu_z(\mathbf{r})\left(1 - \frac{F}{1+(i\gamma_2/f)-(f_0^2/f^2)}\right). \tag{4.8}$$

For the components larger than unity (ε_ϕ, μ_ϕ), we assume a non-dispersive dependence [63, 145], given in our case by Eq. (4.4). Following Ref. [145], we take $\gamma_1 = \gamma_2 = \gamma$ and $F = 0.78$. Moreover, to achieve a realistic cloak, we have to consider the particularities of the device in the proximity of its inner boundary ($r = R_1$), in which the components of ε and μ either become infinity or zero. A multilayer cloak with truncated values has

been conceived to solve these issues. Complete information about the used model can be found in the Appendix C.3.

To validate this TO device, we simulate its response when cloaking a dielectric disk of radius $r_D = R_1$ and with a refractive index $n_{OBJ} = 1.04$. A design frequency $f_0 = 193.55$ THz (corresponding to a wavelength $\lambda_0 = 1.55\ \mu m$) is chosen, and the dimensions of the cloak are taken to be $R_1 = 2\ \mu$m and $R_2 = 2R_1$. The simulation of the electric field at f_0 for this configuration is shown in Fig. 4.7.

To compare the detection sensibility of the SCS and DT approaches, we study the frequency range from $0.98 f_0$ to $1.016 f_0$, initially considering a lossless material ($\gamma = 0$). We take 1000 projections over a detector with a length $w_D = 100\lambda_0$ and sample the field of each projection at 1000 points. The tomogram of the uncloaked object is depicted in Fig. 4.8(b), which, as seen in Fig. 4.8(c), exhibits the typical ripple that arises when tomography is applied over a large circular object [78]. In line with the results reported in [145] and [63], Fig. 4.8 shows that the curve representing O_{SCS} as a function of frequency has a V shape, with a spectral region around f_0 where the SCS of the cloaked configurations is lower than that produced by the bare object. Beyond these limits, the cloaked object scatters more energy than the bare one [values greater than 0 dB in Fig. 4.8(a)]. Although the device was designed to have ideal parameters at f_0, the minimum of O_{SCS} is achieved at $f = 0.998 f_0$. This slight change may be due to the truncated values used for modeling the cloak, as well as to the numerical error introduced by the simulation software.

The relative observability obtained with DT is also depicted in Fig. 4.8(a), showing a minimum approximately at f_0 and the same trend as the O_{SCS} curve. However, the mentioned low observability region found in the SCS analysis is considerably narrowed when using DT for both the Born and the Rytov approximations. Moreover, $O_{DT} > O_{SCS}$ in almost all the analyzed spectrum (especially a frequencies below f_0), confirming that DT is more sensitive to lossless realistic cloaks than SCS measurements.

To understand this behavior, the Rytov tomograms of the cloaked object at five different frequencies [indicated by colored dots in Fig. 4.8(a)] are shown in Fig. 4.8(b). The RI values of these tomograms along a line passing through the center of the cloak are depicted in Fig. 4.8(c). The Born approximation gives similar results, which are not shown. The effect of the cloak in the scattered field at the frequency for which O_{DT} reaches its lowest value [yellow line in Fig. 4.8(c)] gives rise to a tomogram that corresponds to a thinner object than the original one (as in the SC case) and with RI values below n_{BG}. As a consequence, while the presence of the cloaked object is quite reduced with respect to that of the uncloaked object, this makes $O_{DT} > O_{SCS}$ at f_0. As might be expected, the detection is more precise at frequencies different from f_0. In particular, the tomograms associated with the other four frequencies show a variation of the RI spanning a circular region with approximately the same size as the cloak, thus providing information on

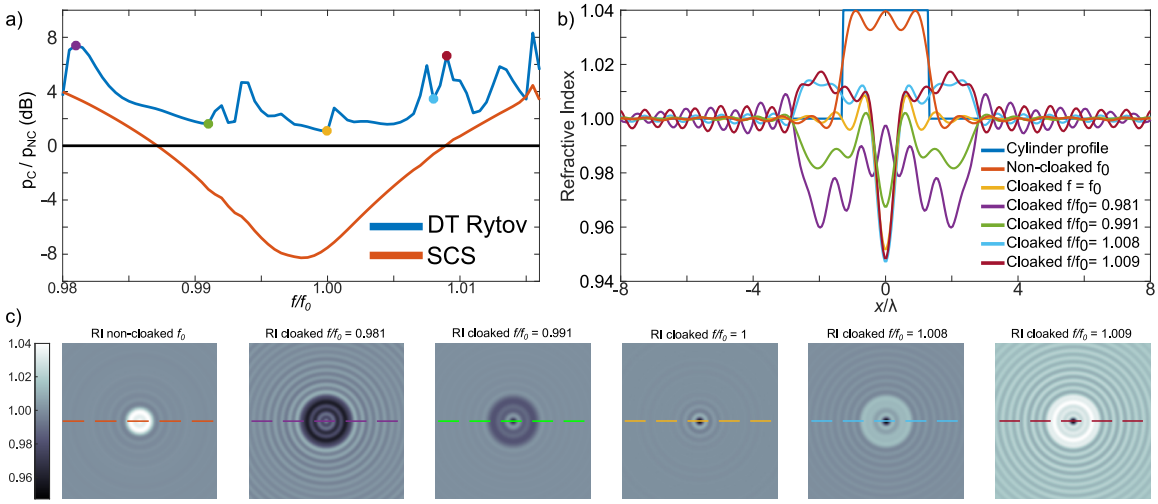

Fig. 4.8 (a) Comparison between the relative observability of a TO-cloaked dielectric cylinder obtained via SCS and DT (Rytov approximation). (b) Tomograms associated with the non-cloaked cylinder and the cloaked cylinder for different frequencies [corresponding to the color dots in (a)]. The size of the tomograms is $16\lambda_0 \times 16\lambda_0$ (c) Detail of the RI along the dashed lines depicted in (b).

the shape of the device [see Figs. 4.8(b) and 4.8(c)]. In addition to these variations, a concentric ripple of the RI is observed for the frequencies that are farther from f_0, i.e., $f = 0.989 f_0$ (purple line) and $f = 1.012 f_0$ (magenta line), which results in higher observability values.

The Drude and Lorentz approximations used to model the cloak also allow us to study the impact of losses in the detection. To this end, we relate γ to the design frequency as follows:

$$\gamma = 10^{o} f_0, \tag{4.9}$$

where o is termed the loss order. A high value of o will be related to a high value of loss. We sweep the value of o from -3.5 to 1.5 (keeping the frequency constant at f_0) and show the corresponding observability in Fig. 4.9. For low losses, the results correspond to the values in Fig. 4.8 at $f = f_0$. However, the SCS becomes more sensitive than DT for $o > -1.9$. Interestingly, the maximum values of the observability are achieved around $o = -1$. For $o > 1$, the observability associated with the SCS and DT methods has similar values.

4.4 Transformation optics - polygonal cloak

The practical implementation of the ideal TO invisibility cloak studied in the previous section is challenging due to the inhomogeneous character of the ε and μ tensors, as well

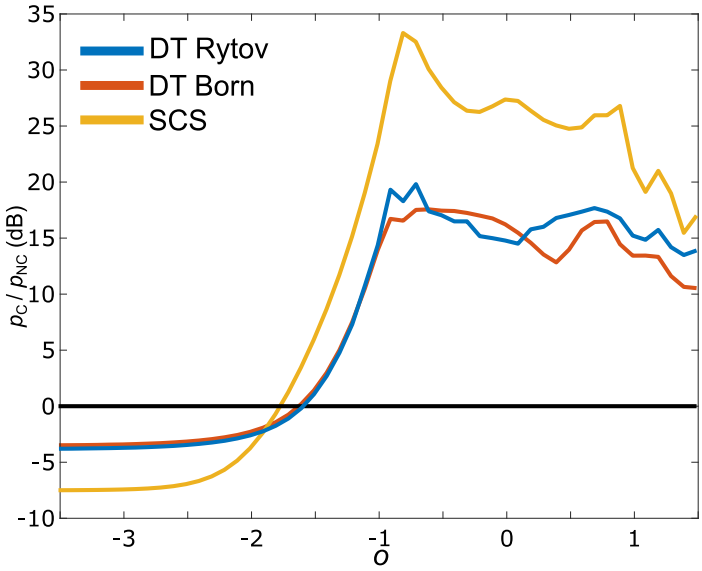

Fig. 4.9 Comparison between the relative observability obtained via SCS and the Born and Rytov approximations of DT as a function of the loss order.

as to the extreme values of these tensors near the inner limits of the cloak. One way to address this drawback is to apply a piecewise linear transformation to a polygonal region divided into segments, which results in a homogeneous device with finite constitutive parameters [137]. A simplified version of this cloak can even be implemented with natural birefringent crystals. Moreover, the study of this kind of device allows us to test the DT detection ability for cloaks with non-cylindrical shapes. In particular, here we consider a hexagonal cloak and a square cloak following the transformations in [137] and [146], respectively. Details on these transformations and on the corresponding parameters can be found in the Appendix C.4 and C.5. In the case of the hexagonal cloak, the employed dimensions are $r_2 = 4.8\lambda$, $r_1 = r_2/3$, and $r_0 = 0.03\lambda$. The response of this cloak under a TE plane wave is shown in Fig. 4.10(a,b) for two different angles of illumination (0 rad and $\pi/6$ rad). As for the square cloak, the inner and outer square boundaries have a side length of 2λ and 8.5λ, respectively. A simulation of its behavior for 0 rad and $\pi/4$ rad illumination angles are shown in Fig. 4.10(c,d).

To analyze the behavior of the considered polygonal cloaks under the SCS and DT paradigms, a hexagon and a square with a refractive index $n_{\mathrm{OBJ}} = 1.05$, have been placed inside the cloaks ($n_{\mathrm{BG}} = 1$). In the case of the hexagonal cloak, the hidden hexagonal object has a radius r_1 and the hidden square has a side length r_1. In the case of the square cloak, the hidden hexagon has a radius of $r = 1.02\lambda$. Through this study, we have verified that, although polygonal invisibility devices work well for any angle of illumination, their performance has a slight angle dependence by construction (the region of virtual space that is expanded is not a point, but a finite domain without cylindrical symmetry). For

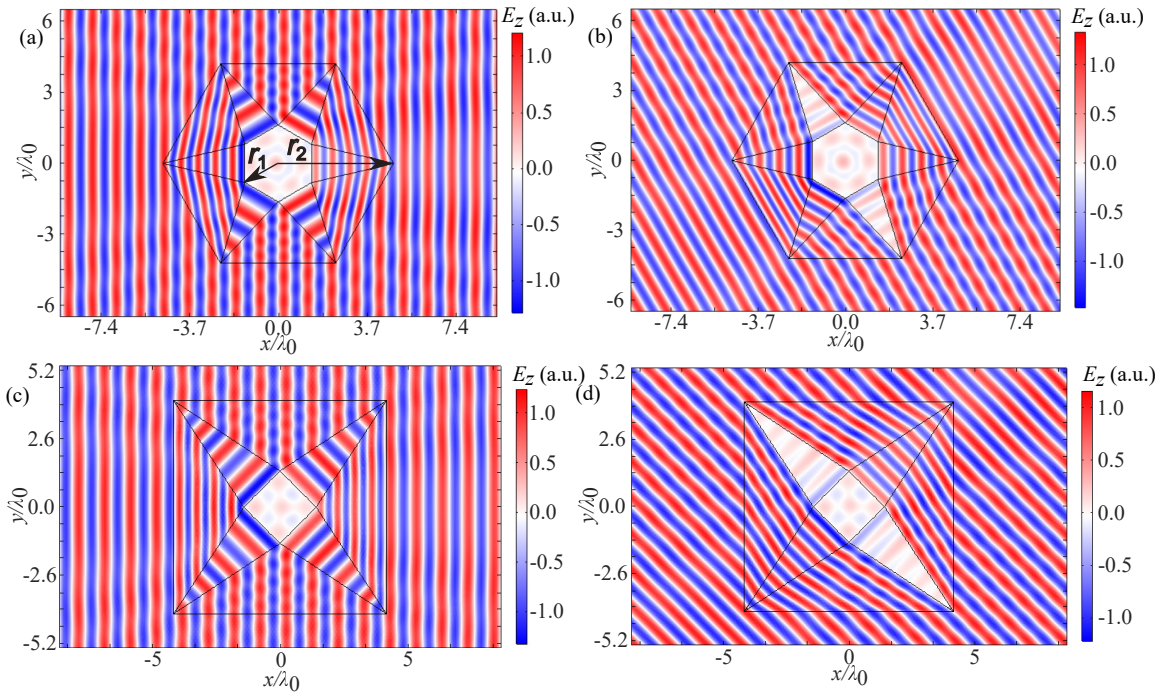

Fig. 4.10 Simulated z component of the electric field resulting from the illumination of different polygonal TO cloaks with an x-directed plane wave. (a) Hexagonal cloak illuminated at an angle of 0 rad (b) Hexagonal cloak illuminated at an angle of $\pi/6$ rad. (c) Square cloak illuminated at an angle of 0 rad (d) Square cloak illuminated at an angle of $\pi/4$ rad.

instance, when the hidden object is the hexagon, O_{SCS} varies from 0.22 in the worst case (angle of illumination of $\pi/6$ rad) to 0.19 when the illumination angle is 0 rad. The SCS ratios for the rest of the cases are gathered in Table 4.1. In all cases, the SCS is significantly reduced, especially by the square cloak.

Cloak	Object	O_{SCS}	O_{DT}
H	H	0.22 - 0.19	0.74
H	S	0.52 - 0.47	1.69
S	H	0.40 - 0.18	1.51
S	S	0.13 - 0.05	0.81

Table 4.1 SCS and DT relative observability for each cloak-object combination. H: Hexagonal, S: Square

The same analysis is now repeated using DT under the Rytov approximation. The tomograms of the two considered bare objects are shown in Fig. 4.11(a) and are used as a reference. The tomograms of the different cloak-object combinations can be seen in Fig. 4.11(b) and 4.11(c). The values of O_{DT} for each case are shown in Table 4.1. As

seen, the relative observability associated with the DT approach is always significantly higher than that associated with the SCS method, being higher than unity in some cases (meaning that the cloak enhances the presence of the object in the eyes of tomography).

In addition, the tomograms of Fig. 4.11 evidence the imaging ability of DT for non-cylindrical cloaks. First, they show a clear correspondence between the size of the retrieved index profile and the outer boundaries of both cloaks. Second, the tomograms possess the same symmetries as the cloaks, as can be seen in Fig. 4.11(b,c). Hence, although the hidden objects are not unmasked by the tomograms, the latter provide important information on the cloaking device, revealing its presence. This means that, while small changes in the scattered energy as a function of the illumination angle do not compromise the cloak performance in terms of SCS (with low values of O_{SCS} well below unity in all cases), they are magnified by DT due to the smart combination of the measured complex field at different angles. Therefore, the high values of O_{DT}, together with the ability of DT to determine the shape of the cloak, makes this technique a much better candidate for the identification of this kind of device than the SCS. Furthermore, the most remarkable fact is that this identification has been done at the design frequency of the cloak, i.e., for the exact ideal parameters of the device. It is for this reason that we have not carried out a frequency sweep to analyze the spectral dependence of the observability in this case, although one would expect an increment in the values of this parameter as moving away from f_0.

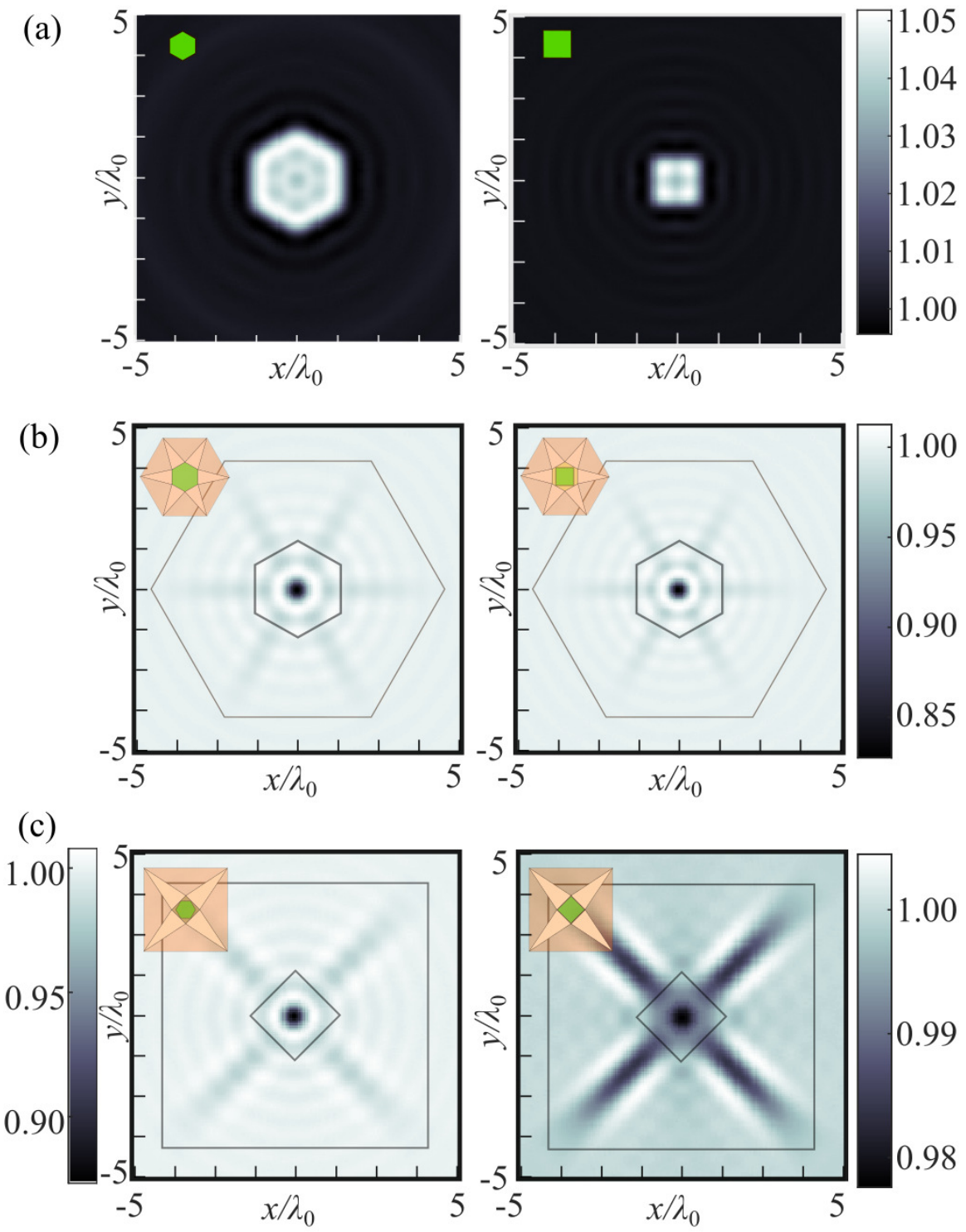

Fig. 4.11 Tomograms (Rytov approximation) of: (a) a bare hexagon and a bare square. (b) Each of these objects hidden within a hexagonal cloak and (c) within a square cloak. The boundaries of the cloaks are depicted as a reference. The schematic insets represent the cloak (pink) and the hidden object (green) for each configuration.

Chapter 5

Conclusions and discussion

Throughout this chapter, we discuss the results obtained in the thesis. Conclusions are drawn based on the initial objectives, and the lines of future work are detailed. Finally, some brief personal observations will conclude the main work of this thesis.

5.1 General discussion of the results

5.1.1 ODT Algorithms

The concepts of *sinogram* and *projection* have been presented via the study and application of the Inverse Radon Transform. From here, the study and implementation of the 2D ODT algorithms based on the Helmholtz equation have been achieved. First, we have obtained successful results for the three phantoms suggested in this essay with the implementation based on linear detectors. To achieve this, we have developed a system to get the sinogram for any RI model with the COMSOL MULTIPHYSICS software. This system has been validated through the obtained tomograms, since they match the input RI models. Later, the implementation for circular detectors has given excellent results for the Shepp-Logan adapted phantom, a benchmark mask used in the verification of most tomography algorithms. However, the implementation of the algorithm for biological elements such as cells has room for improvement.
The chapter concludes with a comparison between both ODT techniques. On the one hand, circular detector tomography can resolve small areas in the Shepp-Logan mask that cannot be seen via the linear detector ODT, even by using more detector points per λ. On the other hand, the NTC logo mask with a small size factor is poorly reconstructed by applying linear detector tomography, while its complex resolution is resolved via circular detector ODT.

5.1.2 Tomographic Phase Microscopy via LoC technology

The contribution of TPM technology to society, as well as the scientific breakthroughs it has generated, are unquestionable. Nevertheless, the limitations of this technology (expensive, heavy, and bulky systems) led us to pursue the idea of fully integrated on-chip TPM, a challenging concept that could be a milestone in this field. A list of objectives has been presented to achieve this purpose, and three of them have been addressed in this thesis.

SNOM Measurements

Firstly, silicon nanoantennas have been chosen as the elementary component of the on-chip TPM device, since a NA could illuminate the object under study, and an array of these NAs could extract the scattering produced by the studied object. These NAs have been experimentally verified previously, although their near-field behavior is tested in this thesis for the first time. We have experimentally demonstrated antenna-to-antenna propagation via SNOM at 0.1 μm of vertical distance. The field concentration between NA directors has also been measured at a height of 0.4 μm. Both characterizations are in good agreement with the simulations. This first approach to the near-field characterization in radiating elements at the nanoscale will pave the way for the analysis of other advanced integrated photonic devices such as lab-on-a-chip sensors or wireless on-chip networks.

First cross-port circular design

The next step in the pursuit of on-chip TPM is the modeling, fabrication, and characterization of the first circular cross-port design. The purpose of this device is to verify the possibility of a wireless SOI multi-port device operating with low-directivity NAs (necessary to have a broad wavefront covering the whole sample under study, similar to plane wave illumination), capable of measuring the back-scattered signal. All of these issues have been resolved. On the one hand, NAs without directors have been validated to establish a working link with a greater distance than in the previous 12-port crossing presented in [52]. On the other hand, the input signal has been detected for all orientations, even those greater than 90º, which proves that the back-scattered signal can be captured. With these considerations, the fully studied cross-port circular device is on the way towards the first LoC TPM.

Circular tomography in baseline system

The path to the on-chip TPM device is then divided into two lines. In the first one, a microfluidic channel is the technology considered to place the sample under study sample inside the SOI PIC. The other way is to verify the implementation of the ODT

algorithm for a circular detector through a baseline system. We have considered the second one, in which an axially symmetric object (a cylinder) is chosen to be detected. Since 22 NAs work as the detector in this baseline system, a 43×43 sinogram has been obtained, due to the symmetry of the object under study. Two materials have been considered to test two different scenarios, ethanol and a 60% concentration of sucrose in DIW dilution. Finally, four configurations have been characterized, since a background scenario and a configuration using only DIW have also been considered. Although the measurements are in line with the expected results, the algorithm cannot be verified, since the corresponding tomograms are far from the expected ones. Therefore, the last step taken in this thesis towards achieving on-chip TPM has been unsuccessful, forcing us to further develop the employed ODT algorithm. Particularly, its next version should take into account two issues not addressed so far. On the one hand, the use of NAs introduces an effect not considered in the algorithm, both in the emission and reception of the signal. On the other hand, a two-dimensional version of the algorithm has been implemented, while the experimentally studied object has a finite size in the off-plane dimension, thus representing a three-dimensional problem. In addition to these algorithm concerns, it will be necessary to develop a phase-aware holographic SOI system.
Although the on-chip TPM objective has not been attained with this device, its characterization has allowed us to notice an important feature. Specifically, we have found positions in the NAs array at which the field is not well detected due to its low values. This fact can play in our favor, since these positions could be the region to place the OF channel (which will carry/extract the biological samples to/from the SOI device). This would still make it possible to read the forward and backward scattered field by placing the OF channel in this perpendicular area, a necessary condition for tomography based on circular detection.

5.1.3 Invisibility Pasive Devices

The work presented in this dissertation represents the first known approach to the study and detection of realistic invisibility devices via tomography, in line with the original purpose of one of the first devised invisibility cloaks [57], and beyond the broad use of the SCS parameter in the evaluation of the performance of these cloaks.
The behavior of the cloaks based on scattering cancellation first considered in our study turned out to be compromised when they were analyzed with the DT technique. Besides, the results indicate that cloaked objects appear to be shrunk from a tomographic point of view. This suggests that a possible application of scattering cancellation cloaks could be a potential resolution improvement when it comes to imaging small particles, which may help to better understand biological samples. The sensitivity of the DT technique at different spectral regions has been compared with the SCS ability to detect targets, DT

resulting more capable of exposing the presence of an object concealed via a scattering cancellation cloak.
Regarding lossless realistic cloaks based on transformation optics, the presence of the cloaked object has been compared to that of the uncloaked one for different frequencies, finding a big difference in terms of sensitivity between the SCS and DT approaches. On the one hand, the frequency band at which the object possesses a low observability under SCS is reduced for the DT technique. On the other hand, at the frequencies for which the cloaked object scatters more energy than the uncloaked one is better detected via a DT analysis. This result corroborates that lossless invisibility cloaks based on transformation optics will be a more detectable target for tomographic systems than for SCS meters. On the contrary, for lossy cloaks with losses higher than $10^{-1.6} f_0$, tomography has not proven to be a more efficient method for object detection than the SCS at the design frequency.
Finally, polygonal invisibility devices have been verified to do a good job in hiding objects at their design frequency as far as the SCS parameter is concerned. However, DT is able to image the shape of polygonal cloaks and can therefore reveal their presence, compromising their effectiveness. A remarkable point of this disclosure lies in the fact that only the field scattered at the design frequency for different angles of illumination is needed by DT to unmask the hidden target, instead of a pulse composed of different frequencies, as used in previous studies.

5.2 Main conclusions

To conclude the analysis of the results of this thesis, we compare the initial objectives with those finally achieved . Figure 5.1 shows the achievements in a darker color, while the objectives that become future tasks remain with a lighter color, and are explained in the following section of this chapter.

Regarding optical diffraction tomography (central path in Fig. 5.1), the algorithms based on linear and circular detectors have been implemented correctly, as evidenced by the satisfactory achieved results. Moreover, circular detector algorithms provide a better resolution in two different scenarios. On the one hand, a complex input with different RI values and shapes (the Shepp-Logan phantom) verifies this resolution improvement. On the other hand, we can distinguish shapes $\lambda/4$ apart using the mask formed by the NTC logo. Up to date, circular algorithms have only been tested using a concentric axial system in the literature [86]. To our knowledge, our study is the first that compares the resolution of linear and circular ODT schemes and especially in the context of TPM, showing that circular ones could improve the resolution of the ubiquitous linear detectors. As a result, a manuscript is being prepared for publication in a peer-reviewed journal.

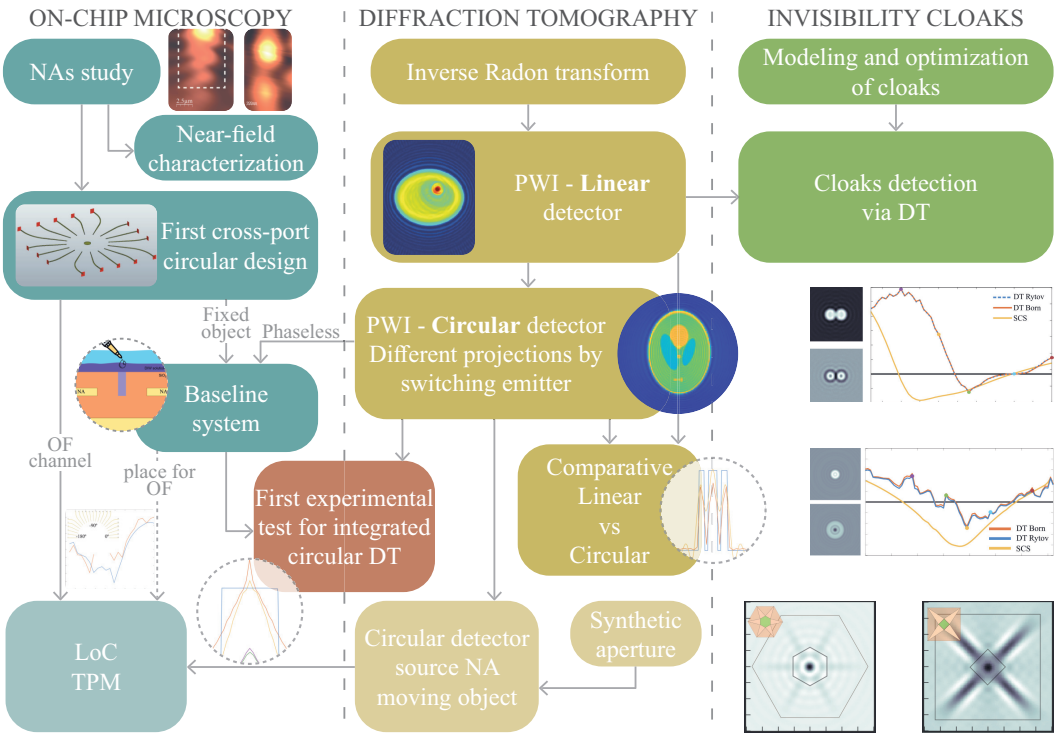

Fig. 5.1 Thesis objectives. (NAs: Nanoantennas, PWI: Plane wave illumination, DT: Diffraction Tomography, OF: Opto-fluidic, TPM: Tomographic Phase Microscopy).

Concerning the two applications of these algorithms, we found a roadblock in the path to on-chip TPM when we attempted to verify the integrated circular tomography in a LoC. This is due to two issues: the fact that NAs introduce an effect not considered in the algorithm and the fact that the 3D nature of the studied object has not been taken into account. The other approach to achieve the ultimate goal of a fully integrated on-chip microscope (flowing sample TPM) is detailed in the following section. On the other hand, the first steps along this path have been completed: the experimental study of the near-field behavior of NAs via SNOM measurements, and the verification of a first wireless optical cross-port for TPM. Nevertheless, the decisive step to achieve on-chip tomography still remains to be taken.

Finally, concerning the second application of ODT, the study on the detection of three kinds of invisibility cloaks has been completed. We have established that ODT can be used as a more suitable tool for the detection of passive invisibility devices, as can be inferred from the results. This is because we have demonstrated that ODT is more sensitive than the SCS in the detection of scattering cancellation and transformation optics cloaks at the design frequency of these devices. This could be exploited for the design of new cloaks and devices that attempt to mislead and provide a false result when analyzed under tomography. Moreover, ODT can reveal the shape and the size of realistic cloaks based

on transformation optics, which is a remarkable finding. The possibility of detecting the presence of passive invisibility devices offered by DT opens up a range of potential benefits in a variety of fields, from electromagnetic studies in science to bioimaging and warfare applications in technology.

5.3 Future work

In this section, we develop the work that we will have to perform to finalize the objectives initially proposed in this thesis. Since the application of ODT algorithms to the **detection of invisibility cloaks** has been completed, the work to be done in this line is to carry out the revisions of the corresponding manuscript according to its publication process. Afterward, we will be able to devise new invisibility cloaks that can be hidden even for the new diffraction tomography benchmark presented in this thesis. Therefore, the future work to be developed is based primarily on the ODT and LoC TMP lines, which are related at this stage of the study.

5.3.1 Diffraction Tomography

Plain Wave Illumination

The comparison between the linear and circular detector tomography will be present in a manuscript. Moreover, we comment some improvements that can be made to the algorithms already implemented. For example, an **autofocus** function can be implemented in the tomography algorithm for linear detectors, as explained in [83]. This function will not be relevant for the application of the algorithm to study invisibility cloaks, since the tomograms of the uncloaked objects match the RI input profile. Nevertheless, this autofocus advance could improve the result for biological specimens, and perhaps the algorithm for tomography with circular detector may also benefit from this upgrade.

Regarding the **circular detector** algorithm, the results show a constant offset out of the phantom region in the tomograms, and issue to be solved. In addition, the implementation without the far-field approximation should be studied to achieve a general solution.

Concerning the impasse reached when we tried to verify the phaseless algorithm in the baseline system, an important task arises: ODT algorithms must **consider** the effect introduced by the **input and outputs NAs**, as well as 3D character of the device under study. Sinograms generated in the 2D framework of the COMSOL software have helped us to test the algorithms, but from now on, we must use simulations performed in a 3D

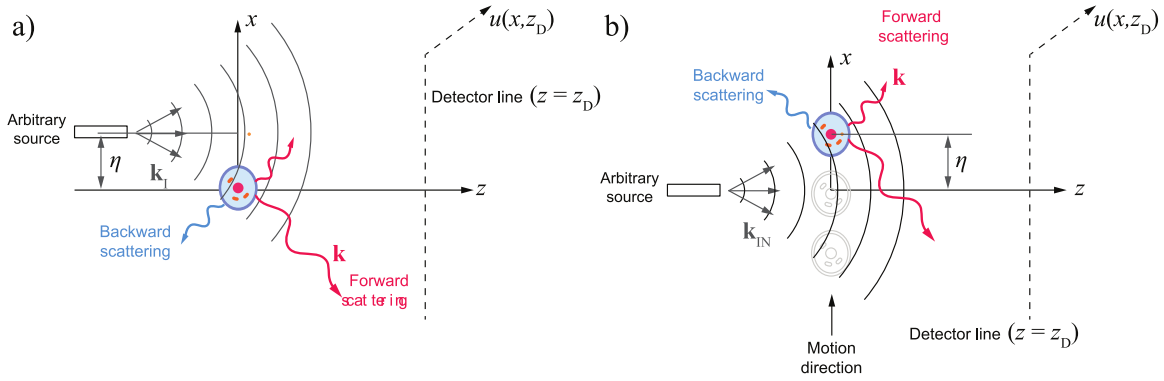

Fig. 5.2 a) Synthetic aperture tomography with a moving source. b) Tomography of a moving sample.

scenario. Once these issues have been incorporated into the algorithm, we will consider the last step to be taken in the line of ODT objectives, as we will see below.

Synthetic Aperture

Previous implementations have been performed considering that the studied sample is illuminated by a plane wave, while the object (or the measure system) is rotating to get the different illumination angles to form the sinogram. Synthetic aperture (SA) algorithms have to be studied and implemented to move towards the final algorithm. A point source is applied in these algorithms, and the different projections are achieved moving the source or the studied sample, resulting in a linogram [1].

First, the algorithm can be implemented for mobile sources (see Fig. 5.2 a), following the steps described in [148]. In this case, the Fourier Transform of the scattered field $u(x,z)$ is related to the object function of the sample as follows:

$$\hat{U}_{\mathrm{B}\phi}(k_x, z_\mathrm{D}; k_{\mathrm{I}x}) = i\sqrt{\frac{\pi}{2}}\hat{A}(k_{\mathrm{I}x})\hat{F}(\mathbf{k}-\mathbf{k}_\mathrm{I})\frac{1}{k_z}e^{ik_z z_\mathrm{D}}. \tag{5.1}$$

Once we have implemented this scenario, we can move on to tomography with an object moving longitudinally (see Fig. 5.2 b), as is the case that we will have within the TPM on-chip system, but solving it first for a linear detector. After that, we will be ready to address the last objective of the ODT line: The development and implementation of an ODT algorithm for a circular detector, considering the effects of NAs as point source and detectors, obtaining the different projections thanks to the longitudinal displacement of the sample.

[1] Previously, the points in the collected data form a sinusoidal curve, making the set of projections known as a sinogram. For SA diffraction tomography, the points fall on a straight line, which results in the set of projections being called a linogram [147].

5.3.2 Towards LoC TPM

We will discuss the work to be carried out towards the first tomography microscopy device with LoC technology. Regarding the performed work, it might be interesting to improve the near-field measurements by using a thinner SNOM tip and taking into account the tilt of the SNOM tip. However, the following advances are the most important to achieve the first on-chip TPM.

On-chip wireless photonics platform for visible light

The OWP devised in this thesis uses the silicon NAs as a base element. As explained before, it was developed over silicon-on-insulator (SOI) technology and for telecom wavelengths ($\lambda = 1.55$ μm). However, most TPM microscopes work in the visible spectrum (0.38 μm $< \lambda < 0.78$ μm), since the wavelength limits the best achievable resolution to $\lambda/2$. Moving from telecom to the visible could provide a resolution improvement factor of 3, but Si is opaque for $\lambda < 1$ μm and cannot be used to build PICs in the visible regime. Hence, a visible OWP platform must be based on a different transparent material, which we propose to be silicon nitride (SiN), the material of choice to create PICs for visible light for its broadband low-loss properties, maturity, and CMOS compatibility [149]. The RI of SiN in the visible is ~ 2, while that of Si at $\lambda = 1.55$ μm is 3.45. This change in wavelength ($1.55 \rightarrow 0.5$ μm) and RI ($3.45 \rightarrow 2$) is not trivial and implies that the electromagnetic modes supported by PIC structures (e.g. waveguides) are significantly different in each case. Consequently, the NAs of the existing OWP SOI platform cannot be easily modified to operate in the visible. Therefore, we will create a completely new set of SiN-based NAs that will form the basis of the first visible OWP platform. This ambitious task will have to take into account that the transmitting antenna must have low directivity. Finally, we will seek to mimic the design of silicon-based NAs, and we will finish this task by developing directors for the receiving antennas. The achievement of the first on-chip wireless photonic platform for visible light would be a significant breakthrough in the field of LoC PICs.

Microfluidic channel

To illuminate moving samples, a channel is needed to introduce/extract them into/from the chip. This purpose will be achieved by a microfluidic channel. This task will not be a difficult challenge, since this kind of technology has already been used in the NTC [53]. Two advantages stand out among the main benefits provided by this technology. On the one hand, the moving parts of current TPM setups are eliminated. On the other hand, the use of this OF channel ensures high sample reading throughput.

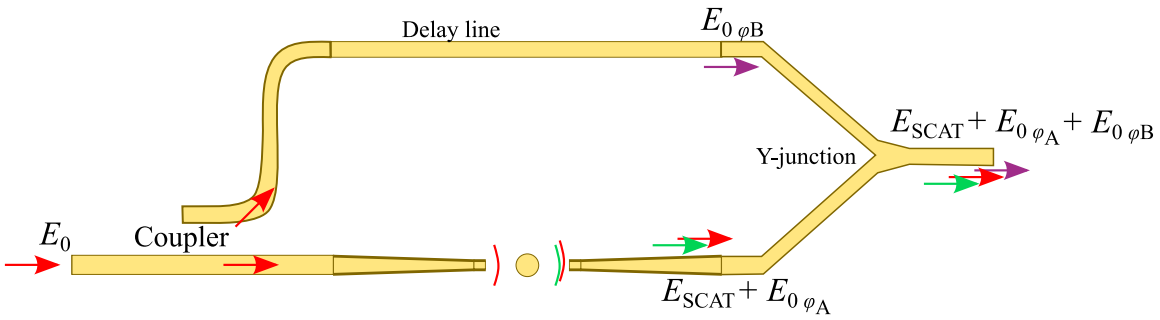

Fig. 5.3 Holographic detector. A directional coupler splits the input signal: one path is carried to the emitter antenna and the other to the delay line. The y-junction combines the scattered field received by the antenna with the delayed input signal.

Holographic detector

The last breakthrough to achieve will be the development of a method to retrieve the phase of the scattered field. For this purpose, we propose to develop the first on-chip holographic detector. As in the studied TPM systems, this implies comparing input and output signals to obtain the phase information, which is essential for tomographic reconstruction. The technologically simplest approach is off-axis interferometry, which exploits spatial modulation and yields a phase map from a single intensity recording [56]. The clear advantage of off-axis methods is their single-shot capability, allowing high-speed imaging, in line with the aforementioned high throughput. To this end, input and output signals could be compared via Y-junctions and directional couplers as shown in Fig. 5.3. This objective must be addressed carefully since the success in obtaining the first integrated TPM on LoC technology will critically depend on the correct retrieval of the scattered field phase.

5.4 Concluding remarks

Broadly speaking, we have only achieved excellent results in two of the three main lines of research in this thesis. On the one hand, we demonstrate the resolution improvement using circular detection tomography. On the other hand, the application of ODT algorithms for the detection of invisibility cloaks has produced remarkable results. However, we have to recognize that the goal of achieving the first fully integrated tomography device through LoC technology has been far from being achieved, although the roadmap has been established and the next steps to be taken are already clear. Despite the large amount of work done in this line, on a personal note, I would like to admit that perhaps a lot of this work has been done in parts that did not require as much attention as it has been given. This is independent of the fact that, undoubtedly, the objective to be pursued was also very ambitious. I recall a recent conversation with my supervisor,

Prof. Javier Martí, in which he commented that science tends to imagine futures that can sometimes seem unrealistic. In this regard, he pointed that the actual work achieved in any project can be considered as a projection of a very ambitious goal. The task of the researcher will be to make this projection as large as possible. As far as the on-chip TPM goal is concerned in this thesis, this projection has been truncated. Nevertheless, I believe that the future work to be done is perfectly defined, which will allow us to reach the device in the near future.

In addition to the responsibility of the researcher, who must work without losing sight of rigor and critical sense, I do not want to end this dissertation without discussing a problem that appears behind the pursuit of excellence. The high speed of production and consumption of today's society has been transferred to science, as broadly explained in the conclusions of [150]. Although it may seem trivial, this accelerated tempo can take a physical toll on the mental health of graduate students [151]. A compilation of different studies published this year concludes with the devastating finding that 24% of doctoral students show symptoms of depression [152]. Moreover, data across Europe consistently show that around 30 - 40 % of researchers are at risk of developing a common psychiatric disorder [153]. Therefore, I consider necessary to listen to all those who recommend seeking help in this regard [154]. Likewise, I would like to remark that universities usually have offices specialized in mental health issues and student support. Personally, the GOPU [2] of the UPV helps me, in addition to the following people, to focus and carry out the work.

I do not wish to duplicate the contents of the acknowledgments section, but, certainly, the countless talks with Dr. Carlos García-Meca and Dr. Sergio Lechago have helped me to focus on my work during these years. As a fruit of one of these conversations, a simile emerged that is worth mentioning. I find similarities between the writing process and the traditional family harvest in the vineyards (perhaps because I grew up in La Mancha). Both tasks may seem the hardest exercises to an outside viewer, however, they should be the most rewarding process. The task of writing is nothing more than the celebration of a job well done. If the hard work has given the fruits of good results, the moment of writing is a sweet task, in which the progress achieved can be finally divulged to the world. Something similar happens in the vineyards, since the pruning and maintenance of plants is an arduous task that is rewarded when the grapes are harvested.

Coming back to the mental-health issues, I also encourage seeking help outside of the academy. In my case, acting (in theater and improv) has helped me to have a balanced mind. On the other hand, I cannot have addressed all the work without enjoying the art of the music [3]. In this regard, I would like to end this thought by pointing out that

[2] Gabinete de Orientación Psicopedagógica Universitaria - Instituto de Ciencias de la Educación (UPV)

[3] A compilation of the songs most listened to in the progress of this thesis can be found on the Spotify playlist called Novel ap. of Optical Diffraction Tomography: On-chip Microscopy and Detection of Invisibility Cloaks

although science undoubtedly helps society, improving and extending our lives, we must not lose sight of those around us, and of culture, which is what really provides value to our existence. Accordingly, I believe there is no better way to express the relationship of science with art than the following:

"Art and science have much more in common than it seems. They both are driven by creativity and curiosity of thinking about things that do not exist yet, and perhaps, for being recognized by others. (...) The freedom of creating something was my motivation, just like a craftsman when carving a handmade wooden figure. After all, we are just trying to understand the world we live in, in the most enjoyable manner possible."

- Luis Torrijos [155]

Appendix A

Tomography phantoms

In this appendix we have collected the phantoms used as inputs in the different implementations of ODT algorithms, in order to have access to them at any time during the reading process, or to be replicated by the reader if desired.

A.1 Cell phantom

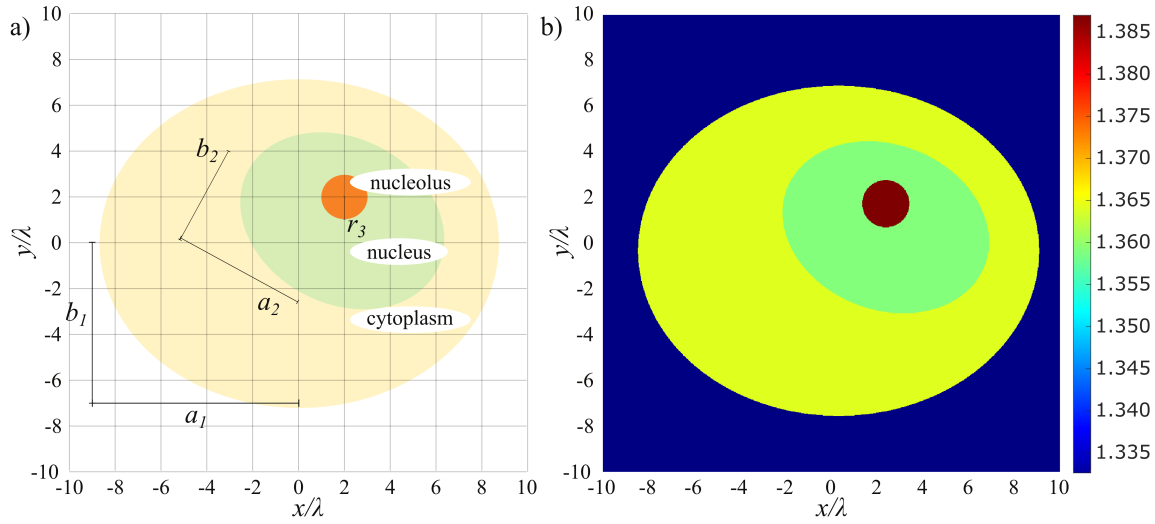

Fig. A.1 Cell model. a) Geometry of the phantom [82]. b) MATLAB representation in colormap *jet*.

The cell phantom used to test the algorithms of this thesis has been the proposed by Müller in [82], whose RI values have been taken considering them as valid for biological specimens. Moreover, the fact that cell nuclei have lower RI than the cytoplasm has been discussed and demonstrated [156, 157]. The schematic draw of the phantom can be found

in figure A.1 a). The cytoplasm has a RI of 1.365, centered in the simulation space, its major axis is $a_1 = 8.5\lambda$, while the minor one is $b_1 = 7\lambda$. The nucleus axes are $a_2 = 4.5\lambda$ and $b_2 = 3.5\lambda$, and it is centered at $(2\lambda, \lambda)$ and rotated 0.5 rad, with a RI of 1.360. The RI of the nucleolus is higher (1.387), and it is positioned at $(2\lambda, 2\lambda)$ with a $r_3 = \lambda$ radius. The colormap used in the MATLAB version of the phantom (Fig. A.1 b) is *jet*, which helps to differentiate the three parts of the cell from the background.

A.2 Shepp-Logan adapted phantom

Introduced in 1974 in the computerized tomography framework, the Shepp-Logan phantom is a broadly used test envisioned to simulate a cross-sectional image of a head [74]. Moreover, this phantom has been used in different diffraction tomography approaches, such as those based on ultrasound [158], or even in advanced imaging techniques such as ankyloscopy [159]. To adapt this phantom to a biological specimen scenario, two parameters allow its adaptation: either by its size relative to the wavelength with the size factor f_S, or by its refractive index using the index factor f_N. Moreover, we change the value of the outer ellipse from its classical value of 1 to a gray level of 0.7, inspired by [148]. This change allows us to reduce the range between maximum and minimum values. We describe the RI for each region of the phantom in table A.1. The intersections between ellipses d-e and d-g count with a variation of RI with the medium of $\triangle n = 0.45 f_N$. The RI variation arises to $\triangle n = 0.8 f_N$ in the space between ellipses e-f. An example for $f_S = 1$ and $f_N = 1$ can be seen in figure A.2. The colormap used in MATLAB is *parula*.

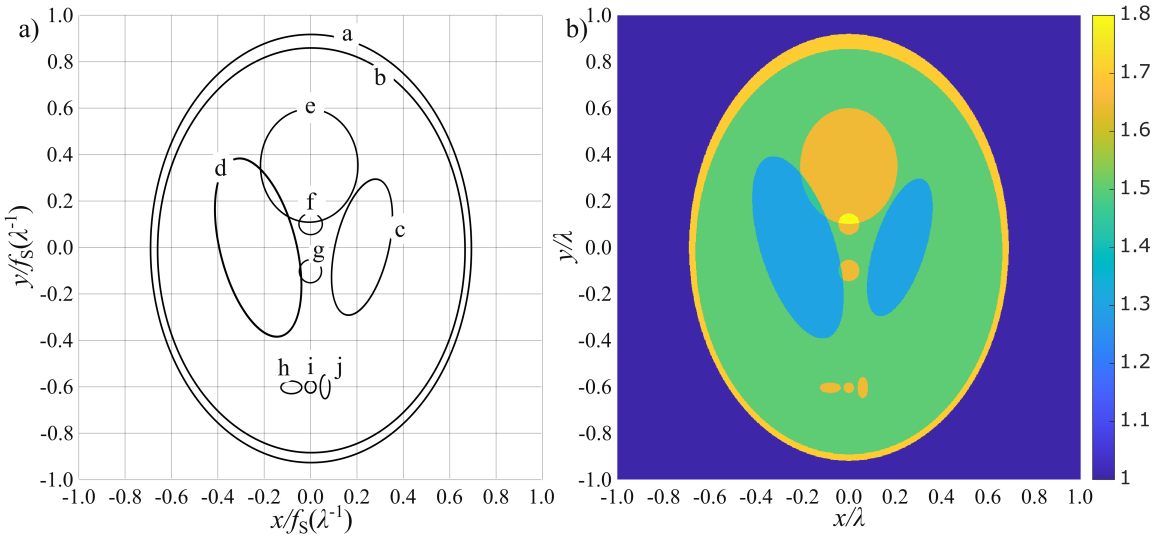

Fig. A.2 Shepp-Logan phantom. a) Geometry of the phantom for $f_S = 1$. b) Values for $f_N = 1$.

Ellipse	Centre	A Major Axis	B Minor axis	Rotation angle (deg)	$n_S - n_M$
a	$(0,0)f_S$	$0.92f_S$	$0.69f_S$	90	$0.7f_N$
b	$(0,-0.0184)f_S$	$0.874f_S$	$0.6624f_S$	90	$0.5f_N$
c	$(0.22,0)f_S$	$0.31f_S$	$0.11f_S$	72	$0.3f_N$
d	$(-0.22,0)f_S$	$0.41f_S$	$0.16f_S$	108	$0.3f_N$
e	$(0,0.35)f_S$	$0.25f_S$	$0.21f_S$	90	$0.45f_N$
f	$(0,0.1)f_S$	$0.046f_S$	$0.046f_S$	0	$0.65f_N$
g	$(0,-0.1)f_S$	$0.046f_S$	$0.046f_S$	0	$0.65f_N$
h	$(-0.080,-0.605)f_S$	$0.046f_S$	$0.023f_S$	0	$0.65f_N$
i	$(0,-0.605)f_S$	$0.023f_S$	$0.023f_S$	0	$0.65f_N$
j	$(0.06,-0.605)f_S$	$0.046f_S$	$0.023f_S$	90	$0.65f_N$

Table A.1 Parameters of the component ellipses of the test image Shepp-Logan adapted. The size parameters are related to f_S, while the RI parameters are related to f_N.

A.3 NTC logo phantom

We look for a phantom with a pair of symmetry axes, with simple shapes and a unique refractive index, to test the resolution of the tomography with a circular detector. Therefore, the old logo of our center covers all these requirements. A size factor f_S is defined like in the previous phantom. A schematic of the mask is shown in figure A.3 a) for a size factor of $f_S = 1$. As can be seen, the radius of the circles is $R = 1.5\lambda f_S$. The central circles are placed at $\triangle x = 2f_S$, while the centers of the upper and lower circles are placed on the same vertical axes for $x = \pm 2\lambda f_S$ and $\triangle y = \pm 4\lambda f_S$. These last four circles are cut off and only take RI value at $y_c < |4.5|\lambda f_S$. An example of this phantom, for a RI of $n_{OBJ} = 1.05$ is shown in Fig. A.3. The colormap used in MATLAB for the colored version is *parula*.

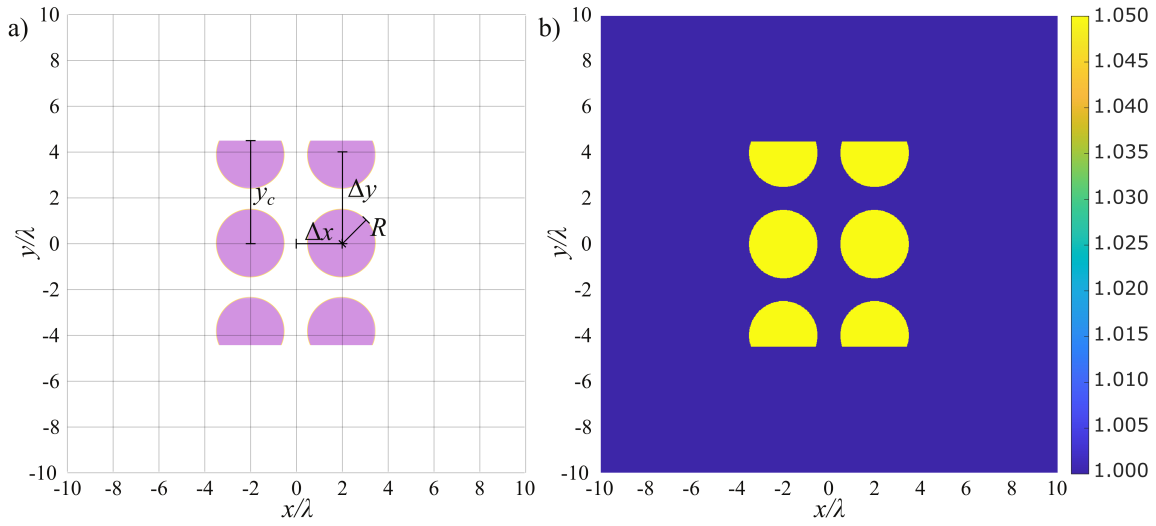

Fig. A.3 NTC logo phantom. a) Geometry for $f_{\mathrm{S}} = 1$ b) Values for $f_{\mathrm{S}} = 1$ and RI $= 1.05$.

Appendix B

Supporting material for tomography

One of the motivations of this thesis is to serve as a manual for the implementation of diffraction tomography algorithms. In this regard, we have decided to include all the detailed steps.

B.1 Variable change in Fourier Slice Theorem

Starting from equation 2.5:

$$\hat{F}(k_{\mathrm{Dx}}, k_v) = \frac{1}{2\pi} \iint f_{\phi_0}(x_{\mathrm{D}}, v) e^{-i(k_{\mathrm{Dx}} x_{\mathrm{D}} + k_v v)} dk_{\mathrm{Dx}} dv \,, \tag{B.1}$$

and considering from the figure 2.1 that

$$x = x_{\mathrm{D}} \cos\phi_0 - v \sin\phi_0 \,, \tag{B.2}$$

$$y = v \cos\phi_0 + x_{\mathrm{D}} \sin\phi_0 \,, \tag{B.3}$$

the variable change $(kx, ky) \rightarrow (k_{\mathrm{Dx}}, \phi_0)$ is easy to be performed:

$$k_x = k_{\mathrm{Dx}} \cos\phi_0 - k_v \sin\phi_0 \,, \tag{B.4}$$

$$k_y = k_{\mathrm{Dx}} \sin\phi_0 + k_v \cos\phi_0 \,, \tag{B.5}$$

besides, the Fourier Slice Theorem is defined for $k_v = 0$, then, the first step to the variable change is trivially achieved as:

$$k_x = k_{\mathrm{Dx}} \cos\phi_0, \;\; k_y = k_{\mathrm{Dx}} \sin\phi_0 \,. \tag{B.6}$$

To finish the variable change, the Jacobian determinant should be calculated:

$$|det(J)| = \left| det\left(\frac{\partial(k_x,k_y)}{\partial(k_{\mathrm{Dx}},\phi_0)}\right)\right| = \begin{vmatrix} \frac{\partial k_x}{\partial k_{\mathrm{Dx}}} & \frac{\partial k_x}{\partial \phi_0} \\ \frac{\partial k_y}{\partial k_{\mathrm{Dx}}} & \frac{\partial k_y}{\partial \phi_0} \end{vmatrix} = \left| \frac{\partial k_x}{\partial k_{\mathrm{Dx}}}\frac{\partial k_y}{\partial \phi_0} - \frac{\partial k_x}{\partial \phi_0}\frac{\partial k_y}{\partial k_{\mathrm{Dx}}} \right| \tag{B.7}$$

$$= |\cos\phi_0 k_{\mathrm{Dx}} \cos\phi_0 - (-\sin\phi_0 k_{\mathrm{Dx}} \sin\phi_0)| \tag{B.8}$$

$$= \left|k_{\mathrm{Dx}}(\cos^2\phi_0 + \sin^2\phi_0)\right| = |k_{\mathrm{Dx}}| \ . \tag{B.9}$$

Finally, the inverse 2D Fourier Transform of the figure function,

$$f(x,y) = \frac{1}{2\pi}\iint \hat{F}(k_x,k_y)e^{i(k_x x + k_y y)}dxdy \ , \tag{B.10}$$

can be adapted to the Fourier Transform for a certain angle $\hat{F}(k_{\mathrm{Dx}})$ by using equations B.9 and B.6:

$$f(x,y) = \frac{1}{2\pi}\int\int_0^{\pi} |k_{\mathrm{Dx}}|\,\hat{F}(k_{\mathrm{Dx}})e^{ik_{\mathrm{Dx}}(x\cos\phi_0 + y\sin\phi_0)}d\phi_0 dk_{\mathrm{Dx}} \ . \tag{B.11}$$

B.2 Reduction of the scattering field in circular boundary

At first, $u(\mathbf{r})$ should be separated in two components, the illumination wave $u_0(\mathbf{r})$ and a scattered wave $u_{\mathrm{s}}(\mathbf{r})$

$$u(\mathbf{r}) = u_0(\mathbf{r}) + u_{\mathrm{s}}(\mathbf{r}) \ . \tag{B.12}$$

Illumination wave satisfies the homogeneous Helmholtz equation (Eq. 2.12), therefore, $o(\mathbf{r})\,|_{u_0(\mathbf{r})} = 0$, and then, we can express the following:

$$(\nabla^2 + k_{\mathrm{M}}^2)u_{\mathrm{s}}(\mathbf{r}) = k_{\mathrm{M}}^2 o(\mathbf{r})u(\mathbf{r}) \ . \tag{B.13}$$

Besides, $e^{-ik\mathbf{sr}}$ satisfies the homogeneous Helmholtz equation:

$$(\nabla^2 + k_{\mathrm{M}}^2)e^{-ik\mathbf{sr}} = 0 \ . \tag{B.14}$$

Multiplying Eq. B.13 by $e^{-ik\mathbf{sr}}$ and Eq. B.14 by $u_{\mathrm{s}}(\mathbf{r})$ and subtracting both resulting equations (Eq. B.15 - Eq. B.16 = Eq. B.17):

$$(\nabla^2 + k_M^2)u_s(\mathbf{r}))e^{-ik\mathbf{sr}} = \quad k_M^2 o(\mathbf{r})u(\mathbf{r})e^{-ik\mathbf{sr}} \tag{B.15}$$

$$-(\nabla^2 e^{-ik\mathbf{sr}} + k_M^2 e^{-ik\mathbf{sr}})u(\mathbf{r}) = \quad 0 \tag{B.16}$$

$$\nabla^2 u_s(\mathbf{r})e^{-ik\mathbf{sr}} + k_M^2 u_s(\mathbf{r})e^{-ik\mathbf{sr}} - \nabla^2 e^{-ik\mathbf{sr}}u(\mathbf{r}) - k_M^2 e^{-ik\mathbf{sr}}u(\mathbf{r}) = \quad k_M^2 o(\mathbf{r})u(\mathbf{r})e^{-ik\mathbf{sr}} \tag{B.17}$$

$$\nabla^2 u_s(\mathbf{r})e^{-ik\mathbf{sr}} - \nabla^2 e^{-ik\mathbf{sr}}u_s(\mathbf{r}) = \quad k_M^2 o(\mathbf{r})u(\mathbf{r})e^{-ik\mathbf{sr}}\,. \tag{B.18}$$

This equation is integrated to $\mathbf{r}$ throughout the volume of space bounded by Σ. Besides, Green's theorem is applied:

$$\iint k_M^2 o(\mathbf{r})u(\mathbf{r})e^{-ik\mathbf{sr}}\,d^2r = \quad \iint (\nabla^2 u_s(\mathbf{r})e^{-ik\mathbf{sr}} - \nabla^2 e^{-ik\mathbf{sr}}u(\mathbf{r}))\,d^2r \tag{B.19}$$

$$\iint k_M^2 o(\mathbf{r})u(\mathbf{r})e^{-ik\mathbf{sr}}\,d^2r = \quad \oint_\Sigma \left[e^{-ik\mathbf{sr}'}\frac{\delta}{\delta\mathbf{n}}u_s(\mathbf{r}') - u_s(\mathbf{r}')\frac{\delta}{\delta\mathbf{n}}e^{-ik\mathbf{sr}'}\right]dl'\,, \tag{B.20}$$

being $\dfrac{\delta}{\delta\mathbf{n}}$ the derivative along the outward normal to the boundary Σ and dl' is the differential element of length on this boundary. Finally, changing $\dfrac{\delta}{\delta\mathbf{n}}e^{-ik\mathbf{sr}} = -ik\mathbf{n}\cdot\mathbf{s}\,e^{-ik\mathbf{s}\cdot\mathbf{r}}$:

$$k_M^2 \iint o(\mathbf{r})u(\mathbf{r})e^{-ik\mathbf{sr}}\,d^2r = \oint_\Sigma \left[\frac{\delta}{\delta n}u_s(\mathbf{r}') + ik\mathbf{n}\cdot\mathbf{s}\,u_s(\mathbf{r}')\right]e^{-ik\mathbf{sr}'}dl'\,, \tag{B.21}$$

where $\mathbf{s}$ is the unitary vector which covers all the unitary circular boundary, dl' is the differential element in Σ, $\mathbf{n}$ is the normal vector to Σ in $\mathbf{r}'$ and $\dfrac{\delta}{\delta\mathbf{n}}$ is its derivation over $\mathbf{n}$. It's trivial to elucidate that the scattered wave component is the total field minus the incident field $u_s(\mathbf{r}) = u(\mathbf{r}) - u_0(\mathbf{r})$. The left-hand side in Eq. B.21 is the scattering amplitude as Eq. 2.66 defines, consequently:

$$f(\mathbf{s},\mathbf{s}_o) = \oint_\Sigma [\frac{\delta}{\delta\mathbf{n}}u_s(\mathbf{r}') + ik\mathbf{n}\cdot\mathbf{s}\,u_s(\mathbf{r}')]e^{-ik\mathbf{sr}'}dl'\,. \tag{B.22}$$

In most applications, measure both $\dfrac{\delta}{\delta\mathbf{n}}u_s(\mathbf{r})$ and $u_s(\mathbf{r})$ at the same time become impossible. Nevertheless, it is possible to obtain an exact relationship between one of them and the scattering amplitude only for boundaries which one of the coordinate axes of a curvilinear coordinate system in which the Helmholtz equation separates [87]. For the case of a circular boundary, one finds that the previous equation reduces to [87]:

$$f(\mathbf{s},\mathbf{s}_o) = 4i\int_0^{2\pi} u_s(\sigma;\mathbf{s}_o)F_R(\chi-\sigma)d\sigma\,. \tag{B.23}$$

In this case, σ and χ are the angles made by $\mathbf{r}'$ and $\mathbf{s}$ with and arbitrary reference direction. $u^{(s)}(\sigma;\mathbf{s}_o)$ denotes the scattered field at the angle σ and the function $F_R(X)$ is given by:

$$F_{\mathrm{R}}(\chi-\sigma)=\frac{1}{2(2\pi)^2}\sum_{n=-\infty}^{\infty}\frac{i^n}{H_n(kR)}e^{in(\chi-\sigma)}\,, \tag{B.24}$$

where H_n is the n-th order Hankel function of the first kind, and $(\chi-\sigma)$ is the difference between the angle associated with the detecting point and the integration angle.

B.3 Reverse mapping for circular detector algorithm

From (k_x,k_y) space to (χ_0,χ), a reversed map is achieved starting for Eq. 2.85

$$\cos\chi-\cos\chi_0=\frac{k_x}{k_{\mathrm{M}}},\qquad \sin\chi-\sin\chi_0=\frac{k_y}{k_{\mathrm{M}}}\,. \tag{B.25}$$

The first relation between the two previous equation is trivial:

$$\left(\frac{k_x}{k_{\mathrm{M}}}+\cos\chi_0\right)^2=\cos^2\chi,\qquad \left(\frac{k_y}{k_{\mathrm{M}}}+\sin\chi_0\right)^2=\sin^2\chi\,. \tag{B.26}$$

Adding both relations:

$$\left(\frac{k_x}{k_{\mathrm{M}}}\right)^2+\left(\frac{k_y}{k_{\mathrm{M}}}\right)^2+\cos^2\chi_0+\sin^2\chi_0+\frac{2}{k_{\mathrm{M}}}(k_x\cos\chi_0+k_y\sin\chi_0)=\cos^2\chi+\sin^2\chi\,, \tag{B.27}$$

$$\left(\frac{k_x+k_y}{2k_{\mathrm{M}}}\right)^2+k_x\cos\chi_0+k_y\sin\chi_0=0\,. \tag{B.28}$$

Now, p is defined, and we use an identity of the cos:

$$p=\left(\frac{k_x+k_y}{2k_{\mathrm{M}}}\right)^2\,, \tag{B.29}$$

$$\cos\chi_0=\sqrt{1-\sin^2\chi_0}\,, \tag{B.30}$$

then, the relation could be simplified:

$$p+k_y\sin\chi_0=\pm kx\sqrt{1-\sin^2\chi_0}\,, \tag{B.31}$$

$$(p+k_y\sin\chi_0)^2=k_x^2(1-\sin^2\chi_0)\,, \tag{B.32}$$

$$p^2+k_y^2\sin^2\chi_0+2pk_y\sin\chi_0=k_x^2-k_x^2\sin^2\chi_0\,, \tag{B.33}$$

$$(k_x^2+k_y^2)\sin^2\chi_0+2pk_y\sin\chi_0+p^2-k_x^2=0\,. \tag{B.34}$$

Solving the second-grade equation:

$$\sin\chi_0 = \frac{-2pk_y \pm \sqrt{4p^2k_y^2 - 4(k_x^2+k_y^2)(p^2-k_x^2)}}{2(k_x^2+k_y^2)} \tag{B.35}$$

$$= \frac{-pk_y \pm \sqrt{p^2k_y^2 - (k_x^2+k_y^2)(p^2-k_x^2)}}{(k_x^2+k_y^2)}\,. \tag{B.36}$$

On other hand,

$$\begin{aligned} p^2k_y^2 - (k_x^2+k_y^2)(p^2-k_x^2) =& p^2k_y^2 - k_x^2p^2 - k_x^2p^2 + k_x^4 + k_y^2k_x^2 \\ =& -k_x^2p^2 + k_x^4 + k_y^2k_x^2 = k_x^2(k_x^2+k_y^2-p^2) = k_x^2p^2\left(\frac{2}{p}-1\right). \end{aligned} \tag{B.37}$$

From Eq. B.35 and Eq. B.37

$$\begin{aligned} \sin\chi_0 =& \frac{-pk_\pm\sqrt{k_x^2p^2\left(\frac{2}{p}-1\right)}}{k_x^2+k_y^2} \\ =& \frac{-pk_y \pm pk_x\sqrt{\left(\frac{2}{p}-1\right)}}{2p} \\ =& \frac{-k_y \pm k_x\sqrt{\left(\frac{2}{p}-1\right)}}{2}\,. \end{aligned} \tag{B.38}$$

In the same way, $\cos\chi_0$ could be obtained as

$$\cos\chi_0 = \frac{-k_x \pm k_y\sqrt{\left(\frac{2}{p}-1\right)}}{2}\,, \tag{B.39}$$

then χ_0 could be easily obtained:

$$\tan\chi_0 = \frac{\sin\chi_0}{\cos\chi_0} \tag{B.40}$$

$$\chi_0 = \arctan\frac{-k_y \mp k_x\sqrt{\left(\frac{2}{p}-1\right)}}{-k_x \pm k_y\sqrt{\left(\frac{2}{p}-1\right)}}\,. \tag{B.41}$$

Therefore, four solutions of χ_0 arise. We will manage this issued after emulating the about procedure to obtaining the relation of χ with the coordinates in (k_x, k_y) space, getting the next expression with another 4 solutions:

$$\chi_{=} \arctan \frac{k_y \mp k_x \sqrt{\left(\frac{2}{p}-1\right)}}{k_x \pm k_y \sqrt{\left(\frac{2}{p}-1\right)}} . \tag{B.42}$$

Combining both relations, 16 solutions appear, but we performed different tests mapping points in the (k_x, k_y) space to (χ_0, χ) space and vice versa. These tests indicate that there are two pairs of equations in which this reverse mapping is valid. In the first solution, the root component should be subtracted in the numerator and added to the denominator:

$$\chi = \arctan \frac{k_y - k_x \sqrt{\left(\frac{2}{p}-1\right)}}{k_x + k_y \sqrt{\left(\frac{2}{p}-1\right)}}, \; \chi_0 = \arctan \frac{-k_y - k_x \sqrt{\left(\frac{2}{p}-1\right)}}{-k_x + k_y \sqrt{\left(\frac{2}{p}-1\right)}}. \tag{B.43}$$

These symbols change in the other valid solution:

$$\chi = \arctan \frac{k_y + k_x \sqrt{\left(\frac{2}{p}-1\right)}}{k_x - k_y \sqrt{\left(\frac{2}{p}-1\right)}}, \; \chi_0 = \arctan \frac{-k_y + k_x \sqrt{\left(\frac{2}{p}-1\right)}}{-k_x - k_y \sqrt{\left(\frac{2}{p}-1\right)}} , \tag{B.44}$$

both pairs of solutions with

$$p = \frac{k_x^2 + k_y^2}{2k_{\mathrm{M}}^2} . \tag{B.45}$$

Appendix C

Supporting material for Invisibility Passive Devices

One of the motivations of this thesis is to serve as a manual for the realization of devices that require tomography as a technique to be implemented. That is why we have decided to include all the detailed steps.

C.1 Scattering Cross Section (SCS)

To evaluate the rate of the electromagnetic energy that is scattered by a particle, the scattering cross-section [160] is defined as:

$$\mathrm{SCS} = \frac{W_{\mathrm{SCA}}}{P_{\mathrm{INC}}}\,, \tag{C.1}$$

where P_{INC} is the incident irradiance, defined as energy flux of the incident wave [W/m]. W_{SCA} is the scattered energy rate [W], which, in 2D, is derived by contour integration of the Poynting vector associated with the scattered field ($\mathscr{P}_{\mathrm{SCA}}$) over a circumference enclosing the particle (L):

$$W_{\mathrm{SCA}} = \oint_{L} \mathscr{P}_{\mathrm{SCA}} \cdot \mathbf{n}\, dl, \tag{C.2}$$

where $\mathbf{n}$ is the unit vector normal to the imaginary circle.

C.2 Scattering cancellation - cloak modeling

Two cloaks have been scrutinized. Firstly, we chose an inner cylinder with favorable characteristics for tomography, such as a size similar to the wavelength, and a small RI variation with the medium. From there, we perform simulations sweeping frequencies

to lay out the scattered energy rate for each configuration, and we model them looking for the minimum SCS. In particular, ε_S and r_S (S: Shell) are the parameters that have been swept to find the minimum scattered energy rate. This parameter sweep has been done to hide a cylinder of radius λ on the one hand, and a cylinder of $\lambda/2$ radius on the other hand. The obtained results of the SCS, both using a RI of the hidden object of $n_{OBJ} = 1.05$, are shown in figure C.1.

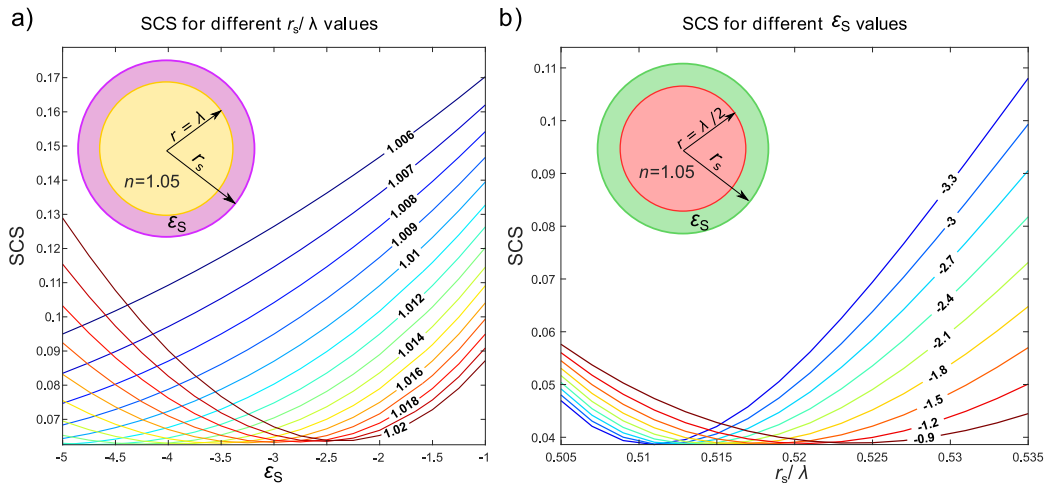

Fig. C.1 SCS for different configurations of scattering cancellation. a) A cylinder of $r = \lambda$ is cloaked, and the lines represent the value of the cloak radius (λ^{-1}). b) A cylinder of $r = \lambda/2$ is cloaked, and the lines represent the value of the cloak ε.

Although these parameters do not achieve a high hiding performance in terms of SCS due to the large size of the object to hide (caused by the aforementioned limitations in the tomography), we can see a local minimum by fixing one design parameter, therefore, we can choose a configuration with a low SCS and see the effect of tomography. To test this technique, a cloak with $\varepsilon_S = -2.7$ and $r_S = 0.51248$ is used to hide a $r = 0.5\lambda$ cylinder of refractive index of $n_{OBJ} = 1.05$ (blue light line in Fig C.1 b). Both tomograms can be seen in the main text.

C.3 Transformation optics cloak

We performed the design of the cloak without frequency dependence in the first place, following equation 4.4, but we want to consider that the metamaterial used in the cloak could exits. For this purpose, the Drude and Lorentz model are applied to ε and μ tensors respectively, following [145]. Furthermore, these models not only allow us to observe the frequency response of the cloak, but we can also check the effects of the losses. These models follow:

$$Drude: \varepsilon_{r\mathrm{D},\phi\mathrm{D},z\mathrm{D}} = \varepsilon_{r,\phi,z}\left(1 - \frac{f_0^2}{f(f+i\gamma_1)}\right), \tag{C.3}$$

$$Lorentz: \mu_{r\mathrm{L},\phi\mathrm{L},z\mathrm{L}} = \mu_{r,\phi,z}\left(1 - \frac{F}{1+i(\gamma_2/f)-(f_0^2/f^2)}\right). \tag{C.4}$$

(C.5)

Following [145] we will take $\gamma_1 = \gamma_2 = \gamma$ to define the losses and $F = 0.78$.
In first place, we apply these models to the cylindrical parameters describe in Eq. (4.4) and then transform them to Cartesian coordinates through Eq. (**??**). We take a look at the cylindrical parameters profile along the line $x = (-1.5R_2, 1.5R_2), y = 0$.

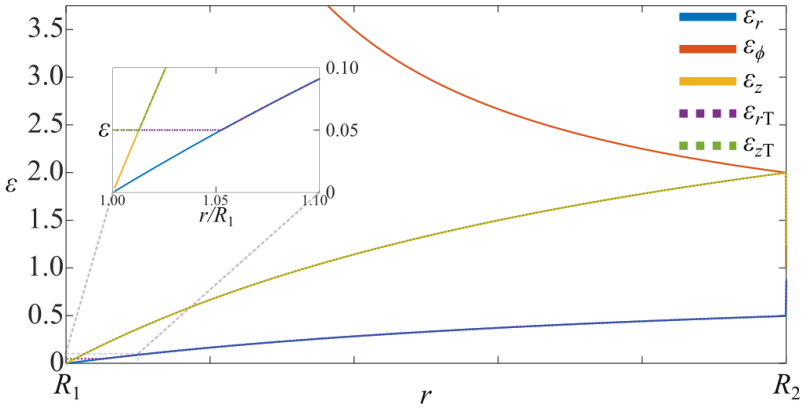

Fig. C.2 Profile of the ε cylindrical parameters.

As we can see in Fig. C.2, there are two types of approach to the R_1 boundary: ε_r and ε_z tend to 0, and ε_ϕ tends to ∞. This last parameter is always above unity, therefore we are not going to change it with the Drude and Lorentz approximations. The problem arises in the other two parameters, where the approach to zero requires the next design. The space between $r = R_2$ and $r = R_1$ are going to be divided in two different layers: One of them, where the value of ε is equal to or less than 0.05, and the rest of the cloak will be another layer. The boundary in the case of the ε_r parameter will be $R_r = 1.05R_1$, and the frontier in the case of ε_r will be $R_z = 1.01R_1$. In the end, there will be three areas to model them in COMSOL (ε and μ remain unity outside the cloak), where the parameters ε_t and μ_t for r or z coordinates follow table C.1.

layer	A: $R_1 < r < 1.01R_1$	B:$1.01R_1 < r < 1.05R_1$	C: $1.05R_1 < r < R_2$
ε_{rn}	ε_{T}	ε_{T}	$\varepsilon_{r\mathrm{D}}(\mathbf{r})$
ε_{zn}	ε_{T}	$\varepsilon_{z\mathrm{D}}(\mathbf{r})$	$\varepsilon_{z\mathrm{D}}(\mathbf{r})$
μ_{rn}	μ_{T}	μ_{T}	$\mu_{r\mathrm{L}}(\mathbf{r})$
μ_{zn}	μ_{T}	$\mu_{z\mathrm{L}}(\mathbf{r})$	$\mu_{z\mathrm{L}}(\mathbf{r})$

Table C.1 Multilayer description, for Drude, Lorentz, and Truncated parameters.

Considering these parameters, Drude and Lorentz models are applied as follows:

$$\varepsilon_{r\mathrm{D}}(\mathbf{r}) = \varepsilon_r(\mathbf{r})\left(2 - \frac{f_0^2}{f(f+i\gamma)}\right), \tag{C.6}$$

$$\varepsilon_{z\mathrm{D}}(\mathbf{r}) = \varepsilon_z(\mathbf{r})\left(2 - \frac{f_0^2}{f(f+i\gamma)}\right), \tag{C.7}$$

$$\varepsilon_{\mathrm{T}} = \left(0.1 - \frac{0.05 f_0^2}{f(f+i\gamma)}\right), \tag{C.8}$$

$$\mu_{r\mathrm{L}}(\mathbf{r}) = \mu_r(\mathbf{r})\left(1 - \frac{F}{1+(i\gamma/f)-(f_0^2/f^2)}\right), \tag{C.9}$$

$$\mu_{z\mathrm{L}}(\mathbf{r}) = \mu_z(\mathbf{r})\left(1 - \frac{F}{1+(i\gamma/f)-(f_0^2/f^2)}\right), \tag{C.10}$$

$$\mu_{\mathrm{T}} = \left(0.05 - \frac{0.05F}{1+(i\gamma/f)-(f_0^2/f^2)}\right), \tag{C.11}$$

and then they are transformed onto Cartesian coordinates to get these values for components x, xy, yx, y for the three areas. We model this multilayer cloak in COMSOL. The results of the tomography can be seen in the main text.

C.4 Hexagonal polygonal cloak

We follow [137] to design the cloak. The problems that arise in classical TO cloaks [60] (singularities close to the hiding area) are solved by dividing the cloak in a segmented polygon, with linear homogeneous transformation in each segment. Two kinds of segments appear as shown in Fig C.3.

As we can see in the figure C.3, the transformation from virtual to physical coordinate space has to be done for two different kinds of segments:

C.4.1 Segment I, local coordinate u_{a} to u'_{a}

The virtual hiding space that can be seen in Fig. C.3 (a) will be open to a bigger space. Then, the u_{a} coordinate takes values from r_2 to the inner side of the hexagon [which

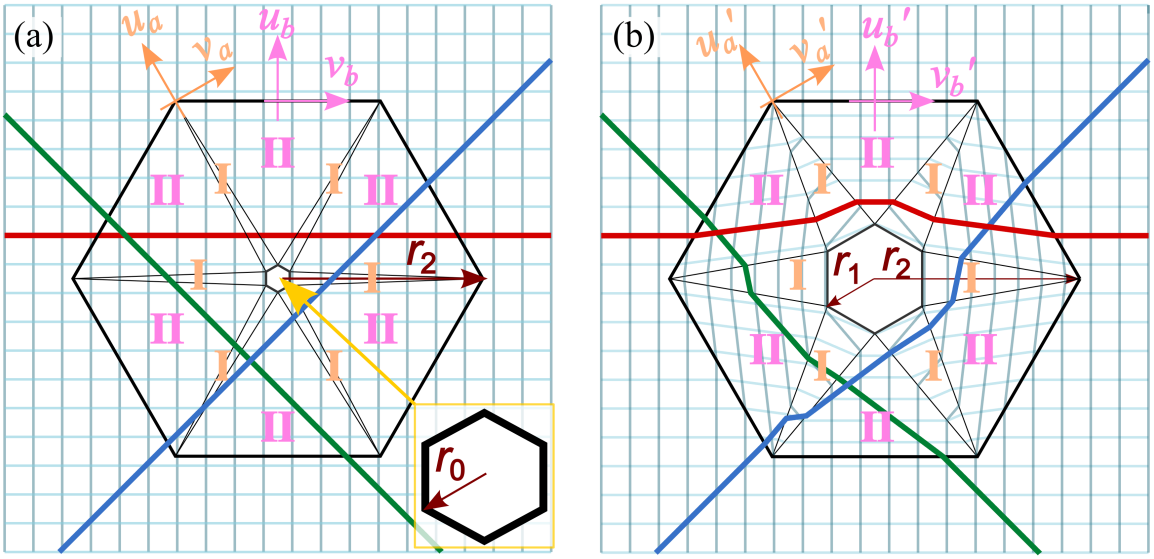

Fig. C.3 (a) Virtual coordinated space (b) Physical coordinate space. [137]

value will be $r_0 \cos\left(\frac{\pi}{6}\right)]$ in virtual space, while in the physical space should be placed in the values of u_a' from r_2 to the new inner hexagon $\left[r_1 \cos\left(\frac{\pi}{6}\right)\right]$. Consequently, the transformation could be done as:

$$u_a' = u_a \frac{r_2 - r_1 \cos\left(\frac{\pi}{6}\right)}{r_2 - r_0 \cos\left(\frac{\pi}{6}\right)}. \tag{C.12}$$

For convenience, κ_u is defined as $\kappa_u = \dfrac{r_2 - r_0 \cos\left(\frac{\pi}{6}\right)}{r_2 - r_1 \cos\left(\frac{\pi}{6}\right)}$, thus the transformation could be sum as

$$u_a' = \frac{u_a}{\kappa_u}. \tag{C.13}$$

C.4.2 Segment I, local coordinate v_a to v_a'

The virtual hiding space that can be seen in Fig. C.3 (a) should be enlarged in the v_a' coordinate. Then the v_a coordinate takes the values close to the inner side of the hexagon in virtual space (r_0), and this space will be placed along the side of the hexagon of radius r_1 in physical space. Consequently, the transformation could be done as

$$v_a' = \frac{r_1}{r_0} v_a, \tag{C.14}$$

nevertheless, as we proceeded with the previous coordinate, we define κ_v as $\kappa_v = \frac{r_1}{r_0}$, then

$$v'_{\mathrm{a}} = v_{\mathrm{a}}\kappa_v. \tag{C.15}$$

At this point, it is worth mentioning that the coordinate transversal to the polygonal plane remains without change:

$$w'_{\mathrm{a}} = w_{\mathrm{a}}. \tag{C.16}$$

C.4.3 Segment II, local coordinate u_{b} to u'_{b}

In the same way that in coordinate u_{a} of segment I, the virtual hiding space that can be seen in Fig. C.3 (a) should be opened to a bigger space. In this case, the u_{b} coordinate takes values from the outer side of the hexagon $\left[r_2\cos\left(\frac{\pi}{6}\right)\right]$ to the inner hexagon vertex (r_0) in virtual space, which will be placed in the physical space from the same outer hexagon to the inner hexagon vertex of value r_1. Consequently, the transformation could be done as:

$$u'_{\mathrm{b}} = u_{\mathrm{b}}\frac{r_2\cos\left(\frac{\pi}{6}\right) - r_1}{r_2\cos\left(\frac{\pi}{6}\right) - r_0}. \tag{C.17}$$

For convenience, κ is defined as $\kappa = \dfrac{r_2\cos\left(\frac{\pi}{6}\right) - r_0}{r_2\cos\left(\frac{\pi}{6}\right) - r_1}$, therefore the transformation can be sum as:

$$u'_{\mathrm{a}} = \frac{u_{\mathrm{a}}}{\kappa}. \tag{C.18}$$

C.4.4 Segment II, local coordinate v_{b} to v'_{b}

It is easy to see in figure C.3 that, in segment II, the virtual space in v_{b} coordinate remains without changes in v'_{b} coordinate, then

$$v'_{\mathrm{b}} = v_{\mathrm{b}}. \tag{C.19}$$

In the same way, like in segment I, perpendicular coordinate w_{b} remains without change in the physical space

$$w'_{\mathrm{b}} = w_{\mathrm{b}}. \tag{C.20}$$

C.4.5 Electromagnetic Parameters

Once the transformation is clear, equation 3 in [146] will help us to perform the electromagnetic parameters transformation:

$$\varepsilon' = \frac{\Lambda\varepsilon\Lambda^T}{det\Lambda}, \tag{C.21}$$

where Λ is the Jacobian matrix of the coordinate transformation and Λ^T its transformation.

Segment I

Here, as Λ will be a diagonal matrix, its transformation has the same value:

$$\Lambda = \Lambda^T = \begin{pmatrix} \kappa_u^{-1} & 0 & 0 \\ 0 & \kappa_v & 0 \\ 0 & 0 & 1 \end{pmatrix}. \tag{C.22}$$

This determinant can be calculated easily as $|\Lambda| = \frac{\kappa_v}{\kappa_u}$. Using relation C.21:

$$\varepsilon'_{\mathrm{a}} = \frac{\Lambda\varepsilon_{\mathrm{a}}\Lambda^T}{det\Lambda} = \frac{\begin{pmatrix} \kappa_u^{-1} & 0 & 0 \\ 0 & \kappa_v & 0 \\ 0 & 0 & 1 \end{pmatrix}\begin{pmatrix} \varepsilon_{u_{\mathrm{a}}} & 0 & 0 \\ 0 & \varepsilon_{v_{\mathrm{a}}} & 0 \\ 0 & 0 & \mu_{z_{\mathrm{a}}} \end{pmatrix}\begin{pmatrix} \kappa_u^{-1} & 0 & 0 \\ 0 & \kappa_v & 0 \\ 0 & 0 & 1 \end{pmatrix}}{\frac{\kappa_v}{\kappa_u}} = \begin{pmatrix} \frac{\varepsilon_{u_{\mathrm{a}}}}{\kappa_u^2} & 0 & 0 \\ 0 & \varepsilon_{v_{\mathrm{a}}}\kappa_v^2 & 0 \\ 0 & 0 & \mu_{z_{\mathrm{a}}} \end{pmatrix}\frac{\kappa_u}{\kappa_v} \tag{C.23}$$

Segment II

As in the previous section, the λ matrix is the same as its transformation:

$$\Lambda = \Lambda^T = \begin{pmatrix} \kappa^{-1} & 0 & 0 \\ 0 & 1 & 0 \\ 0 & 0 & 1 \end{pmatrix}, \tag{C.24}$$

which determinant can be easily calculated as $|\Lambda| = \kappa^{-1}$.

The transformation in segment II follows:

$$\varepsilon'_{\mathrm{b}} = \frac{\Lambda\varepsilon_{\mathrm{b}}\Lambda^T}{det\Lambda} = \frac{\begin{pmatrix} \kappa^{-1} & 0 & 0 \\ 0 & 1 & 0 \\ 0 & 0 & 1 \end{pmatrix}\begin{pmatrix} \varepsilon_{u_{\mathrm{b}}} & 0 & 0 \\ 0 & \varepsilon_{v_{\mathrm{b}}} & 0 \\ 0 & 0 & \mu_{z_{\mathrm{b}}} \end{pmatrix}\begin{pmatrix} \kappa^{-1} & 0 & 0 \\ 0 & 1 & 0 \\ 0 & 0 & 1 \end{pmatrix}}{\frac{1}{\kappa}} = \begin{pmatrix} \frac{\varepsilon_{u_{\mathrm{b}}}}{\kappa^2} & 0 & 0 \\ 0 & \varepsilon_{v_{\mathrm{b}}} & 0 \\ 0 & 0 & \mu_{z_{\mathrm{b}}} \end{pmatrix}\kappa \quad \text{(C.25)}$$

Both segments

To summarize, the physical from virtual space transformation follows as:

$$\varepsilon'_{u_{\mathrm{a}}} = \frac{\varepsilon_{u_{\mathrm{a}}}}{\kappa_u\kappa_v}, \quad \text{(C.26)}$$

$$\varepsilon'_{v_{\mathrm{a}}} = \varepsilon_{v_{\mathrm{a}}}\kappa_u\kappa_v, \quad \text{(C.27)}$$

$$\mu'_{w_{\mathrm{a}}} = \frac{\mu_{u_{\mathrm{a}}}\kappa_u}{\kappa_v}, \quad \text{(C.28)}$$

$$\varepsilon'_{u_{\mathrm{b}}} = \frac{\varepsilon_{u_{\mathrm{b}}}}{\kappa}, \quad \text{(C.29)}$$

$$\varepsilon'_{v_{\mathrm{b}}} = \varepsilon_{v_{\mathrm{b}}}\kappa, \quad \text{(C.30)}$$

$$\mu'_{w_{\mathrm{b}}} = \mu_{u_{\mathrm{b}}}\kappa_u, \quad \text{(C.31)}$$

where $\kappa_u = \dfrac{r_2 - r_0\cos\left(\frac{\pi}{6}\right)}{r_2 - r_1\cos\left(\frac{\pi}{6}\right)}$, $\kappa_v = \dfrac{r_1}{r_0}$ and $\kappa = \dfrac{r_2\cos\left(\frac{\pi}{6}\right) - r_0}{r_2\cos\left(\frac{\pi}{6}\right) - r_1}$.

C.4.6 Transformation to Cartesian coordinates

To model this cloak in the COMSOL Multiphysics software, these parameters must be changed to cardinal coordinates (except for the μ_z components that remain without change). For both types of segments, the transformation in each piece will depend on their position. As we can see in figure C.3, the upper segment of the region II, the $(v_{\mathrm{b}}, u_{\mathrm{b}})$ coordinates could be associated with (x, y), but for the rest of the segments, a rotation will be applied. The rotation angle, ϕ, will be different for each segment for each kind of region, I or II, but could be calculated using equation C.21 as before. In this case, only 2 dimensions will be considered to perform the $(v_{\mathrm{b}}, u_{\mathrm{b}})$ to (x, y) transformation. The Jacobian matrix, its transformation, and its determinant are:

$$\Lambda = \begin{pmatrix} \cos\phi & -\sin\phi \\ \sin\phi & \cos\phi \end{pmatrix}, \quad \text{(C.32)}$$

$$\Lambda^T = \begin{pmatrix} \cos\phi & \sin\phi \\ -\sin\phi & \cos\phi \end{pmatrix}, \quad \text{(C.33)}$$

$$|\Lambda| = \cos^2\phi + \sin^2\phi = 1; \quad \text{(C.34)}$$

Then, for both regions I and II, the transformation matrix follows:

$$\varepsilon = \begin{pmatrix} \cos\phi & -\sin\phi \\ \sin\phi & \cos\phi \end{pmatrix} \begin{pmatrix} \varepsilon_v & 0 \\ 0 & \varepsilon_u \end{pmatrix} \begin{pmatrix} \cos\phi & \sin\phi \\ -\sin\phi & \cos\phi \end{pmatrix},$$
$$\varepsilon = \begin{pmatrix} \varepsilon_v \cos^2\phi + \varepsilon_u \sin^2\phi & \varepsilon_v \cos\phi \sin\phi - \varepsilon_v \cos\phi \sin\phi \\ \varepsilon_v \cos\phi \sin\phi - \varepsilon_v \cos\phi \sin\phi & \varepsilon_v \sin^2\phi + \varepsilon_u \cos^2\phi \end{pmatrix}, \tag{C.35}$$

expressed as tensor. Then, the parameters could be defined as follows.

$$\varepsilon_{xx} = \varepsilon_v \cos^2\phi + \varepsilon_u \sin^2\phi, \tag{C.36}$$
$$\varepsilon_{xy} = \varepsilon_{yx} = (\varepsilon_v - \varepsilon_v)\cos\phi \sin\phi, \tag{C.37}$$
$$\varepsilon_{yy} = \varepsilon_u \cos^2\phi + \varepsilon_v \sin^2\phi\ . \tag{C.38}$$

Last considerations

The last step to calculate the parameters will be the definition of the ϕ angles for each region and segment.

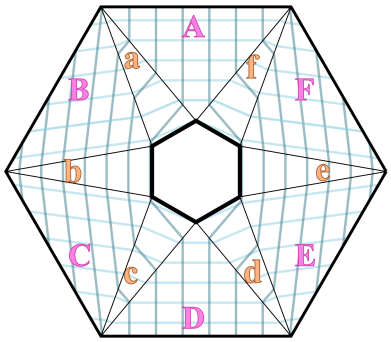

Fig. C.4 Nomenclature of segments in the hexagonal cloak

Region I	ϕ_a	ϕ_b	ϕ_c	ϕ_d	ϕ_e	ϕ_f
Angle [rad]	$\pi/6$	$\pi/2$	$5\pi/6$	$7\pi/6$	$3\pi/2$	$11\pi/6$
Region II	ϕ_A	ϕ_B	ϕ_C	ϕ_D	ϕ_E	ϕ_F
Angle [rad]	0	$\pi/3$	$2\pi/3$	π	$4\pi/3$	$5\pi/3$

Table C.2 Angles of transformation (rad).

Since $\cos^2\phi$, $\sin^2\phi$ and $\cos\phi\sin\phi$ are going to be equal in pairs a-d, A-D, b-e, B-E, c-f and C-F, only six transformations should be performed.

C.5 Square polygonal cloak

To model the square cloak, we follow [146]. Like in the previous hexagonal cloak, we can exploit the symmetry of the cloak, as Figure C.5 shows.

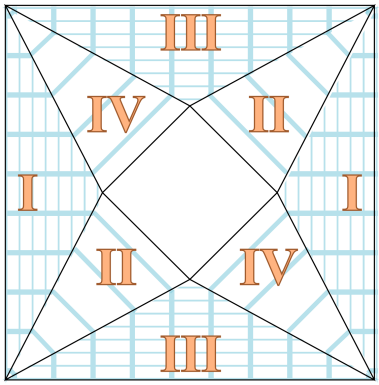

Fig. C.5 Nomenclature of segments

The model parameters will be named as: a is the side of the outer square, b_1 is the side of the hiding virtual space, and b_2 is the side of the real inner square. Equation C.21 leads the transformation, but each segment will be different, as the next sections show.

C.5.1 Segment I

Defining $k_1 = \dfrac{a-\sqrt{2}b_1}{a-\sqrt{2}b_2}$, the Λ matrix for the transformation is

$$\Lambda = \Lambda^T = \begin{pmatrix} k_1^{-1} & 0 & 0 \\ 0 & 1 & 0 \\ 0 & 0 & 1 \end{pmatrix}, \tag{C.39}$$

whose determinant is calculated easily as $|\Lambda| = k_1^{-1}$. Using relation C.21:

$$\varepsilon'_a = \frac{\Lambda\varepsilon_a\Lambda^T}{det\Lambda} = \frac{\begin{pmatrix} k_1^{-1} & 0 & 0 \\ 0 & 1 & 0 \\ 0 & 0 & 1 \end{pmatrix}\begin{pmatrix} \varepsilon_{u_I} & 0 & 0 \\ 0 & \varepsilon_{v_I} & 0 \\ 0 & 0 & \mu_{z_I} \end{pmatrix}\begin{pmatrix} k_1^{-1} & 0 & 0 \\ 0 & 1 & 0 \\ 0 & 0 & 1 \end{pmatrix}}{\dfrac{1}{k_1}} = \begin{pmatrix} \dfrac{\varepsilon_{u_I}}{k_1} & 0 & 0 \\ 0 & \varepsilon_{v_I}k_1 & 0 \\ 0 & 0 & \mu_{z_I}k_1 \end{pmatrix}. \tag{C.40}$$

C.5.2 Segment II

Defining $k_2 = \frac{b_2}{b_1}$, the Λ matrix for the transformation is

$$\Lambda = \begin{pmatrix} k_2 & 0 & 0 \\ -k_2 & 1 & 0 \\ 0 & 0 & 1 \end{pmatrix}, \Lambda^T = \begin{pmatrix} k_2 & -k_2 & 0 \\ 0 & 1 & 0 \\ 0 & 0 & 1 \end{pmatrix}, \tag{C.41}$$

whose determinant is calculated easily as $|\Lambda| = k_2$. Using relation C.21:

$$\varepsilon'_a = \frac{\Lambda \varepsilon_a \Lambda^T}{det\Lambda} = \frac{\begin{pmatrix} k_2 & 0 & 0 \\ -k_2 & 1 & 0 \\ 0 & 0 & 1 \end{pmatrix} \begin{pmatrix} \varepsilon_{u_{II}} & 0 & 0 \\ 0 & \varepsilon_{v_{II}} & 0 \\ 0 & 0 & \mu_{z_{II}} \end{pmatrix} \begin{pmatrix} k_2 & -k_2 & 0 \\ 0 & 1 & 0 \\ 0 & 0 & 1 \end{pmatrix}}{k_2} = \begin{pmatrix} k_2\varepsilon_{u_{II}} & -k_2\varepsilon_{u_{II}} & 0 \\ -k_2\varepsilon_{u_{II}} & k_2\varepsilon_{u_{II}} + \frac{\varepsilon_{v_{II}}}{k_2} & 0 \\ 0 & 0 & \frac{\mu_{z_I I}}{k_2} \end{pmatrix}. \tag{C.42}$$

C.5.3 Segment III

Similar to Segment I, with $k_1 = \frac{a-\sqrt{2}b_1}{a-\sqrt{2}b_2}$, the Λ matrix for the transformation is

$$\Lambda = \Lambda^T = \begin{pmatrix} 1 & 0 & 0 \\ 0 & k_1^{-1} & 0 \\ 0 & 0 & 1 \end{pmatrix}, \tag{C.43}$$

whose determinant is calculated easily as $|\Lambda| = k_1^{-1}$. Using relation C.21:

$$\varepsilon'_a = \frac{\Lambda \varepsilon_a \Lambda^T}{det\Lambda} = \frac{\begin{pmatrix} 1 & 0 & 0 \\ 0 & k_1^{-1} & 0 \\ 0 & 0 & 1 \end{pmatrix} \begin{pmatrix} \varepsilon_{u_{III}} & 0 & 0 \\ 0 & \varepsilon_{v_{III}} & 0 \\ 0 & 0 & \mu_{z_{III}} \end{pmatrix} \begin{pmatrix} 1 & 0 & 0 \\ 0 & k_1^{-1} & 0 \\ 0 & 0 & 1 \end{pmatrix}}{\frac{1}{k_1}} = \begin{pmatrix} \varepsilon_{u_{III}} k_1 & 0 & 0 \\ 0 & \frac{\varepsilon_{v_{III}}}{k_1} & 0 \\ 0 & 0 & \mu_{z_{III}} k_1 \end{pmatrix}. \tag{C.44}$$

C.5.4 Segment IV

Similar to Segment II, with $k_2 = \frac{b_2}{b_1}$, the Λ matrix for the transformation is

$$\Lambda = \begin{pmatrix} k_2 & 0 & 0 \\ +k_2 & 1 & 0 \\ 0 & 0 & 1 \end{pmatrix}, \Lambda^T = \begin{pmatrix} k_2 & +k_2 & 0 \\ 0 & 1 & 0 \\ 0 & 0 & 1 \end{pmatrix}, \tag{C.45}$$

whose determinant is calculated easily as $|\Lambda| = k_2$. Using relation C.21:

$$\varepsilon'_{\mathrm{a}} = \frac{\Lambda \varepsilon_{\mathrm{a}} \Lambda^T}{det\Lambda} = \frac{\begin{pmatrix} k_2 & 0 & 0 \\ k_2 & 1 & 0 \\ 0 & 0 & 1 \end{pmatrix} \begin{pmatrix} \varepsilon_{u_{IV}} & 0 & 0 \\ 0 & \varepsilon_{v_{IV}} & 0 \\ 0 & 0 & \mu_{z_{IV}} \end{pmatrix} \begin{pmatrix} k_2 & k_2 & 0 \\ 0 & 1 & 0 \\ 0 & 0 & 1 \end{pmatrix}}{k_2} = \begin{pmatrix} k_2\varepsilon_{u_{IV}} & k_2\varepsilon_{u_{IV}} & 0 \\ k_2\varepsilon_{u_{IV}} & k_2\varepsilon_{u_{IV}} + \frac{\varepsilon_{v_{IV}}}{k_2} & 0 \\ 0 & 0 & \frac{\mu_{z_IV}}{k_2} \end{pmatrix}. \tag{C.46}$$

C.5.5 Summary of parameter changes

$$I: \quad \varepsilon_{x_I} = \frac{\varepsilon_x}{k_1}, \tag{C.47}$$

$$\varepsilon_{y_I} = \varepsilon_y k_1, \tag{C.48}$$

$$\varepsilon_{z_I} = \varepsilon_z k_1, \tag{C.49}$$

$$II: \quad \varepsilon_{x_{II}} = \varepsilon_x k_2, \tag{C.50}$$

$$\varepsilon_{xy_{II}} = \varepsilon_{yx_{II}} = -\varepsilon_x k_2, \tag{C.51}$$

$$\varepsilon_{y_{II}} = \varepsilon_x k_2 + \frac{\varepsilon_y}{k_2}, \tag{C.52}$$

$$\varepsilon_{z_{II}} = \frac{\varepsilon_z}{k_2}, \tag{C.53}$$

$$III: \quad \varepsilon_{x_{III}} = \frac{\varepsilon_x}{k_1}, \tag{C.54}$$

$$\varepsilon_{y_{III}} = \varepsilon_y k_1, \tag{C.55}$$

$$\varepsilon_{z_{III}} = \varepsilon_z k_1, \tag{C.56}$$

$$IV: \quad \varepsilon_{x_{IV}} = \varepsilon_x k_2, \tag{C.57}$$

$$\varepsilon_{xy_{IV}} = \varepsilon_{yx_{IV}} = \varepsilon_x k_2, \tag{C.58}$$

$$\varepsilon_{y_{IV}} = \varepsilon_x k_2 + \frac{\varepsilon_y}{k_2}, \tag{C.59}$$

$$\varepsilon_{z_{IV}} = \frac{\varepsilon_z}{k_2}. \tag{C.60}$$

Author's Merits

Journal articles

Main contributions:

[122] **Francisco J. Díaz-Fernández**, Elena Pinilla-Cienfuegos, Carlos García-Meca, Sergio Lechago, Amadeu Griol and Javier Martí, "Characterisation of on-chip wireless interconnects based on silicon nanoantennas via near-field scanning optical microscopy," *IET Optoelectronics* **13 (2)**, 72-76 (2019).
2020 Premium Award for **Best Paper** in *IET Optoelectronics*.

Preprint 1 **Francisco J. Díaz-Fernández**, Javier Martí and Carlos García-Meca, "Imaging cloaked objects: diffraction tomography of realistic invisibility devices".

Preprint 2 **Francisco J. Díaz-Fernández**, Paul Müller, Jochen Gück, Javier Martí and Carlos García-Meca, "Resolution improvement in tomographic phase microscopy using a circular detector".

Other contributions:

[126] Jad Sabek, **Francisco J. Díaz-Fernández**, Luis Torrijos-Morán, Zeneida Díaz-Betancor, Ángel Maquieira, María-José Bañuls, Elena Pinilla-Cienfuegos, and Jaime García-Rupérez, "Experimental study of an evanescent-field biosensor based on 1D photonic bandgap structures," *Beilstein Journal of Nanotechnolgy* **10**, 967–974 (2019).

[48] Alba Espinosa-Soria, Elena Pinilla-Cienfuegos, **Francisco J. Díaz-Fernández,** Luis Torrijos-Morán, Amadeu Griol, Javier Martí, Alejandro Martínez, "Coherent Control of a Plasmonic Nanoantenna Integrated on a Silicon Chip," *ACS Photonics* **5 (7)**, 2712-2717 (2018).

Conferences

[Conf. 1] **Francisco J. Díaz-Fernández**, Elena Pinilla-Cienfuegos, Carlos García-Meca, Sergio Lechago, Amadeu Griol and Javier Martí, "Characterization of On-Chip Wireless Interconnects Based on Silicon Nanoantennas via Near-Field Scanning Optical Microscopy," Poster, *20th European Conference on Integrated Optics (ECIO)*, València (2018).

[Conf. 2] **Francisco J. Díaz-Fernández**, Elena Pinilla-Cienfuegos, Carlos García-Meca, Sergio Lechago, Amadeu Griol and Javier Martí, "Near-Field Scanning Optical Microscope Measurements of On-Chip Wireless Interconnects Based on Silicon Nanoantennas," Poster, *X Reunión del Grupo Especializado de Física del Estado Sólido (GEFES)*, València (2017).

Research stays

[Stay] Max Planck Institute for the Science of Light. GuckLab. (Erlangen, Germany). *Python implementation of the algorithm for far-field circular detector tomography,* supervised by Prof. Jochen Gück (2021)[1].

[1] This stay was conducted remotely, due to travel restrictions caused by the Covid-19 pandemic, from April to July 2021.

References

[1] S. Standring, "A brief history of topographical anatomy," *Journal of Anatomy*, vol. 229, pp. 32–62, June 2016.

[2] W. Röntgen, "Über eine neue art von strahlen," *Sitzungsberichte der Physikalisch-medicinischen Gesellschaft zu Würzburg*, pp. 132–141, Jan. 1895.

[3] P. C. Goodman, "The new light: discovery and introduction of the x-ray.," *American Journal of Roentgenology*, vol. 165, pp. 1041–1045, Nov. 1995.

[4] J. Radon, "Über die Bestimmung von Funktionen durch ihre Integralwertelängs gewisser Mannigfaltigkeiten," *Akademie der Wissenschaften*, vol. 69, pp. 262–277, Apr. 1917.

[5] A. Kak, "Computerized tomography with x-ray, emission, and ultrasound sources," *Proceedings of the IEEE*, vol. 67, pp. 1245–1272, Sept. 1979.

[6] P. J. Withers, C. Bouman, S. Carmignato, V. Cnudde, D. Grimaldi, C. K. Hagen, E. Maire, M. Manley, A. D. Plessis, and S. R. Stock, "X-ray computed tomography," *Nature Reviews Methods Primers*, vol. 1, p. 18, Feb. 2021.

[7] M. Fatemi, "Ultrasonic b-scan imaging: Theory of image formation and a technique for restoration," *Ultrasonic Imaging*, vol. 2, pp. 1–47, Jan. 1980.

[8] M. A. Aldhaeebi, K. Alzoubi, T. S. Almoneef, S. M. Bamatraf, H. Attia, and O. M. Ramahi, "Review of microwaves techniques for breast cancer detection," *Sensors*, vol. 20, p. 2390, Apr. 2020.

[9] S. Pan and A. Kak, "A computational study of reconstruction algorithms for diffraction tomography: Interpolation versus filtered-backpropagation," *IEEE Transactions on Acoustics, Speech, and Signal Processing*, vol. 31, pp. 1262–1275, Oct. 1983.

[10] J. J. Vaquero and P. Kinahan, "Positron emission tomography: Current challenges and opportunities for technological advances in clinical and preclinical imaging systems," *Annual Review of Biomedical Engineering*, vol. 17, pp. 385–414, Dec. 2015.

[11] R. Liang, ed., *Biomedical Optical Imaging Technologies*. Springer Berlin Heidelberg, 2013.

[12] E. Wolf, "Three-dimensional structure determination of semi-transparent objects from holographic data," *Optics Communications*, vol. 1, pp. 153–156, Sept. 1969.

[13] E. Wolf, "Determination of the amplitude and the phase of scattered fields by holography," *Journal of the Optical Society of America*, vol. 60, pp. 18–20, Jan. 1970.

[14] A. Devaney, "A filtered backpropagation algorithm for diffraction tomography," *Ultrasonic Imaging*, vol. 4, pp. 336–350, Oct. 1982.

[15] M. Slaney and A. C. Kak, "Diffraction tomography," in *Inverse Optics I* (A. J. Devaney, ed.), SPIE, Sept. 1983.

[16] A. C. Kak and M. Slaney, "Imaging with diffraction tomography," Tech. Rep. Paper 540, Department of Electrical and Computer EngineeringTechnical Reports., 1985.

[17] T. Noda, S. Kawata, and S. Minami, "Three-dimensional phase contrast imaging by an annular illumination microscope," *Applied Optics*, vol. 29, pp. 3810–3815, Sept. 1990.

[18] M. Lambert and D. Lesselier, "Binary-constrained inversion of a buried cylindrical obstacle from complete and phaseless magnetic fields," *Inverse Problems*, vol. 16, pp. 563–576, May 2000.

[19] V. Lauer, "New approach to optical diffraction tomography yielding a vector equation of diffraction tomography and a novel tomographic microscope," *Journal of Microscopy*, vol. 205, pp. 165–176, Feb. 2002.

[20] D. Huang, E. Swanson, C. Lin, J. Schuman, W. Stinson, W. Chang, M. Hee, T. Flotte, K. Gregory, C. Puliafito, and al. et, "Optical coherence tomography," *Science*, vol. 254, pp. 1178–1181, Nov. 1991.

[21] F. Charrière, A. Marian, F. Montfort, J. Kuehn, T. Colomb, E. Cuche, P. Marquet, and C. Depeursinge, "Cell refractive index tomography by digital holographic microscopy," *Optics Letters*, vol. 31, pp. 178–180, Jan. 2006.

[22] W. Choi, C. Fang-Yen, K. Badizadegan, S. Oh, N. Lue, R. R. Dasari, and M. S. Feld, "Tomographic phase microscopy," *Nature Methods*, vol. 4, pp. 717–719, Aug. 2007.

[23] Y. Sung, W. Choi, C. Fang-Yen, K. Badizadegan, R. R. Dasari, and M. S. Feld, "Optical diffraction tomography for high resolution live cell imaging," *Optics Express*, vol. 17, pp. 266–277, Jan. 2009.

[24] D. Jin, R. Zhou, Z. Yaqoob, and P. T. C. So, "Tomographic phase microscopy: principles and applications in bioimaging [invited]," *Journal of the Optical Society of America B*, vol. 34, pp. B64–B77, Apr. 2017.

[25] G. E. Moore, "Cramming more components onto integrated circuits," *Electronics*, pp. 114–117, Apr. 1965.

[26] M. M. Waldrop, "The chips are down for moore's law," *Nature*, vol. 530, pp. 144–147, Feb. 2016.

[27] D. Thomson, A. Zilkie, J. E. Bowers, T. Komljenovic, G. T. Reed, L. Vivien, D. Marris-Morini, E. Cassan, L. Virot, J.-M. Fédéli, J.-M. Hartmann, J. H. Schmid, D.-X. Xu, F. Boeuf, P. O'Brien, G. Z. Mashanovich, and M. Nedeljkovic, "Roadmap on silicon photonics," *Journal of Optics*, vol. 18, p. 073003, June 2016.

[28] R. Kirchain and L. Kimerling, "A roadmap for nanophotonics," *Nature Photonics*, vol. 1, pp. 303–305, June 2007.

[29] N. C. Harris, G. R. Steinbrecher, M. Prabhu, Y. Lahini, J. Mower, D. Bunandar, C. Chen, F. N. C. Wong, T. Baehr-Jones, M. Hochberg, S. Lloyd, and D. Englund, "Quantum transport simulations in a programmable nanophotonic processor," *Nature Photonics*, vol. 11, pp. 447–452, June 2017.

[30] Editorial, "The rise of integrated quantum photonics," *Nature Photonics*, vol. 14, pp. 265–265, Apr. 2020.

[31] G. Moody, V. Sorger, P. Juodawlkis, W. Loh, C. Sorace-Agaskar, A. E. Jones, K. Balram, J. Matthews, A. Laing, M. Davanco, L. Chang, J. Bowers, N. Quack, C. Galland, I. Aharonovich, M. Wolff, C. Schuck, N. Sinclair, M. Loncar, T. Komljenovic, D. M. Weld, S. Mookherjea, S. Buckley, M. Radulaski, S. Reitzenstein, G. S. Agarwal, B. Pingault, B. Machielse, D. Mukhopadhyay, A. V. Akimov, A. Zheltikov, K. Srinivasan, W. Jiang, T. McKenna, J. Lu, H. Tang, A. H. Safavi-Naeini, S. Steinhauer, A. Elshaari, V. Zwiller, P. Davids, N. Martinez, M. Gehl, J. Chiaverini, K. Mehta, J. Romero, N. Lingaraju, A. M. Weiner, D. Peace, R. Cernansky, M. Lobino, E. Diamanti, R. Camacho, and L. T. Vidarte, "Roadmap on integrated quantum photonics," *Journal of Physics: Photonics*, Aug. 2021.

[32] H. Subbaraman, X. Xu, A. Hosseini, X. Zhang, Y. Zhang, D. Kwong, and R. T. Chen, "Recent advances in silicon-based passive and active optical interconnects," *Optics Express*, vol. 23, pp. 2487–2511, Jan. 2015.

[33] M. Haurylau, G. Chen, H. Chen, J. Zhang, N. A. Nelson, D. H. Albonesi, E. G. Friedman, and P. M. Fauchet, "On-chip optical interconnect roadmap: Challenges and critical directions," *IEEE Journal of Selected Topics in Quantum Electronics*, vol. 12, pp. 1699–1705, Nov. 2006.

[34] B. J. Shastri, A. N. Tait, T. F. de Lima, W. H. P. Pernice, H. Bhaskaran, C. D. Wright, and P. R. Prucnal, "Photonics for artificial intelligence and neuromorphic computing," *Nature Photonics*, vol. 15, pp. 102–114, Jan. 2021.

[35] R. Yu, S. Cheung, Y. Li, K. Okamoto, R. Proietti, Y. Yin, and S. J. B. Yoo, "A scalable silicon photonic chip-scale optical switch for high performance computing systems," *Optics Express*, vol. 21, pp. 32655–32667, Dec. 2013.

[36] J. Chan, G. Hendry, A. Biberman, and K. Bergman, "Architectural exploration of chip-scale photonic interconnection network designs using physical-layer analysis," *Journal of Lightwave Technology*, vol. 28, pp. 1305–1315, May 2010.

[37] R. Soref and J. Lorenzo, "Single-crystal silicon: a new material for 1.3 and 1.6 μm integrated-optical components," *Electronics Letters*, vol. 21, pp. 953–954, Oct. 1985.

[38] D. Duval, A. B. González-Guerrero, S. Dante, J. Osmond, R. Monge, L. J. Fernández, K. E. Zinoviev, C. Domínguez, and L. M. Lechuga, "Nanophotonic lab-on-a-chip platforms including novel bimodal interferometers, microfluidics and grating couplers," *Lab on a Chip*, vol. 12, pp. 1987–1994, Apr. 2012.

[39] J. Ducrée, "Efficient development of integrated lab-on-a-chip systems featuring operational robustness and manufacturability," *Micromachines*, vol. 10, p. 886, Dec. 2019.

[40] X. Fan and I. M. White, "Optofluidic microsystems for chemical and biological analysis," *Nature Photonics*, vol. 5, pp. 591–597, Sept. 2011.

[41] A. Hochstetter, "Lab-on-a-chip technologies for the single cell level: Separation, analysis, and diagnostics," *Micromachines*, vol. 11, p. 468, Apr. 2020.

[42] A. B. González-Guerrero, J. Maldonado, S. Herranz, and L. M. Lechuga, "Trends in photonic lab-on-chip interferometric biosensors for point-of-care diagnostics," *Analytical Methods*, vol. 8, pp. 8380–8394, Nov. 2016.

[43] A. Alù and N. Engheta, "Wireless at the nanoscale: Optical interconnects using matched nanoantennas," *Physical Review Letters*, vol. 104, p. 213902, May 2010.

[44] L. Novotny and N. van Hulst, "Antennas for light," *Nature Photonics*, vol. 5, pp. 83–90, Feb. 2011.

[45] P. Bharadwaj, B. Deutsch, and L. Novotny, "Optical antennas," *Advances in Optics and Photonics*, vol. 1, pp. 438–483, Aug. 2009.

[46] I. S. Maksymov, A. R. Davoyan, and Y. S. Kivshar, "Enhanced emission and light control with tapered plasmonic nanoantennas," *Applied Physics Letters*, vol. 99, p. 083304, Aug. 2011.

[47] G. Calò, G. Bellanca, B. Alam, A. E. Kaplan, P. Bassi, and V. Petruzzelli, "Array of plasmonic vivaldi antennas coupled to silicon waveguides for wireless networks through on-chip optical technology - WiNOT," *Optics Express*, vol. 26, pp. 30267–30277, Nov. 2018.

[48] A. Espinosa-Soria, E. Pinilla-Cienfuegos, F. J. Díaz-Fernández, A. Griol, J. Martí, and A. Martínez, "Coherent control of a plasmonic nanoantenna integrated on a silicon chip," *ACS Photonics*, vol. 5, pp. 2712–2717, June 2018.

[49] V. Giannini, A. I. Fernàndez-Domìnguez, S. C. Heck, and S. A. Maier, "Plasmonic nanoantennas: Fundamentals and their use in controlling the radiative properties of nanoemitters," *Chemical Reviews*, vol. 111, pp. 3888–3912, June 2011.

[50] M. L. Brongersma, "Engineering optical nanoantennas," *Nature Photonics*, vol. 2, pp. 270–272, May 2008.

[51] A. E. Krasnok, A. E. Miroshnichenko, P. A. Belov, and Y. S. Kivshar, "All-dielectric optical nanoantennas," *Optics Express*, vol. 20, pp. 20599–20604, Aug. 2012.

[52] C. García-Meca, S. Lechago, A. Brimont, A. Griol, S. Mas, L. Sánchez, L. Bellieres, N. S. Losilla, and J. Martí, "On-chip wireless silicon photonics: from reconfigurable interconnects to lab-on-chip devices," *Light: Science & Applications*, vol. 6, pp. e17053–e17053, Mar. 2017.

[53] S. Lechago, C. García-Meca, N. Sánchez-Losilla, A. Griol, and J. Martí, "High signal-to-noise ratio ultra-compact lab-on-a-chip microflow cytometer enabled by silicon optical antennas," *Optics Express*, vol. 26, pp. 25645–25656, Sept. 2018.

[54] F. Merola, P. Memmolo, L. Miccio, M. Mugnano, and P. Ferraro, "Phase contrast tomography at lab on chip scale by digital holography," *Methods*, vol. 136, pp. 108–115, Mar. 2018.

[55] S. O. Isikman, W. Bishara, O. Mudanyali, I. Sencan, T.-W. Su, D. K. Tseng, O. Yaglidere, U. Sikora, and A. Ozcan, "Lensfree on-chip microscopy and tomography for biomedical applications," *IEEE Journal of Selected Topics in Quantum Electronics*, vol. 18, pp. 1059–1072, May 2012.

[56] Y. Park, C. Depeursinge, and G. Popescu, "Quantitative phase imaging in biomedicine," *Nature Photonics*, vol. 12, pp. 578–589, Sept. 2018.

[57] A. Greenleaf, M. Lassas, and G. Uhlmann, "Anisotropic conductivities that cannot be detected by EIT," *Physiological Measurement*, vol. 24, pp. 413–419, Apr. 2003.

[58] N. Engheta and R. W. Ziolkowski, eds., *Metamaterials: Physics and Engineering Explorations*. Wiley, 2006.

[59] A. Alù and N. Engheta, "Achieving transparency with plasmonic and metamaterial coatings," *Physical Review E*, vol. 72, p. 016623, July 2005.

[60] J. B. Pendry, "Controlling electromagnetic fields," *Science*, vol. 312, pp. 1780–1782, June 2006.

[61] D. Schurig, J. J. Mock, B. J. Justice, S. A. Cummer, J. B. Pendry, A. F. Starr, and D. R. Smith, "Metamaterial electromagnetic cloak at microwave frequencies," *Science*, vol. 314, pp. 977–980, Nov. 2006.

[62] D. Rainwater, A. Kerkhoff, K. Melin, J. C. Soric, G. Moreno, and A. Alù, "Experimental verification of three-dimensional plasmonic cloaking in free-space," *New Journal of Physics*, vol. 14, p. 013054, Jan. 2012.

[63] F. Monticone and A. Alù, "Do cloaked objects really scatter less?," *Physical Review X*, vol. 3, p. 041005, Oct. 2013.

[64] W. W. Orrison and J. A. Sanders, "Clinical brain imaging: Computerized axial tomography and magnetic resonance imaging," in *Functional Brain Imaging*, pp. 97–144, Elsevier, 1995.

[65] B. P. Medoff, W. R. Brody, M. Nassi, and A. Macovski, "Iterative convolution backprojection algorithms for image reconstruction from limited data," *Journal of the Optical Society of America*, vol. 73, pp. 1493–1500, Nov. 1983.

[66] P. Müller, M. Schürmann, and J. Guck, "The theory of diffraction tomography," *arXiv:1507.00466v3*, Oct. 2016.

[67] A. C. Kak and M. Slaney, *Principles of Computerized Tomographic Imaging*. IEEE Press, Jan. 1988.

[68] H. Jiang, *Diffuse optical tomography : principles and applications*. CRC Press, Jan. 2011.

[69] M. R. Hajihashemi, S. R. Grobmyer, S. Z. Al-Quran, and H. Jiang, "Noninvasive evaluation of nuclear morphometry in breast lesions using multispectral diffuse optical tomography," *PLoS ONE*, vol. 7, p. e45714, Sept. 2012.

[70] S. L. Jacques, "Optical properties of biological tissues: a review," *Physics in Medicine and Biology*, vol. 58, pp. R37–R61, May 2013.

[71] H. Jiang, B. W. Pogue, M. S. Patterson, K. D. Paulsen, and U. L. Osterberg, "Simultaneous reconstruction of optical absorption and scattering maps in turbid media from near-infrared frequency-domain data," *Optics Letters*, vol. 20, pp. 2128–2130, Oct. 1995.

[72] A. J. Devaney, "Geophysical diffraction tomography," *IEEE Transactions on Geoscience and Remote Sensing*, vol. GE-22, pp. 3–13, Jan. 1984.

[73] P. Targowski, B. Rouba, M. Góra, L. Tymińska-Widmer, J. Marczak, and A. Kowalczyk, "Optical coherence tomography in art diagnostics and restoration," *Applied Physics A*, vol. 92, pp. 1–9, Mar. 2008.

[74] L. A. Shepp and B. F. Logan, "The fourier reconstruction of a head section," *IEEE Transactions on Nuclear Science*, vol. 21, pp. 21–43, June 1974.

[75] J. C. Maxwell, "VIII. a dynamical theory of the electromagnetic field," *Philosophical Transactions of the Royal Society of London*, vol. 155, pp. 459–512, Dec. 1865.

[76] R. F. Harrington and D. G. Dudley, *Time-harmonic electromagnetic fields*. New York: IEEE Press Wiley-Interscience, 2001.

[77] P. M. Morse and H. Feshbach, *Methods of theoretical physics*. New York: McGraw-Hill, 1953.

[78] B. Chen and J. J. Stamnes, "Validity of diffraction tomography based on the first born and the first rytov approximations," *Applied Optics*, vol. 37, pp. 2996–3006, May 1998.

[79] A. J. Devaney, "Inverse-scattering theory within the rytov approximation," *Optics Letters*, vol. 6, pp. 374–376, Aug. 1981.

[80] R. Mueller, M. Kaveh, and G. Wade, "Reconstructive tomography and applications to ultrasonics," *Proceedings of the IEEE*, vol. 67, pp. 567–587, Apr. 1979.

[81] T. C. Wedberg and J. J. Stamnes, "Experimental examination of the quantitative imaging properties of optical diffraction tomography," *Journal of the Optical Society of America A*, vol. 12, pp. 493–500, Mar. 1995.

[82] P. Müller, M. Schürmann, and J. Guck, "ODTbrain: a python library for full-view, dense diffraction tomography," *BMC Bioinformatics*, vol. 16, p. 367, Nov. 2015.

[83] P. Müller, *Optical Diffraction Tomography for Single Cells*. PhD thesis, Technischen Universität Dresden, 2016.

[84] Z. Qin, J. Ylitalo, and J. Oksman, "Circular-array ultrasound holography imaging using the linear-array approach," *IEEE Transactions on Ultrasonics, Ferroelectrics and Frequency Control*, vol. 36, pp. 485–493, Sept. 1989.

[85] J. Rius, M. Ferrando, L. Jofre, E. de Los Reyes, A. Elias, and A. Broquetas, "Microwave tomography: an algorithm for cylindrical geometries," *Electronics Letters*, vol. 23, pp. 564–565, May 1987.

[86] P. Naidu, A. Vasuki, P. Satyamurthy, and L. Anand, "Diffraction tomographic imaging with a circular array," *IEEE Transactions on Ultrasonics, Ferroelectrics and Frequency Control*, vol. 42, pp. 787–789, July 1995.

[87] A. Devaney, "Diffraction tomography using arbitrary transmitter and receiver surfaces," *Ultrasonic Imaging*, vol. 6, pp. 181–193, Apr. 1984.

[88] R. Porter, "Determination of structure of weak scatterers from holographic images," *Optics Communications*, vol. 39, pp. 362–364, Nov. 1981.

[89] M. Abramowitz and I. A. Stegun, eds., *Handbook of mathematical functions*. National bureau of standards applied mathematics series, Dec. 1972.

[90] K. Lee, K. Kim, J. Jung, J. Heo, S. Cho, S. Lee, G. Chang, Y. Jo, H. Park, and Y. Park, "Quantitative phase imaging techniques for the study of cell pathophysiology: From principles to applications," *Sensors*, vol. 13, pp. 4170–4191, Mar. 2013.

[91] G. Popescu, Y. Park, N. Lue, C. Best-Popescu, L. Deflores, R. R. Dasari, M. S. Feld, and K. Badizadegan, "Optical imaging of cell mass and growth dynamics," *American Journal of Physiology-Cell Physiology*, vol. 295, pp. C538–C544, Aug. 2008.

[92] M. Mir, Z. Wang, Z. Shen, M. Bednarz, R. Bashir, I. Golding, S. G. Prasanth, and G. Popescu, "Optical measurement of cycle-dependent cell growth," *Proceedings of the National Academy of Sciences*, vol. 108, pp. 13124–13129, July 2011.

[93] Y. Sung, A. Tzur, S. Oh, W. Choi, V. Li, R. R. Dasari, Z. Yaqoob, and M. W. Kirschner, "Size homeostasis in adherent cells studied by synthetic phase microscopy," *Proceedings of the National Academy of Sciences*, vol. 110, pp. 16687–16692, Sept. 2013.

[94] Y. Sung, W. Choi, N. Lue, R. R. Dasari, and Z. Yaqoob, "Stain-free quantification of chromosomes in live cells using regularized tomographic phase microscopy," *PLoS ONE*, vol. 7, p. e49502, Nov. 2012.

[95] K. L. Cooper, S. Oh, Y. Sung, R. R. Dasari, M. W. Kirschner, and C. J. Tabin, "Multiple phases of chondrocyte enlargement underlie differences in skeletal proportions," *Nature*, vol. 495, pp. 375–378, Mar. 2013.

[96] S. Abuhattum, K. Kim, T. M. Franzmann, A. Eßlinger, D. Midtvedt, R. Schlüßler, S. Möllmert, H.-S. Kuan, S. Alberti, V. Zaburdaev, and J. Guck, "Intracellular mass density increase is accompanying but not sufficient for stiffening and growth arrest of yeast cells," *Frontiers in Physics*, vol. 6, p. 131, Nov. 2018.

[97] K. Kim, H. Yoon, M. Diez-Silva, M. Dao, R. R. Dasari, and Y. Park, "High-resolution three-dimensional imaging of red blood cells parasitized by plasmodium falciparum and in situ hemozoin crystals using optical diffraction tomography," *Journal of Biomedical Optics*, vol. 19, p. 011005, June 2013.

[98] H. Park, S.-H. Hong, K. Kim, S.-H. Cho, W.-J. Lee, Y. Kim, S.-E. Lee, and Y. Park, "Characterizations of individual mouse red blood cells parasitized by babesia microti using 3-d holographic microscopy," *Scientific Reports*, vol. 5, p. 10827, June 2015.

[99] P. Hosseini, S. Z. Abidi, E. Du, D. P. Papageorgiou, Y. Choi, Y. Park, J. M. Higgins, G. J. Kato, S. Suresh, M. Dao, Z. Yaqoob, and P. T. C. So, "Cellular normoxic biophysical markers of hydroxyurea treatment in sickle cell disease," *Proceedings of the National Academy of Sciences*, vol. 113, pp. 9527–9532, Aug. 2016.

[100] A. M. Zysk, E. J. Chaney, and S. A. Boppart, "Refractive index of carcinogen-induced rat mammary tumours," *Physics in Medicine and Biology*, vol. 51, pp. 2165–2177, Apr. 2006.

[101] Y. Cotte, F. Toy, P. Jourdain, N. Pavillon, D. Boss, P. Magistretti, P. Marquet, and C. Depeursinge, "Marker-free phase nanoscopy," *Nature Photonics*, vol. 7, pp. 113–117, Jan. 2013.

[102] Y. Sung, N. Lue, B. Hamza, J. Martel, D. Irimia, R. R. Dasari, W. Choi, Z. Yaqoob, and P. So, "Three-dimensional holographic refractive-index measurement of continuously flowing cells in a microfluidic channel," *Physical Review Applied*, vol. 1, p. 014002, Feb. 2014.

[103] P. Hosseini, Y. Sung, Y. Choi, N. Lue, Z. Yaqoob, and P. So, "Scanning color optical tomography (SCOT)," *Optics Express*, vol. 23, pp. 19752–19762, July 2015.

[104] www.tomocube.com.

[105] S. O. Isikman, W. Bishara, H. Zhu, and A. Ozcan, "Optofluidic tomography on a chip," *Applied Physics Letters*, vol. 98, p. 161109, Apr. 2011.

[106] S. O. Isikman, W. Bishara, U. Sikora, O. Yaglidere, J. Yeah, and A. Ozcan, "Field-portable lensfree tomographic microscope," *Lab on a Chip*, vol. 11, pp. 2222–2230, May 2011.

[107] M. Habaza, M. Kirschbaum, C. Guernth-Marschner, G. Dardikman, I. Barnea, R. Korenstein, C. Duschl, and N. T. Shaked, "Rapid 3d refractive-index imaging of live cells in suspension without labeling using dielectrophoretic cell rotation," *Advanced Science*, vol. 4, p. 1600205, Oct. 2016.

[108] M. Schürmann, G. Cojoc, S. Girardo, E. Ulbricht, J. Guck, and P. Müller, "Three-dimensional correlative single-cell imaging utilizing fluorescence and refractive index tomography," *Journal of Biophotonics*, vol. 11, p. e201700145, Sept. 2017.

[109] U. S. Kamilov, I. N. Papadopoulos, M. H. Shoreh, A. Goy, C. Vonesch, M. Unser, and D. Psaltis, "Learning approach to optical tomography," *Optica*, vol. 2, pp. 517–522, May 2015.

[110] T. Kim, R. Zhou, M. Mir, S. D. Babacan, P. S. Carney, L. L. Goddard, and G. Popescu, "White-light diffraction tomography of unlabelled live cells," *Nature Photonics*, vol. 8, pp. 256–263, Jan. 2014.

[111] A. Greenbaum, W. Luo, T.-W. Su, Z. Göröcs, L. Xue, S. O. Isikman, A. F. Coskun, O. Mudanyali, and A. Ozcan, "Imaging without lenses: achievements and remaining challenges of wide-field on-chip microscopy," *Nature Methods*, vol. 9, pp. 889–895, Aug. 2012.

[112] P. Paiè, R. M. Vázquez, R. Osellame, F. Bragheri, and A. Bassi, "Microfluidic based optical microscopes on chip," *Cytometry Part A*, vol. 93, pp. 987–996, Sept. 2018.

[113] Y. Wu and A. Ozcan, "Lensless digital holographic microscopy and its applications in biomedicine and environmental monitoring," *Methods*, vol. 136, pp. 4–16, Mar. 2018.

[114] J. P. Robinson and M. Roederer, "Flow cytometry strikes gold," *Science*, vol. 350, pp. 739–740, Nov. 2015.

[115] M. Padgett and R. Bowman, "Tweezers with a twist," *Nature Photonics*, vol. 5, pp. 343–348, May 2011.

[116] Y. Yang, Q. Li, and M. Qiu, "Broadband nanophotonic wireless links and networks using on-chip integrated plasmonic antennas," *Scientific Reports*, vol. 6, Jan. 2016.

[117] E. M. Strohm, V. Gnyawali, J. A. Sebastian, R. Ngunjiri, M. J. Moore, S. S. H. Tsai, and M. C. Kolios, "Sizing biological cells using a microfluidic acoustic flow cytometer," *Scientific Reports*, vol. 9, Mar. 2019.

[118] G. Bellanca, G. Calò, A. E. Kaplan, P. Bassi, and V. Petruzzelli, "Integrated vivaldi plasmonic antenna for wireless on-chip optical communications," *Optics Express*, vol. 25, pp. 16214–16227, June 2017.

[119] A. E. Krasnok, C. R. Simovski, P. A. Belov, and Y. S. Kivshar, "Superdirective dielectric nanoantennas," *Nanoscale*, vol. 6, pp. 7354–7361, Apr. 2014.

[120] T. Kosako, Y. Kadoya, and H. F. Hofmann, "Directional control of light by a nano-optical yagi–uda antenna," *Nature Photonics*, vol. 4, pp. 312–315, Mar. 2010.

[121] S. Lechago, C. García-Meca, A. Griol, M. Kovylina, L. Bellieres, and J. Martí, "All-silicon on-chip optical nanoantennas as efficient interfaces for plasmonic devices," *ACS Photonics*, vol. 6, pp. 1094–1099, May 2019.

[122] F. J. Díaz-Fernández, E. Pinilla-Cienfuegos, C. García-Meca, S. Lechago, A. Griol, and J. Martí, "Characterisation of on-chip wireless interconnects based on silicon nanoantennas via near-field scanning optical microscopy," *IET Optoelectronics*, vol. 13, pp. 72–76, Apr. 2019.

[123] J. Sun, E. Timurdogan, A. Yaacobi, E. S. Hosseini, and M. R. Watts, "Large-scale nanophotonic phased array," *Nature*, vol. 493, pp. 195–199, Jan. 2013.

[124] K. V. Acoleyen, H. Rogier, and R. Baets, "Two-dimensional optical phased array antenna on silicon-on-insulator," *Optics Express*, vol. 18, pp. 13655–13660, June 2010.

[125] B. Bhushan, ed., *Scanning Near-Field Optical Microscopy*. Springer Netherlands, 2012.

[126] J. Sabek, F. J. Díaz-Fernández, L. Torrijos-Morán, Z. Díaz-Betancor, Á. Maquieira, M.-J. Bañuls, E. Pinilla-Cienfuegos, and J. García-Rupérez, "Experimental study of an evanescent-field biosensor based on 1d photonic bandgap structures," *Beilstein Journal of Nanotechnology*, vol. 10, pp. 967–974, Apr. 2019.

[127] P. Dvořák, Z. Édes, M. Kvapil, T. Šamořil, F. Ligmajer, M. Hrtoň, R. Kalousek, V. Křápek, P. Dub, J. Spousta, P. Varga, and T. Šikola, "Imaging of near-field interference patterns by aperture-type SNOM – influence of illumination wavelength and polarization state," *Optics Express*, vol. 25, pp. 16560–16573, July 2017.

[128] P. Bazylewski, S. Ezugwu, and G. Fanchini, "A review of three-dimensional scanning near-field optical microscopy (3d-SNOM) and its applications in nanoscale light management," *Applied Sciences*, vol. 7, p. 973, Sept. 2017.

[129] I. Horcas, R. Fernández, J. M. Gómez-Rodríguez, J. Colchero, J. Gómez-Herrero, and A. M. Baro, "WSXM: A software for scanning probe microscopy and a tool for nanotechnology," *Review of Scientific Instruments*, vol. 78, p. 013705, Jan. 2007.

[130] A. Sakai, H. Go, and T. Baba, "Sharply bent optical waveguide silicon-on-insulator substrate," in *Physics and Simulation of Optoelectronic Devices IX*, SPIE, July 2001.

[131] J. García-Rupérez, V. Toccafondo, M. J. Bañuls, J. G. Castelló, A. Griol, S. Peransi-Llopis, and Á. Maquieira, "Label-free antibody detection using band edge fringes in SOI planar photonic crystal waveguides in the slow-light regime," *Optics Express*, vol. 18, pp. 24276–24286, Nov. 2010.

[132] J. E. Saunders, C. Sanders, H. Chen, and H.-P. Loock, "Refractive indices of common solvents and solutions at 1550 nm," *Applied Optics*, vol. 55, pp. 947–953, Feb. 2016.

[133] M. Kadic, T. Bückmann, R. Schittny, and M. Wegener, "Experiments on cloaking in optics, thermodynamics and mechanics," *Philosophical Transactions of the Royal Society A: Mathematical, Physical and Engineering Sciences*, vol. 373, p. 20140357, Aug. 2015.

[134] P.-Y. Chen, J. Soric, and A. Alù, "Invisibility and cloaking based on scattering cancellation," *Advanced Materials*, vol. 24, pp. OP281–OP304, Oct. 2012.

[135] F. Monticone and A. Alù, "Invisibility exposed: physical bounds on passive cloaking," *Optica*, vol. 3, pp. 718–724, July 2016.

[136] R. Fleury, F. Monticone, and A. Alù, "Invisibility and cloaking: Origins, present, and future perspectives," *Physical Review Applied*, vol. 4, p. 037001, Sept. 2015.

[137] H. Chen and B. Zheng, "Broadband polygonal invisibility cloak for visible light," *Scientific Reports*, vol. 2, p. 255, Feb. 2012.

[138] F. Gömöry, M. Solovyov, J. Souc, C. Navau, J. Prat-Camps, and A. Sanchez, "Experimental realization of a magnetic cloak," *Science*, vol. 335, pp. 1466–1468, Mar. 2012.

[139] R. Schittny, M. Kadic, T. Buckmann, and M. Wegener, "Invisibility cloaking in a diffusive light scattering medium," *Science*, vol. 345, pp. 427–429, June 2014.

[140] A. Alù and N. Engheta, "Cloaking a sensor," *Physical Review Letters*, vol. 102, p. 233901, Jun 2009.

[141] M. G. Silveirinha, A. Alù, and N. Engheta, "Parallel-plate metamaterials for cloaking structures," *Physical Review E*, vol. 75, p. 036603, Mar. 2007.

[142] P. B. Johnson and R. W. Christy, "Optical constants of the noble metals," *Physical Review B*, vol. 6, pp. 4370–4379, Dec. 1972.

[143] U. Leonhardt, "Optical conformal mapping," *Science*, vol. 312, pp. 1777–1780, June 2006.

[144] S. A. Cummer, B.-I. Popa, D. Schurig, D. R. Smith, and J. Pendry, "Full-wave simulations of electromagnetic cloaking structures," *Physical Review E*, vol. 74, p. 036621, Sept. 2006.

[145] B. Zhang, B.-I. Wu, H. Chen, and J. A. Kong, "Rainbow and blueshift effect of a dispersive spherical invisibility cloak impinged on by a nonmonochromatic plane wave," *Physical Review Letters*, vol. 101, p. 063902, Aug. 2008.

[146] B. Orazbayev, M. Beruete, A. Martínez, and C. García-Meca, "Diffusive-light invisibility cloak for transient illumination," *Physical Review A*, vol. 94, p. 063850, Dec. 2016.

[147] P. R. Edholm and G. T. Herman, "Linograms in image reconstruction from projections," *IEEE Transactions on Medical Imaging*, vol. 6, pp. 301–307, Dec. 1987.

[148] D. Nahamoo, S. Pan, and A. Kak, "Synthetic aperature diffraction tomography and its interpolation-free computer implementation," *IEEE Transactions on Sonics and Ultrasonics*, vol. 31, pp. 218–229, July 1984.

[149] D. J. Blumenthal, "Photonic integration for UV to IR applications," *APL Photonics*, vol. 5, p. 020903, Feb. 2020.

[150] J. E. Vázquez-Lozano, *Spin-Dependent Optical Phenomena: Fundamentals and Applications*. PhD thesis, Universitat Politècnica de València, 2021.

[151] T. M. Evans, L. Bira, J. B. Gastelum, L. T. Weiss, and N. L. Vanderford, "Evidence for a mental health crisis in graduate education," *Nature Biotechnology*, vol. 36, pp. 282–284, Mar. 2018.

[152] E. N. Satinsky, T. Kimura, M. V. Kiang, R. Abebe, S. Cunningham, H. Lee, X. Lin, C. H. Liu, I. Rudan, S. Sen, M. Tomlinson, M. Yaver, and A. C. Tsai, "Systematic review and meta-analysis of depression, anxiety, and suicidal ideation among ph.d. students," *Scientific Reports*, vol. 11, p. 14370, July 2021.

[153] S. Guthrie, C. Lichten, J. van Belle, S. Ball, A. Knack, and J. Hofman, *Understanding mental health in the research environment: A Rapid Evidence Assessment*. RAND Corporation, 2017.

[154] C. Woolston, "Feeling overwhelmed by academia? you are not alone," *Nature*, vol. 557, pp. 129–131, May 2018.

[155] L. Torrijos-Morán, *Photonic applications based on bimodal interferometry in periodic integrated waveguides*. PhD thesis, Universitat Politècnica de València, 2021.

[156] M. Schürmann, J. Scholze, P. Müller, J. Guck, and C. J. Chan, "Cell nuclei have lower refractive index and mass density than cytoplasm," *Journal of Biophotonics*, vol. 9, pp. 1068–1076, Mar. 2016.

[157] P. Müller and J. Guck, "Response to comment on "cell nuclei have lower refractive index and mass density than cytoplasm"," *Journal of Biophotonics*, vol. 11, p. e201800095, May 2018.

[158] O. M. Gaddoura and M. Ding, "Diffraction tomography: It's application in ultrasound," *International Journal of Engineering and Manufacturing*, vol. 1, pp. 10–17, Aug. 2011.

[159] L. S. Martin, C.-C. Chen, and J. Miao, "Multi-shell ankylography," *arXiv:1311.4517*, Nov. 2013.

[160] S. Yushanov, J. S. Crompton, and K. C. Koppenhoefer, eds., *Mie Scattering of Electromagnetic Waves*, COMSOL Conference in Boston, Oct. 2013.

List of figures

List of tables

List of acronyms

1D	One-Dimensional
2D	Two-Dimensional
3D	Three-Dimensional
ANN	Artificial Neural Network
AU	Arbitrary Units
CMOS	Complementary Metal–Oxide–Semiconductor
CST	Computer Simulation Technology
CT	Computed Tomography
DIW	Deionized Water
DT	Diffraction Tomography
ECL	External Cavity Laser
EIT	Electric Impedance Tomography
FDTD	Finite Difference Time Domain
FEDER	European Regional Development Fund
FFT	Fast Fourier Transform
FIT	Finite Integration Technique
GOPU	Gabinete de Orientación Psicopedagógica Universitaria
HSQ	Hydrogen Silsesquioxane
iFFt	inverse Fourier transform

LoC	Lab on a Chip
MCP	Missing cone problem
NA	Nanoantenna
NTC	Nanophotonics Technology Center
ODT	Optical Diffraction Tomography
OF	Opto-Fluidic
OWP	On-chip wireless photonics
PET	Positron Emission Tomography
PhD	Doctor of Philosophy
PIC	Photonic Integrated Circuit
PoC	Point of Care
PWI	Plain Wave Illumination
QPI	Quantum Phase Imaging
RI	Refractive Index
RMS	Root-Mean-Square
SA	Synthetic aperture
SCS	Scattering Cross Section
SEM	Scanning Electron Microscope
SFD	Spatial Frequency Domain
SiN	Silicon Nitride
SNOM	Scanning Near-field Optical Microscopy
SOI	Silicon On Insulator
TE	Transverse Electric
TPM	Tomographic Phase Microscopy
UPV	Universitàt Politècnica de València